bedankt - blagodaria -

danke schön - thanks - merci

Toen Sonja onze groep verliet, had Prof. Em. R. Coussement, alias Romain, schrik en de rest van het IKS hoop dat het aantal decibels in onze gang gevoelig zou afnemen. Niets bleek minder waar: Nico was er nog en ook de gulle lach van Dana is ondertussen iedereen bekend. Dat de goede sfeer al jaren het handelsmerk van onze groep is, hebben we in de eerste plaats aan Romain te danken. Hij is de mening toegedaan dat plezier in het werk een nodige voorwaarde voor goede fysica is. Zijn enthousiasme lijkt alleen maar toe te nemen sinds hij emeritus is en ook zijn creativiteit is alombekend. Nu is het aan Gerda om het roer over te nemen en ik wens haar hierbij alle succes toe, iets wat natuurlijk ook voor Jos geldt. Gerda is degene die met een interessante thesis binnenvalt op het ogenblik dat ik een 'writer's block' heb, of die zorgt dat ik de bibliotheek binnen kan als de gemeenschappelijke IKS-sleutel weer eens verdwenen is. Ze heeft het vermogen om haar doctoraatsstudenten veel verantwoordelijkheid te geven, maar toch steeds met een helpende hand klaar te staan. Als ik nu zonder problemen een LEMS-experiment kan leiden, of iets van het schillenmodel afweet, dan is dat in de eerste plaats aan haar te danken. *Although officially not my promotor, also Dimiter was following my work from nearby. This thesis would not exist if he would not have been thinking about K-isomers and magnetic rotors as interesting cases to study. He has guided me through the nuclear physics world and his interest in my work gave me the necessary motivation. He made me understand that nuclei are fascinating objects to study.* Goede bazen mogen dan al onont-

beerlijk zijn voor het klaarstomen van een thesis, goede teamgenoten zijn dat evenzeer. Dus, dank je wel, Nico, voor het bijna missen van je trein, Stéphanie, voor de morele steun in tijden van hoogoplopende frustraties, *Georgi, for finding back disappeared books*, Dana, voor je eeuwig goede humeur, Riet, voor de vele babbeluren, ikoontjes e.a., Wim, voor het brengen van wat rust, en Jos, voor het plaatsen van komma's tot je er bij neervalt. Een dank je wel ook aan de thesisstudenten, ex-groepsleden en *foreign guests*, die steeds voor een aangename afwisseling zorgden.

Ook over de groepsgrenzen heen zijn er heel wat mensen die een plaatsje op deze pagina's verdienen. Stefaan b.v., die al heel wat tijd besteed heeft aan het maken van WIEN berekeningen voor mij en bij wie ik altijd met mijn naïeve vragen terecht kan. Verder zou geen enkel experiment mogelijk zijn zonder de hulp van het technisch personeel met Erik, Willy S., Maurice, Guido, Willy C., Eddy en alle anderen, inclusief Luc Verwilst en Willy Schollaert. Als ik twee dagen voor een experiment nog een nieuwe detectortafel nodig had, hoefde ik er maar één te kiezen uit Willy's grote toverhoed. Na datzelfde experiment was het aan Maurice om zich met veel geduld en vakmanschap door een stapel elektronica heen te worstelen, waarvan de helft uiteindelijk helemaal niet kapot bleek te zijn. Josee, Sally, Katia, Inge en in een vorig leven ook Marie-Anne houden dan weer met de glimlach de bureaucratische molen draaiende. *Evidemment je ne veux pas oublier les ingénieurs (Guido, Marc,...) et les méchaniciens (Emile, Fernand, Jacques,...) au cyclotron CYCLONE á Louvain-la-Neuve pour toujours pourvoir les meilleurs faisceaux et pour toujours être prêt á aider la fille. Merci aussi, Carmen, pour le sourire avec lequel tu guides toutes les demandes.*

During my Ph. D. I had the luck to travel regularly and meet a lot of scientists from abroad. Apart from the pleasant memories, these contacts have also been very fruitful from scientific point of view. I've enjoyed very much the collaboration with the group of Prof. H. Hübel and I'm glad that he proposed me to measure the quadrupole moment of the $(I^{\pi} = 11^{-})$ *isomer in* ^{196}Pb *at the Cape Toum conference. Sebastian, I guess that it should be possible that some day you play the organ here in Leuven. Thanks already for the many efforts you did on the*

TAC calculations. Prof. P. M. Walker pointed to the $^{179}W(I^{\pi} = 35/2^{-})$ *case and he was always ready to send me level schemes or explanations, whenever I needed them. Prof. F. Dönau and his group gave me a warm welcome during my stay in Rossendorf. This thesis is partly the result of his excellent teaching skills.* Prof. K. Heyde stond dan weer klaar met prompte e-mailantwoorden als ik vastzat bij de schillenmodelberekeningen. *Thanks also to all the people who provided me useful comments on this thesis: the jury members, Prof. Em. R. Coussement, Dr. G. Neyens, Prof. D. L. Balabanski, Prof. J. Odeurs, Prof. P. Van Duppen, Dr. P. Lievens, Prof. H. Hübel and Prof. P. M. Walker, but also Prof. K. Heyde, Prof. F. Dönau and Prof. P. Blaha.*

Tot slot een woordje van dank aan die mensen bij wie ik na elke verre reis telkens opnieuw mag thuiskomen: mijn ouders, broers Wim en Piet, schoonzus An en neefje Thibault.

Contents

Introduction 1

1 Physics motivation 7

1.1 Deformed nuclei near the closed shells 7

1.1.1 The nuclear shell model 7

1.1.2 The deformed shell model 10

1.1.3 Intruder states in the Pb region 13

1.1.4 Measured deformations of intruder states in the Pb region 17

1.1.5 The $(I^{\pi} = 11^{-})$ intruder states in Pb 20

1.2 Deformed nuclei in between the closed shells 23

1.2.1 Rotation of a deformed nucleus 23

1.2.2 K-isomers 26

1.2.3 Rotational band crossings 29

1.2.4 A qualitative approach to pairing 31

1.2.5 The $(I^{\pi} = K^{\pi} = 35/2^{-})$ isomer in ^{179}W 33

1.3 Rotational bands in spherical nuclei: magnetic rotation 38

1.3.1 The shears mechanism 38

1.3.2 Shears bands in ^{196}Pb 41

1.4 The tilted axis cranking (TAC) theory 44

1.4.1 A quantitative approach to pairing correlations 45

1.4.2 Quasi-particle states 47

1.4.3 The $\hat{Q} \cdot \hat{Q}$ interaction 49

1.4.4 The Strutinsky shell correction procedure 49

1.4.5 The Cranking Hamiltonian 51
1.4.6 The tilted axis cranking (TAC) Hamiltonian 52
1.4.7 Physical quantities extracted from the TAC code 54
1.4.8 TAC and symmetry breaking in nuclei 56
1.5 Conclusion 59

2 Level mixing spectroscopy **61**
2.1 Basic principles of LEMS 61
2.1.1 The LEMS Hamiltonian 61
2.1.2 Study of the electromagnetic perturbation via the angular distribution of the γ radiation 63
2.2 Double perturbations 69
2.2.1 Time-differential expression for the double perturbation factor 70
2.2.2 Time-integrated expression for the double perturbation factor 71
2.2.3 Influence of the direct feeding 72
2.3 The experimental setup and analysis 74
2.3.1 The LEMS setup 74
2.3.2 The LEMS analysis 74
2.3.3 Pulsing of the beam 75
2.4 LEMS in a recoil-shadow geometry 77
2.4.1 Improvement of the peak to background ratio in a recoil-shadow geometry 77
2.4.2 Experimental results on the influence of the $\vec{I}\cdot\vec{J}$ interaction on the LEMS technique 78

3 Quadrupole moments of the $I^\pi = 11^-$ intruder isomers in ^{194,196}Pb **85**
3.1 Introduction 85
3.2 Experimental details 86
3.2.1 Production and detection of the ^{194,196}Pb($I^\pi = 11^-, I^\pi = 12^+$) isomers 86
3.2.2 The choice of Re as a target and a LEMS host 88

3.3 Experimental results on ^{196}Pb 89
3.3.1 The EFG of Pb in Re 89
3.3.2 The quadrupole moment of the ^{196}Pb($I^\pi = 11^-$) isomer . . 92
3.4 Discussion of the quadrupole moment of the ^{196}Pb($I^\pi = 11^-$) intruder isomer 95
3.4.1 Quadrupole moments within the spherical shell model . . . 95
3.4.2 A comparison of the quadrupole moments of the ^{198}Po($I^\pi = 11^-$) isomer and the ^{196}Pb($I^\pi = 11^-$) isomer 96
3.4.3 A comparison of the quadrupole moments of the ^{197}Bi($I^\pi = 9/2^-$) ground-state and the ^{195}Tl($I^\pi = 9/2^-$) isomer 99
3.4.4 The influence of the $1i_{13/2}$ proton on the quadrupole moments of the ($I^\pi = 11^-$) isomers in ^{198}Po and ^{196}Pb 101
3.4.5 Theoretical approach to the quadrupole moments of the 11^- isomers in Pb and Po, the $9/2^-$ isomers in Tl and the $9/2^-$ ground-states in Bi 102
3.5 The quadrupole moment of the ^{196}Pb($I^\pi = 16^-$) magnetic rotational bandhead 108
3.5.1 The coupling of $Q_s(I^\pi = 11^-)$ and $Q_s(I^\pi = 12^+)$ to $Q_s(I^\pi = 16^-)$ 108
3.5.2 Discussion 110
3.6 Experimental results on ^{194}Pb 112
3.6.1 Systematics of the measured spectroscopic quadrupole moments in the even Pb isotopes 116
3.7 Conclusion 118

4 Quadrupole moment of the 5-quasiparticle $I^\pi = K^\pi = 35/2^-$ isomer in ^{179}W **119**
4.1 Introduction 119
4.2 Experimental details 120
4.2.1 Production and detection of the ^{179}W($K^\pi = I^\pi = 35/2^-$) isomer 120

4.2.2 Choice of Tl as a LEMS host 121
4.3 Experimental results of the LEMS measurement on the ($I^\pi = 35/2^-$) isomer in ^{179}W 122
4.4 The electric field gradient of W in Tl 126
4.4.1 Ab initio calculation of the EFG of W in Tl at 0 K 127
4.4.2 The inverted LEMS technique 129
4.4.3 Experimental results of the inverted LEMS measurement on WTl 131
4.5 Discussion of the experimental results 133
4.5.1 The quadrupole moment of the $K^\pi = 35/2^-$ isomer in ^{179}W 133
4.5.2 The electric field gradient of W in Tl 138
4.6 Conclusions and outlook 141

5 Conclusions and outlook 143

A Deformation parameters and quadrupole moments - definitions 149
A.1 Intrinsic versus spectroscopic quadrupole moment 149
A.2 The deformation of atomic nuclei 151

B Measurable quantities allowing to extract the intrinsic quadrupole moment and the deformation of atomic nuclei 159
B.1 The spectroscopic quadrupole moment 159
B.2 The $B(E2)$ reduced transition probabilities 160
B.3 Nuclear radii - $E0$ moments 162
B.4 The mixing ratio 162

C The influence of the $\vec{I} \cdot \vec{J}$ interaction on the LEMS technique 165
C.1 The combined magnetic + $\vec{I} \cdot \vec{J}$ interaction 165
C.2 The LEMS formalism including the $\vec{I} \cdot \vec{J}$ interaction 169

D Calculating the double perturbed fraction and the direct feedings 173

E Calculation of the quadrupole moment of the $\pi(3s_{1/2}^{-2}1h_{9/2}1i_{13/2})_{11^-}$ isomer in ^{200}Pb by taking into account particle-core coupling 179

Samenvatting 187

Introduction

Nuclear structure information is of particular importance at the limits of nuclear existence. Exactly there, at the extremes of excitation energy, E_x, total nuclear angular momentum, I, neutron number, N, and proton number, Z, new curiosa are expected to appear. This thesis focuses on a detailed study of nuclear metastable states, the so called 'isomeric' states, at high excitation energy and high angular momentum. Due to their long life times these isomeric states provide the opportunity to extract directly detailed information on the basic nuclear properties, i.e., their proton-neutron configuration and their deformation. Several reasons may cause a delay in the nuclear decay of an excited state. It is difficult for them either to change their shape to match the states to which they are decaying, the 'shape isomers', or to change their spin, the 'spin traps', or to change their spin orientation relative to an axis of symmetry, the 'K-traps' [Wal99]. Usually the long-lived states in atomic nuclei are classified accordingly.

Their long life times make the isomers fascinating objects to study. The first question to address is: are the states isomeric because they have to change their shape, their spin or the orientation of their spin ? Furthermore, the life times give access to otherwise inaccessible pieces of information. They allow isomers to interact with the magnetic fields and/or electric fields in their surroundings. By studying the magnetic dipole interaction the nuclear magnetic dipole moment can be extracted and, in a similar way, the spectroscopic quadrupole moment can be extracted from the study of the electric quadrupole interaction. Both nuclear moments help us to understand the structure of the nucleus. The magnetic moment, $\vec{\mu}$, is a fingerprint of the orbitals which are occupied by the nucleons

which did not pair off to spin 0 and their proton-versus-neutron character. The spectroscopic quadrupole moment, Q_s, provides information on the deformation of the nucleus. A spherical nucleus, e.g., has $Q_s = 0$ in its ground-state.

Since the mid-eighties the Leuven group of Prof. R. Coussement has been developing several techniques, the so-called level mixing techniques [Cou85, Sch89, Har91b, Ney94, Cou99], to measure nuclear moments, concentrating on nuclear quadrupole moments. One of the variants, the level mixing spectroscopy technique (LEMS), which is explained in chapter 2, is especially suitable for measuring quadrupole moments of high spin isomers, although also other information, which is valuable for other fields of physics, such as electric field gradients, can be extracted. This thesis illustrates the wide variety of possible applications of the LEMS technique and its extensions and variants, with the emphasis on the nuclear structure information which can be derived from a LEMS experiment.

The critical reader might wonder why such efforts have been made to be able to extract nuclear deformations. Chapter 1 shows in detail how in the different regions of the nuclear map the deformation plays a crucial role for the understanding of the nuclear properties. The entry point is simple. In the vicinity of the closed shells (similar to the atoms a shell structure exists in nuclei and full proton and/or neutron shells give the nucleus extra stability) the nucleus is expected to be nearly spherical. If both the proton and the neutron number are far away from the closed shells the nuclei are deformed. Whereas the excitations of closed shell nuclei are mainly determined by exciting the individual nucleons, a deformed, axially symmetric nucleus can also rotate as a whole about an axis that is perpendicular to its symmetry axis. As this is a rotation of an asymmetric charge distribution, it is referred to as 'electric rotation'. Quantum-mechanically there is no collective rotation about the nuclear symmetry axis because the time evolution would result in a system that is indistinguishable from the original. The latter is the reason why a spherical nucleus cannot rotate.

Nevertheless, several experimental discoveries reveal that this picture is oversimplified. In the Pb nuclei, e.g., which have a closed $Z = 82$ proton shell and, therefore, are thought to be nearly spherical, rotational bands have been discov-

ered [Bal91, Ami00]. This has led to an extension of the concept of rotation in quantal systems. Not an asymmetric charge distribution, but an asymmetric current distribution allows these nuclei to rotate [Fra00a]. Hence the name 'magnetic rotation' has been adopted for these excitations. However, an immediate question that needs to be addressed is whether these rotors are indeed nearly spherical.

Another interesting phenomenon in closed shell nuclei is the occurrence of particle-hole excitations across the shell gap which are surprisingly low in energy [VD84, Hey83, Woo92]. Now it is understood that these excitations involve the so-called 'intruder orbitals'. These orbitals reduce their energies compared to the corresponding spherical shell model energy when the nucleus takes a deformed shape. Furthermore, 2particle-2hole excitations across the shell gap are energetically favored compared to the (odd particle)-(odd hole) excitations. E.g., it has recently been discovered that the 2particle-2hole and 4particle-4hole excitations across the $Z = 82$ shell gap in ^{186}Pb are the first excited states in this nucleus [And00]. This indicates that, apart from the deformation, also the pairing plays a crucial role in these excitations. However, despite of the fact that the deformation is one of the two important parameters for the understanding of the intruder states, only for a few of them the deformation has been determined experimentally in the Pb region [Bou85, Wal87]. Section 1.1 treats in some more detail the physics background behind the intruder states.

The interplay between the deformation (i.e., the long range part of the nucleon-nucleon interaction) and the pairing (i.e., the short range part of the nucleon-nucleon interaction) is also important far away from the closed shells. For example the moment of inertia of a collective rotor is less, by a factor of 3, than the rigid body value. This is due to the pairing correlations between the nucleons. The ground-state is a superposition of 0^+ paired configurations. This pairing of two fermions is similar to the electron-electron pairing in superconductors. Superconductivity in metals can be quenched by heat and/or magnetic fields. The analogues in nuclei are internal excitation energy and collective rotation. The main difference between nuclei and superconducting metals is the number of par-

ticles. The limited number of particles makes that no sharp phase transition takes place, but that the pairing is reduced step-by-step. The question arises how many pairs need to break up before all pairing correlations are fully blocked [Wal99]. The way to learn something about pairing in nuclei is by extracting experimentally the moment of inertia which depends on both the pairing and the deformation. Yet, direct measurements of the deformation of collective rotors are a must for a thorough study of the pairing correlations in nuclei.

Section 1.4 explains how K-isomers and magnetic rotors can be described theoretically by the tilted axis cranking (TAC) theory. In these calculations the nucleus is allowed to rotate around an axis that is tilted away from the principal axes of the nucleus. Both the K-isomers and the magnetic rotors rotate in such a way. This will be explained in sections 1.2 and 1.3, respectively.

One of the major nuclear physics goals of this work is to determine experimentally the spectroscopic quadrupole moment of a magnetic rotor. However, this is not straightforward due to the short life times of the states involved. Therefore, we have measured the spectroscopic quadrupole moment of the ^{196}Pb($I^\pi = 11^-$) shape isomer, which has the same $\pi(3s_{1/2}^{-2}1h_{9/2}1i_{13/2})_{11^-}$ proton configuration as suggested for the $I^\pi = 16^-$ magnetic rotational bandhead. This result allows a deduction of the spectroscopic quadrupole moment of a magnetic rotational bandhead. Also the deformation of the ^{196}Pb($I^\pi = 11^-$) isomer by itself is interesting, because of the intruder configuration of the isomer.

The nuclear reaction to produce ^{196}Pb isomers has been chosen such that also the ^{194}Pb($I^\pi = 11^-$) isomer has been populated. Besides the ($I^\pi = 11^-$) shape isomer the ^{196,194}Pb isotopes contain the $I^\pi = 12^+$ spin trap. Both of them influence the LEMS curve. The analysis of the transitions in ^{194}Pb provides an excellent experimental test for the LEMS formalism, taking into account the perturbations due to two isomers. This formalism has been applied for the first time in practice to extract the spectroscopic quadrupole moment of the ^{194}Pb($I^\pi = 11^-$) isomer. This information was otherwise not accessible in our series of experiments. Experimental and theoretical results on the Pb isomers are discussed in chapter 3.

The next chapter shows the experimental results on the spectroscopic quadrupole moment of the ^{179}W($I^\pi = K^\pi = 35/2^-$) isomer. Five unpaired nucleons are the building blocks for the ^{179}W($I^\pi = K^\pi = 35/2^-$) K-trap. This makes it a suitable isomer for studying the reduction of the pairing correlations in nuclei. The usual way to do it is by extracting the moment of inertia of the rotational band built on this K-trap and comparing it with the moment of inertia of the ground-state band. So far, it is usually assumed that the deformation of the ground-state and the isomeric state are the same. However, is this a valid assumption? The ^{179}W($I^\pi = K^\pi = 35/2^-$) is an extra interesting case because its life time is much shorter than predicted by its K-trap character [Wal91].

The quadrupole moments are determined by measuring their interaction with an electric field gradient provided by a crystalline material. The Pb nuclei were implanted in a Re lattice and the W nuclei in a Tl lattice. The choices of these lattices are well motivated as explained in chapters 3 and 4. The electric field gradients of Pb in Re and W in Tl were not known before this work was initiated and are hence new solid state results. Therefore, chapters 3 and 4 contain a section discussing the electric field gradients in Re and in Tl, respectively. In addition the electric field gradient in Tl is strongly temperature dependent. Subsection 4.4.2 explains how a variant of the LEMS technique, the 'inverted LEMS technique' allows the determination of the temperature dependence of the electric field gradient. Such an experiment was performed for the first time.

The quadrupole moments, obtained from the several experiments, have been compared with shell model calculations, taking into account the interaction between the valence nucleons and the underlying core, and TAC calculations. They reveal the importance of measured quadrupole moments to test the current nuclear models.

Chapter 1

Physics motivation

1.1 Deformed nuclei near the closed shells

Rutherford's scattering experiments [Rut11] revealed that the atom consists of a small positively charged nucleus and electrons which move around the nucleus in an almost empty space. The nucleons in the nucleus are kept together by the strong interaction. However, until today the exact potential of the nucleon-nucleon interaction within the nucleus is not fully understood. Therefore, the best one can do at this point is describing the nuclear potential by a well chosen approximation.

1.1.1 The nuclear shell model

The nuclear shell model [May49] is probably the most famous approach for the nuclear many body problem. One of the strongest motivations for the formulation of a nuclear shell model comes from the occurrence of the so-called magic numbers 2, 8, 20, 28, 50, 82 and 126. Nuclei with a magic proton and/or neutron number are exceptionally strongly bound. This is proven experimentally by, e.g., the single-particle separation energy or the binding energy as derived from the nuclear masses. Therefore, because of the analogy with the atomic situation where inert noble gases exist, a model has been developed with the basic assumption that the nucleons move independently from each other in an average

potential created by themselves. As a potential $V(r)$ a square well, harmonic oscillator, a Woods-Saxon [Woo54], or a modified oscillator potential [Nil55, Gus67] is often chosen[1]. Important is the introduction of an extra interaction, the spin-orbit coupling $\propto \vec{l} \cdot \vec{s}$, in order to reproduce the experimental magic numbers. It arises from the coupling of the orbital angular momentum, $\vec{l}$, and the intrinsic angular momentum, $\vec{s}$, such that $\vec{j} = \vec{l} + \vec{s}$. A negative proportionality constant assures the experimentally observed fact that the $j = l + 1/2$ levels are lowered in energy while the $j = l - 1/2$ levels are pushed up. Each energy level in the shell model is labeled by the quantum numbers (N, l, j), with N the principal oscillator quantum number, and each j-shell is $(2j + 1)$ degenerate [Rin80].

Quantitatively the Hamiltonian can be written as [Nil95]

$$h = -\frac{\hbar^2}{2m}\Delta + V(r). \tag{1.1}$$

Most commonly the Woods-Saxon potential is used, because it reproduces well the experimentally observed density distribution of the nucleons within the nucleus [Rin80]. Including the spin-orbit term, the potential takes the form [Woo54]

$$V(r) = V_{l.s} + V_{WS} = \zeta(r)\vec{l} \cdot \vec{s} - \frac{V_0}{1 + exp[\frac{r - R_0}{a}]}, \tag{1.2}$$

where $\zeta(r) = \lambda \frac{1}{r}\frac{dV}{dr}$, r is the radial distance from the centre of the potential and a is a parameter that determines how sharply the potential decreases to zero at the nuclear radius R_0. In practical applications the Woods-Saxon potential has the disadvantage that it cannot be solved analytically, except for the $l = 0$ wave. This is contrary to the modified oscillator potential, which can be expressed as [Gus67, Nil95]

$$V_{MO} = \frac{1}{2}\hbar\omega_0\rho^2 - \kappa\hbar\omega_0[2\vec{l}.\vec{s} + \mu(\vec{l}^2 - \langle\vec{l}^2\rangle_N)] \tag{1.3}$$

in which $\rho = \sqrt{\frac{m\omega_0}{\hbar}}r$ and

$$\begin{aligned} \hbar\omega_0 &\approx 41A^{-1/3}[1 + \frac{1}{3}(\frac{N-Z}{A})] \text{ MeV for neutrons} \\ \hbar\omega_0 &\approx 41A^{-1/3}[1 - \frac{1}{3}(\frac{N-Z}{A})] \text{ MeV for protons.} \end{aligned} \tag{1.4}$$

[1] In her original paper Mayer considered the square well and the harmonic oscillator, noting that a well with rounded corners will have a behaviour in between these two potentials [May49].

$\langle l^2 \rangle_N$ is the expectation value of $\vec{l}^2$ averaged over one major shell with oscillator quantum number N. The $(\vec{l}^2 - \langle l^2 \rangle_N)$ contribution ensures that within one major shell the levels with higher l-values are shifted downward. It has the effect of interpolating between the pure harmonic oscillator and the square well and is hence approximating the Woods-Saxon shape. The parameters κ and μ are adjusted such that the observed energy levels in the vicinity of the closed shells are reproduced. To get a good fit, different values for κ and μ for different shells are used. Widely accepted values for κ and μ exist for each region of the nuclear chart [Gus67].

The shell structure of the nucleus allows a description of the nucleus as a spherical core plus a few valence nucleons (particles or holes) around the core. This concept turns out to work well in the neighbourhood of doubly magic nuclei. When more valence nucleons outside the closed shell are present, also the interactions amongst the valence nucleons themselves, the residual interactions, and in a further step the polarising effect of the valence nucleons on the core need to be considered. As a result the nucleus might become deformed. Sometimes even near the closed shell regions deformed nuclear states occur at low excitation energies.

Appendix A gives an overview of several possible definitions of deformation. In the literature mostly the symbol β_2 is used to denote the quadrupole deformation. It is defined by

$$R(\theta, \phi) = R_{av}[1 + \sum_{\lambda=0}^{\infty} \beta_\lambda Y_\lambda^0(\theta, \phi)] \tag{1.5}$$

where R_{av} is the radius of a sphere with the same volume usually taken equal to $r_0 A^{1/3}$ with $r_0 = 1.2$ fm. In this text often an approximation for β_2 is used, denoted by β_q and defined as

$$R(\theta, \phi) = R_{av}(1 + \frac{\beta_q^2}{4\pi} + \beta_q Y_2^0(\theta, \phi). \tag{1.6}$$

The next sections illustrate the influence of the deformation on the energy levels.

1.1.2 The deformed shell model

Nilsson was the first to calculate the single particle energies for protons and neutrons in a deformed potential, a theory which is nowadays well known as the Nilsson model [Nil55]. He made use of an anisotropic modified oscillator

$$h = h_0 - \kappa\hbar\omega_0[2\vec{l}.\vec{s} + \mu(\vec{l}^2 - \langle\vec{l}^2\rangle_N)] \tag{1.7}$$

$$h_0 = -\frac{\hbar^2}{2m}\Delta' + \frac{m}{2}(\omega_{x'}^2 x'^2 + \omega_{y'}^2 y'^2 + \omega_{z'}^2 z'^2) \tag{1.8}$$

in which $\omega_{x'}$, $\omega_{y'}$ and $\omega_{z'}$ denote the anisotropic oscillator frequencies in the body-fixed system[2]. In the case of axial symmetry they can be written as a function of one single parameter of deformation δ.

$$\omega_{x'}^2 = \omega_{y'}^2 = \omega_0(\delta)^2(1 + \frac{2}{3}\delta) \tag{1.9}$$

$$\omega_{z'}^2 = \omega_0(\delta)^2(1 - \frac{4}{3}\delta). \tag{1.10}$$

The Hamiltonian can be rewritten as

$$H = \overset{0}{h}_0 + h_\delta - \kappa\hbar\omega_0[2\vec{l}.\vec{s} + \mu(l^2 - \langle l^2\rangle_N)]. \tag{1.11}$$

in which $\overset{0}{h}_0$ is the isotropic harmonic oscillator Hamiltonian. For $\delta = 0$ the Hamiltonian reduces to the isotropic modified oscillator Hamiltonian with quantum numbers (N, l, j). In a deformed nucleus the spherical quantum numbers (N, l, j) are no longer valid. The only conserved quantum numbers are the parity (π) and the projection of the total angular momentum on the symmetry axis (Ω). For sufficiently large deformations the situation again simplifies. For this case the Hamiltonian can be approximated by a pure anisotropic harmonic oscillator with the $\vec{l}.\vec{s}$ and $\vec{l}^2$ terms as a perturbation. In this limit the single particle levels can be labeled with a set of asymptotic quantum numbers $\Omega^\pi[Nn_z\Lambda]$, where N is the principal oscillator quantum number, n_z is the number of nodes along the symmetry axis and Λ the projection of the angular momentum l on the symmetry axis. Usually the quantum numbers $\Omega^\pi[Nn_z\Lambda]$ are also used to label the

[2] In his original paper Nilsson did not consider the $\langle\vec{l}^2\rangle_N$ contribution. He used as a Hamiltonian $h = h_0 + C\vec{l}.\vec{s} + D\vec{l}^2$ [Nil55].

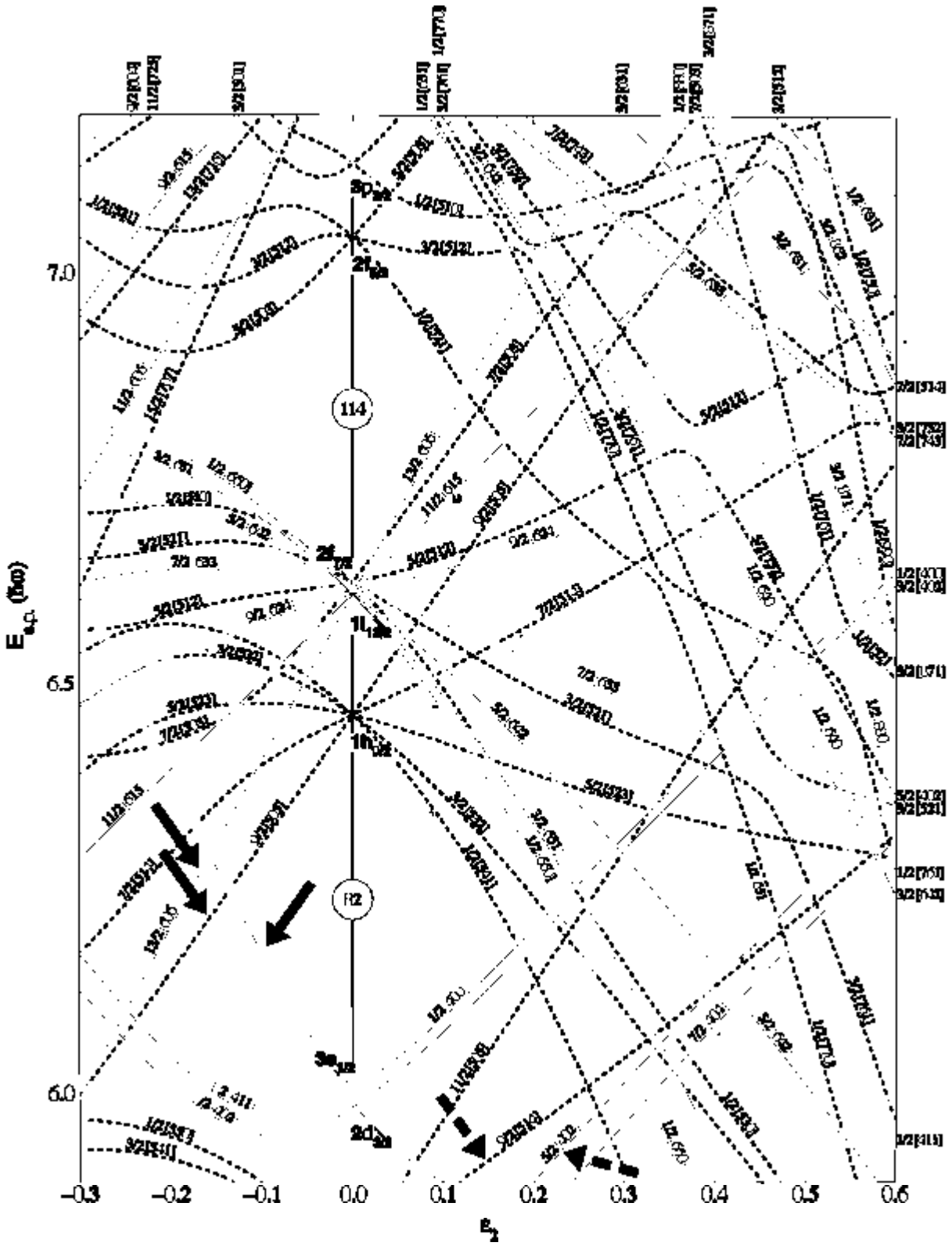

Figure 1.1: *Nilsson diagram for protons $Z \geq 82$ ($\epsilon_2 \approx 0.95\beta_q$)[Fir96]. The arrows point to the orbitals which are of importance in this thesis. The solid arrows refer to the involved proton orbitals in the Pb region (section 1.1.3), the dashed arrow to the orbitals occupied by the quasi-protons in the $^{179}W(K^\pi = 35/2^-)$ isomer (section 1.2.5).*

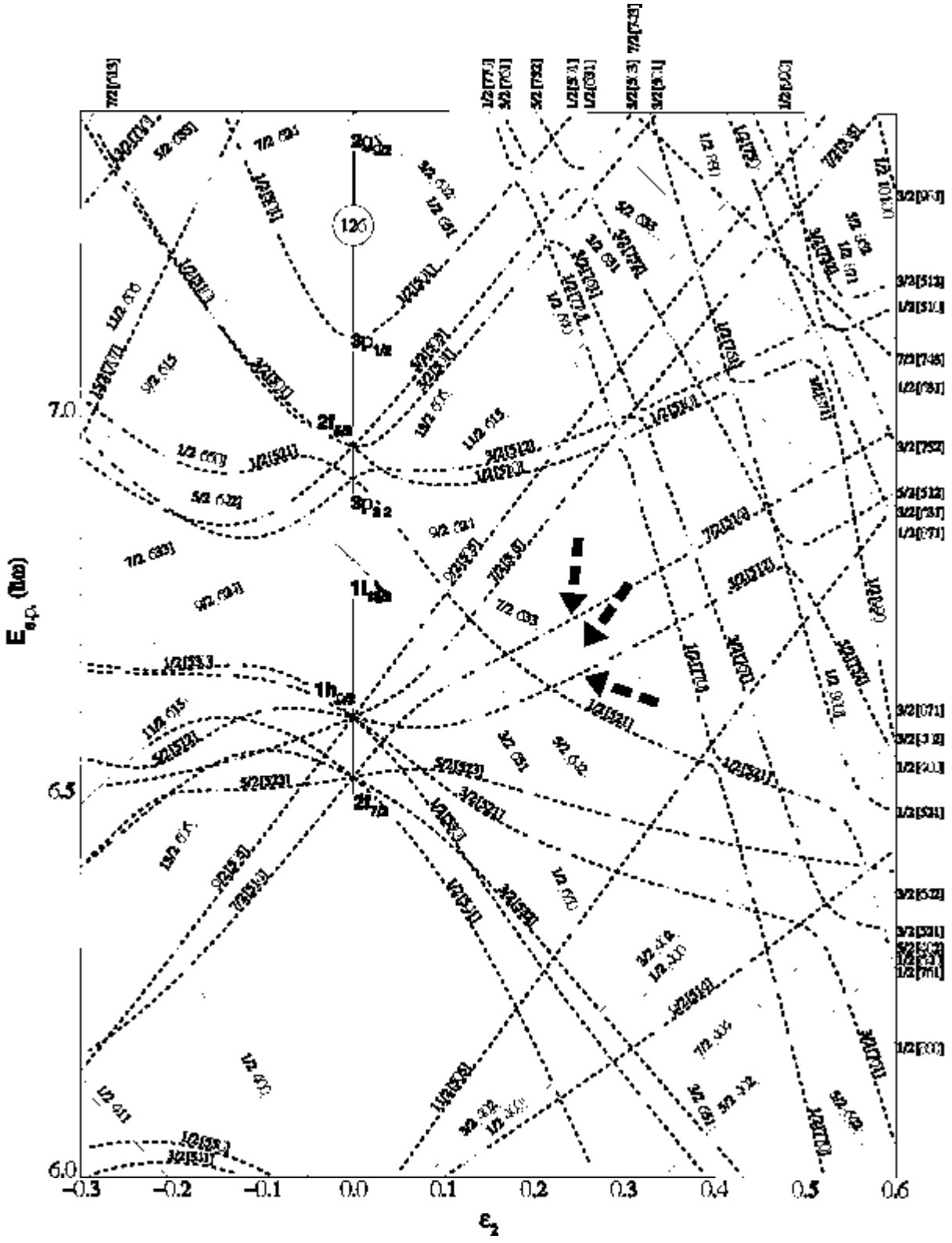

Figure 1.2: *Nilsson diagram for neutrons* $82 \leq N \leq 126$ *(*$\epsilon_2 \approx 0.95\beta_q$*)[Fir96]. The dashed arrows point to the orbitals occupied by the quasi-neutrons in* $^{179}W(K^\pi = 35/2^-)$ *isomer (section 1.2.5).*

energy levels at intermediate deformations, in which Ω is the projection of $\vec{j}$ on the symmetry axis of the nucleus and π the parity.

As a consequence of the deformation the $(2j+1)$ degeneracy is lifted and only a two-fold degeneracy $\pm\Omega$ remains, which is due to the reflection symmetry of an axially symmetric nucleus. For example the $i_{13/2}$ orbital can have $|\Omega|$ equal to 13/2, 11/2, 9/2, 7/2, 5/2, 3/2 and 1/2. The ordering of these levels depends on the particular shape of the nucleus. In prolate nuclei ($\beta_2 > 0$) the low-Ω orbits have maximal spatial overlap with the core nucleus and are therefore lowered in energy. Likewise, the high-Ω orbits overlap with the oblate core ($\beta_2 < 0$) and are consequently lowered in energy with an increasing oblate deformation (Figures 1.1 and 1.2).

If the energy of an orbital is lowered such that the orbital appears in a shell with different principal quantum number, N, it is called an 'intruder orbital'. Usually these orbitals are quite pure since mixing of levels with different parity cannot occur.

1.1.3 Intruder states in the Pb region

The $_{82}$Pb nuclei have a magic proton number. Proton-excitations across the $Z = 82$ gap are therefore expected to occur at very high excitation energies only (few MeV). In reality several low-lying excited 0^+ states, which have been interpreted as proton $2p-2h$ excitations across the shell gap, have been observed in the Pb isotopes via alpha decay studies [VD84, Woo92]. They are displayed in Figure 1.3 together with the $9/2^-$ intruder states in Tl. In the pure shell model the excitation of the nucleus into a spherical proton $2p-2h$ configuration costs almost twice the energy gap at $Z = 82$, i.e., $E_x \approx 2(\epsilon_p - \epsilon_h) \approx 7$ MeV. However, if the nucleus takes an oblate quadrupole-deformed shape, the excitation energy is lowered if the particles are put in the strongly down-sloping $9/2^-[505]$ and $13/2^+[606]$ orbitals and the two holes in the up-sloping $1/2^+[400]$ orbitals (Figure 1.1). Thus, at a given deformation the intruder configuration can become competitive with the regular spherical configuration.

The appearance of different shapes at similar excitation energies within one nucleus is called 'shape coexistence'. Recently, the first nucleus, ^{186}Pb, has been discovered where the ground-state and the two first excited states are three 0^+ states. It has been interpreted as a shape coexistence of a spherical ground-state, an oblate $2p-2h$ excitation and a prolate $4p-4h$ excitation [And00]. Also in odd nuclei intruder states appear, e.g., in the $_{81}$Tl isotopes as proton $1p-2h$ states among proton $1h$ states [Hey83].

Heyde *et al.* developed a formalism to describe both the low excitation energy of the intruder states and the particular A-dependence of the intruder states ([Hey87] and Figure 1.3). In this approach the energy of an intruder state is calculated as

$$E_{intruder} = 2(\epsilon_{j\pi} - \epsilon_{j'\pi}) - \Delta E^{\pi\pi}_{pairing} + \Delta E^{\pi\nu}_{M} + \Delta E^{\pi\nu}_{Q}. \qquad (1.12)$$

$\epsilon_{j\pi}$ and $\epsilon_{j'\pi}$ denote the proton single-particle energies in the two major shells. $\Delta E^{\pi\pi}_{pair}$ is the gain in energy due to the proton pairing correlations. The monopole term $\Delta E^{\pi\nu}_{M}$ contains a correction on the $\epsilon_{j\pi}$ and $\epsilon_{j'\pi}$ energies due to the interac-

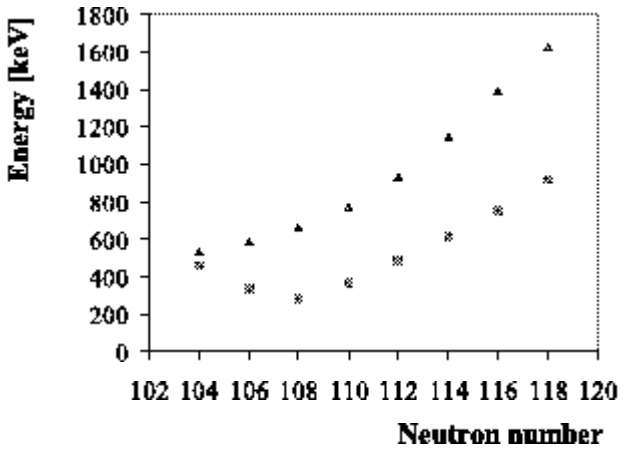

Figure 1.3: *Systematics of the oblate 0^+_2 intruder state in Pb (triangles) and the $9/2^-$ intruder state in Tl (squares) as a function of the neutron number. The data are taken from [Hey83, Bij98, And00].*

tion with the valence neutrons. This shift depends on the overlap of the proton and neutron wave functions. Since only the monopole part of the residual proton-neutron interaction determines this variation in single-particle energy, this shift is called the 'monopole correction' . The quadrupole part of the proton-neutron interaction is taken into account by the $\Delta E_Q^{\pi\nu}$ term. This component induces a $I^\pi = 0^+ \rightarrow I^\pi = 2^+$ pair breaking for both protons and neutrons. It is the deformation driving part of the Hamiltonian. It can be calculated by using a schematic proton-neutron quadrupole-quadrupole interaction ($\chi_{\pi\nu}\hat{Q}\cdot\hat{Q}$). Figure 1.4 illustrates the contribution of the several terms of the Hamiltonian.

Summarising, the surprisingly low energy of the intruder states can be explained by the creation of an extra hole pair, resulting in a gain of pairing energy, in combination with the strongly attractive interaction between the excited protons and the valence neutrons (Figure 1.5). Therefore, intruder states are characterised by the following features [Huy91]:

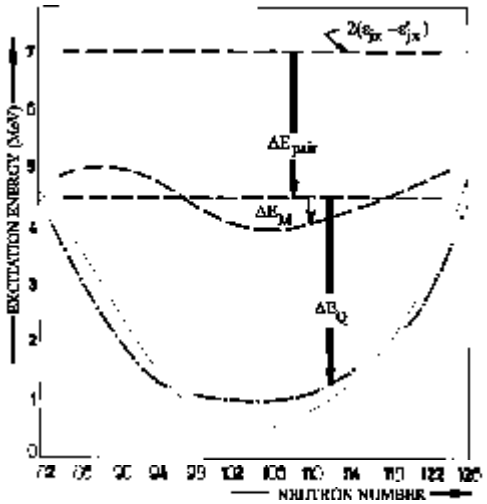

Figure 1.4: *The total energy correction (full line) for the lowest 0^+ intruder state. The different contributions due to the pairing energy (straight dashed line) ΔE_{pair}, the monopole correction (dashed line) ΔE_M and the quadrupole correction (dot-dashed line) ΔE_Q are indicated for the $Z = 82$ region. The upper straight dashed line is the unperturbed energy [Hey87].*

i. The strength of the proton-neutron interaction depends on the number of valence neutrons. Therefore, the excitation energy of the intruder states in an isotope (isotone) chain is ranging from maximal at the closed neutron (proton) shell to minimal for mid-shell neutron (proton) numbers to become maximal again at the next shell closure (Figure 1.3).
ii. The intruder states are deformed. Therefore, collective rotational bands are built on them (see also section 1.2.1).
iii. As deformation is an important feature of intruder states, direct evidence for the intruder character comes from the measurement of the charge radius of the state or from a measured quadrupole moment.
iv. Due to the different structure of the intruder states compared to the ground-state structure, the intruder states are often isomeric (shape isomers).
v. Magnetic moments are directly related to the single particle structure of a state and, therefore, provide a direct experimental evidence for the intruder character.

The intruder states have mainly been identified on the basis of the features *i*, *ii* and *iv*.

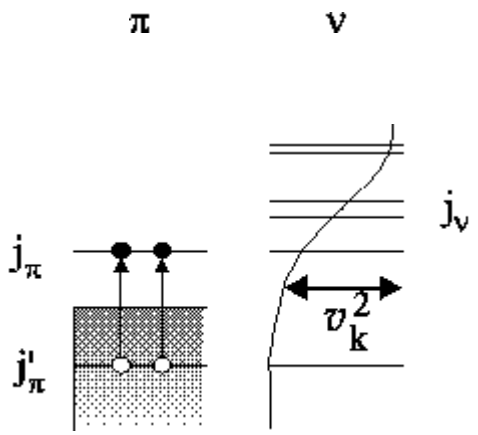

Figure 1.5: *Schematic representation of a proton intruder $2p-2h$ configuration where j'_π denotes the regular orbital, j_π the intruder orbital, and j_ν the neutron orbitals. The solid line through the neutron orbitals shows the probability v_k^2 for the occupation of the orbits (see section 1.4.1). The figure is adapted from [Hey87].*

1.1.4 Measured deformations of intruder states in the Pb region

Although the deformation is one of the main features of an intruder state, only a few direct measurements of the deformation have been performed. An important reason for this striking lack of experimental information is the 0^+ spin of the intruder states in the even-even nuclei. The spectroscopic quadrupole moment of a 0^+ state is 0, regardless the deformation. The only ways to learn something about the deformation of isomeric 0^+ states are, therefore, by measuring the charge radii, applying the laser spectroscopy technique [Bil95, Neu88] or by measuring the cross-section of the Coulomb-excitation from the 0^+ to the 2^+ state [Ald56].

In the odd-Z nuclei the laser spectroscopy technique [Bil95, Neu88] has been used to measure the charge radii of the $_{79}$Au and $_{81}$Tl isotopes. In the $^{197-185}$Au chain the experiments revealed a sudden increase of the nuclear ground-state radius for ^{186}Au and ^{185}Au ([Wal87] and Figure 1.6). This is due to the intruding $\pi 1h_{9/2}$ orbital which becomes lower in energy than the spherical $2d_{3/2}$ level once the neutron number is far enough from a closed shell (Figure 1.7). In the $^{189-193}$Tl chain a systematic increase of the deformation of the $\pi 1h_{9/2}$ isomeric state has been observed by taking more neutrons away from the closed $N = 126$ shell ([Bou85] and Figure 1.8). Again the proton-neutron interaction is responsible for this behaviour. Note that in these experiments the deformations have been derived, both from the charge radii and the spectroscopic quadrupole moment (see appendix B). The tendency of the deformation as a function of the neutron number is the same in the two cases, but the absolute values of the deformation differ (Figure 1.9). In order to extract the deformation, β_q, from the spectroscopic quadrupole moment Q_s the standard formulae $Q_s = Q_0 \frac{3K^2 - I(I+1)}{(I+1)(2I+3)}$ and $Q_0 = \frac{3}{\sqrt{5\pi}} Z A^{2/3} R_0^2 \beta_q (1 + 0.36\beta_q)$ have been used with $R_0 = r_0 A^{1/3}$ in which $r_0 = 1.2$ fm (see appendix A and Ref. [Löb70]). However, the relation between Q_s and Q_0 holds only if K is a good quantum number (see also appendix A). This is the case in the strong coupling limit and for axial symmetry (see also

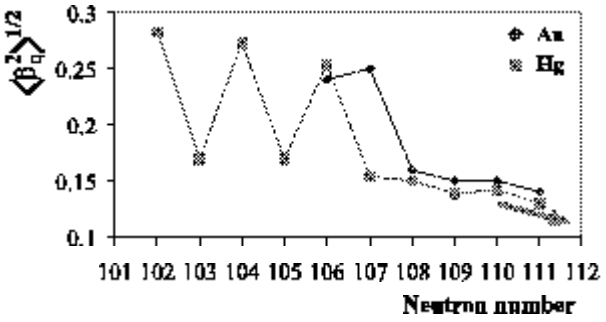

Figure 1.6: $(\beta_q^2)^{1/2}$ *of the Au and Hg ground-states as a function of the neutron number. The data are taken from [Wal87, Ulm86]. The error bars of the Hg data are smaller than the labels, the error bars of the Au data are not indicated in the paper. The arrow indicates that the deformations of the Hg ground-states are measured up to* $N = 126$.

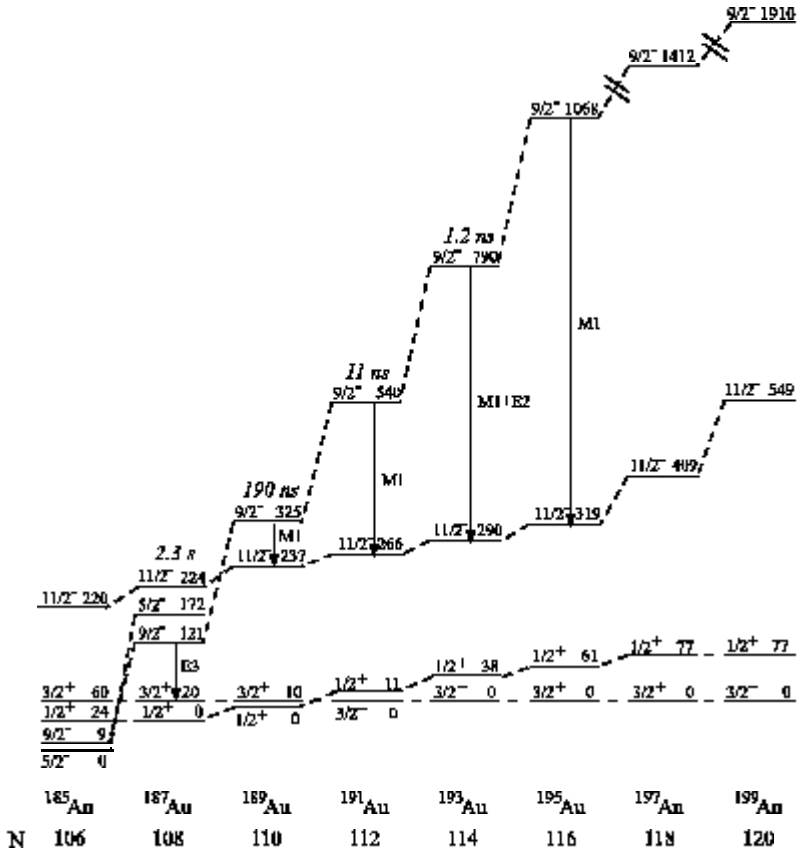

Figure 1.7: *The systematics of the* $\pi 1h_{9/2}$ *intruder state in the odd-Au isotopes. The strongest* γ*-decay branches are shown. Half-lives are given to the intruder states, where known. The* $\pi 1h_{9/2}$ *states in* ^{197,199}*Au are not located to scale [Hey83]. Also in lighter Au isotopes, down to* ^{173}*Au, the level schemes have been established [MM84, Mue99, Kon00]. However, the* $3/2^+$ *level, which is the level of reference in Figure 1.7, has not been observed and, therefore, these Au isotopes are not added in the picture.*

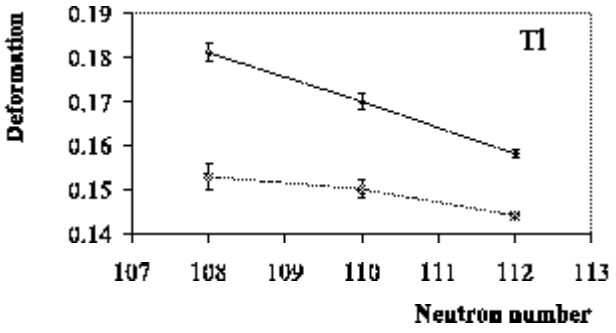

Figure 1.8: *Squares: $|\beta_q|$, deduced from the measured spectroscopic quadrupole moment as a function of the neutron number. Diamonds: $\langle\beta_q^2\rangle^{1/2}$, deduced from the charge radius (see appendix B), as a function of the neutron number [Bou85].*

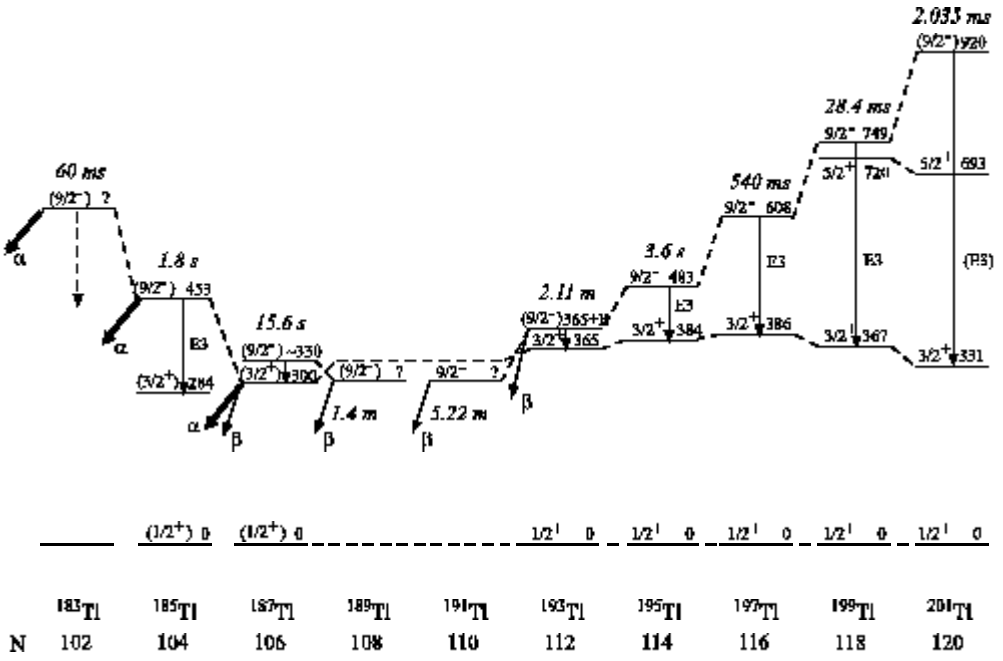

Figure 1.9: *The systematics of the $\pi 1h_{9/2}$ intruder state in the odd-Tl isotopes. The strongest γ-decay branches and the established α-, β and γ-decay branches are shown. Half-lives are given to the intruder states, where known [Hey83].*

section 1.2.1). It is believed that the disagreement of the absolute values of the deformations is because these conditions are not fulfilled [Bou85]. Note further that also fluctuations in the nuclear shape can contribute to $\langle\beta_q^2\rangle^{1/2}$ while β_q is the purely static deformation.

The probably most striking example is the $_{80}$Hg chain, where a pronounced odd-even staggering has been observed (Figure 1.6) in the lighter isotopes. It has been understood as a prolate-oblate shape-coexistence, where the highly deformed prolate intruder configuration becomes the ground-state in the light odd Hg isotopes [Bon72, Fra74].

1.1.5 The $(I^\pi = 11^-)$ intruder states in Pb

Information about the deformation of the intruder states in the even-even nuclei can be obtained by measuring the spectroscopic quadrupole moment of isomeric intruder states with $I^\pi \neq 0^+$. The $(\pi 3s_{1/2}^{-2} 1h_{9/2} 1i_{13/2})_{11^-}$ isomers in the ^{192,194,196}Pb nuclei are good candidates to measure. The systematics of the $I^\pi = 11^-$ levels in the even-even Pb nuclei is shown in Figure 1.10. The configuration of the $I^\pi = 11^-$ isomer in ^{196}Pb has been confirmed by a g-factor measurement [Pen87]. However, this is the only measured g-factor of an $I^\pi = 11^-$ isomer in Pb. Nevertheless, the systematics and the isomeric character of the ^{194,192}Pb$(I^\pi = 11^-)$ levels favour the $(\pi 3s_{1/2}^{-2} 1h_{9/2} 1i_{13/2})_{11^-}$ configuration for these isomers as well [Fan91, Lag91]. This configuration is also predicted by configuration-constrained shell model calculations [Ben89b]. The half-life of the 11^- state in ^{198}Pb has not been measured. Also in the ^{198}Pb nucleus the $(\pi 3s_{1/2}^{-2} 1h_{9/2} 1i_{13/2})_{11^-}$ configuration has been assigned to the 11^- level, based on the systematics ([Cla93, Gör] and Figure 1.10). The observed 11^- states in ^{200,202,204,206}Pb do not have the $(\pi 3s_{1/2}^{-2} 1h_{9/2} 1i_{13/2})_{11^-}$ configuration [Fan87, Lin78, Ori73]. The non-yrast character of the $(\pi 3s_{1/2}^{-2} 1h_{9/2} 1i_{13/2})_{11^-}$ configuration is believed to be the reason for not observing the $(\pi 3s_{1/2}^{-2} 1h_{9/2} 1i_{13/2})_{11^-}$ levels (an yrast state is the lowest energy state for a given spin).

A reasonable estimation of the energy of the $(\pi 3s_{1/2}^{-2} 1h_{9/2} 1i_{13/2})_{11^-}$ state can

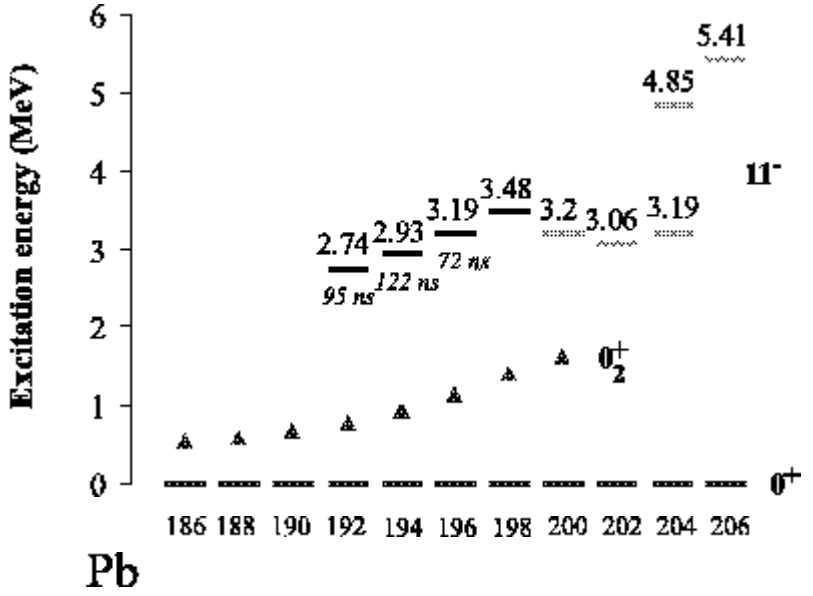

Figure 1.10: *Systematics of the* 11^- *levels in the even-even Pb nuclei. The excited levels indicated in black are the* $(\pi 3s^{-2}_{1/2} 1h_{9/2} 1i_{13/2})_{11^-}$ *intruder states. The measured half-lives are given as well. The excited levels in grey are* 11^- *levels with other configurations. The data are taken from [Ori73, Lin78, Fan87, Pen87, Fan91, Lag91]. For comparison the excited* 0^+_2 *intruder states are added in the figure by triangles.*

be made as follows. The excitation energy of the $(\pi 3s^{-2}_{1/2} 1h^2_{9/2})_{0^+_2}$ configuration is 1.14 MeV. The 11^- state has a broken pair of particles and will therefore have an energy equal to the excitation energy of the 0^+_2 state + the loss in pairing energy due to the breaking of the particle pair. The change in proton-pairing energy $\Delta E^{\pi\pi}_{pair}$ can be estimated from the 1 proton separation energies S_p and the 2 proton separation energies S_{2p} as [Woo92]

$$\Delta E^{\pi\pi}_{pair}(p) = 2S_p(Z+1,N) - S_{2p}(Z+2,N) \tag{1.13}$$

and is about 2 MeV. Hence, the estimated energy for the $(\pi 3s^{-2}_{1/2} 1h_{9/2} 1i_{13/2})_{11^-}$ state is 3.14 MeV, which is in good agreement with the experimentally observed 3.19 MeV. The same reasoning can be made for the energy of the 11^- isomer

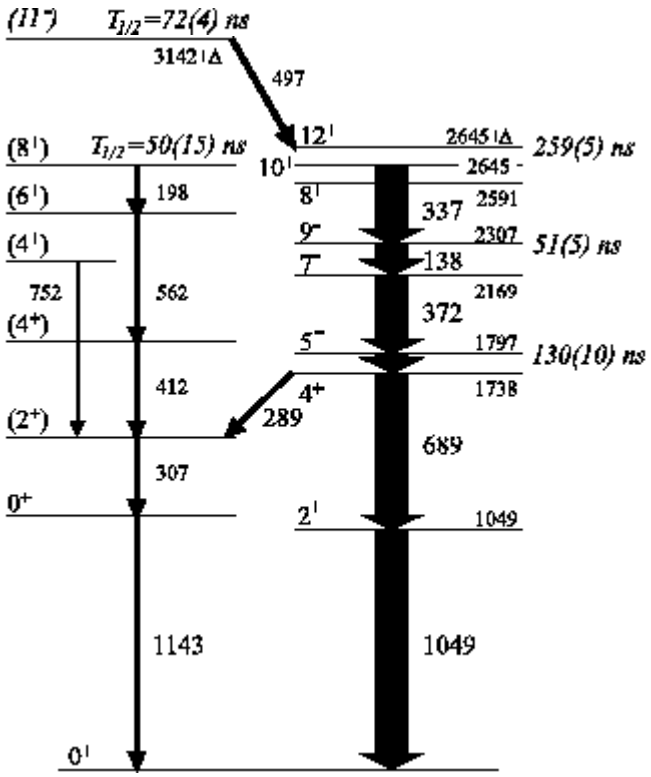

Figure 1.11: *Lower energy part of the level scheme of* ^{196}*Pb [Pen87].*

in ^{194}Pb. In this nucleus the first excited 0_2^+ state is situated at an energy of 0.93 MeV, while the 11^- isomer has an energy of 2.93 MeV. The difference is again the pairing energy of 2 MeV. Note that the assumption is made that the deformations of the 0_2^+ states and the 11^- states are the same.

From the discussion above it is clear that the deformation is a parameter of uttermost importance for a good understanding of the relatively low excitation energy of the 11^- energy. Therefore, determining the spectroscopic quadrupole moment of the 11^- isomer in ^{196}Pb has been one of the three major nuclear physics goals in this work. It is interesting to compare the deformation of the $(\pi 3s_{1/2}^{-2} 1h_{9/2} 1i_{13/2})_{11^-}$ intruder state in ^{196}Pb with the deformation of the corresponding normal $(\pi 1h_{9/2} 1i_{13/2})_{11^-}$ state in ^{198}Po to investigate the influence of the two $3s_{1/2}$ holes on the deformation of the nucleus (Figure 1.12). The same com-

parison can be made for the quadrupole moments of the ^{195}Tl($I^\pi = 9/2^-, \tau = 3.6$ s) isomer, which has a $\pi 3s^{-2}_{1/2} 1h_{9/2}$ configuration, and the ^{197}Bi($I^\pi = 9/2^-$) ground-state, which has a $\pi(1h_{9/2})$ configuration. This allows an experimental verification of the influence of the $1i_{13/2}$ particle on the polarisation of the nuclear core. This will be further discussed in chapter 3.

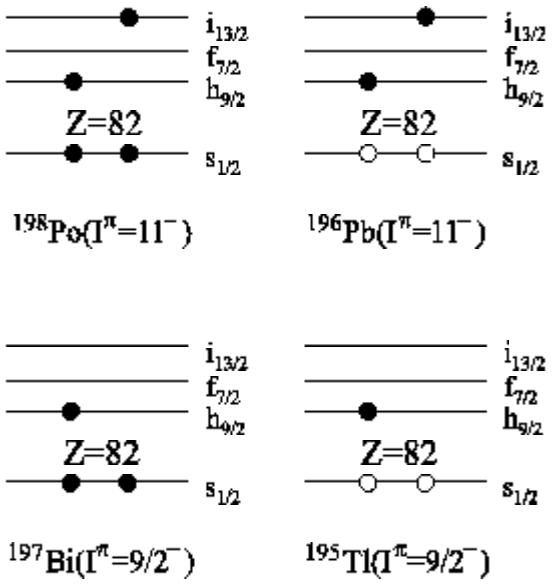

Figure 1.12: *The proton configurations of an* $(\pi 1h_{9/2} 1i_{13/2})_{11^-}$ *isomer in Po, a* $(\pi 3s^{-2}_{1/2} 1h_{9/2} 1i_{13/2})_{11^-}$ *isomer in Pb, a* $(\pi 1h_{9/2})$ *ground-state in Bi and a* $(\pi 3s^{-2}_{1/2} 1h_{9/2})_{9/2^-}$ *isomer in Tl. The open circles indicate the holes, while the filled circles correspond with the particles.*

1.2 Deformed nuclei in between the closed shells

1.2.1 Rotation of a deformed nucleus

Far away from the closed shells the many valence nucleons outside the core make shell model calculations very complicated. A much more simple picture has been proposed by Bohr and Mottelson [Boh53a]. They consider the nucleus as a deformed collective rotating core with the unpaired particles (or more generally a

subgroup of particles near the Fermi level) as valence nucleons around it. The Hamiltonian decomposes in two parts:

$$H = H_{intr} + H_{coll} \tag{1.14}$$

H_{intr} contains the contribution of the valence nucleons. Often the Nilsson or the Woods-Saxon Hamiltonian is chosen. H_{coll} describes the rotation of the inert core (see, e.g., in [Rin80]):

$$H_{coll} = \frac{R_{x'}^2}{2\Im_{x'}} + \frac{R_{y'}^2}{2\Im_{y'}} + \frac{R_{z'}^2}{2\Im_{z'}} \tag{1.15}$$

where the R_i are the body-fixed components of the collective angular momentum of the core and $\Im_i$ the corresponding moments of inertia. In the case of an axially symmetric deformed nucleus the z'-axis can be chosen as the axis of symmetry, that is, $\Im_{x'} = \Im_{y'} = \Im$ with $\Im$ representing the *static* moment of inertia. Quantum mechanically a system cannot rotate around an axis of symmetry, because this would result in a system which is indistinguishable from the original. Therefore, $\Im_{z'} = 0$ and the z'-component of $\vec{R}$ has to vanish and the deformed nucleus rotates around an axis perpendicular to its symmetry axis, i.e., the x'-axis. This also means that spherical nuclei cannot rotate unless some symmetry breaking mechanism other than an asymmetric charge distribution is present in the nucleus (see section 1.3).

Taking into account that the total angular momentum of the nucleus $\vec{I}$ equals the sum of the angular momentum of the valence particles $\vec{j}$ and the collective angular momentum $\vec{R}$, i.e., $\vec{I} = \vec{R} + \vec{j}$ (Figure 1.13), the collective part of the Hamiltonian becomes

$$H_{coll} = H_{rot} + H_{rec} + H_{cor} \tag{1.16}$$

with

$$H_{rot} = \frac{\vec{I}^2 - I_{z'}^2}{2\Im}, \tag{1.17}$$

$$H_{rec} = \frac{1}{2\Im}(j_{x'}^2 + j_{y'}^2), \tag{1.18}$$

$$H_{cor} = -\frac{1}{\Im}(I_{x'}j_{x'} + I_{y'}j_{y'}) = -\frac{1}{2\Im}(I_+j_- + I_-j_+). \tag{1.19}$$

The recoil term H_{rec} acts only on the intrinsic coordinates. It is often neglected because in practice the single-particle energies e^i_Ω, i.e., the eigenvalues of H_{intr} (the subscript i refers to the ith particle), are adjusted to the experimental data.

The z'-component K of the total angular momentum $\vec{I}$ does not commute with the Coriolis term H_{cor} of the total Hamiltonian. This means that K is only a good quantum number if H_{cor} is negligible compared to the other terms of the total Hamiltonian $H = H_{intr} + H_{coll}$ (1.14). More precisely, the contribution of H_{cor} should be small compared to the level splitting of the single-particle energies in the Nilsson model for the different values of Ω. This is the case [Rin80]

i. for large deformations β_2, because the level splitting in the Nilsson Hamiltonian is $\propto \beta_2$, whereas one can show empirically that $\hbar^2/2\Im \propto \beta_2^{-2}$.

ii. for small Coriolis matrix elements. From (1.19) it can be seen that the Coriolis matrix elements are $\propto [(I(I+1)-K^2)(j(j+1)-\Omega^2)]^{1/2}$. That is, they are small either for low spin I or for nucleons in orbitals with small particle angular momenta j. For large j-values, e.g., for $i_{13/2}$ nucleons, they can only be neglected for high Ω values. The limit where H_{cor} is neglected is called the 'strong coupling' or 'deformation aligned' limit, because in this case the particle angular momentum $\vec{j}$ is strongly coupled to the core of the nucleus and precesses around the z'-axis as illustrated in Figure 1.13. It follows from the above Hamiltonian that the

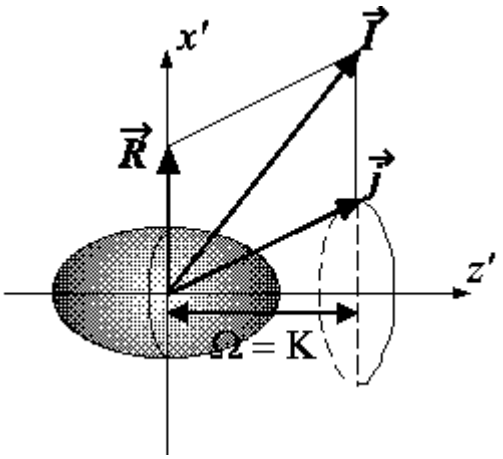

Figure 1.13: *The strong coupling scheme.*

energies in the strong coupling limit are given by

$$E^i_{IK} = |e^i_{\Omega=K} - \lambda| + \frac{\hbar^2}{2\Im}[I(I+1) - K^2] \tag{1.20}$$

where the single-particle particle energy e^i_K is counted relative to the Fermi level λ. This gives rise to nuclear level schemes characterised by rotational bands with a $I(I+1)$ level spacing built on single particle states, such as, e.g., in Figure 1.16. The moment of inertia $\Im$ comes in as a scaling parameter. Note that if pairing is considered, the 'single-particle' energies are replaced by 'quasiparticle' energies as will be explained in section 1.4.1.

1.2.2 K-isomers

Nuclei in the $A \approx 180$ region have both neutron and proton orbitals with large spin projections on the symmetry axis, Ω, occuring near the Fermi surface. This results in intrinsic states with high K values, competing with collective rotational states to generate angular momentum. Nuclei in this mass region are strongly prolate deformed ($\beta_2 \approx 0.2 - 0.3$), which means that K is an approximately conserved quantum number.

It is difficult for a nucleus to change drastically the orientation of its spin with respect to the symmetry axis. This is quantified by the selection rule

$$\Delta K \leq \lambda \tag{1.21}$$

where ΔK is the change in K between the initial and the final state and λ is the multipolarity of the transition[3]. Mathematically, this is understood from the fact that the collective $B(E$ or $M\lambda)$ reduced transition probability, defined as $B(E$ or $M\lambda; K_i I_i \rightarrow K_f I_f) = \frac{1}{2I_i+1} \mid \langle K_i I_i \| T_\lambda \| K_f I_f \rangle \mid^2$ in which T^μ_λ is an electric or magnetic tensor operator of order λ, is zero when the selection rule is not fulfilled [deS74].

The degree of K-forbiddenness for a transition, ν, is defined as

$$\nu = \Delta K - \lambda. \tag{1.22}$$

[3]More precisely the K-selection rule is $\Delta K \leq \lambda$ or $K_i + K_f \leq \lambda$ [deS74].

If a transition is K-forbidden, the half-life of the state is increased compared to the normal single-particle values. Löbner found that, empirically, for each extra unit of K-forbiddenness, the half-life increases with a factor of about 100 [Löb68]. This is expressed as $f_\nu \approx 100$, where f_ν, the hindrance per degree of K-forbiddenness (or the reduced hindrance), is defined as

$$f_\nu = \left[\frac{T^\gamma_{1/2}}{T^W_{1/2}}\right]^{1/\nu} = [F_W]^{1/\nu}. \tag{1.23}$$

Here $T^\gamma_{1/2}$ is the partial γ-ray half-life and $T^W_{1/2}$ is the Weisskopf single-particle estimate (see appendix B.2). This allows transitions of different energies and K-forbiddenness to be compared.

Textbook examples of high-K isomers are the $K^\pi = 16^+$ isomer in ^{178}Hf [Hel68] and the $K^\pi = 9^-$ isomer in ^{180}Ta [Bur80]. The ^{178}Hf$(I, K^\pi = 16, 16^+)$ decays via a 4 times forbidden $M4$ transition to the ^{178}Hf$(I, K^\pi = 8, 8^-)$ band with a half-life of 31(1) years [Hel73]. Note that in principle the 16^+ isomer can decay by a K-allowed transition with $\lambda = 8$. However, the higher the multipolarity the slower the transition and, hence, this decay branch is not competitive. Another even more extreme case, where spin and K-trapping reinforce each other, is the 9^- isomer in ^{180}Ta [Bur80]. A $\lambda = 8$ transition to the 1^+ ground-state is in principle K-allowed. However, the combination of the high multipolarity and the low transition energy ($E_\gamma = 75$ keV) makes this decay branch improbable. This makes the ^{180}Ta$(I^\pi = 9^-)$ spin trap the only nuclear isomer existing naturally on Earth [Bur80] with a half-life $> 1.2 \cdot 10^{15}$ years [Cum85], which is longer than the existence of the Earth. (see appendix B.2 for the dependence of the transition rate on the multipolarity and the energy of the transition).

Although the existence of these extremely long lived isomers confirms the K-selection rule, also notable exceptions with very small reduced hindrances ($2 < f_\nu < 10$) exist. The most striking case is the 3.3 MeV isomer in ^{179}W with a half-life of 750 ns, decaying predominantly via a $\Delta K = 14$ decay branch with $f_\nu \approx 2$ [Ber78a, Wal91]. Compared to the rule of thumb of $f_\nu = 100$, the transition goes at a rate which is a factor of 10^{20} too fast [Wal99]. The quadrupole moment of exactly this isomer has been derived in this work. The features of this isomer

are explained in more detail in section 1.2.5. The experimental results will be presented in chapter 4.

However, the $^{179}W(K^\pi = 35/2^-)$ isomer is not the only exception with a very small reduced hindrance as shown in Figure 1.14. There, the systematics of the f_ν values is plotted as a function of the excitation energy of the nucleus, or, more specifically, the excitation energy relative to the rotor energy that approximates the yrast line . For simplicity in Figure 1.14, the energies are given relative to a rigid rotor with the same mass and deformation as the corresponding nucleus [Wal97]. Substantial reduction in f_ν is seen to accompany increasing relative energy. The correlation can be explained in terms of the statistical density of

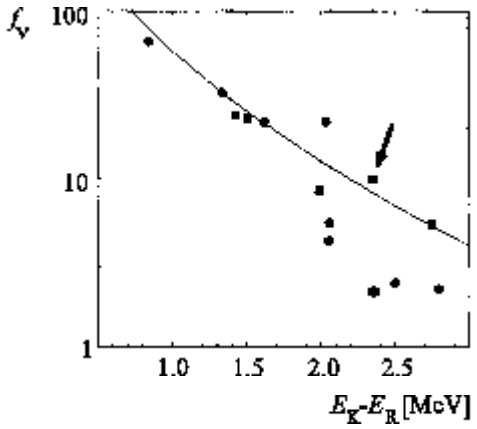

Figure 1.14: *Reduced hindrance as a function of the excitation energy relative to a rigid rotor for 4- and 5-quasiparticle isomers (circles and squares respectively), decaying via E2 and E3 transitions. For the 5-quasiparticle isomers, 0.9 MeV has been added to the energy to account for the pairing energy difference ($\approx 12/A^{1/2}$ MeV). In the figure the maximum value of f_ν corresponds to the decay of the $K^\pi = 16^+$, 31 year isomer in ^{178}Hf and the minimum value to he $K^\pi = 16^+$, 6 ns isomer in ^{182}Os. The curve corresponds to a density-of-states model estimate. The arrow points to the f_ν-value of the $^{179}W(K^\pi = 35/2^-)$ isomer, assuming a $\Delta K = 6$ transition. The asterisk refers to the f_ν value of the same isomer, assuming a $\Delta K = 14$ transition. The figure is adapted from [Wal97].*

states. If an isomer has a high excitation energy compared to the yrast energy, it will be embedded in a high density of states with different K-values. Statistical K-mixing will hence reduce the f_ν-values. The solid line in Figure 1.14 represents a statistical model estimate for $\nu = 4$ [Wal97], arbitrarily renormalised to the high f_ν-values. In other words, such a model can predict the trend, but not the absolute values.

However, even taking into account a reduction of f_ν due to statistical K-mixing, it is evident from Figure 1.14 that several of the higher-energy data points still have too low f_ν-values. This is understood as due to an additional Coriolis K-mixing effect (see above) [Wal99]. This will be worked out for the ^{179}W($K^\pi = 35/2^-$) isomer in section 1.2.5, where detailed γ spectroscopy studies have revealed that the bands to which the isomer decays are highly K-mixed.

A shape change forms an alternative explanation to K-mixing for the exceptional low f_ν-values [Cho88, Ben89c]. It is understood as a change from an axially symmetric prolate shape with the angular momentum along the symmetry axis (high-K state) through triaxial and oblate shapes to an axially symmetric prolate nucleus with the angular momentum oriented perpendicular to the symmetry axis of the nucleus (low K-state). This decay mode is only possible for γ-soft nuclei, i.e., for nuclei that can easily change to triaxial shapes (see appendix A for the definition of γ deformation).

1.2.3 Rotational band crossings

In the region between 10 and 20 units of angular momentum, the regular $E \propto I(I+1)$ structure of the yrast rotational bands is disturbed in many nuclei [Joh71]. Such an effect can be easily reproduced as the crossing of two rotational bands with different moments of inertia (Figure 1.15). The second band arises from breaking up a pair of nucleons [Ste72] and has a higher moment of inertia than the ground-state band. Due to the higher moment of inertia the rotational energy is reduced. The effect is called 'backbending', because often for increasing angular momentum, I, the rotational frequency, ω_{rot}, decreases, producing a plot

of $I(\omega_{rot})$ that bends back. The breaking of a pair of nucleons results in a loss of pairing energy. Therefore, the backbend occurs at a rotational frequency where the Coriolis force compensates for the effect of pairing correlations [Lie78].

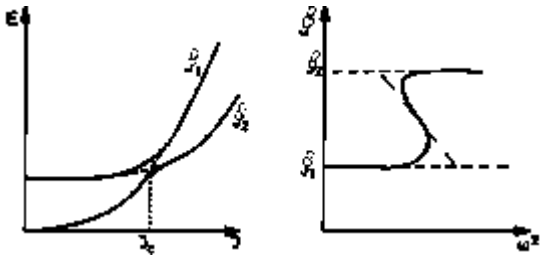

Figure 1.15: *Schematic picture of two crossing bands with different moments of inertia* $\Im_1$ *and* $\Im_2$ *and the corresponding backbending plot.* ω *is the rotational frequency. The picture is taken from [Rin80].*

In the rare earth region the $1i_{13/2}$ neutrons play an essential role in many band crossings. In the mass-180 region the $1i_{13/2}$ neutrons are competing with the $1h_{9/2}$ protons to cause the backbend. Other high-j orbits may play similar roles in different regions of the periodic table [Rin80].

The unpaired particles can couple to a state with $K \approx |\Omega_1 - \Omega_2|$, usually referred to as a s-band, or to a state with $K \approx |\Omega_1 + \Omega_2|$. Usually the low-$K$ coupling is energetically favoured, because this results in the largest Coriolis contribution H_{cor} (1.19) and, hence, the lowest total energy. However, ^{179}W provides the first studied case where the high-K coupling becomes yrast and causes a backbending [Wal91, Wal94]. This phenomenon of two competing $1i^2_{13/2}$ couplings is well described with the tilted axis cranking (TAC) model ([Fra93] and section 1.4.6). The high-K band has a large component of angular momentum in the direction of the symmetry axis of the nucleus. As a result, the total angular momentum is 'tilted' between the symmetry axis and the rotation axis and, therefore, this high-K backbend has been called a t-band as distinct from the usual low-K s-band. More recently discovered t-bands appear in ^{180}W [Wal93], ^{181,182}Os [Kut95] and ^{181}Re [Pea97].

1.2.4 A qualitative approach to pairing

Since Mottelson and Valatin [Mot60] predicted a phase transition from the superfluid phase in nuclei (all nucleons pair off to spin 0) to a normal-fluid phase (pairing correlations fully blocked), nuclear physicists have been fascinated by the superconductivity and its quenching in nuclei. From the discussion above about backbending it is clear that individual pairs can break up, blocking the overall pairing correlations and destroying the superfluidity. The rotation plays in nuclei the role of the magnetic field in metals. However, whereas the rotation acts to uncouple pairs of particles and destroys the correlations pair by pair, the application of magnetic fields in metals causes a sudden quenching of the superconductivity. In nuclei it is due to the finite particle number that the reduction of the pairing correlations in nuclei occurs step-by-step. Hence, contrary to the superfluid to normal phase transition in metals, a sharp first order-phase transition has not been observed in nuclei.

The orbitals of unpaired particles (also called 'quasiparticles') are not available anymore for pairs of nucleons. They are 'blocked' for the pairing correlations. As a result the pairing gap Δ is reduced (see also section 1.4.1). For uniform level densities, the pairing gap was initially estimated to depend on the number of unpaired particles, i.e., the seniority, ν, and the level spacing, d, as $\Delta \approx \sqrt{\Delta_0(\Delta_0 - \nu \times d)}$ [Dra98]. Since both proton and neutron pairing values (Δ_0) are about 1 MeV and the average spacing is about 300 keV, on that basis, pairing should have collapsed for a critical seniority of 3 or 4 in each nucleon type.

Experimentally, pairing is studied by extracting the moments of inertia from a rotational band. They can be compared to the moment of inertia of the fully paired ground-state band and to the rigid-body value. Due to the pairing correlations the moment of inertia of the ground-state band is reduced with a factor 2-3 compared to the rigid-body value [Boh53b]. Studies like in Ref. [Pas75] show that, if pairing is fully quenched, the moment of inertia approximates closely the rigid-body value, although shell structure effects might cause some modulations [Wal99].

Especially the rotational bands built on the yrast multi-quasiparticle K-isomers provide valuable information. Due to the yrast character of these states the effects of internal energy on the pairing (comparable to the effect of heat on a superconducting metal) can be isolated. In addition, the metastability of the K-traps implies that the nucleon orbitals are rather pure. This can be understood from the fact that often rather pure intruder orbitals are involved in the structure of these isomers. K-trap observables, such as the spin quantum number I (resulting from the broken nucleon pairs) can, therefore, be used to specify which pairs are broken and thus reducing the pairing correlations [Wal99].

The rotating K-traps with the most unpaired nucleons observed experimentally to date are the two ^{178}W ten-quasiparticle states with $K^\pi = 29^+$ and $K^\pi = 34^+$, respectively, both of them having six unpaired neutrons and 4 unpaired protons [Cul00]. However, the rotational bands built on these states are not established well enough to be able to extract the moments of inertia. The deduced moments of inertia of the eight-quasiparticle rotational bands built on the ^{178}W($K^\pi = 25^+, 28^-$ and 30^+) states [Pur95, Cul00] seem to saturate at 60% of the rigid-body value, despite the sizeable number of unpaired particles (four unpaired protons and four unpaired neutrons). This compares with 34% for the ^{178}W ground-state band.

A straightforward conclusion would be that pairing correlations persist even if there are four unpaired nucleons of each type, although substantially less strongly than in the ground-state [Wal99]. Indeed, neutron pairing gaps calculated with the Lipkin-Nogami method (see for example [Sat94, Pra73] and section 1.4.1) show discrete successive reductions of the pairing gap

$$\Delta_\nu \approx 0.75 \times \Delta_{\nu-2}, \tag{1.24}$$

so that even with six orbitals blocked near the Fermi surface the pairing remains at $\sim 40\%$ of the unblocked (fully paired) value. Similar results were obtained for the protons [Dra98].

However, a new viewpoint comes from the tilted axis cranking calculations (see [Fra00a] and section 1.4.6). These calculations allow to extract the kinematic

moment of inertia as $\Im^{(1)} = I/\omega$ and the dynamic moment of inertia as $\Im^{(2)} = dI/d\omega$. They show that the nuclear moment of inertia will only adhere to the classical rigid-body value *on the average*. The experimental moments of inertia of the multi-quasiparticle states in ^{178}W [Cul00] are reproduced without invoking pairing correlations. In other words, the conclusion from these calculations is that even if the pairing is fully quenched the moments of inertia in the mass ≈ 180 region are lower than the rigid-body value [Fra00d].

An important point in all the discussions above is that the moments of inertia depend on both the pairing and the deformation and, therefore, the deformation needs to be measured independently to be able to isolate the information about the pairing. Prior to our experiments on the five-quasiparticle ^{179}W($I^\pi = K^\pi = 35/2^-$) isomer only the quadrupole moments of the high-K isomers in ^{182}Os($K^\pi = 25^+$) [Bro91], ^{178}Hf($K^\pi = 16^+$) [Boo94, Lub96] and ^{177}Lu($K^\pi = 23/2^-$) [Geo98] were known. Most often it is assumed that the deformation of the high-K multi-quasiparticle states is similar to the deformation of the ground-state. The validity of this assumption will be further discussed in chapter 4.

1.2.5 The $(I^\pi = K^\pi = 35/2^-)$ isomer in ^{179}W

The anomalous decay of the $(I^\pi = K^\pi = 35/2^-)$ isomer in ^{179}W

As mentioned above, the decay of the 5-quasiparticle ^{179}W($I^\pi = K^\pi = 35/2^-, T_{1/2} = 750(80)$ ns, $E_i = 3349$ keV) isomer is one of the most striking examples of an apparent violation of the K-selection rule [Ber78b]. Figure 1.16 shows a partial level scheme of the ^{179}W nucleus with $K^\pi = 7/2^-$ 1-quasi-neutron ground-state band and the rotational bands built on the 3-quasi-neutron $K^\pi = 23/2^-$ state and the $K^\pi = 35/2^-$ isomeric state [Wal91]. The ^{179}W($I^\pi = K^\pi = 35/2^-, T_{1/2} = 750(80)$ ns, $E_i = 3349$ keV) isomer has a $3\nu(5/2^-[512] \otimes 7/2^-[514] \otimes 7/2^+[633])$ $2\pi(5/2^+[402] \otimes 9/2^-[514])$ configuration. The strongly populated $K^\pi = 35/2^-$ isomer decays directly via the 610 and 597 keV $E2$ transitions to a rotational state based on a $K^\pi = 7/2^-$, $7/2^-[514]$ ground-state, with apparently less than 5% going through the $K^\pi = 23/2^-$ 3-quasiparticle structures. This highly forbidden

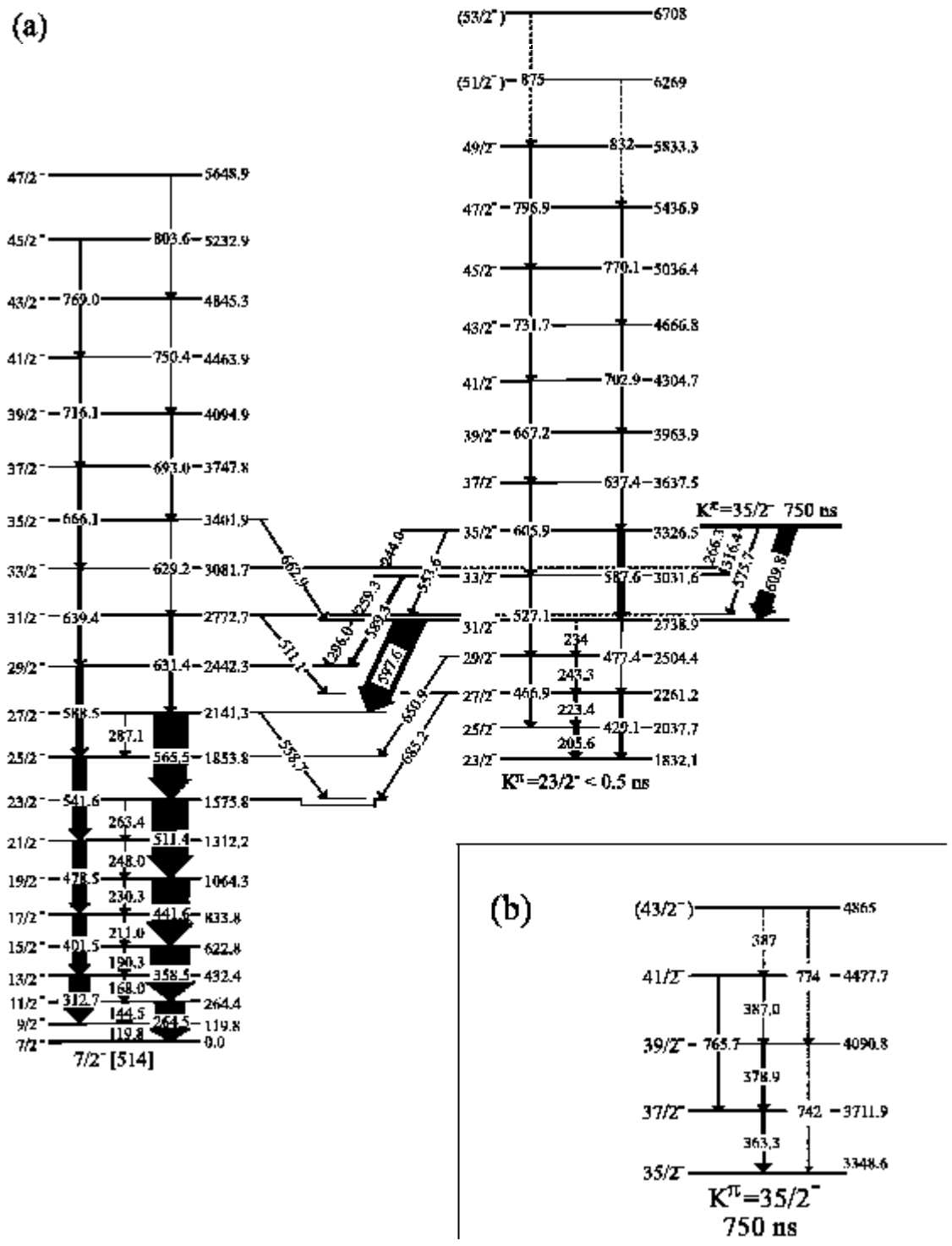

Figure 1.16: *(a) A partial level scheme of the ^{179}W nucleus, showing the ground-state band, the 3-quasi-neutron $K^\pi = 23/2^-$ band and the $K^\pi = 35/2^-$ isomer. (b) The rotational band built on the $K^\pi = 35/2^-$ isomer [Wal91, Wal94].*

$\Delta K = 14$ transition has a reduced hindrance f_ν of only 2.

Walker et al. removed this anomaly by showing that the 3-quasiparticle band is a t-band and not a low-K s-band [Wal91, Wal94]. The t-band arises from the high-K coupling of two Coriolis-mixed $1i_{13/2}$ quasi-neutrons, corresponding with the $7/2^+[633]$ and $9/2^+[624]$ Nilsson quantum numbers, respectively, to $K \approx (\Omega_1 + \Omega_2 \approx 8)$. Together with the $7/2^-[514]$ quasi-neutron this results in the $3\nu(7/2^-[514], 7/2^+[633], 9/2^+[624])_{23/2^-}, K^\pi = 23/2^-$ configuration for the 3 quasiparticle bandhead. This was the first case where an yrast high-K t-band was established. As a consequence, the change in K due to the 610 keV transition is only 6 and, hence, much smaller than assumed before. In addition, Walker et al. have shown that the near degeneracy of the $(I, K^\pi = 31/2, 7/2^-)$ and $(I, K^\pi = 31/2, 23/2^-)$ levels is responsible for the decay path via the 597 keV transition directly to the $K^\pi = 7/2^-$ ground-state band. Band crossing calculations have revealed that the two $31/2^-$ levels are highly K-mixed, each of them being about 50 % $K^\pi = 23/2^-$ and 50% $K^\pi = 7/2^-$. Furthermore, the calculations could show that destructive interference prohibits the decay path to the $(I, K^\pi = 23/2, 23/2^-)$ level. This can be understood as follows [Wal94]. The highly mixed levels, with $K = a$ and $K = b$ respectively, can be expressed in terms of the pure states, ϕ_a and ϕ_b:

$$\psi_-(I) = \alpha\phi_a + \beta\phi_b, \tag{1.25}$$

$$\psi_+(I) = -\beta\phi_a + \alpha\phi_b, \tag{1.26}$$

with $\alpha,\ \beta > 0$ and the normalisation $\alpha^2 + \beta^2 = 1$. The subscripts -,a and +,b refer to the lower and upper states, respectively. The rotational-model expression for the intra-band reduced transition probability from spin I_i to I_f ([deS74] and equation B.6):

$$\begin{aligned} B(E2, KI_i \rightarrow KI_f) &= \frac{5}{16\pi} e^2 (Q_0)^2 (2I_f + 1) \begin{pmatrix} I_f & 2 & I_i \\ -K & 0 & K \end{pmatrix}^2 \\ &= \frac{5}{16\pi} e^2 (Q_0)^2 \mid \langle I_i K 20 \mid I_f K \rangle \mid^2 \end{aligned} \tag{1.27}$$

with $\langle I_i K 20 \mid I_f K \rangle$ the Clebsch-Gordan coefficient, becomes for transitions from

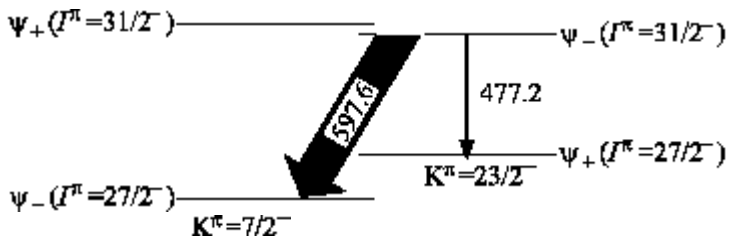

Figure 1.17: *Schematic picture of the positive and negative interference in the decay of the 31/1$^-$ level in ^{179}W (see text).*

$\psi_-(I_i)$ to $\psi_-(I_f)$:

$$B(E2) = \frac{5}{16\pi} e^2 Q_0^2 [\alpha(I_i)\alpha(I_f)C_{1Ka} + \beta(I_i)\beta(I_f)C_{1Kb}]^2 \qquad (1.28)$$

where $C_{1K} = \langle I_i K 20 \mid I_f K \rangle$, and it is assumed that the intrinsic quadrupole moment, Q_0, is the same for each of the configurations. For a ψ_- to ψ_+ transition, the $B(E2)$ reduced transition probability becomes

$$B(E2) = \frac{5}{16\pi} e^2 Q_0^2 [-\alpha(I_i)\beta(I_f)C_{1Ka} + \alpha(I_i)\beta(I_f)C_{1Kb}]^2. \qquad (1.29)$$

Note the combination of the negative and the positive sign in the term between brackets, causing a destructive interference between the two decay paths. This makes that a ψ_- to ψ_- (1.28) transition is favored over a ψ_- to ψ_+ transition (1.29). The 597 keV ($31/2^- \rightarrow 27/2^-$) transition is a ψ_- to ψ_- decay branch, while the 477 keV ($31/2^- \rightarrow 27/2^-$) transition is a ψ_- to ψ_+ transition (Figure 1.17). This explains why the 597 keV transition, directly to the ground-state band, is highly favoured over the 477 keV decay branch. In a similar way, a three-level-mixing scenario explains that it is due to destructive interference as well that the 576 keV transition from the $K^\pi = 35/2^-$ isomer is dramatically reduced, being only $(1.2 \pm 0.3)\%$ of the main 610 keV branch. Here the destructive interference arises from the near degeneracy of the $(I, K^\pi = 35/2, 7/2^-)$, $(I, K^\pi = 35/2, 23/2^-)$ and $(I, K^\pi = 35/2, 35/2^-)$ levels.

These arguments indicate that the decay from the $K^\pi = 35/2^-$ isomer is only 4 times forbidden ($\Delta K = 6$ and the multipolarity $\lambda = 2$) instead of 12 times.

As a consequence, the reduced hindrance f_ν is not 2, but $f_\nu = 2^{12/4} = 8$, which removes the decay-rate anomaly as shown in Figure 1.14.

Blocking of the pairing correlations

The ^{179}W($K^\pi = 35/2^-$) isomer is a (3-quasi-neutron + 2-quasi-proton) state. Hence it is an interesting case to study the reduction of the pairing gap Δ. Blocked BCS calculations [Zen83], as outlined in section1.4.1, have been performed by Walker et al. for the different multi-quasiparticle states [Wal94]. For the 1-quasi-neutron ground-state they result in a pairing gap Δ_ν of about 80% of the odd-even mass difference, as expected and often assumed. Already for the lowest 3-quasi-neutron states, Δ_ν is fully collapsed to below 1 keV. The proton pairing gap, Δ_π, is significantly reduced for the 2-quasi-proton excitations (1-quasi-neutron + 2-quasi-proton states). It has essentially vanished in the 4-quasi-proton excitations. The ^{179}W nucleus contains also two (3-quasi-neutron + 4-quasi-proton) states with $K^\pi = 43/2^-$ and $K^\pi = 45/2^{(-)}$ respectively. The blocked BCS calculations lead to the conclusion that both neutron and proton pairing correlations collapse in these high-K states.

However, in the calculations it is assumed that for all multi-quasiparticle states the deformation is the average value of the ground-state deformation for ^{178}W and ^{180}W [Wal94], i.e., $\epsilon_2 = 0.236$ and $\epsilon_4 = 0.044$ [Ben86]. This approximation is somewhat crude as the configurations of multi-quasiparticle states are not at all the same as the configurations of the ground-state. In our experiments the spectroscopic quadrupole moment of the ^{179}W($K^\pi = 35/2^-$) isomer has been determined. It allows to verify whether the assumption, that the multi-quasiparticle states have the same deformation as the ground-state, is valid. The experiments, in combination with a reinterpretation of the old ^{182}Os data [Bro91], show that that this is not the case. The results are discussed in chapter 4.

1.3 Rotational bands in spherical nuclei: magnetic rotation

1.3.1 The shears mechanism

The unusual features of long regular cascades of magnetic dipole ($M1$) transitions in the light Pb and Bi isotopes [Bal91, Ami00], and also in nuclei around mass numbers $A = 80$ [Sch99], $A = 110$ [Gad97] and 140 [Bra96, Juu94], led to an extension of the concept of rotation in quantal systems. The $M1$ sequences follow the rotational $I(I+1)$ behaviour which is typical for well-deformed nuclei, while lifetime measurements and the weak $E2$ crossover transitions suggest that the nuclear states in these bands are only weakly deformed ($|\beta| \leq 0.1$) [Cla97]. The ratio $B(M1)/B(E2)$ is, therefore, quite large, with values $\sim 10-100(\mu_N/eb)^2$. In normal rotational bands this ratio is less than 1 $(\mu_N/eb)^2$ [Ami00]. Furthermore, the ratio of the moment of inertia to the $B(E2)$ value, $\Im^{(2)}/B(E2)$, is > 100 MeV$^{-1}(eb)^{-1}$, which is a huge value as compared to normal and super deformed nuclei for which the ratio is typically 15 and 5 MeV$^{-1}(eb)^{-1}$, respectively. This shows that only a fraction of the inertia is created by the rotation of the deformed density distribution [Bal94, Fra97]. Hence the question rises whether and how nearly spherical nuclei can rotate and where the substantial dynamic moment of inertia is coming from. A consistent explanation for this enigma came from the tilted axis cranking (TAC) theory ([Fra93, Fra97, Fra00a] and section 1.4.6). This theory highlighted that the bands were originating from a new kind of symmetry-breaking in the nucleus, other than the breaking of the spherical symmetry of the nuclear charge distribution.

A common feature of the dipole bands is that they are built on a high-j proton-particle excitation coupled to a high-j neutron-hole state (or vice versa). In the Pb region proton-particle excitations across the $Z = 82$ shell gap are coupled to neutron holes in the $1i_{13/2}$ subshell. Typical configurations are the $\{\pi(3s_{1/2}^{-2}1h_{9/2}1i_{13/2})_{11^-} \otimes \nu 1i_{13/2}^{-1}\}_{29/2^-}$ state in ^{193}Pb [Chm97] and the $\{\pi(3s_{1/2}^{-2}1h_{9/2}1i_{13/2})_{11^-} \otimes \nu(1i_{13/2}^{-2})_{12^+}\}_{16^-}$ state in ^{196}Pb [Hug93]. The configura-

tion of the $I = 29/2$ isomer in ^{193}Pb has been confirmed unambiguously by a g-factor measurement [Chm97]. Note that no magnetic dipole bands have been observed on pure proton-excitations nor on pure neutron-hole states, but only on the coupling of them.

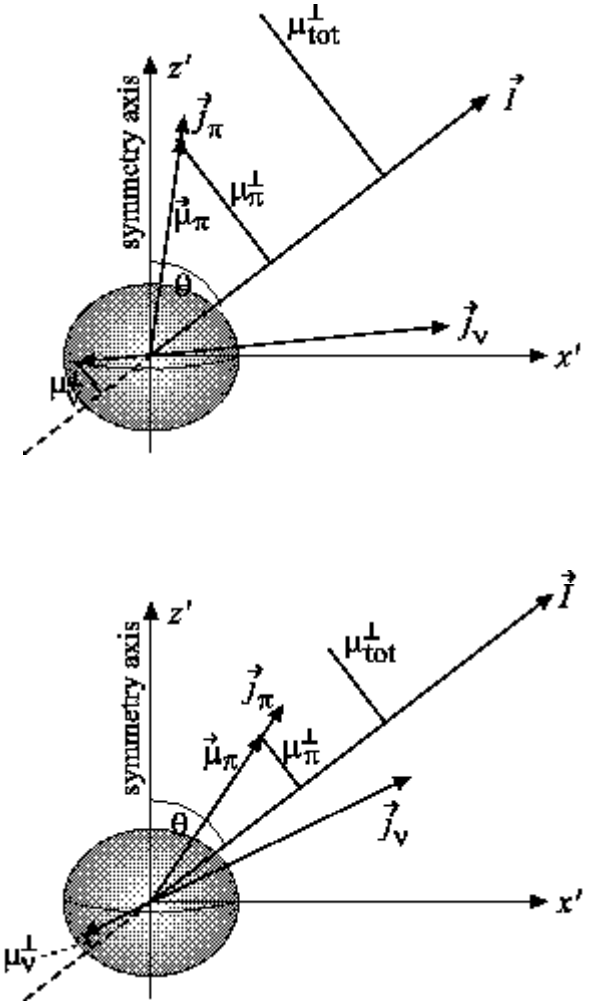

Figure 1.18: *Coupling scheme of the shears mechanism for a small oblate deformation near the bandhead (up) and higher up in the band (down) [Ami00].*

The combination of proton particles and neutron holes favours energetically an almost perpendicular coupling of the proton angular momentum j_π and the neutron angular momentum j_ν with respect to each other. This can be understood from the fact that the toroidal proton $1h_{9/2}$ and $1i_{13/2}$ density distributions

will drive the nucleus to an oblate shape with the proton angular momentum parallel to the symmetry axis of the nucleus to maximize the overlap of the orbits with the core of the nucleus. The neutron $1i_{13/2}$ holes are dumbbell (sphere minus a torus) shaped. They will maximize their overlap with the oblate density distribution if the neutron angular momentum is oriented perpendicular with respect to the symmetry axis of the oblate density distribution. Due to the perpendicular coupling of j_π and j_ν, with j_π oriented parallel to the symmetry axis of the nucleus, the total angular momentum I is pointing in between these two directions, i.e., in between the x'- and z'-direction and hence making an angle θ with the symmetry axis of the nucleus (Figure 1.18).

TAC calculations, assuming a deformation of $\epsilon \approx -0.1$, show that the angle θ keeps a value of about 45° along the bands [Fra93]. This means that the total angular momentum and the corresponding excitation energy are predominantly generated by aligning the proton-particle and the neutron-hole spins step by step in the direction of the total angular momentum. As this resembles the closing of a pair of shears, the bands are called 'shears bands'. Only a small fraction of the angular momentum is due to collective rotation [Bal94, Cla] and only 1/3 of the total moment of inertia $\Im^{(2)}$ due to the deformation [Fra97]. The almost constant angle θ in the dipole bands is in striking contrast to the changing angle θ in the bands built on high-K states in strongly deformed nuclei, where $\cos\theta = K/I$. In the latter bands θ is close to zero for the bandhead, where the total spin is dominated by the quasiparticle angular momenta near the bandhead ($I \approx K$) (deformation alignment). With increasing frequency, the collective rotational angular momentum, which is oriented perpendicular to the symmetry-axis, gains more and more influence ($I >> K$), causing the angle θ to tilt in the direction of the collective rotational angular momentum (rotational alignment) [Bal94]. Consequently, θ changes from 0° to 90° in the normal high-K bands.

Due to the large angle between the proton spin and the neutron spin a large component of the magnetic dipole moment perpendicular to the total angular momentum $\vec{I}$ is present. This specifies an orientation in space and hence is causing a symmetry breaking of the nucleus (Figure 1.18). The magnetic dipole vector

rotates around $\vec{I}$, generating the strong $M1$ radiation, just like the rotation of an asymmetric charge distribution generates strong $E2$ radiation. Because of the magnetic character of the rotation the name 'magnetic rotation' has been introduced as a distinct from 'electric rotation' [Fra97]. The closing of the shears gives rise to a gradually reduced transverse component of the magnetic dipole. As a consequence, the $B(M1)$ transition probabilities decrease by going up in the band. This decrease has been confirmed experimentally by lifetime measurements in the Pb isotopes [Cla97, Cla98]. These measurements together with the experimental g-factor confirm that a component of the magnetic moment perpendicular to the total angular momentum is present, which reduces gradually along the band and hence that an orientation in space is defined by a transverse magnetic dipole moment.

However, this still does not exclude that normal electric rotation of a moderately deformed oblate nucleus might be the engine behind the observed rotational bands. Therefore, experimental evidence that the bandhead is nearly spherical is necessary. An indication for the small deformation is given by the weak $B(E2)$ transition probabilities, resulting in $|\beta_2| \sim 0.1$ [Cla97, Nef95]. However, a precise experimental determination of the $B(E2)$ values is difficult because of the poor statistics in the $E2$ transitions compared to the strong $M1$ lines. Furthermore, systematic errors introduced through the treatment of the stopping powers might be present [Cla97]. Therefore, the experimental determination of the quadrupole moment of a shears bandhead is the final missing link in the picture of magnetic rotation.

1.3.2 Shears bands in ^{196}Pb

An overview of all shears bands measured to date is given in [Ami00]. Our measurements aimed to determine experimentally the spectroscopic quadrupole moment of the $(I^{\pi} = 16^{(-)})$ shears bandhead in ^{196}Pb. Figure 1.19 shows the level scheme of ^{196}Pb, including the higher energy part. Three shears bands have been observed, from which only for band 2 the linking transitions with the lower energy

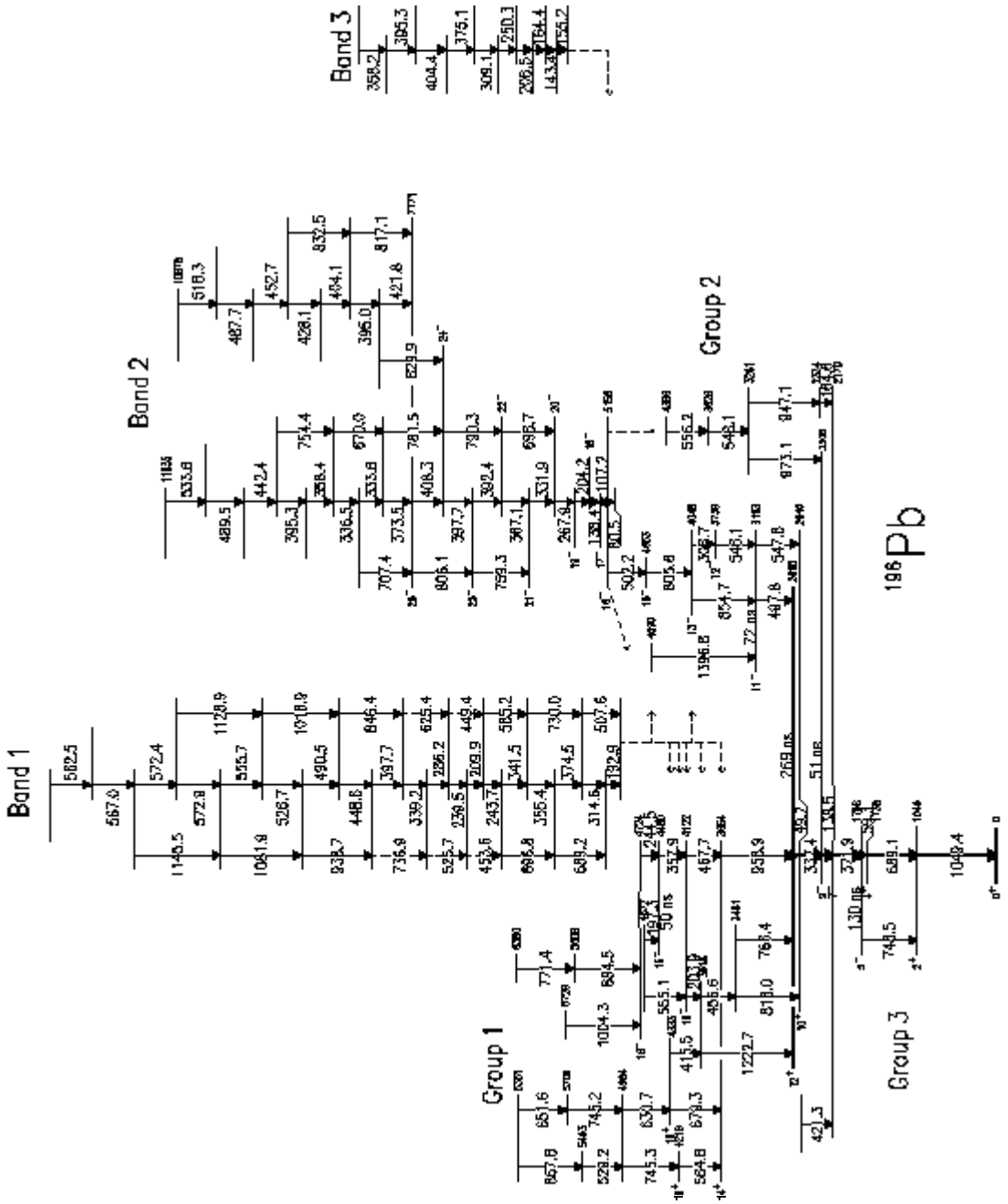

Figure 1.19: *Level scheme of ^{196}Pb, including the shears bands at high exciation energies [Bal00].*

part of the level scheme have been established. This allows to determine the spin and probable parity of this bandhead as $I^\pi = 16^{(-)}$. The spin assignments and excitation energies of bands 1 and 3 are unsure because of the lacking linking transitions [Hug93].

The $I^\pi = 16^{(-)}$ shears bandhead mainly decays through the 11^- isomeric level. Based on the measured g-factor this state has been assigned the $\pi(3s_{1/2}^{-2}1h_{9/2}1i_{13/2})$ configuration ([Pen87] and section 1.1.5). Meanwhile it is well known that the strong $M1$ bands in the Pb-region are built on proton excitations across the $Z = 82$ shell gap coupled to neutron-hole states [Hüb97]. The g-factor measurement of the $29/2^-$ state in ^{193}Pb provided the experimental proof that the proton angular momentum and the neutron angular momentum are oriented perpendicular with respect to each other [Chm97]. This leads to the conclusion that band 2 is built on the $\pi(1h_{9/2}1i_{13/2})_{11^-} \otimes \nu(1i_{13/2}^{-2})_{12^+}$ configuration. This assignment is consistent with the configuration assignment in Ref. [Hug93]. There total Routhian surface (TRS) calculations have been performed to decide which neutron configuration should be coupled to the proton $\pi(1h_{9/2}1i_{13/2})_{11^-}$ configuration to create the $I^\pi = 16^{(-)}$ bandhead.

Band 2 remains regular up to a transition energy $\hbar\omega \approx 0.4$ MeV, i.e., up to $I = 25$. Above spin $I = 25$ the band splits up in two pathways [Bal96]. The left branch could arise from a band crossing due to the breaking of a second $1i_{13/2}$ pair [Hug93]. This could mean that the band built on the $\pi(1h_{9/2}1i_{13/2})_{11^-} \otimes \nu(1i_{13/2}^{-2})_{12^+}$ configuration terminates at $I = 25$. Such an interpretation fits in the idea of the shears mechanism. The maximal spin that can be obtained by aligning the proton spin $I = 11$ and the neutron spin $I = 12$ is $I = 23$. Taking into account a typical collective core contribution of 10% [Cla], the spins in the band can reach at most a value of 25.

In practice, the measurement of a spectroscopic quadrupole moment of a shears bandhead is not straightforward due to the short lifetimes (the longest known half life of a shears bandhead is $T_{1/2} = 9$ ns for the $I = 29/2$ state in ^{193}Pb). Therefore, we have measured the spectroscopic quadrupole moment of the ($I^\pi = 11^-, T_{1/2} = 72$ ns, $\mu = 10.56(88)\mu_N$) isomer in ^{196}Pb which has the

same $\pi(3s_{1/2}^{-2}1h_{9/2}1i_{13/2})_{11^-}$ proton configuration as the $\{\pi(3s_{1/2}^{-2}1h_{9/2}1i_{13/2})_{11^-} \otimes \nu(1i_{13/2}^{-2})_{12^+}\}_{16^-}$ shears bandhead. Prior to this work the quadrupole moment of the $\nu(1i_{13/2}^{-2})_{12^+}$ isomer in ^{196}Pb has already been measured by applying the TDPAD method [Zyw81]. By coupling the quadrupole moments for the 12^+ isomer and the 11^- isomer, both built on a rather pure intruder configuration, information about the quadrupole moment of the 16^- shears bandhead can be obtained.

1.4 The tilted axis cranking (TAC) theory

In both the rotational bands built on the high-K isomers and the magnetic rotational bands the total angular momentum is tilted away from the principal axes of the nucleus. In the case of the high-K rotational bands this is due to the high-K coupling of the angular momentum of the unpaired particles, which gives rise to a large component of the angular momentum in the direction of the symmetry axis, in combination with a contribution to the spin due to the collective rotation of the nucleus around the axis perpendicular to the symmetry axis. In the case of a magnetic rotor, it is due to the perpendicular coupling of the proton and neutron spin, with the proton spin in the direction of the symmetry axis of the nucleus. Therefore, the tilted axis cranking theory (TAC), which allows rotation of the nucleus around an axis which is tilted away from the principal axes, is the suitable theory to describe theoretically these isomeric states and the rotational bands on top of them.

In the nuclear shell model (spherical or deformed, see sections 1.1.1 and 1.1.2) the nuclear many-body problem has been approached under the assumption that all the nucleons move independently from each other in an average potential created by themselves. A natural expansion of this is to consider the two-nucleon interactions as well. The Hamiltonian becomes

$$H = \sum_{i=1}^{A} -\frac{\hbar^2}{2m}\Delta_i + \sum_{i<j}^{A} v(i,j) \tag{1.30}$$

$$= \sum_{i=1}^{A} -\frac{\hbar^2}{2m}\Delta_i + \sum_{i=1}^{A} V(i) + V_{res} \quad (1.31)$$

$$= H_{sh} + V_{res}. \quad (1.32)$$

V_{res} is the residual interaction and in this thesis usually H_{sh} is chosen as the deformed modified oscillator Hamiltonian (1.7). In the spherical shell model in its purest form (see section 1.1.1), the residual interactions are neglected. However, throughout history nuclear physicists have developed different approaches for V_{res}, from which the Strutinsky renormalisation procedure is one example ([Str67] and section 1.4.4). In the TAC theory V_{res} is approached by the long range quadrupole-quadrupole + the short range pairing interaction. TAC calculations allow a self-consistent deduction (see below) of the spectroscopic quadrupole moment and the pairing gap Δ. An alternative approach is to use the experimentally deduced spectroscopic quadrupole moments or $B(E2)$ transition probabilities to fix the quadrupole coupling constant, χ. This pins down one unknown parameter in the TAC Hamiltonian, which illustrates the importance of measured quadrupole moments.

1.4.1 A quantitative approach to pairing correlations

The BCS approach

Bardeen, Cooper and Schrieffer determined the ground-state of a superconductor as [Bar57, Rin80]

$$\mid BCS\rangle = \prod_{k>0} (u_k + v_k a_k^+ a_{\overline{k}}^+) \mid -\rangle, \quad (1.33)$$

where u_k and v_k represent variational parameters. a_k^+ creates a particle in the state $\mid k\rangle$, a_k is the corresponding annihilation operator. In a superconducting metal k characterizes the momentum of an electronic state, whereas in the nuclear system it denotes the quantum numbers of a single particle state, i.e., $\Omega^\pi[Nn_z l]$ for a deformed state or (N, l, j, m_j) for a spherical state. $\mid \overline{k}\rangle$ is the time-reversed state of $\mid k\rangle$. u_k^2 and v_k^2 are the probabilities that a certain pair $\{k, \overline{k}\}$ is free or

occupied, respectively, in the bare vacuum such that

$$u_k^2 + v_k^2 = 1 \tag{1.34}$$

and also

$$2\sum_{k>0} v_k^2 = N \tag{1.35}$$

with N the particle number.

As in superconductors the BCS state takes the pairing interaction in an approximate way into account. The pairing part of the Hamiltonian can be written as

$$H_{pairing} = -G \sum_{kk'>0} a_k^+ a_{\bar{k}}^+ a_{k'} a_{\bar{k}'} \tag{1.36}$$

$$= -G\hat{P}^+\hat{P} \qquad \text{where} \qquad \hat{P}^+ = \sum_{k>0} a_k^+ a_{\bar{k}}^+, \tag{1.37}$$

in which G is the monopole pairing strength. It is the strength for the scattering of a pair of nucleons from a paired state $(k, -k)$ into $(k', -k')$. The parameters u_k and v_k of the trial wave function are determined by minimising the energy.

The use of a BCS wave function in nuclear physics has the disadvantage that $\mid BCS\rangle$ is a superposition of different numbers of pairs and hence no longer has a sharp particle number N. Whereas in solid state physics, where $N \approx 10^{23}$, the violation of N has essentially no influence on any physical quantity, it is clear that in nuclear physics it is important to maintain the correct number of protons and neutrons within the nucleus, when defining the theory. Therefore, the extra condition that the expectation value of the particle number operator, $\widehat{N}$, has to be the desired value N needs to be fulfilled:

$$\langle BCS \mid \widehat{N} \mid BCS\rangle = 2\sum_{k>0} v_k^2 = N. \tag{1.38}$$

This can be achieved by adding the term $-\lambda\widehat{N}$ to the Hamiltonian. The Lagrange multiplier λ is called the 'chemical potential' or the 'Fermi energy', because it represents the increase of the energy $E = \langle BCS \mid H \mid BCS\rangle$ for a change

in the particle number, $\lambda = \frac{d\epsilon}{dN}$. Hence the Hamiltonian including the pairing interaction and accounting for the correct particle number becomes

$$H_{BCS} = H_{sh} + H_{pairing} - \lambda\widehat{N} \qquad \text{and} \qquad H = H_{BCS} + \lambda\widehat{N}. \tag{1.39}$$

H_{sh}, written in the second quantisation formalism, equals

$$H_{sh} = \sum_{k>0} \epsilon_k (a_k^+ a_k + a_{\bar{k}}^+ a_{\bar{k}}) \tag{1.40}$$

with ϵ_k the single particle energy.

The pairing gap Δ is given by [Nil95]

$$\Delta = G \sum_{k>0} u_k v_k \tag{1.41}$$

and one can calculate that the probability for an occupied pair state is given by

$$v_k^2 = \frac{1}{2}\left[1 - \frac{(\widetilde{\epsilon}_k - \lambda)}{E_k}\right] \tag{1.42}$$

in which

$$E_k = \sqrt{(\widetilde{\epsilon}_k - \lambda)^2 + \Delta^2} \quad \text{with} \quad \widetilde{\epsilon}_k = \epsilon_k - G v_k^2. \tag{1.43}$$

E_k is the excitation energy of the quasiparticle (see below) relative to the Fermi surface. Usually the $-Gv_k^2$ term is neglected, because its only effect is a renormalisation of the single particle energies, and $\widetilde{\epsilon}_k = \epsilon_k$. Note that when the pairing gap Δ is equal to zero the probabilities $v_k^2 = 1$ and $u_k^2 = 0$ for occupied orbits.

In the Lipkin-Nogami approach, as mentioned in section 1.2.4, also the second order term in $\widehat{N}$ is taken into account in the formalism [Sat94, Pra73]:

$$H_{LN} = H - \lambda_1 \widehat{N} - \lambda_2 \widehat{N}^2. \tag{1.44}$$

This generally results in bigger pairing gaps Δ.

1.4.2 Quasi-particle states

There is an equivalent formulation of the BCS state (1.33) using the 'quasiparticle' operators [Rin80, Nil95]:

$$|\, BCS\rangle \propto \prod_k \alpha_k \,|\, -\rangle. \tag{1.45}$$

The quasiparticle operators are related to the operators a_k and $a_{\bar{k}}^+$ by the so-called Bogoliubov transformation:

$$\begin{aligned} \alpha_k^+ &= u_k a_k^+ - v_k a_{\bar{k}} \\ \alpha_{\bar{k}}^+ &= u_k a_{\bar{k}}^+ + v_k a_k. \end{aligned} \tag{1.46}$$

They have some features of a bare particle and of a bare hole. Above the Fermi-surface (v_k small) it is nearly a particle, below the Fermi surface (v_k large and hence u_k small) it is nearly a hole. The transformation to quasiparticles achieves a representation of pairwise interacting particles by means of a gas of non-interacting quasiparticles. As creation and annihilation operators are mixed, it is clear that again the particle number is not conserved.

The BCS state is the pair correlated ground-state of an even-even mass system. The ground-state of an odd-mass system is obtained as a one-quasiparticle excitation, i.e.,

$$\begin{aligned} \alpha_{k_1}^+ \mid BCS\rangle &= a_{k_1}^+ \prod_{k \neq k_1} (u_k + v_k a_k^+ a_{\bar{k}}^+ \mid -\rangle \\ \alpha_{\bar{k}_1}^+ \mid BCS\rangle &= a_{\bar{k}_1}^+ \prod_{k \neq k_1} (u_k + v_k a_k^+ a_{\bar{k}}^+ \mid -\rangle. \end{aligned} \tag{1.47}$$

Breaking up additional pairs results in multi-quasiparticle states. These states can be easily described by extending equations (1.47). It follows that, e.g., a '5-quasiparticle state' means that the state consists of 5 unpaired particles. An even-mass (odd-mass) nucleus always has an even (odd) number of quasiparticles.

The blocking effect

If an unpaired particle occupies level k_1, the probability $v_{k_1}^2$ for a pair to occupy the time-reversed states $\{k_1, \bar{k}_1\}$ is zero, as seen from equations (1.47). This means that the levels $\{k_1, \bar{k}_1\}$ cannot contribute to the pairing correlations. The formalism derived above remains valid, but the corresponding level is 'blocked' and needs to be excluded. The pairing gap Δ for an odd-A nucleus, e.g., becomes:

$$\Delta = G \sum_{k \neq k_1} u_k v_k. \tag{1.48}$$

It is immediately clear that the pairing gap Δ is reduced if unpaired particles are present and, accordingly, other physical quantities become influenced by the blocking.

1.4.3 The $\widehat{Q} \cdot \widehat{Q}$ interaction

The two-body interaction can be written as a multipole expansion [Rin80]

$$V(|\vec{r}_1 - \vec{r}_2|) = \sum_l V_l(r_1, r_2) \sum_m Y_l^{m*}(\theta_1, \phi_1) Y_l^m(\theta_2, \phi_2), \tag{1.49}$$

if it only depends on the relative distance between the nucleons. The low l components of this expansion correspond to the long range part of the residual interaction, contrary to the pairing interaction, which corresponds to the short rang part. If only the $l = 2$ component is considered, $V_l(r_1, r_2)$ is in a good approximation $\propto r_1^2 r_2^2$. V_Q reduces to

$$V_Q = -\frac{\chi}{2} \sum_{\mu=-2}^{2} \hat{Q}_\mu^+ \cdot \hat{Q}_\mu \tag{1.50}$$

with [Fra00a]

$$\hat{Q}_\mu = \sum_{kk'} \sqrt{\frac{4\pi}{5}} \langle k \mid r^2 Y_2^\mu \mid k' \rangle a_k^+ a_{k'}. \tag{1.51}$$

This part of the interaction can induce a quadrupole deformation of the mean field.

1.4.4 The Strutinsky shell correction procedure

In the (deformed) shell model the nucleus is considered as consisting of different nucleons which move independently from each other in an average potential. In the preceding sections this picture is refined by considering the residual interactions as well. This approach reproduces very well those nuclear properties in which only nucleons near the Fermi surface are involved. However, these models fail to reproduce correctly the properties of the nucleus in which all nucleons contribute (the so-called 'bulk' properties), like, e.g., the total binding energy.

A theory that describes well the bulk properties of the nucleus is the liquid drop model (LDM). This model allows to calculate the binding energy $B(N,Z)$ of the nucleus as a function of the mass number, by taking into account the volume of the nucleus, the Coulomb repulsion of the protons, the surface energy, the symmetry (neutron to proton ratio) and the pairing [vW35, Bet36].

$$B(N,Z) = a_V A + a_S A^{2/3} + a_C \frac{Z^2}{A^{1/3}} + a_I \frac{(N-Z)^2}{A} - \delta(A) \qquad (1.52)$$

in which a_V, a_S, a_C, a_I and $\delta(A)$ can be obtained be fitting the theoretical curve through the experimental masses. $\delta(A)$ is a term, which takes into account the pairing. It is positive for even-even nuclei, 0 for odd-even nuclei and negative for odd-odd nuclei. This is one more experimental indication that the nucleons prefer to occupy the orbitals pairwise. However, although the LDM can reproduce the average properties of most nuclei, there are significant deviations near the closed shells where the LDM underestimates the binding energy (or overestimates the nuclear mass).

Strutinsky invented an elegant method to reconcile the (deformed) shell model and the liquid drop model, eliminating their defects, but keeping their qualities [Str67, Rin80]. The oscillations in the binding energy are reflecting the oscillations

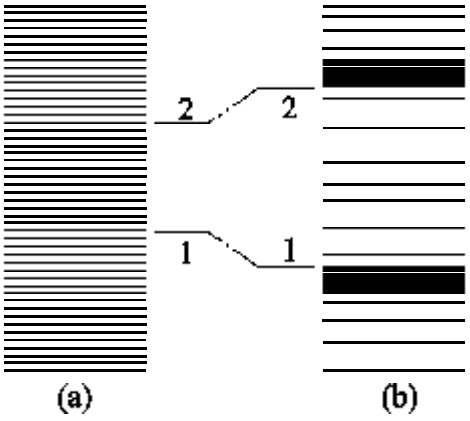

Figure 1.20: *Comparison of an equally spaced level density to a schematic shell model level density. For the Fermi level (1) the binding in (b) is stronger than in (a), whereas for (2) the opposite is true. The picture is taken from [Rin80].*

of the level density near the Fermi surface. If the Fermi level is situated just above a closed shell, the binding energy turns out to be more than on the average. Vice versa, the binding energy is less than on the average if the Fermi level is situated just below a closed shell (Figure 1.20). Hence the binding energies corresponding to the shell distribution oscillate around the ones given by the average level density. It is the average level density which is calculated wrongly in the shell model. Therefore, Strutinsky has approached the nuclear binding energy E by

$$E = E_{LDM} + E_{osc} \tag{1.53}$$

with E_{LDM} the liquid drop energy, representing the smooth part of the energy, and E_{osc} representing the oscillatory part of the energy. Strutinsky's method allows to calculate the fluctuating part within the shell model by dividing the shell model energy E_{sh} into an oscillating part E_{osc} and a smooth part $\tilde{E}_{sh}$, such that $E_{osc} = E_{sh} - \tilde{E}_{sh}$. As a result the total energy is given by

$$E = E_{LDM} + E_{sh} - \tilde{E}_{sh} \,. \tag{1.54}$$

1.4.5 The Cranking Hamiltonian

In section 1.2.1 the rotation of the nucleus has been treated by considering the nucleus as a whole. The treatment of the rotation of the nucleus on a microscopic level is usually done by considering the Hamiltonian in the rotating frame [Rin80]. This way the collective angular momentum is described as a sum of single-particle momenta. Therefore, collective rotation and single-particle rotation are handled on the same footing. A disadvantage of this approach is that the resulting wave functions are not eigenstates of the angular momentum operators.

The Hamiltonian in the rotating frame is

$$H_\omega = H - \vec{\omega} \cdot \vec{I} \tag{1.55}$$

with $\vec{\omega}$ the rotational frequency and $\vec{I}$ the angular momentum. The specific Hamiltonian H_ω is often called a 'Routhian'. The rotational frequency can be considered as a Lagrange multiplier.

In this approach the kinetic moment of inertia is derived as $\Im^{(1)} = I/\omega$, while the dynamic moment of inertia is derived as $\Im^{(2)} = dI/d\omega$.

1.4.6 The tilted axis cranking (TAC) Hamiltonian

The tilted axis cranking Routhian has the form [Fra00a]

$$H' = H_{sh} - \frac{\chi}{2} \sum_{\mu=-2}^{2} \hat{Q}_\mu^+ \cdot \hat{Q}_\mu - G\hat{P}^+\hat{P} - \lambda\widehat{N} - \vec{\omega} \cdot \vec{J} \tag{1.56}$$

where the different contributions have been discussed in the preceding sections. Because of the two-body interactions involved, the direct diagonalisation of the above TAC Routhian (1.56) is not possible. The TAC model means to apply instead the self-consistent mean field approximation by replacing one of the operator factors in the products $\hat{Q}_\mu^+ \cdot \hat{Q}_\mu$ and $\hat{P}^+\hat{P}$ by its expectation value. This leads to the mean field Routhian h':

$$h' = H_{sh} - \chi \sum_{\mu=-2}^{2} \langle\hat{Q}_\mu\rangle\hat{Q}_\mu^+ - G\langle\hat{P}\rangle(\hat{P}^+ + \hat{P}) - \lambda\widehat{N} - \vec{\omega} \cdot \vec{J} \tag{1.57}$$

in which it is used that $\langle P\rangle = \langle P^+\rangle$ [Nil95]. Equation (1.57) is usually written as

$$h' = H_{sh} - \sum_{\mu=-2}^{2} q_\mu\hat{Q}_\mu^+ - \Delta(\hat{P}^+ + \hat{P}) - \lambda\widehat{N} - \vec{\omega} \cdot \vec{J} \tag{1.58}$$

with as self-consistent conditions

$$q_\mu = \chi\langle\hat{Q}_\mu\rangle \tag{1.59}$$

$$\Delta = G\langle\hat{P}\rangle \tag{1.60}$$

and implicitly the chemical potential λ by

$$N = \langle\widehat{N}\rangle. \tag{1.61}$$

In the body-fixed axis system $\langle\hat{Q}_{-1}\rangle = \langle\hat{Q}_1\rangle = 0$ and $\langle\hat{Q}_{-2}\rangle = \langle\hat{Q}_2\rangle$. Then

$$q_0 = \hbar\omega_0\beta_2 cos\gamma \tag{1.62}$$

$$q_{-2} = q_2 = \hbar\omega_0\beta_2\frac{sin\gamma}{\sqrt{2}} \tag{1.63}$$

in which $\hbar\omega_0 \approx 41A^{-1/3}$ MeV (see equations (1.4)).

The eigenfunctions of the Routhian h' are products of the quasiparticle operators

$$\alpha_i^+ = \sum_k u_{ki} a_k^+ + v_{ki} a_k \tag{1.64}$$

which obey the equations of motion

$$[h', \alpha_i^+] = e_i' \alpha_i^+. \tag{1.65}$$

These equations determine the quasiparticle amplitudes u_{ki} and v_{ki}. They are solved for protons and neutrons separately from which the proton wave function ψ_P and the neutron wave function ψ_N are deduced. The final energy is calculated from the expectation value of the Routhian (1.56) $\langle \psi_N \psi_P \mid H' \mid \psi_N \psi_P \rangle$.

The TAC code includes the option to perform a Strutinsky shell correction procedure. This approach is preferred for well deformed nuclei. In the Pb region the Strutinsky-TAC version results in a typical deformation of $\epsilon \approx -0.15$, while the TAC calculations without Strutinsky normalisation procedure yield a value of $\epsilon \approx -0.11$. The latter deformation is in better agreement with the experimental data [Fra00b]. If no Strutinsky normalisation procedure is performed a proper choice of the quadrupole coupling constant, χ, is important. Usually it is chosen such that the quadrupole deformations ϵ and γ come as close as possible to the ones obtained by means of the shell correction method. However, one may also adjust it to the static quadrupole moments of high spin states and the $B(E2)$ values of the transitions between them. It seems promising to use this experimental information for a fine tuning of χ [Fra00b, Chm01], provided of course that the experimental information exists. Therefore, measured quadrupole moments of isomers with their angular momentum tilted away from the principal axes are important as they allow to fix one parameter in the calculations. Note that the coupling constant, χ, is assumed to be equal for protons and neutrons.

1.4.7 Physical quantities extracted from the TAC code

The TAC Hamiltonian contains seven parameters (+ the Nilsson parameters κ and μ): the Fermi level λ, the quadrupole and hexadecupole deformations ϵ_2 and ϵ_4, the triaxiality γ, the pairing gap Δ, the rotational frequency ω and the tilted angle θ. Besides these parameters also the configuration of the state is of uttermost importance. It is defined by indicating which levels relative to the Fermi-surface are occupied. If the hexadecupole deformation ϵ_4 is not known, it is optionally determined by Strutinsky's method (minimum energy) or put equal to zero. If the nucleus is axially symmetric, contrary to the convention chosen in this work, its symmetry axis is chosen parallel to the x'-axis. This implies that for an axially symmetric prolate nucleus, e.g., γ is taken $-120°$. For a particular set of parameters, the Routhian h' (1.58) is solved for the protons and neutrons separately, from which the wave functions ψ_P and ψ_N are determined in an iterative way, fulfilling the self-consistent conditions (1.59) and (1.60). Once these wave functions are known, all relevant physical quantities, such as the energy of the state, the corresponding spin, the quadrupole moment and the $B(E2)$ and $B(M1)$ transition probabilities can be determined, by taking the corresponding operator $\hat{O}$ and calculating the expectation value $\langle \psi_P \psi_N \mid \hat{O} \mid \psi_P \psi_N \rangle$.

In order to optimise the set of seven parameters (which reduces to five parameters if ϵ_4 and γ are kept fixed), first the Fermi-level λ is determined, so that

$$N = \langle \widehat{N} \rangle. \tag{1.66}$$

Once the Fermi-level is fixed, one can determine the deformation ϵ_2 and the pairing gap Δ self-consistently at the bandhead. This is done by calculating the corresponding energy for several values of ϵ_2 and/or Δ. The optimal values for ϵ_2 and Δ correspond with the lowest energy. An alternative approach is to make use of experimental values for ϵ_2 and/or Δ. Once the parameters λ, ϵ_2, ϵ_4, γ and Δ are fixed, one can go up in the band by changing the frequency ω. For each ω value the tilted angle θ can be varied and the angle corresponding with

the lowest energy can be found. If, while going up in band A, it crosses a band B, one can either choose to continue to follow band A (diabatic approach), or one can choose to follow the levels with the lowest energy, i.e., band B, which is called the adiabatic approach.

In this thesis we are especially interested in the quadrupole moment. In the TAC program it is calculated in the axis system with its z-axis parallel to the angular momentum J, further called the angular momentum (AM) axis system , as

$$Q_{TAC} = \langle JM_{AM} = J \mid \hat{Q}_2^0 \mid JM_{AM} = J \rangle. \tag{1.67}$$

It can be calculated that [Fra00c]

$$Q_{TAC} = \frac{1}{\sqrt{2J+1}} \langle J \| \hat{Q}_2 \| J \rangle. \tag{1.68}$$

Note that this approach is only valid for high spins, $J >> 1$. Hence, the spectroscopic quadrupole moment Q_s for high spin states can be extracted from Q_{TAC} by applying the Wigner-Eckart theorem[4]. The relationship between the spectroscopic quadrupole moment Q_s and Q_{TAC} becomes:

$$\begin{aligned} Q_s &\equiv \langle JM = J \mid \hat{Q}_2^0 \mid JM = J \rangle & (1.69)\\ &= \begin{pmatrix} J & 2 & J \\ -J & 0 & J \end{pmatrix} \langle J \| \hat{Q}_2 \| J \rangle & (1.70)\\ &= \begin{pmatrix} J & 2 & J \\ -J & 0 & J \end{pmatrix} \sqrt{2J+1} Q_{TAC} & (1.71)\\ &= \langle J2J0 \mid JJ \rangle Q_{TAC}. & (1.72) \end{aligned}$$

For high spins the Clebsch-Gordon coefficient $\langle J2J0 \mid JJ \rangle$ is in a good approximation equal to $\frac{J}{J+3/2}$. Notice that this ratio approaches one for $J >> 1$.

[4]The definition for the reduced matrix element used here is that of Racah [Rac42] and Edmonds [Edm57]. It is the convention which is used in most nuclear physics textbooks, such as in Refs. [deS74], [Boh75], [Rin80] and [Hey94]. Wigner [Wig59] and Rose [Ros57] define reduced matrix elements which are $\frac{1}{\sqrt{2J+1}}$ times those used in this thesis. The latter convention is used in textbooks like Ref. [Bri68].

The angular momentum J is determined as

$$J = \langle \hat{J}_z \rangle, \tag{1.73}$$

in the axis system with $\vec{J}$ parallel to the z-axis. Due to a quantal correction the calculated angular momentum J and the experimental angular momentum I differ by 1/2:

$$J = I + 1/2. \tag{1.74}$$

TAC calculations have been performed for the $I^\pi = K^\pi = 35/2^-$ isomer in ^{179}W and the $I^\pi = 16^-$ isomer in ^{196}Pb. The results will be discussed in chapters 3 and 4.

1.4.8 TAC and symmetry breaking in nuclei

One can show that for a self-consistent solution of the Routhian, h', the corresponding energy is the lowest if the angular velocity $\vec{\omega}$ is oriented parallel to the angular momentum $\vec{I}$ [Ker81], i.e.,

$$\vec{\omega} \| \vec{I}. \tag{1.75}$$

This allows a classification of the cranked solutions according to the orientation of the angular momentum $\vec{I}$ [Fra00a]. If the nucleus is axial-symmetrically deformed, the symmetry with respect to a rotation around an axis perpendicular to the symmetry axis of the nucleus, the x'-axis, is broken. This is the prerequisite for the appearance of rotational bands. Two cases can be distinguished.

i. The angular momentum is in the direction of a principal axis.

In this case the two-body Routhian (1.56) is invariant with respect to a $\mathcal{R}_x(\pi) = \exp(i\pi I_x)$ rotation about the x-axis by an angle of π, where the axis system (x, y, z) is chosen such that $\vec{I} \parallel x$-axis (Figure 1.21). The quantum number, expressing this symmetry, is called 'signature' [Ben79]. Each eigenvalue, r_x, of the operator $\mathcal{R}_x$ corresponds with a different signature quantum number α, where α can take the values 1/2, -1/2, 0 and 1, corresponding to r_x equal to $+i$, $-i$, $+1$

and -1 respectively. This can be understood as follows. If the angular momentum is oriented parallel to the rotational axis x, the eigenvalue r_x of the operator $\mathcal{R}_x$ yields

$$r_x = \exp(i\pi I). \tag{1.76}$$

Therefore

$$\begin{aligned}
\text{signature } \alpha = +1/2 \quad &: \quad r_x = +i \quad \text{for} \quad I = 1/2, 5/2, 9/2, ... \\
\text{signature } \alpha = -1/2 \quad &: \quad r_x = -i \quad \text{for} \quad I = 3/2, 7/2, 11/2, ... \\
\text{signature } \alpha = 0 \quad &: \quad r_x = +1 \quad \text{for} \quad I = 0, 2, 4, ... \\
\text{signature } \alpha = 1 \quad &: \quad r_x = -1 \quad \text{for} \quad I = 1, 3, 5, ...
\end{aligned}$$

Hence, rotational bands with a good signature quantum number α have an angular momentum I that changes in steps of 2. Total Routhian surface (TRS) calculations are principal axis cranking (PAC) calculations.

ii. The angular momentum is in a principal plane.

If the angular momentum $\vec{I}$ is tilted away from the principal axes, but still lies in one of the three principal planes (the latter is always the case for an axial shape), the Routhian is no longer invariant with respect to $\mathcal{R}_x(\pi)$ and signature is no longer a good quantum number. There is no extra selection rule and the rotational band has a $\Delta I = 1$ spacing. The members of the $\Delta I = 1$ bands are linked by $E2$ transitions between the states I and $I-2$ as well as by $M1$ and $E2$ transitions between the states I and $I-1$. Hence, the occurrence of the strong $B(M1)$ transition probabilities in a magnetic rotational band arises in a natural way from tilting away the angular momentum from the principal axes.

A third case occurs when the nucleus is triaxial.

iii. The angular momentum is out of the principal planes.

If the nucleus is triaxial, also rotation about an axis outside the principal planes is possible. This results in the breaking of the so-called 'chiral symmetry'. The chiral operator is $\mathcal{R}_y(\pi)\mathcal{T}$, in which $\mathcal{R}_y(\pi)$ denotes a rotation about the y-axis with an angle of π and $\mathcal{T}$ is the time reversal operator [Fra00a, Dim00]. The $\mathcal{R}_y(\pi)$

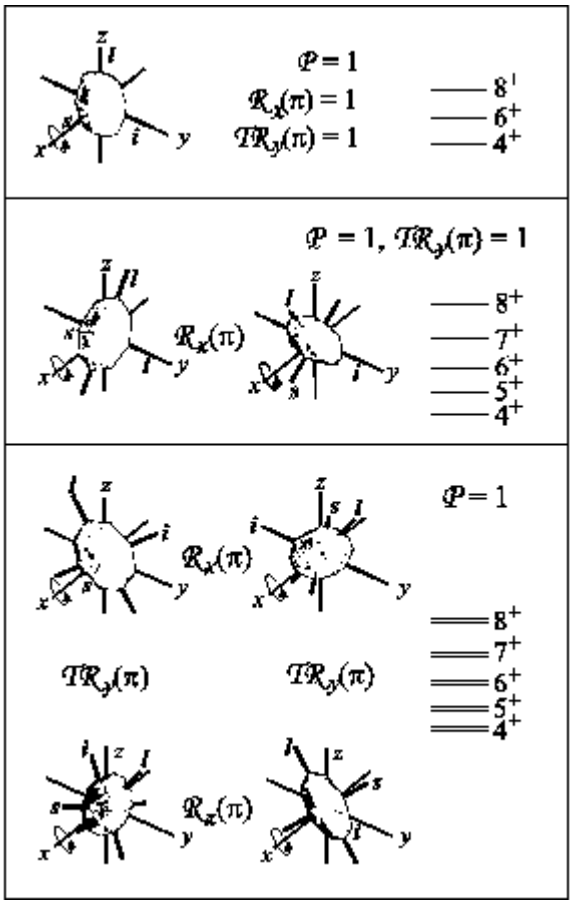

Figure 1.21: *The discrete symmetries of the mean field of a rotating triaxial reflection symmetric nucleus. The labels s, i and l denote the short, intermediate and long principle axis of the nucleus respectively. For an axially symmetric prolate nucleus, s equals i. The axis of rotation, x, is marked by the circular arrow. Its direction coincides with the direction of the angular momentum $\vec{I}$. The structure of the rotational bands associated with each symmetry is illustrated on the right side. The picture is adapted from [Dim00].*

changes the spin $\vec{I} = (I_x, 0, 0)$ to $-\vec{I} = (-I_x, 0, 0)$ and the nuclear coordinates (x, y, z) to $(-x, y, -z)$. The time reversal operator changes $-\vec{I}$ back to $\vec{I}$, but does not influence the nuclear coordinates. Hence the orientation of the spin $\vec{I}$ is changed with respect to the orientation of the nucleus and the chiral symmetry is broken. This is illustrated by the lower panel of Figure 1.21. In the planar case,

ii, the symmetry with respect to the (x, z) plane makes that for each point with coordinates (x, y, z) also a point with coordinates $(-x, y, -z)$ exists on the nuclear surface. This is not the case for the aplanar solutions. Therefore, contrary to the aplanar solutions, the chiral symmetry is maintained for the planar solutions.

A triaxial nucleus is called right-handed if the short, intermediate and long principal axis are oriented counterclockwise, and left-handed if they are ordered clockwise. The breaking of the $\mathcal{R}_y(\pi)\mathcal{T}$ symmetry causes a doubling of the rotational levels. There are two identical $\Delta I = 1$ sequences with the same parity, which represent the left-handed and right-handed mean field solutions [Fra00a].

In all three cases the nuclear mean field is invariant for replacing the coordinates (x, y, z) by $(-x, -y, -z)$. The 'space inversion' operator is denoted by $\mathcal{P}$. The corresponding quantum number is the parity, π, which is hence conserved in all rotational bands.

Both the rotational bands built on the $I^\pi = 16^-$ isomer in ^{196}Pb and on the $35/2^-$ isomer in ^{179}W, are $\Delta I = 1$ sequences (Figures 1.19 and 1.16), which is an experimental fingerprint that in these bands the angular momentum is tilted away from the principal axes of the nucleus.

1.5 Conclusion

This chapter has shown how the nuclear deformation provides valuable information about the structure of the nucleus, both near the closed shells and in between the closed shells. In concreto, the quadrupole moments of the ^{196}Pb$(I^\pi = 11^-)$ and the 5 quasiparticle ^{179}W$(I^\pi = K^\pi = 35/2^-)$ isomer have been measured. The aim of the measurement of the 11^- isomer in ^{196}Pb is two-fold. First, it provides information about the deformation of an intruder state. Second, it allows to test experimentally whether the bandhead of a magnetic rotor is nearly spherical indeed. The measurement on the ^{179}W$(I^\pi = K^\pi = 35/2^-)$ isomer is important in the frame of the pairing correlations in nuclei. The tilted axis cranking theory is

the modern approach to describe the magnetic rotational bands and the bands built on high-K isomers, because in both cases it is believed that the total angular momentum is tilted away from the principal axes.

Chapter 2

Level mixing spectroscopy

The family of level mixing techniques has proven to be a very powerful tool for measuring quadrupole moments of a wide variety of nuclei. While recently the level mixing resonance (LMR) technique [Sch89] has been extended for quadrupole moment studies of β-decaying nuclei away from the β-stability line [Ney94, Ney97a, Ney99, Cou99], its variant level mixing spectroscopy (LEMS) is suitable for measuring quadrupole moments of γ-decaying nuclei with high spin [Har91a, Har91b, Ney93b, Bal01]. The principles of the LEMS technique have been extensively treated in Refs. [Har91a, Har91b, Ney93a, Ter98a]. Here the main features, necessary for a good understanding of the extensions and variants developed in this thesis (sections 2.2, 2.4 and 4.4.2), will be briefly repeated.

2.1 Basic principles of LEMS

2.1.1 The LEMS Hamiltonian

Similar to all level mixing techniques the electric quadrupole interaction in a LEMS measurement is studied by submitting the isomers of interest to a combined electric quadrupole and magnetic dipole interaction which are misaligned with an angle β. The change of the anisotropy of the emitted radiation as a function of the magnetic field strength is measured. The electric field gradient (EFG) is provided by the internal crystalline fields after in-beam implantation of the

reaction residues in a non-cubic host lattice. The magnetic field is provided by a superconducting magnet (Figure 2.1).

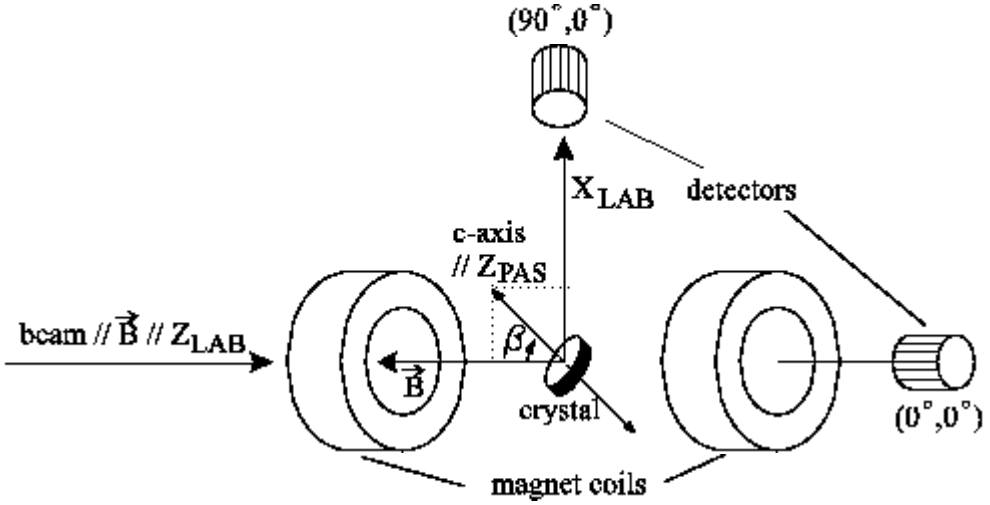

Figure 2.1: *Schematic LEMS setup.*

In the axis system with the Z-axis parallel to the magnetic field direction (LAB system), the Hamiltonian of the magnetic interaction can be written as

$$\mathcal{H}_B = -\omega_B \hat{I}_{Z_{LAB}} \tag{2.1}$$

where $\omega_B = g\mu_N B_0/\hbar$ is the magnetic interaction frequency. For an axially symmetric EFG the Hamiltonian of the quadrupole interaction can be written in the principal axis system (PAS) of the EFG as

$$\mathcal{H}_Q = \frac{\omega_Q}{\hbar}(3\hat{I}^2_{Z_{PAS}} - \hat{I}^2) \tag{2.2}$$

where $\omega_Q = \frac{eQ_s V_{ZZ}}{\hbar I(2I-1)}$ is the electric quadrupole frequency and Q_s is the spectroscopic quadrupole moment. For a nonaxially symmetric EFG the Hamiltonian $\mathcal{H}_Q$ includes an extra parameter, the asymmetry parameter η [Ste75]. In the LEMS experiments described in this thesis only crystals having an axially symmetric EFG, namely hcp Re and hcp Tl, have been used. In addition, LEMS is insensitive for deviations from the axial symmetry [Har91a]. Therefore, only the axially symmetric terms are considered here.

It is possible to orient the crystal such that the c-axis (Z_{PAS} axis) is in the (X_{LAB}, Z_{LAB}) plane. In this configuration the transformation from the PAS to the LAB system is characterized by only one angle, the misalignment angle β, due to the axial symmetry of both the magnetic dipole and electric quadrupole interaction. Transforming $\mathcal{H}_Q$ from the PAS to the LAB system and combining both interactions results in the following nonvanishing elements for the LEMS Hamiltonian $\mathcal{H}_{LEMS}$ [Mat62]:

$$\begin{aligned}
\langle m_I \mid \mathcal{H}_{LEMS} \mid m_I \rangle &= -\hbar\omega_B m_I + \hbar\omega_Q \frac{1}{2}(3\cos^2\beta - 1)[3m_I^2 - I(I+1)] \\
\langle m_I \mid \mathcal{H}_{LEMS} \mid m_I - 1 \rangle &= -\frac{3}{2}\hbar\omega_Q \cos\beta \sin\beta (1 - 2m_I)\sqrt{(I - m_I + 1)(I + m_I)} \\
\langle m_I \mid \mathcal{H}_{LEMS} \mid m_I - 2 \rangle &= \\
&\frac{3}{4}\hbar\omega_Q \sin^2\beta \sqrt{(I + m_I - 1)(I + m_I)(I - m_I + 1)(I - m_I + 2)}.
\end{aligned} \tag{2.3}$$

The nondiagonal elements involve a mixing of the populations of the different m_I states and are thus responsible for the change of the orientation of the nuclear ensemble. They are only present if the misalignment angle β differs from zero. When polycrystals are used the perturbation factors $G_{kk'}^{nn'}(I, \mathcal{H}_{LEMS}, \tau)$ (see below, expression (2.14)) need to be integrated over all possible angles β.

2.1.2 Study of the electromagnetic perturbation via the angular distribution of the γ radiation

The angular distribution function

The influence of the perturbation, governed by $\mathcal{H}_{LEMS}$, on an isomeric state, can be studied by observing the subsequent radiation of this state. The perturbed angular distribution of the radiation is given by [Ste75]

$$W(\theta, \phi, t) = \sqrt{4\pi} \sum_{k,n} \frac{1}{\sqrt{2k+1}} A_k U_k B_k^n(I, t) Y_k^n(\theta, \phi), \tag{2.4}$$

with A_k being the radiation parameters of the observed transitions (k even for γ radiation), U_k describing the loss of orientation due to nondetected preceding

γ rays, $B_k^n(I,t)$ being the orientation tensors at time t and $Y_k^n(\theta,\phi)$ being the spherical harmonics in which θ and ϕ define the detection directions with respect to the magnetic field direction. Usually only the $k = 2,4$ components are considered.

The A_k, U_k and $Y_k^n(\theta,\phi)$ tensors are only important in the sense that they influence the amplitude of the LEMS curve (Figure 2.3). The U_k factors are often close to 1 and have only a small influence. The A_k values increase if the multipolarity λ of the γ rays, depopulating the isomer of interest, increases. Therefore, γ rays with high multipolarty are more advantageous to study, because they result in a larger LEMS amplitude. Furthermore, the A_2 value of a transition with $\lambda = 1$ has an opposite sign compared to the A_2 value of γ transitions with $\lambda = 2,3,....$ This means that, if a transition with $\lambda = 2$ in a certain detector results in an increasing LEMS curve, a transition with $\lambda = 1$ in the same detector will result in a decreasing LEMS curve. A more important consequence is that mixed $M1/E2$ transitions can result in A_2 values close to zero, making a LEMS measurement impossible. A similar argumentation can be made for the $Y_k^n(\theta,\phi)$ tensors. A detector in the direction of the magnetic field has $Y_0^2(0°,0°) = 1$. In this direction the LEMS curve with the largest amplitude is observed.

The B_k^n tensors describe the orientation of the nuclear ensemble. This orientation is changed by the magnetic dipole and electric quadrupole interaction. Due to the change of the orientation tensors by these interactions, the ratio ν_Q/μ can be extracted.

Production and orientation in a fusion-evaporation reaction

It is obvious that, in order to detect a change of the orientation of the nuclear ensemble via a change in the angular distribution of the γ rays, first the nuclear ensemble needs to be oriented. In a standard LEMS experiment the nuclei of interest are produced in a fusion-evaporation reaction, which also provides an axially symmetric orientation around the beam axis ([She66] and Figure 2.2). The energy of the beam needs to be above the Coulomb barrier in this case. The projectile and target nucleus fuse together and form a compound nucleus at

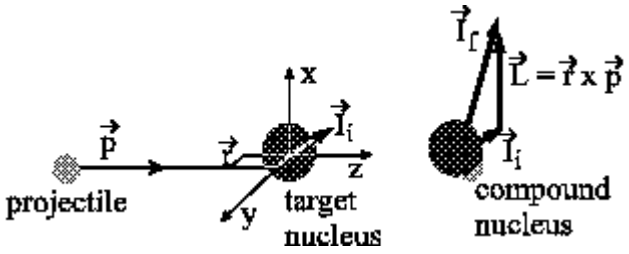

Figure 2.2: *Orientation obtained in a fusion-evaporation reaction. $\vec{I}_i$ denotes the initial spin of the target nucleus. $\vec{L}$ denotes the contribution to the angular momentum of the compound nucleus, generated by the nuclear reaction. $\vec{L} = \vec{r} \times \vec{p}$ with $\vec{r}$ the randomly oriented impact parameter and $\vec{p}$ the momentum of the projectile. The final spin $\vec{I}_f = \vec{I}_i + \vec{L}$ is oriented preferentially perpendicular to the beam axis.*

high excitation energy. The compound nucleus subsequently evaporates particles (mostly neutrons, sometimes also protons and α particles) before further decaying by γ-ray emission. The fusion-evaporation reaction imparts a transfer of a large quantity of angular momentum from the projectile to the compound nucleus. This angular momentum is oriented preferentially perpendicular to the beam axis, i.e., the initial orientation axis, which is illustrated by Figure 2.2. Usually the magnetic field is oriented parallel to the beam axis. This allows an easy description of the orientation of the nuclear ensemble in the LAB system (Figure 2.1). A Gaussian distribution of the spins with respect to $m_I = 0$, with m_I the projection of $\vec{I}$ on the Z_{LAB} axis, is assumed [New67]:

$$P(m_I) = \frac{\exp(\frac{-m_I^2}{2\sigma^2})}{\sum_{m_I'} \exp(\frac{-m_I'^2}{2\sigma^2})}. \tag{2.5}$$

$P(m_I)$ is the probability of occupation of a state m_I. The amount of initial orientation is hence fully determined by the Gaussian width σ. Normalised with respect to the total spin I, σ/I is typically in the range of 0.3 to 0.4 for heavy ion reactions [Mor76]. Expression (2.5) allows to calculate the density matrix elements at the moment of production $t = 0$ in an easy way:

$$\langle m_I \mid \rho(t=0) \mid m_I' \rangle = \delta_{m_I m_I'} \rho_{m_I m_I'}(t=0) = \delta_{m_I m_I'} P(m_I). \tag{2.6}$$

The perturbation factors

The orientation tensor B_k^n as used in expression (2.4) is related to the density matrix $\rho(t)$ via [Fan59]

$$B_k^n(I,t) = \sqrt{2I+1}\sqrt{2k+1} \sum_{m_I, m_I'} (-1)^{I+m_I} \begin{pmatrix} I & I & k \\ -m_I & m_I' & n \end{pmatrix} \langle m_I \mid \rho(t) \mid m_I' \rangle. \tag{2.7}$$

It can be written as a function of the initial orientation $B_{k'}^{n'}(t=0)$ as [Ste75]

$$B_k^n(I,t) = \sum_{k'n'} G_{kk'}^{nn'}(I, \mathcal{H}_{LEMS}, t) B_{k'}^{n'}(t=0). \tag{2.8}$$

The functions $G_{kk'}^{nn'}(I, \mathcal{H}_{LEMS}, t)$ are the perturbation factors that describe the influence of the Hamiltonian on the orientation of the nuclear ensemble, as described by the density matrix ρ or, equivalently, by the orientation tensors B_k^n [Ste75]. The perturbation factors can be calculated explicitly by solving the von Neumann equation $i\hbar\frac{d\rho}{dt} = [\mathcal{H}, \rho]$ from which the time evolution of the density matrix [Fan59] is deduced, using the eigenstates of $\mathcal{H}_{LEMS}$. For static interactions the solution of this equation is [Ste75]

$$\rho(t) = \exp(\frac{-i\mathcal{H}t}{\hbar}) \rho(t=0) \exp(\frac{i\mathcal{H}t}{\hbar}). \tag{2.9}$$

Via the direct relationship between the orientation tensors $B_k^n(I,t)$ and the density matrix elements $\langle m_I \mid \rho(t) \mid m_I' \rangle$ (2.7) the perturbation factors can be calculated explicitly as

$$\begin{aligned} G_{kk'}^{nn'}(I, \mathcal{H}_{LEMS}, t) &= \sqrt{2k+1}\sqrt{2k'+1} \\ &\times \sum_{m_I, \mu_I, N, N'} (-1)^{m_I - \mu_I} \begin{pmatrix} I & I & k \\ -m_I & m_I' & n \end{pmatrix} \begin{pmatrix} I & I & k' \\ -\mu_I & \mu_I' & n' \end{pmatrix} \\ &\times \exp(-i\omega_{NN'}^{LEMS} t) \langle m_I \mid N \rangle \langle N \mid \mu_I \rangle \langle m_I' \mid N' \rangle^* \langle N' \mid \mu_I' \rangle^* \end{aligned} \tag{2.10}$$

with $\omega_{NN'}^{LEMS} = \frac{E_N - E_{N'}}{\hbar}$. E_N and $\mid N \rangle$ are the eigenvalues and corresponding eigenvectors of $\mathcal{H}_{LEMS}$, derived by a numerical diagonalisation of the matrix (2.3).

The $G_{kk'}^{nn'}(n' \neq 0)$ terms are not necessary to be calculated because of the axial symmetry of the ensemble of compound nuclei produced in a fusion-evaporation reaction. This makes that these perturbation factors are multiplied with the $B_k^{n' \neq 0}(t = 0) = 0$ tensor components in the angular distribution function. If the EFG is provided by a polycrystal and the magnetic field is oriented parallel to the beam axis, only the $G_{kk'}^{00}$ terms need to be taken into account, because of the axial symmetry of the system with respect to the symmetry axis of the initial orientation.

Further the LEMS perturbation factor will be denoted as

$$G_{kk'}^{nn'}(I, \mathcal{H}_{LEMS}, t) = \sum_{NN'} (f_{NN'}^{LEMS})_{kk'}^{nn'} \exp(-i\omega_{NN'}^{LEMS} t). \tag{2.11}$$

As LEMS measurements are time-averaged measurements, a time integration, including a $\exp(-t/\tau)$ weight to incorporate the nuclear lifetime of the isomer, has to be made

$$G_{kk'}^{nn'}(I, \mathcal{H}_{LEMS}, \tau) = \frac{\int_0^\infty G_{kk'}^{nn'}(I, \mathcal{H}_{LEMS}, t) \exp(-t/\tau) dt}{\int_0^\infty \exp(-t/\tau) dt} \tag{2.12}$$

$$= \sum_{NN'} (f_{NN'}^{LEMS})_{kk'}^{nn'} \frac{1}{1 + i\omega_{NN'}^{LEMS} \tau}. \tag{2.13}$$

For $n = n' = 0$ the real part equals

$$G_{kk'}^{00}(I, \mathcal{H}_{LEMS}, \tau) = \sum_{NN'} (f_{NN'}^{LEMS})_{kk'}^{00} \frac{1}{1 + (\omega_{NN'}^{LEMS} \tau)^2}, \tag{2.14}$$

while the imaginary part drops, because it is odd in $\omega_{NN'}^{LEMS}$.

A qualitative approach to LEMS

The result for the anisotropy of the γ radiation as a function of the magnetic field is a decoupling curve (Figure 2.3), which can be explained in a hand waving way as follows. After production and orientation the isomers of interest are caught in a suitable host where they are submitted to a combined electric quadrupole and magnetic dipole interaction. The magnetic field is oriented parallel to the beam axis, i.e., the symmetry axis of the initial orientation. At zero magnetic field only the quadrupole interaction is present and the initial orientation and anisotropy

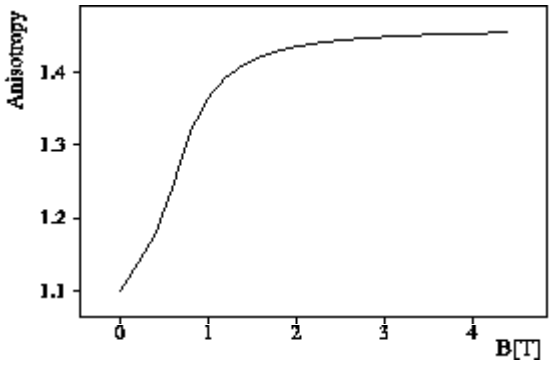

Figure 2.3: *Simulation of a LEMS curve for an isomer with* $I = 10$, *which decays via a* $10^+ \rightarrow 8^+$ *E2 transition. The other parameters are* $\nu_Q = 10$ *MHz,* $\mu = 1$ μ_N, $\sigma/I = 0.35$ *and* $N = 1$. *The isomer is implanted in a polycrystalline material.*

is decreased to the hardcore value. At high magnetic fields (several Tesla), the electric quadrupole interaction is negligible compared to the Larmor precession of the isomeric spins around $\vec{B}$. As the precession axis coincides with the initial orientation axis, the initial anisotropy is measured. At intermediate fields there is a competition between the quadrupole and the magnetic interaction and a smooth change from the hard-core anisotropy to the initial full anisotropy takes place. This part of the LEMS curve is sensitive to the ratio of the quadrupole interaction frequency $\nu_Q = \frac{eQV_{zz}}{h}$ to the magnetic moment μ of the isomer. So, if the magnetic moment is known, the quadrupole interaction frequency can be deduced. Besides the ratio ν_Q/μ, a LEMS curve depends on two more fit parameters: the initial orientation, σ/I, and a normalisation factor, N, depending on the detector efficiencies. The normalisation factor N shifts the LEMS curve as a whole up or down. The amount of initial orientation, quantified by σ/I, influences the LEMS curve in the high magnetic field regime, because at high magnetic fields the initial anisotropy is measured. At 0 Tesla, where the anisotropy is reduced due to the electric quadrupole moment, the LEMS curve is rather insensitive to σ/I. Hence the fit parameter σ/I is related to the amplitude of the LEMS curve. The more initial orientation has been produced by the nuclear reaction, the bigger the LEMS amplitude will be.

The LEMS condition

Notice that a detectable perturbation of the orientation of the nuclear ensemble due to the electric quadrupole interaction is only possible if the lifetime of the isomeric state is long enough. This is the case if the lifetime, τ, the quadrupole interaction frequency, ν_Q, and the nuclear spin, I, fulfill the LEMS condition

$$\nu_Q \tau / I > 0.5. \tag{2.15}$$

This condition is derived empirically in Ref. [Sch88]. When the LEMS condition is fulfilled all $\omega_{NN'}^{LEMS}(N \neq N')$ are large and have a negligible contribution in the time-integrated perturbation factor (2.14). The time-integrated perturbation factor is fully determined by the $N = N'$ terms and reduces to

$$G_{kk'}^{nn'}(I, \mathcal{H}_{LEMS}, \tau) = \sum_N (f_{NN}^{LEMS})_{kk'}^{nn'}. \tag{2.16}$$

The coefficients $(f_{NN}^{LEMS})_{kk'}^{nn'}$ have been defined in equation (2.11).

2.2 Double perturbations

In a fusion-evaporation reaction highly excited states are populated. They decay to the ground-state by passing through a lot of intermediate states. During the γ-decay of the residual nucleus cascades of 20-30 γ-rays are emitted. Several of these intermediate states can be isomeric. All isomeric states fulfilling the LEMS condition (2.15) interact in a detectable way with the surrounding electromagnetic fields. Therefore, the anisotropy of the γ rays originating from an isomeric state will be influenced by all preceding perturbations, each of them with a corresponding ratio ν_Q/μ (Figure 2.4). In this section the time-differential and time-integrated expression for the angular distribution function for the case of two subsequent perturbations will be deduced. In principle a further expansion towards more perturbations is possible. However, in practice the analysis for more than two subsequent perturbations is very complicated due to the many parameters involved [Ney93a]. Therefore, it usually looses its reliability and will not be treated here.

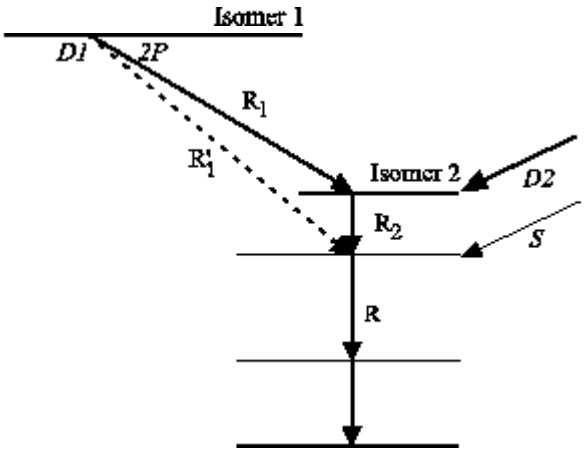

Figure 2.4: *Decay scheme of a nucleus in which two isomers are present. The labels D1, D2, 2P and S denote the direct feeding via isomer 1, the direct feeding via isomer 2, the double perturbed fraction and the side feeding, respectively (see text for the definitions of D1 and D2). The γ rays of interest are labeled R_1, R_2, R'_1 and R.*

2.2.1 Time-differential expression for the double perturbation factor

Assume two isomers 1 and 2, having the nuclear properties $(I_1, \tau_1, Q_1, \mu_1)$ and $(I_2, \tau_2, Q_2, \mu_2)$ respectively. Isomer 1 is populated by prompt γ-decay and decays after a time $t = t_1$, again via a cascade of prompt γ rays to isomer 2. t_1 can be any time in the time interval $[0, \infty]$, however with a probability which is quantified by the exponential $\exp(-t_1/\tau_1)$, in which τ_1 is the nuclear life time of isomer 1. The initial orientation of the isomeric state 1 is given by $B^n_k(I_1, t = 0)$. This orientation is perturbed due to the interaction of the nuclear moments μ_1 and $Q_{s,1}$ with the surrounding electromagnetic fields. At the moment of decay, t_1, the orientation can be written as [Har91a, Ney93a, Ter98a]

$$B^{n_1}_{k_1}(I_1, t = t_1) = \sum_{k,n} G^{n_1 n}_{k_1 k}(I_1, \frac{\nu_{Q_1}}{\mu_1}, t_1) B^n_k(I_1, t = 0). \qquad (2.17)$$

The initial orientation of isomer 2 equals the final orientation of isomer 1 corrected by the desorientation coefficients $U_{k_1}(R_1)$ which take into account the loss of orientation due to the intermediate prompt γ rays. Therefore, the initial ori-

entation of isomer 2 is given by

$$\begin{aligned} B^{n_1}_{k_1}(I_2, t = t_1) &= U_{k_1}(R_1) B^{n_1}_{k_1}(I_1, t = t_1) \\ &= U_{k_2}(R_1) \sum_{k,n} G^{n_1 n}_{k_1 k}(I_1, \frac{\nu_{Q_1}}{\mu_1}, t_1) B^n_k(I_1, t = 0). \end{aligned} \quad (2.18)$$

Isomer 2 interacts with the electromagnetic fields during the time interval $[t_1, t_2]$. At the time $t = t_2$, also isomer 2 decays. t_2 can be any time in the time interval $[t_1, \infty]$, however weighted by the probability function $\exp[-(t - t_1)/\tau_2]$, in which τ_2 is the nuclear lifetime of isomer 2. Its orientation at the moment of decay, t_2, is

$$\begin{aligned} B^{n_2}_{k_2}(I_2, t = t_2) &= \sum_{k1,n1} G^{n_2 n_1}_{k_2 k_1}(I_2, \frac{\nu_{Q_2}}{\mu_2}, t_2 - t_1) B^{n_1}_{k_1}(I_2, t = t_1) \\ &= \sum_{k_1,n_1} G^{n_2 n_1}_{k_2 k_1}(I_2, \frac{\nu_{Q_2}}{\mu_2}, t_2 - t_1) U_{k_1}(R_1) \\ &\qquad \sum_{k,n} G^{n_1 n}_{k_1 k}(I_1, \frac{\nu_{Q_1}}{\mu_1}, t_1) B^n_k(I_1, t = 0) \\ &= \sum_{k,n} G^{n_2 n}_{k_2 k}(I_1, I_2, \frac{\nu_{Q_1}}{\mu_1}, \frac{\nu_{Q_2}}{\mu_2}, t) B^n_k(I_1, t = 0). \end{aligned} \quad (2.19)$$

After the decay of isomer 2 no further change of the orientation takes place. Hence, the perturbation factor for two subsequent perturbations at a time $t > t_2$ is

$$\begin{aligned} G^{n_2 n}_{k_2 k} &(I_1, I_2, \frac{\nu_{Q_1}}{\mu_1}, \frac{\nu_{Q_2}}{\mu_2}, t) \\ &= \sum_{k_1,n_1} G^{n_2 n_1}_{k_2 k_1}(I_2, \frac{\nu_{Q_2}}{\mu_2}, t_2 - t_1) U_{k_1}(R_1) G^{n_1 n}_{k_1 k}(I_1, \frac{\nu_{Q_1}}{\mu_1}, t_1). \end{aligned} \quad (2.20)$$

2.2.2 Time-integrated expression for the double perturbation factor

LEMS measurements are time-integrated measurements. Therefore, a proper time-integration of expression (2.20) needs to be made:

$$\begin{aligned} G^{n_2 n}_{k_2 k}(I_1, I_2, \frac{\nu_{Q_1}}{\mu_1}, \frac{\nu_{Q_2}}{\mu_2}, \tau_1, \tau_2) &= \sum_{N_1,N_1',N_2,N_2',k_1,n_1} (f^{LEMS2}_{N_2 N_2'})^{n_2 n_1}_{k_2 k_1} U_{k_1}(R_1) (f^{LEMS1}_{N_1 N_1'})^{n_1 n}_{k_1 k} \\ \times \frac{\int_0^\infty \exp(-t_1/\tau_1) \exp(-i\omega^{LEMS1}_{N_1 N_1'} t_1) \int_{t_1}^\infty \exp[-(t - t_1)/\tau_2] \exp(-i\omega^{LEMS2}_{N_2 N_2'} t) dt dt_1}{\int_0^\infty \exp(-t_1/\tau_1) \int_{t_1}^\infty \exp[-(t - t_1)/\tau_2] dt dt_1}, \end{aligned} \quad (2.21)$$

in which the coefficients $(f^{LEMS}_{NN'})^{n_1 n}_{k_2 k_1}$ are defined by the equation (2.11). The idea behind this expression is that isomer 2 starts its interaction with the electromagnetic fields at the moment of the decay of isomer 1 (which is t_1) and interacts with the fields during a time span $(t - t_1)$, with $t \in [t_1, \infty]$. An exponential weight $\exp[-(t - t_1)/\tau_2]$ accounts for the nuclear lifetime of isomer 2. The initial orientation of isomer 2 is the final orientation of isomer 1, corrected by the desorientation coefficients $U_{k_1}(R_1)$. The final orientation of isomer 1 is $\propto \exp(-i\omega^{LEMS1}_{N_1 N'_1} t_1)$, where the moment of decay of isomer 1, t_1, is weighted by the exponential $\exp(-t_1/\tau_1)$.

The integrals can be calculated easily in an analytical way:

$$G^{n_2 n}_{k_2 k}(I_1, I_2, \frac{\nu_{Q_1}}{\mu_1}, \frac{\nu_{Q_2}}{\mu_2}, \tau_1, \tau_2) = \sum_{N_1, N'_1, N_2, N'_2, k_1, n_1} (f^{LEMS2}_{N_2 N'_2})^{n_2 n_1}_{k_2 k_1} U_{k_1}(R_1) (f^{LEMS1}_{N_1 N'_1})^{n_1 n}_{k_1 k} \left(\frac{1}{1 + i\omega^{LEMS1}_{N_1 N'_1}\tau_1 + i\omega^{LEMS2}_{N_2 N'_2}\tau_1}\right)\left(\frac{1}{1 + i\omega^{LEMS2}_{N_2 N'_2}\tau_2}\right). \quad (2.22)$$

The time-integrated double perturbation factor is NOT equal to the product of the 2 time-integrated single perturbation factors times the desorientation coefficient $G^{n_1 n}_{k_1 k}(I_1, \frac{\nu_{Q_1}}{\mu_1}, \tau_1) U_{k_1}(R_1) G^{n_2 n_1}_{k_2 k_1}(I_2, \frac{\nu_{Q_2}}{\mu_2}, \tau_2)$, because an extra $i\omega^{LEMS2}_{N_2 N'_2}\tau_1$ term is present in the denominator. However, if the LEMS condition (2.15) for isomer 2 is fulfilled, then similar to (2.16) only the $\omega^{LEMS2}_{N_2 N'_2}\tau_2 \overset{(N_2 = N'_2)}{=} 0$ and thus also only the $\omega^{LEMS2}_{N_2 N'_2}\tau_1 \overset{(N_2 = N'_2)}{=} 0$ terms contribute and the formula reduces to

$$G^{n_2 n}_{k_2 k}(I_1, I_2, \frac{\nu_{Q_1}}{\mu_1}, \frac{\nu_{Q_2}}{\mu_2}, \tau_1, \tau_2) = G^{n_1 n}_{k_1 k}(I_1, \frac{\nu_{Q_1}}{\mu_1}, \tau_1) U_{k_1}(R_1) G^{n_2 n_1}_{k_2 k_1}(I_2, \frac{\nu_{Q_2}}{\mu_2}, \tau_2). \quad (2.23)$$

2.2.3 Influence of the direct feeding

In the most general case a γ ray in the cascade below isomer 2 contains 4 contributions (Figure 2.4): A first fraction $D1$ originates directly from isomer 1, bypassing isomer 2 in its decay. Further, a certain fraction $D2$ of the isomers 2 is not fed via isomer 1, but directly by a cascade of prompt γ rays, which are either discrete or statistical. We will refer to this as the 'direct feeding'. Obviously, also a double perturbed fraction $2P$ is present. Finally, side feeding ensures a

prompt component as well. In practice reliable fit results are obtained by neglecting the prompt component and rescaling the fractions $D1, D2$ and $2P$ such that $D1 + D2 + 2P = 100\%$. Hence the time-integrated angular distribution function for R contains three contributions:

$$W(\theta,\phi) = W(\theta,\phi,D1)D1 + W(\theta,\phi,D2)D2 + W(\theta,\phi,2P)2P. \qquad (2.24)$$

Here

$$W(\theta,\phi,D1) = \sqrt{4\pi}\sum_{k_2 even}\frac{1}{\sqrt{2k_2+1}}A_{k_2}(\gamma)Y^{n2}_{k2}(\theta,\phi)U_{k_2}(R'_1) \\ G^{m_2 n}_{k_2 k}(I_1,\tfrac{\nu_{Q_1}}{\mu_1},\tau_1)B^n_k(I_1,t=0) \qquad (2.25)$$

is the contribution due to the perturbation of isomer 1. The contribution due to the single perturbation of isomer 2 is:

$$W(\theta,\phi,D2) = \sqrt{4\pi}\sum_{k_2 even}\frac{1}{\sqrt{2k_2+1}}A_{k_2}(\gamma)Y^{n2}_{k2}(\theta,\phi)U_{k_2}(R_2) \\ G^{m_2 n}_{k_2 k}(I_2,\tfrac{\nu_{Q_2}}{\mu_2},\tau_2)B^n_k(I_2,t=0) \qquad (2.26)$$

and the contribution due to the double perturbation of isomer 2 is:

$$W(\theta,\phi,2P) = \sqrt{4\pi}\sum_{k_2 even}\frac{1}{\sqrt{2k_2+1}}A_{k_2}(\gamma)Y^{n2}_{k2}(\theta,\phi)U_{k_2}(R_2) \\ G^{m_2 n}_{k_2 k}(I_1,I_2,\tfrac{\nu_{Q_1}}{\mu_1},\tfrac{\nu_{Q_2}}{\mu_2},\tau_1,\tau_2)B^n_k(I_1,t=0). \qquad (2.27)$$

The analysis of a double perturbed decay implies seven parameters: the direct feedings, $D1$ and $D2$, the initial orientations for both isomers, $(\sigma/I)_1$ and $(\sigma/I)_2$, the ratios of the nuclear moments for each isomer, $(\nu_Q/\mu)_1$ and $(\nu_Q/\mu)_2$, and a normalisation factor, N, depending on the detector efficiencies. The fractions of the direct feedings, $D1$ and $D2$, can be determined from the relative intensities of the γ rays R_1, R'_1, R_2 and R (see Figure 2.4 and appendix D) so that only 5 parameters remain.

2.3 The experimental setup and analysis

2.3.1 The LEMS setup

For a detailed description of the experimental setup the reader is referred to [Ter98a, Sch88, Har91a, Ney93a]. Here only the relevant aspects for the experiments performed for this work are summarised. All experiments have been carried out at the CYCLONE cyclotron in Louvain-la-Neuve. The dedicated LEMS setup was utilised, which consists of the split-coil 4.4 T superconducting magnet, a target holder, allowing precise temperature control at the target position in the interval 4 - 600 K, and 4 Ge detectors, which monitor the target through the holes of the magnet and are manufactured to work in considerable magnetic fields (Figure 2.1). They are positioned at 0° and 90° with respect to the beam-axis. The magnetic field is oriented parallel to the beam axis. As the nuclear ensemble is produced in the measurement chamber itself the detectors are exposed to very high counting rates (typically 20000 counts/s). Therefore, the resolution of the 1332 keV ^{60}Co line is usually not better than 2.5 keV. Note that single γ ray spectra are recorded during the experiments.

2.3.2 The LEMS analysis

In the analysis the number of counts of the peak of interest in the detector at 0° and the detectors at 90° is determined with the aid of the *FITEK* program [Sto]. Although in principle it is sufficient to detect the radiation in one direction (Figure 2.5), in practice the ratio $\frac{N(0°)}{N(90°)}$ is determined for each magnetic field. This way of data handling ensures a normalisation for the fluctuations in the beam intensity and results in a curve with a bigger amplitude. If clean intense prompt γ rays are present in the spectra, a second normalisation is made as well. Prompt γ rays originate from levels with a lifetime which is too short to allow a detectable interaction with the surrounding electromagnetic fields. The LEMS condition $\frac{\nu_Q \tau}{I} \geq 0.5$ (2.15) is not fulfilled. Therefore, the anisotropy of the prompt γ radiation does not change as a function of the magnetic field. Deviations are

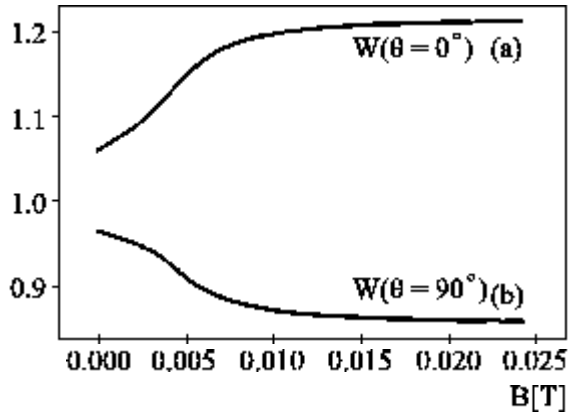

Figure 2.5: *Anisotropy of the γ radiation as a function of the magnetic field measured by (a) a 0° degrees detector and (b) a 90° degrees detector. A polycrystalline material provides the EFG. An isomer with spin $I = 8$, decaying via a $8^+ \rightarrow 6^+ E2$ transition, is assumed.*

fully due to irregularities, such as, e.g., the movements of the beam spot, which are common for all detected γ rays. By dividing the ratio $\frac{N(0°)}{N(90°)}_{isomer}$ by the ratio $\frac{N(0°)}{N(90°)}_{prompt}$ for each magnetic field, these irregularities are ruled out and the only remaining effect is the LEMS effect.

Finally, a theoretical LEMS curve $N\frac{W(0°,0°)}{W(90°,\phi)}$ is fitted through the experimentally deduced ratios. Note that, if a polycrystal is used, the angular distribution of the γ radiation is the same for all detectors positioned at $\theta = 90°$ with respect to the beam axis and thus ϕ independent, because in such a configuration both the quadrupole interaction and the magnetic interaction are axially symmetric around the beam axis.

2.3.3 Pulsing of the beam

Because a time-integrated curve is measured in a LEMS measurement, a pulsed production of the isomers of interest is not necessary. Nevertheless, beam pulsing with a period of the order of the life time of the investigated isomer and collecting data during the beam-off period only is often desirable to reduce the prompt background radiation and enhance the peak to background ratio. At the

CYCLONE facility three types of beam pulsing are available, each of them applicable in a different lifetime region. One can either use the natural frequency of the cyclotron (or HF timing), typically providing a beam burst every 80 ns, or one can apply a changing voltage (block pulses) on a deflection plate between the ion source and the cyclotron [Ney93a, Bro89, Ter98a]. The latter works for pulsing periods larger than 4 μs. Recently, a third method has been developed where a deflection plate (or beam flipper) is added to the beam line immediately after the cyclotron [Sch96, Ter98a, Wyc98]. On this deflection plate an alternating voltage is applied with a constant frequency of 1 MHz. A cyclotron pulse can pass every time it is in coincidence with a zero signal on the deflection plate, i.e., every 500 ns (Figure 2.6). All other cyclotron pulses are deflected by the beam flipper. A disadvantage of the system is that the frequency of the alternating voltage on the deflection plates is fixed. Therefore, the beam flipper can only be used for cyclotron frequencies corresponding with an integer number of beam bursts in a period of 500 ns (with a possible deviation of 2%). Since the cyclotron frequency determines the beam energy, only certain beam energies can be pulsed with this system.

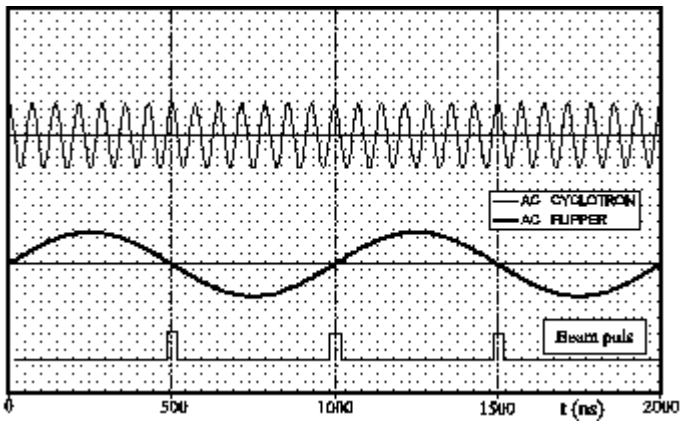

Figure 2.6: *Schematic view of the pulses coming from the cyclotron and how their phase should match the sinusoidal alternating voltage applied to the beam flipper. The period of the flipper AC signal is fixed on 1 μs and only beams with an integer number of beam pulses in a period of 500 ns can be pulsed by using the flipper.*

2.4 LEMS in a recoil-shadow geometry

2.4.1 Improvement of the peak to background ratio in a recoil-shadow geometry

Detection limitations are the main restriction for the applicability of the LEMS method: The number of holes in the magnet and, hence, the number of detector positions is limited so that the usual means to reduce the background radiation in the spectra, e.g., measuring coincidence spectra, cannot be applied due to the low counting rates. Also the use of anti-Compton shields is not straightforward for the simple reason that the phototubes do not work in the stray magnetic field, which can go as high as 1 T. Substantial technical development would be needed for this case. At this point, the only way to reduce the background radiation is by pulsing the beam and measuring during the beam-off period only, as described above.

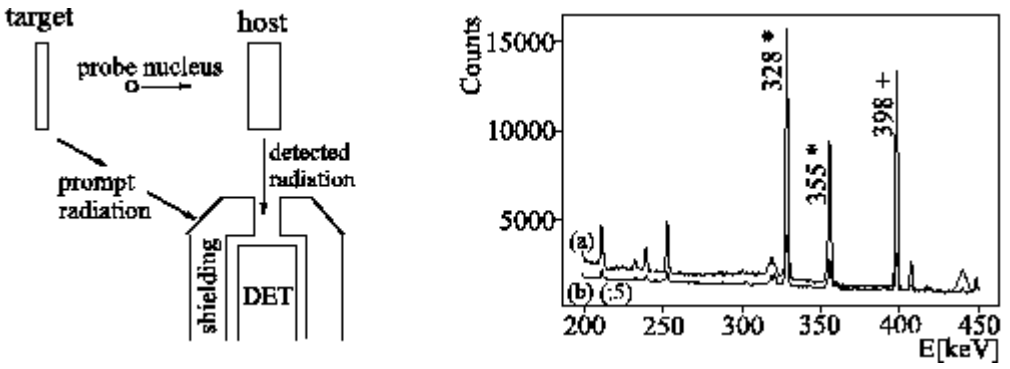

Figure 2.7: *Left: Recoil-shadow configuration. Right: Improvement of the peak to background ratio in a spectrum taken in a recoil-shadow configuration for the* $^{nat}Fe(^{16}O,2pn)^{69}Ge$ *reaction. The peak originating from the* $^{69}Ge(I^{\pi} = 9/2^{+})$ *isomer is marked with a plus, the Coulex peaks on Pt with an asterisk. For spectrum (b) no means to reduce the background radiation have been used. Spectrum (a) is taken in the recoil-shadow configuration. The number of counts of spectrum (b) is divided by a factor of 5 in order to make the background levels of spectrum (a) and spectrum (b) coincide.*

However, the beam flipper can only be used for certain energies. Furthermore, the typical time between the beam bursts in the case of HF timing is 50 to 80 ns, while the time resolution of a Ge detector is typically 10 to 20 ns, which means that the technique loses much of its efficiency. Therefore, the improvement of the peak to background ratio using the recoil-shadow configuration, i.e., separating target and host and shielding the detectors from the target (Figure 2.7, left), has been investigated. An experiment, using the ^{nat}Fe(^{16}O, $2pn$)^{69}Ge reaction with a beam energy of 65 MeV has been performed. The target tickness of 1.57 mg/cm^2 allowed all ^{69m}Ge[$I^\pi = 9/2^+, \tau = 4.05(7)$ μs) recoils to reach the host. The right panel of Figure 2.7 shows that the improvement of the peak to background ratio of the 398 keV $M2$ transition can go as high as a factor of 5 by using the recoil-shadow geometry [Vyv97].

2.4.2 Experimental results on the influence of the $\vec{I} \cdot \vec{J}$ interaction on the LEMS technique

A complicating factor for the application of the recoil-shadow technique is that in most of the cases (usually for the energies of the fusion-evaporation reactions of interest) the recoiling nuclei are not fully stripped. In free atoms the nuclear spin $\vec{I}$ and the atomic spin $\vec{J}$ interact with each other, coupling to a total angular momentum $\vec{F}$, around which both $\vec{I}$ and $\vec{J}$ precess. This means that during the flight through the vacuum (when the recoiling atoms are free), non-fully stripped nuclei will be submitted to this $\vec{I} \cdot \vec{J}$-coupling interaction. As the atomic spin is randomly oriented, the net result of the precession is a lowering of the orientation of the nuclear ensemble. The orientation can be restored by applying a sufficiently high magnetic field parallel to the nuclear orientation axis so that both the atomic and nuclear spins perform a Larmor precession around this magnetic field [Ste75, Gol82, Bro73, Lit80]. This means that the influence of the $\vec{I}.\vec{J}$ interaction on the anisotropy of the radiation, as a function of the magnetic field strength, should be investigated in order to ensure a correct quadrupole moment

determination. The Hamiltonian of the interaction is given by [Ste75]:

$$\mathcal{H}_{IJ} = a\vec{I}\cdot\vec{J} + \vec{\mu}_J\cdot\vec{B} - \vec{\mu}_I\cdot\vec{B}. \tag{2.28}$$

with $a = \frac{\mu_I\langle B_{hf}(0)\rangle}{IJ\hbar^2}$ being the coupling constant, $\vec{\mu}_I$ the nuclear magnetic moment, $\vec{\mu}_J$ the electronic magnetic moment and B_{hf} the hyperfine field induced by the atomic electrons. As the Bohr magneton is about 2000 times larger than the nuclear magneton, the decoupling occurs when $\langle\vec{\mu}_J\cdot\vec{B}\rangle$ is larger than $\langle a\vec{I}\cdot\vec{J}\rangle$. In appendix C it is discussed how the influence of the combined magnetic dipole + $\vec{I}\cdot\vec{J}$ + electric quadrupole interaction on the anisotropy of the γ radiation can be calculated. Here some experimental results are discussed.

The combined magnetic dipole + $\vec{I}\cdot\vec{J}$ interaction

Several experiments using the ^{nat}Fe(^{16}O,2pn)^{69}Ge reaction with a beam energy of 65 MeV have been performed at the CYCLONE cyclotron in Louvain-la-Neuve, Belgium. The target thickness of 1.57 mg/cm^2 was thin enough to release all recoils. The recoil energy is 15 MeV, but because of the energy loss in the target, the average energy with which the nuclei left the target was E_0=9 MeV and the energy spread has been taken as σ_E=5 MeV (TRIM [Zie85] calculations). In a first experiment, the Ge isomers were stopped in a 1.78 mg/cm^2 thick Ni host at a distance of 6 cm from the ^{nat}Fe target. A 50 μm thick Ta foil served as a beam stopper. The combination of a thin Ni foil + high-Z beam stopper was chosen in order to decrease the reactions with the Ni. The Ni foil has been heated up to 450°C to reach its paramagnetic phase. Since Ni is cubic, no EFG and thus no quadrupole interaction is present unless defects are trapped by the probe nuclei. An experiment applying the direct production in a thick Ni foil, using the ^{nat}Ni(^{12}C,2pn)^{69}Ge reaction, proves that indeed no defects are created. This is shown by the analysis of the 398 keV $M2$ transition which does not show a change in the anisotropy as a function of the magnetic field (Figure 2.8, up). So, if a change in the anisotropy is observed in the recoil-distance experiment, it is entirely due to the $\vec{I}.\vec{J}$ interaction during the recoil time of the ^{69}Ge ions. Notice that the recoil time is only about 10 ns, which is much shorter than the

isomeric lifetime of 4 μs.

The $\vec{I} \cdot \vec{J}$ decoupling curve for the ^{69}Ge(I=9/2) isomers with a recoil velocity v_{rec} = 1.7%c is shown in the down panel of Figure 2.8. The fit results in $\frac{\nu_{LI}}{\mu_J} = 0.25^{+0.06}_{-0.01} \frac{GHz}{\mu_B}$ and $J = 2.7(2)$ where μ_B is the Bohr magneton. An estimate of the atomic magnetic moment can be made using the relationship $\vec{\mu}_J = -g_J \vec{J} \mu_B / \hbar$ with the Landé g factor as a good approximation for the atomic gyromagnetic ratio g_J [Sob79]. The Landé g-factor is either 1 when the atomic intrinsic spin is $S = 0$, or 2 when the atomic orbital angular momentum is $L = 0$.

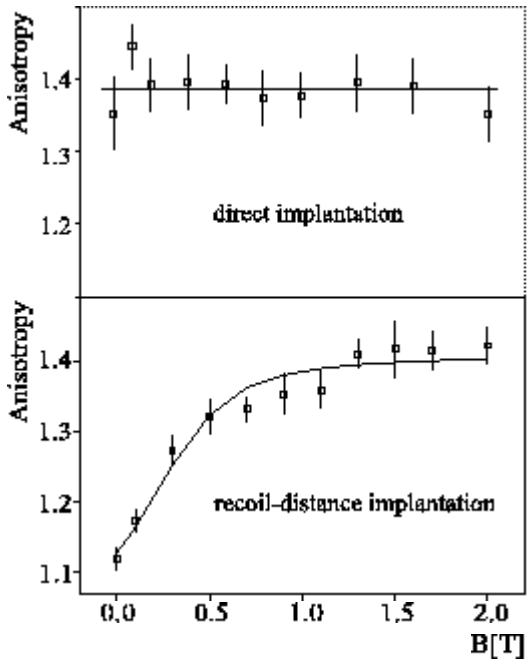

Figure 2.8: *Up: LEMS curve for the ^{69}Ge(I=9/2) isomer in Ni at 450° C using a direct production in the Ni. No change of the spin orientation as a function of the externally applied magnetic field is measured, proving that no defect-associated EFGs in the Ni are present. Down: $\vec{I} \cdot \vec{J}$ decoupling curve for the ^{69}Ge($I = 9/2$, $\tau = 4.05(7)\mu s$) isomers recoiling out a ^{nat}Fe foil with a velocity of 1.7%c and stopped in a Ni foil heated up to 450° C after a 9 ns flight time. The ratio $\frac{\nu_{LI}}{\mu_J} = 0.25^{+0.06}_{0.01} \frac{GHz}{\mu_B}$ with $\nu_{IJ} = \frac{h}{2\pi} a$ and $\mu_J = g_J J \mu_B$ corresponds for the approximate value of $g_J = 1$ with an atomic magnetic hyperfine field of 1080^{+270}_{-175} T [Vyv00].*

The large total atomic angular momentum $J = 2.7(2)$ indicates that a considerable amount of orbital angular momentum must be involved. Indeed, the total atomic angular momentum averaged over the Hund ground states yields only 0.9. Therefore, excited atomic states, where, e.g., several d-electrons couple to high orbital momentum levels, must be present. Combining the fit results with the value obtained for g_J results in an atomic hyperfine field B_{hf} of 1080^{+270}_{-175}T [Vyv00]. Note that these large atomic hyperfine fields allow g-factor measurements of (sub)nanosecond states [Vyv01b].

The combined magnetic dipole + $\vec{I}\cdot\vec{J}$ + electric quadrupole interaction

In order to verify experimentally the combined magnetic dipole + electric quadrupole + $\vec{I}\cdot\vec{J}$ interaction two experiments with the ^{69}Ge atomic nuclei recoiling into a Pt host have been performed. In a first experiment the ^{nat}Fe was evaporated on the Pt, while in a second one the Fe foil was placed at a recoil-distance of 6 cm. Pt is cubic but other experiments [Ter98b] have shown that defects are easily created in this host resulting in a defect-associated EFG. At zero recoil-distance a combined magnetic dipole + electric quadrupole interaction takes place. From the amplitude of the LEMS curve one can determine that 55(7)% of the Ge nuclei end up in a defect-associated site. 24(5)% of the Ge isomers are interacting with a smaller EFG ($\nu_{Q_1} = 6.4(1.5)$ MHz), while 31(5)% with a larger one ($\nu_{Q_2} = 18(2)$ MHz). Figure 2.9 shows that the curve for a 6 cm recoil-distance has a larger amplitude which is caused by an extra lowering in the anisotropy due to the $\vec{I}\cdot\vec{J}$ interaction. In a first fit the $\vec{I}\cdot\vec{J}$ interaction was not taken into account in order to verify the influence of the $\vec{I}\cdot\vec{J}$ interaction on the quadrupole interaction frequencies. The same quadrupole frequencies, within the error bar, have been found as for a zero recoil-distance (table 2.1). Only the fractions of the nuclei submitted to an EFG differ, since they are directly connected to the amplitude of the LEMS curve. In a second fit both the LEMS interaction and the $\vec{I}\cdot\vec{J}$ interaction were taken into account. The $\vec{I}\cdot\vec{J}$ fit parameters were fixed by the experiment with the Ni host and the quadrupole frequencies by the experiment with zero recoil distance. As a result also the fractions agree and the theoretical

Table 2.1: *Fit results for the $^{69}Ge(I^{\pi} = 9/2^{+})$ isomer in Pt with a zero and a 6 cm recoil-distance. For a zero recoil distance only the pure LEMS interaction takes place. For a 6 cm recoil-distance also the $\vec{I} \cdot \vec{J}$ interaction is present, which has been taken into account in [b], but not in [a] [Vyv00].*

d	ν_{Q_1}[MHz]	ν_{Q_2}[MHz]	f_1	f_2	ν_{IJ} [GHz]	J
0	6.4(1.5)	18(2)	0.24(5)	0.31(5)	-	-
6 cm [a]	5.0(0.8)	17(4)	0.50(8)	0.40(5)	not in fit	not in fit
6 cm [b]	6.4	18	0.24(5)	0.31(5)	0.68	2.7

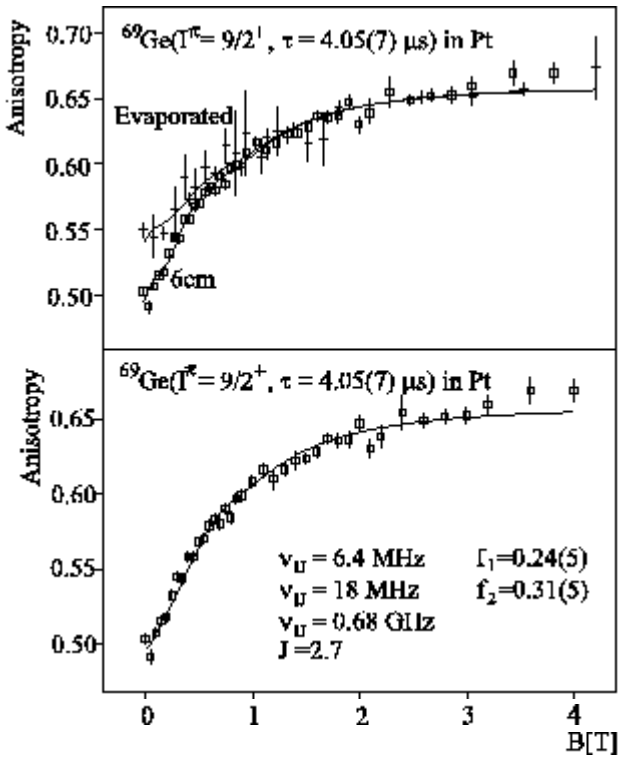

Figure 2.9: *Up: LEMS curves for the $^{69}Ge(I^{\pi} = 9/2^{+})$ isomer in Pt using zero and 6 cm recoil-distances. No $\vec{I} \cdot \vec{J}$ interaction has been taken into account to fit the data. The fit results can be found in table 2.1. Down: Combined LEMS+$\vec{I} \cdot \vec{J}$ fit for the 6 cm recoil-distance[Vyv00].*

curve is in better agreement with the experimental data. The improvement in χ^2 is 10%.

Conclusion

The experiments described above reveal that the influence on the quadrupole frequency due to the $\vec{I} \cdot \vec{J}$ interaction is negligible. Only in exceptional cases, when the $\vec{I} \cdot \vec{J}$ interaction strength is very strong compared to the quadrupole interaction strength, the $\vec{I} \cdot \vec{J}$ interaction should be taken into account. In this case, a combined LEMS + $\vec{I} \cdot \vec{J}$ fit results in the correct quadrupole interaction frequencies and the $\vec{I} \cdot \vec{J}$ fit parameters can be fixed in an experiment where the nuclei of interest recoil into a cubic host.

Chapter 3

Quadrupole moments of the $I^\pi = 11^-$ intruder isomers in ^{194,196}Pb

3.1 Introduction

This chapter shows the experimental results of the measurements on the 11^- and 12^+ isomers in ^{194,196}Pb. The aim of these experiments is to extract the quadrupole moment of the ($I^\pi = 11^-, T_{1/2} = 72(4)$ ns, $\mu = 10.56(88)\mu_N$) in ^{196}Pb. As described in chapter 1 the nuclear physics interest is two-fold. The ^{196}Pb($I^\pi = 11^-$) has the $\pi(3s_{1/2}^{-2}1h_{9/2}1i_{13/2})$ configuration. On the one hand we will investigate the influence of the breaking of the $Z = 82$ proton core and, secondly, the presence of the $1i_{13/2}$ particle on the deformation. Also the results of shell model calculations will be discussed. In these calculations the quadrupole moments of the intruder and the corresponding normal states have been deduced by explicitly taking into account the interaction between the valence protons and the vibrations of the underlying core.

On the other hand the measurement of the quadrupole moment of the 11^- isomer in ^{196}Pb will allow to extract the quadrupole moment of the ^{196}Pb($I^\pi = 16^-$) shears bandhead. A small quadrupole moment proves unambiguously that

magnetic rotation is the only possible explanation for the observed rotational band built on the ^{196}Pb($I^\pi = 16^-$) state. A comparison with TAC calculations will be made.

However, the quadrupole moment of the ^{196}Pb($I^\pi = 11^-$) is not the only information that can be extracted from this series of experiments. In order to measure this quadrupole moment the Pb isotopes were implanted in a Re polycrystal. Therefore, the electric field gradient of Pb in Re could be determined experimentally from the quadrupole interaction frequency of the ^{196}Pb($I^\pi = 12^+$) isomer.

As byproducts, also the 11^- and 12^+ isomers in ^{194}Pb were produced in the nuclear reaction. The analysis of the transitions depopulating the ($11^- \rightarrow 12^+$) cascade provides an experimental test for the double perturbation formalism as deduced in section 2.2. This can be done by comparing the electric field gradient extracted from this analysis with the electric field gradient extracted from the quadrupole interaction frequency of the ^{196}Pb($I^\pi = 12^+$) isomer. Furthermore, the double perturbation fit of the transitions depopulating the ($11^- \rightarrow 12^+$) cascade also includes $\nu_Q(I^\pi = 11^-)$ as a fit parameter. Hence, it provides a way to extract a value for $\nu_Q(I^\pi = 11^-)$ as well, whereas the analysis of the γ transitions directly depopulating the ^{194}Pb($I^\pi = 11^-$) isomer did not allow a reliable result.

3.2 Experimental details

3.2.1 Production and detection of the ^{194,196}Pb($I^\pi = 11^-, I^\pi = 12^+$) isomers

The ^{194,196}Pb($I^\pi = 11^-, 12^+$) isomers were populated in a ^{nat}Re(^{14}N,5n) reaction at a beam energy of 87 MeV. The ^{nat}Re consists of 62.6% ^{187}Re and 37.4% ^{185}Re [Wea71]. The 50 μm thick Re crystal has served as a target, a LEMS host, and a beam stopper at the same time. 6% of the γ-decay of the high-spin states in ^{196}Pb, which are excited in the heavy-ion fusion-evaporation reaction, goes through the

11^- isomer, while 56% goes through the 12^+ isomer [Ruy86]. Typically 16 spectra of 15 minutes were collected for each magnetic field. No beam pulsing was used, because using it was of little help: due to the short lifetime of the 11^- isomer in ^{196}Pb (τ = 104 ns) the HF timing gives the best peak to background ratio. However, although the peak to background improves with a factor of 2 to 3 by using HF timing, the fit error on the number of counts in the 498 keV peak remains the same (Figure 3.2). This is because the neighbouring γ rays with an

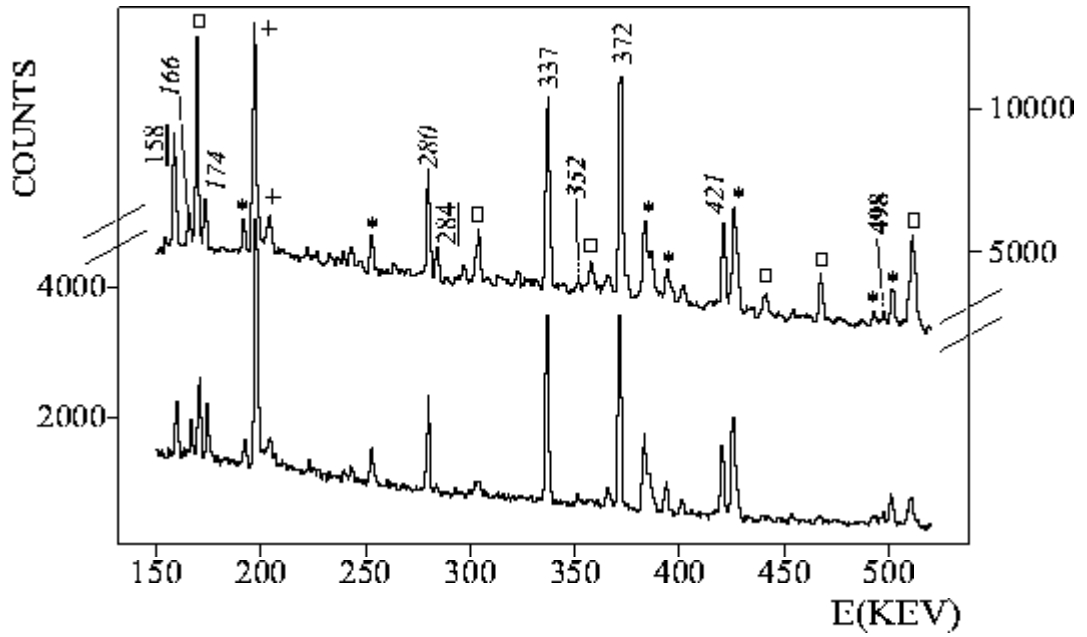

Figure 3.1: *A typical spectrum obtained in the $^{nat}Re(^{14}N,xn)$ reaction at a beam energy of 87 MeV after 15 minutes of measurement time. The peaks coming from the $^{196}Pb(I^\pi = 12^+)$ isomer, the $^{196}Pb(I^\pi = 11^-)$ isomer, the $^{194}Pb(I^\pi = 12^+)$ isomer and the $^{194}Pb(I^\pi = 11^-)$ isomer are indicated in a normal, bold, italic and bold-italic font, respectively (see Figures 1.11 and 3.11 for the level schemes). The energies of the peaks due to Coulomb excitation on ^{nat}Re are underlined. Contaminating radiation, which is either prompt or from other isomers or β decay, is marked with a square, a cross and an asterisk, respectively. The lower part of the figure shows the delayed γ rays. The 60 ns time gate starts 20 ns after the beam burst. The upper part of the figure shows a spectrum without a time gate.*

energy of 493.9 keV and 502.1 keV, respectively, originate from ^{196}Tl, which is populated itself via the β decay of the ^{196}Pb ground-state. Hence, also these γ rays are delayed and not cut by beam pulsing and measuring during the beam-off period only. Furthermore, it is useful to have clean intense prompt peaks as well in the spectra to perform a second normalisation as described in section 2.3.1. A typical spectrum is shown in Figure 3.1.

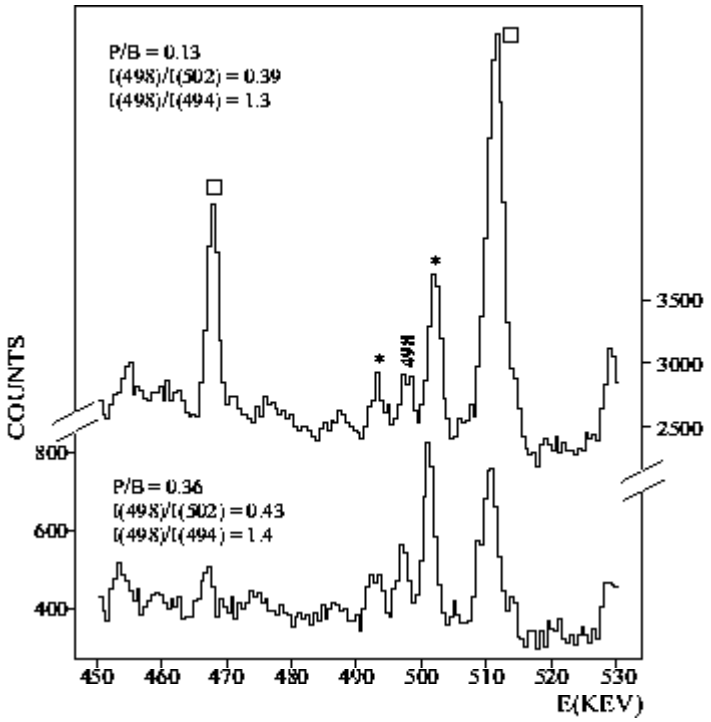

Figure 3.2: *Same as Figure 3.1, but in the energy window 450-530 keV.*

3.2.2 The choice of Re as a target and a LEMS host

A crucial point in performing LEMS measurements is the choice of the host which provides the EFG. Possible candidates are Re and Bi. The best experimental possibility is to use a target which also serves as a host, because this will enhance the production and also improve the peak to background ratio in the measured γ ray spectra [Ter98b]. If the target cannot serve as a host, the isomers of interest need to be recoil-implanted in the host. This has the disadvantages that

contaminating reactions on the host material occur and that the compound nuclei can only recoil out of thin targets. Obviously the use of thin targets decreases the production.

Taking Bi as a LEMS host has the advantage that the EFG of Pb in Bi is known, $V_{ZZ}(T = 293\ \mathrm{K}) = 1.66(5) \cdot 10^{21}\ \mathrm{V/m^2}$ [Haa73], and in the proper range. The EFG should be big enough to ensure that the electric quadrupole interaction is sufficiently strong to disturb the alignment of the nuclear ensemble within its lifetime. On the other hand the quadrupole interaction should be small enough to allow saturation of the LEMS curve within the range of the external magnetic field (4.4 T for our magnet). A disadvantage is that $_{83}$Bi cannot serve as a target to produce $_{82}$Pb in a fusion-evaporation reaction (it has more protons than $_{82}$Pb and in most of the fusion-evaporation reactions only neutrons are evaporated because the Coulomb barrier hinders the emission of charged particles).

To overcome this problem, not $_{83}$Bi, but $_{75}$Re has been chosen as a target and a host. As Re has a hcp lattice structure [Wea71] it is a good candidate for a LEMS host. A disadvantage is that the EFG of Pb in Re was not measured before. However, the systematics of the EFG as a function of the number of valence electrons for several probe nuclei in Re reveals that the EFG of Pb in Re is expected to be in the proper range of $-3 \cdot 10^{21}\ \mathrm{V/m^2}$ (Figure 3.4). In addition, the ^{196}Pb($I^\pi = 12^+$) isomer is produced as well by the nuclear reaction. The quadrupole moment of this isomer has been determined prior to our experiments by applying the TDPAD technique [Zyw81] and, hence, allows an experimental calibration of the EFG of Pb in Re.

3.3 Experimental results on ^{196}Pb

3.3.1 The EFG of Pb in Re

Experimentally the electric field gradient can be calibrated by using the known quadrupole moment of the ($I^\pi = 12^+, T_{1/2} = 269(5)$ ns, $E_\gamma = 2695$ keV, $\mu = -1.920(18)\mu_N, Q = 0.65(5)eb$) isomer in ^{196}Pb [Zyw81]. Figure 3.3 shows the

Table 3.1: *Fit results for the $^{196}Pb(I^\pi = 12^+)$ isomer. The 337 keV transition has been analysed (Figure 3.3). In the upper part of the table it is assumed that the full intensity of the 337 keV is due to the depopulation of the 12^+ isomer. In the lower part the feeding via the 11^- isomer is taken into account via a double perturbation fit. The double perturbed fraction is 12 %, the fraction due to depopulation of the 12^+ isomer 83 % and the fraction directly coming from the 11^- isomer 5%.*

Detector ratio	fixed parameters	$\nu_Q(12^+)$ [MHz]	$\nu_Q(11^-)$ [MHz]	$\sigma/I(12^+)$	N
1	-	38.4(2.4)	-	0.43(3)	0.34(2)
2	-	37.5(2.3)	-	0.43(3)	1.23(4)
1	$\sigma/I(11^-) = 0.35, 174 < \nu_Q(11^-) < 224$	38.5(4.0)	174	0.39(3)	0.34(2)
2	$\sigma/I(11^-) = 0.35, 174 < \nu_Q(11^-) < 224$	37.5(4.0)	174	0.38(3)	1.23(4)

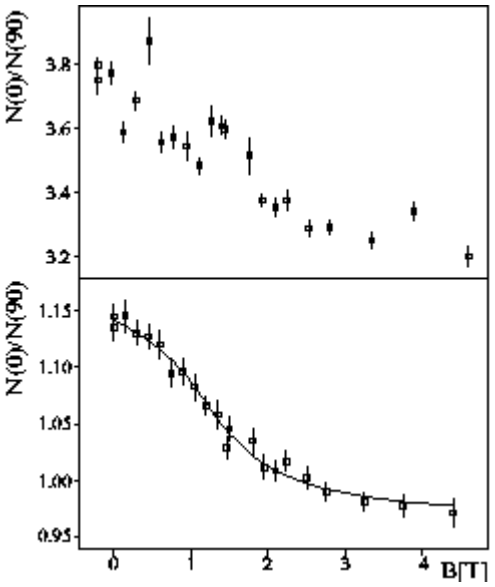

Figure 3.3: *Up: experimental ratios $N(0°)/N(90°)$ for the 337 keV transition depopulating the $^{196}Pb(I^\pi = 12^+)$ isomer, without extra normalisation with the prompt 158 keV transition. Down: Sample LEMS curve for the 337 keV transition after normalisation with the prompt 158 keV transition. The fit results are listed in Table 3.1.*

LEMS curve obtained for the 337 keV ($E1, 10^+ \rightarrow 9^-$) transition, mainly fed via the 12^+ isomer (82%) [Ruy86]. An extra normalisation of the data points with the prompt 158 keV transition, present due to Coulomb excitation on ^{185}Re [Fir96], has been performed. For comparison the experimental ratios $N(0°)/N(90°)$ for the 337 keV without the extra normalisation with the 158 keV transition are added to the picture. The level scheme (Figure 1.11) shows that different decay paths contribute to the intensity of the 337 keV peak. The different fractions have been calculated from the relative intensities of the 337 keV, the 498 keV, the 548 keV and the 959 keV transitions as explained in appendix D.

Besides the fractions of each contribution also the amount of initial orientation, σ/I, is fixed at 0.35 for the 11^- isomer and its quadrupole interaction frequency is only allowed to vary within its experimental error bars 174 MHz $< \nu_Q <$ 224 MHz, as deduced from the analysis of the 498 keV transition (see section 3.3.2). The remaining fit parameters in the double perturbation fit are the quadrupole interaction frequency, ν_Q, and the initial orientation, σ/I, of the 12^+ isomer and a normalisation parameter, N.

The fit, using the measured magnetic moments $\mu(I^\pi = 12^+)$ [Ste83] and $\mu(I^\pi = 11^-)$ [Pen87], results in a quadrupole interaction frequency of $\nu_Q = 38(3)$ MHz. This result includes the correction for the 10% feeding of the 10^+ state via the $11^- \rightarrow 12^+$ cascade and the 5% feeding of the 10^+ state directly from the 11^- isomer by a double perturbation fit (see appendix D). Also the fit, assuming that no contribution via the 11^- isomer is present in the 337 keV γ ray intensity, results in a quadrupole interaction frequency of $\nu_Q = 38(3)$ MHz. This can be understood from the fact that by accident the ratios of nuclear moments $\frac{\nu_Q}{\mu}$ for the 11^- isomer and the 12^+ isomer are almost identical ($\frac{\nu_Q}{\mu} = 19(3)\frac{MHz}{\mu_N}$ for the 11^- isomer and $18(2)\ \frac{MHz}{\mu_N}$ for the 12^+ isomer).

The different detector combinations gave a consistent result for the quadrupole interaction frequency ν_Q and the average value of $\nu_Q = 38(3)$ MHz has been adopted. The spread in the quadrupole frequencies obtained by the different fits lies within the limits of the quoted experimental uncertainty. Using the known quadrupole moment an electric field gradient of $|V_{ZZ}(\text{PbRe})| = 2.42(27)\cdot 10^{21}$

V/m^2 is deduced. This value is in agreement with what is expected from systematics (Figure 3.4). LEMS measurements are not sensitive to the sign of the quadrupole interaction frequency. The systematics show that the minus sign should be adopted.

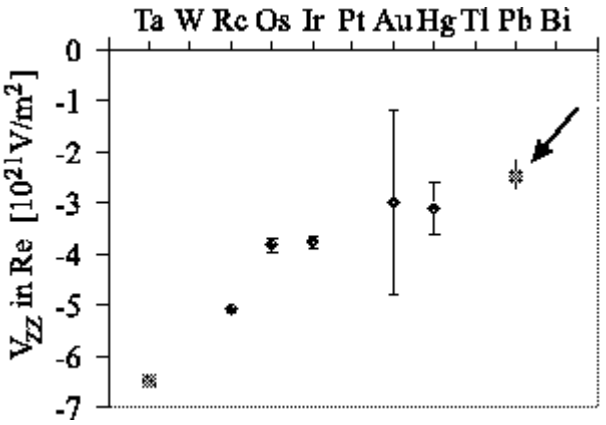

Figure 3.4: *The EFG in Re for different probe nuclei as a function of the number of their valence electrons. The data are taken from [Via87]. For each probe nucleus the weighted mean of all values available in literature are taken. The square indicates that the EFG was measured at room temperature while the diamonds correspond with EFGs taken at low temperatures (T = 0, 2 or 4.2 K). The Debye temperature of Re (θ_D = 430 K [Lup83]) is very high so that the temperature dependence of the EFG in Re is expected to be negligible, contrary to, e.g., the EFG in Tl (section 4.4 and [Sch82]). The arrow points to the value for the EFG of Pb in Re, obtained in this work.*

3.3.2 The quadrupole moment of the ^{196}Pb($I^\pi = 11^-$) isomer

Figure 3.5 shows the LEMS curve obtained for the 498 keV $E1$ transition, depopulating the 11$^-$ isomer. Similar to the analysis of the 337 keV transition, the data for the 498 keV transition are renormalised with respect to the prompt 158 keV transition. In order to reproduce the amplitude of the LEMS curve some

$M2$ admixture for the 498 keV transition is taken into account, such that the radiation parameters increase.

Table 3.2: *Fit results for the $^{196}Pb(I^{\pi} = 11^{-})$ isomer. The 498 $E1$ keV transition has been analysed (Figure 3.5). The amplitude of the experimental LEMS curve could not be reproduced by assuming a pure $E1$ transtion. Therefore, some $M2$ admixture is taken into account in the fit.*

Detector ratio	fixed parameters	$\nu_Q(11^-)$ [MHz]	$\sigma/I(11^-)$	Mixing ratio δ	N
1	$0.3 < \sigma/I(11^-) < 0.4$	189(33)	0.3	0.08(6)	0.30(2)
2	$0.3 < \sigma/I(11^-) < 0.4$	219(46)	0.3	0.06(3)	1.33(3)

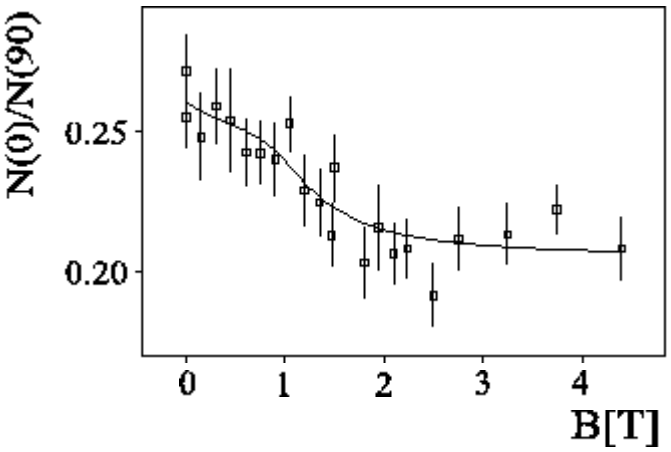

Figure 3.5: *Sample LEMS curve for the 498 $E1$ transition depopulating the 11^- isomer. An extra normalisation by means of the prompt 158 keV has been performed. The fit results are listed in table 3.2.*

The fit is made using the experimental magnetic moment $\mu(I^{\pi} = 11^{-}) = 10.56(88)\mu_N$ [Pen87]. The different detector combinations gave a consistent result for the quadrupole interaction frequency ν_Q (table 3.2) and the average value of $\nu_Q = 199(32)$ MHz has been adopted. The spread in the quadrupole frequencies obtained by the different fits lies within the limits of the quoted experimental

uncertainty. The quoted uncertainty also includes the uncertainty on the magnetic moment.

Using the experimentally deduced electric field gradient a value of $Q_s(I^\pi = 11^-) = (-)3.41(66)$ b is extracted. Assuming that the 11^- isomer is axially deformed with its spin along the deformation axis ($K = I = 11$), we deduce a deformation of $\beta_q = (-)0.156(28)$ by using the formulas (A.5) and (A.22).

Note that LEMS measurements are not sensitive to the sign of the quadrupole interaction frequency. The negative sign is taken from the shell model calculations, taking into account the interaction between the valence protons and the quadrupole vibrations of the underlying Hg-core (see below). The oblate shape can easily be understood in an intuitive way from Figure 3.6. The 11^- isomer has a $1h_{9/2}$ and a $1i_{13/2}$ particle outside the proton core. The $1h_{9/2}$ and $1i_{13/2}$ particles can only couple to a spin $I = 11$ if their spins are maximally aligned, i.e., nearly parallel. Such a configuration is called 'stretched coupling'. Hence, the $1h_{9/2}$ and $1i_{13/2}$ particles are moving in nearly parallel orbits. In order to reduce its energy the nucleus will try to maximize the overlap between the core and the particles around it. As a result the nucleus will take an oblate deformation.

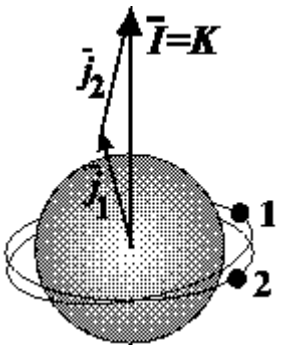

Figure 3.6: *Schematic representation of the stretched coupling.*

3.4 Discussion of the quadrupole moment of the ^{196}Pb($I^\pi = 11^-$) intruder isomer

By comparing the quadrupole moment of the ^{196}Pb$[\pi(3s_{1/2}^{-2}1h_{9/2}1i_{13/2})_{11^-}]$ isomer with the quadrupole moment of the ^{198}Po$[\pi(1h_{9/2}1i_{13/2})_{11^-}]$ isomer it can be verified whether the two $3s_{1/2}$ holes induce a big increase of the deformation of the nucleus (see also section 1.1.5). The quadrupole moment of the ^{198}Po($I^\pi = 11^-$) isomer has not been measured yet. However, a reasonable estimate can be made within the shell model.

3.4.1 Quadrupole moments within the spherical shell model

In the spherical shell model the valence particles are moving around a spherically symmetric core. Hence the core does not contribute to the quadrupole moment $Q_s(I)$. The latter is fully determined by the quadrupole moments $Q_{s.p.}(j)$ of the valence nucleons only and can be written as a linear combination of them:

$$Q_s(I) = \sum_i a_{j_i} Q_{s.p.}(j_i). \tag{3.1}$$

The expansion coefficients a_{j_i} take, by angular momentum algebra, into account how the spins of the valence nucleons j_i couple to the total spin I [Hey94]. In the case of stretched coupling they are equal to 1 and (3.1) reduces to

$$Q_s(I) = \sum_i Q_{s.p.}(j_i). \tag{3.2}$$

$Q_{s.p.}(j)$ can be calculated as

$$Q_{s.p.}(j) = -e_{\pi,\nu} \frac{2j-1}{2j+2} \langle r_j^2 \rangle, \tag{3.3}$$

in which $e_\pi = 1$ for protons and $e_\nu = 0$ for neutrons, respectively. $\langle r_j^2 \rangle$ is the mean square radius for an orbital j. Notice the negative sign in equation (3.3) which is consistent with an oblate deformation for a particle outside the core. In the case of hole states, e_π takes a negative value resulting in a positive quadrupole moment and a prolate deformation.

This theoretical description of the quadrupole moments does not take into account the residual interaction between the valence nucleons themselves nor the polarising effect of the valence particles on the core for maximising (minimising) the overlap of the particles (holes) with the core. These interactions induce an extra effective deformation of the nucleus. Therefore, the spherical shell model underestimates the nuclear quadrupole moments. This problem is solved by replacing the charge $e_{\pi,\nu}$ by the so-called 'effective charge' $e^{eff}_{\pi,\nu}(j)$:

$$e^{eff}_{\pi,\nu}(j) = e_{\pi,\nu} + \delta e(j). \tag{3.4}$$

The orbit-dependent effective charge is either calculated, resulting in the so-called 'effective quadrupole moment' Q^{eff}_s [Sag88] or determined from experimental information, such as measured quadrupole moments. This results in the so-called 'empirical quadrupole moment' Q^{emp}_s.

3.4.2 A comparison of the quadrupole moments of the ^{198}Po$(I^\pi = 11^-)$ isomer and the ^{196}Pb$(I^\pi = 11^-)$ isomer

Only in ^{210}Po, which has a closed neutron shell $N = 126$, the quadrupole moment of the $\pi(1h_{9/2}1i_{13/2})_{11^-}$ isomer has been measured to date [Bec91]. Therefore, the relationship between $Q_s(^{210}\mathrm{Po}_{N=126}(I^\pi = 11^-))$ and $Q_s(^{198}\mathrm{Po}_{N=114}(I^\pi = 11^-))$ needs to be extracted in order to deduce the quadrupole moment of the 11^- isomer in ^{198}Po:

$$Q_s(^{198}\mathrm{Po}_{N=114}(I^\pi = 11^-)) = e^{emp}_\pi(N = 114) Q_s(^{210}\mathrm{Po}_{N=126}(I^\pi = 11^-)), \tag{3.5}$$

in which

$$e^{emp}_\pi(N) = \frac{e^{eff}_\pi(N)}{e^{eff}_\pi(126)} = \frac{Q_s(N)}{Q_s(126)}. \tag{3.6}$$

The problem reduces hence to deducing the 'empirical effective charge' $e^{emp}_\pi(N)$. In this thesis the 'empirical effective charge' refers to an effective charge defined relative to the *measured* quadrupole moment of the same configuration in the $(N = 126)$ isotope. This is to distinguish from the effective charge defined relative to $Q_{s.p.}$.

Figure 3.7 shows the systematics of the quadrupole moments as a function of the neutron number for different proton configurations in the Pb region. For each configuration the quadrupole moments are normalised to the quadrupole moment $Q_s(N = 126)$ for that particular proton configuration. This picture gives several pieces of information:

i. The more neutrons are taken away from the closed $N = 126$ neutron shell, the bigger the quadrupole moment is. So, contrary to expression (3.3), the neutron configuration influences the quadrupole moment. This shows the necessity of the introduction of the effective charges.

ii. All proton configurations $1h^n_{9/2}1i^n_{13/2}$ show the same behaviour for the quadrupole moment as a function of the neutron number [Har91c].

iii. The extrapolated empirical effective charge for the ^{198}Po$_{N=114}[\pi(1h^2_{9/2})_{8^+}]$ isomer is $e^{emp}_\pi(N = 114) = 2.4(2)$.

Assuming, based on *ii*, that the empirical effective charge e^{emp}_π for the $1h_{9/2}1i_{13/2}$ configuration is the same as for the $1h^2_{9/2}$ configuration, $e^{emp}_\pi(114)$ is the same for the ^{198}Po($I^\pi = 11^-$) isomer as for the ^{198}Po($I^\pi = 8^+$) isomer: $e^{emp}_\pi(N = 114) = 2.4(2)$. Taking the experimental value $Q_s(^{210}\text{Po}(I^\pi = 11^-)) = (-)0.86(11)$ barn [Bec91], the final estimate for the quadrupole moment of the ^{198}Po($I^\pi = 11^-$) is

$$\begin{aligned} Q^{emp}_s(^{198}\text{Po}(I^\pi = 11^-)) &= 2.4(2) \times (-)0.86(11)\,\text{b} \\ &= (-)2.06(31)\,\text{b}. \end{aligned}$$

An alternative approach is to deduce $Q_s(^{210}\text{Po}(I^\pi = 11^-))$ by using the calculated quadrupole moments for the $N = 126$ isotones. Sagawa and Arima derived the quadrupole moments of the (Pb-core + 1 valence particle) by calculating the mean square radius of the particle (see equation (3.3)) and taking into account the polarising effect of the particle on the core (i.e., calculating the effective charge). They found $Q^{eff}_s(1h_{9/2}) = -0.404$ and $Q^{eff}_s(1i_{13/2}) = -0.568$ barn [Sag88]. These values are in fairly good agreement with the experimental values of $Q_s(1h_{9/2}) = -0.379(11)$ b [Bee78] (see also below for $Q_s(^{209}\text{Bi}_{N=126}(1h_{9/2}))$) and $Q_s(1i_{13/2}) = -0.45(11)$ b [Bec91]. Hence:

$$Q^{eff}_s(^{210}\text{Po}_{N=126}(I^\pi = 11^-)) = -0.568 - 0.404 = -0.972\,\text{b}$$

Table 3.3: *The measured quadrupole moments for the $^A Po[\pi(1h^2_{9/2})_{8+}]$ isomers and the deduced $e^{emp}_\pi(N)$ of the $1h^2_{9/2}$ proton configuration.*

N	^{A}Po	Q_{exp}[b]	$e^{emp}_\pi(N) = Q_s(N)/Q_s(126)$
126	210	-0.568(3)	1
124	208	-0.90(4)	1.58(7)
122	206	-1.02(4)	1.79(7)
120	204	-1.14(5)	2.00(7)
118	202	-1.21(16)	2.12(30)
116	200	-1.38(7)	2.42(12)

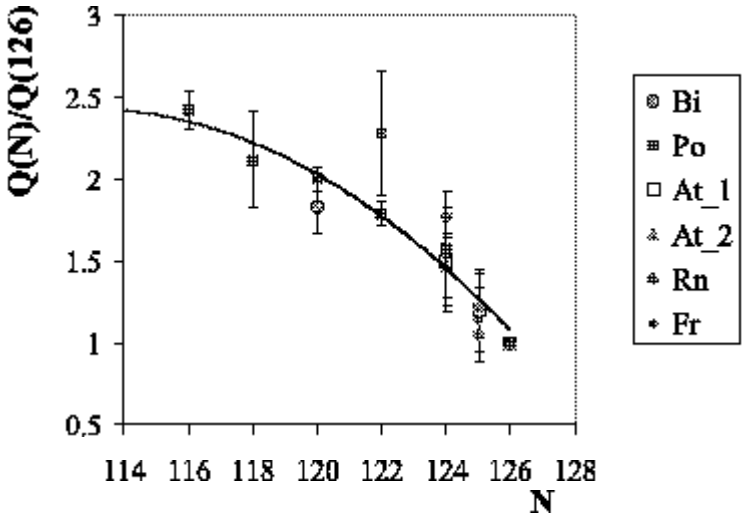

Figure 3.7: *Systematics of the quadrupole moments as a function of the neutron number for several proton configurations. The quadrupole moments are normalised to the quadrupole moment Q(N=126) for the same proton configuration. The proton configurations are $Bi[\pi(1h_{9/2})]$, $Po[\pi(1h^2_{9/2})]$, $At[\pi(1h^3_{9/2})]$, $At(\pi(1h^2_{9/2}1i_{13/2})$, $Rn[\pi(1h^4_{9/2})]$ and $Fr[\pi(1h^4_{9/2}1i_{13/2})]$. A systematic trend is found independent of the occupied proton orbitals. The data are taken from [BF85, Lin59, Mah87, Har91c, Ter98b]. See also text and footnote for $Q_s(^A Bi(I^\pi = 9/2^-))$.*

and, taking again the empirical effective charge $e_\pi^{emp}(N = 114)$ equal to 2.4(2),

$$Q_s^{eff}(^{198}\mathrm{Po}_{N=114}(I^\pi = 11^-)) = 2.4(2) \times -0.972 = -2.33 \text{ b}.$$

The value of $Q_s(^{198}\mathrm{Po}(I^\pi = 11^-)) = -2.33$ b (calculated) or (-)2.06(31) b (empirical) compares with $Q_s(^{196}\mathrm{Pb}(I^\pi = 11^-))$=(-)3.41(66) b. The ratio equals $Q_s(^{196}\mathrm{Pb}(I^\pi = 11^-))/Q_s^{emp}(^{198}\mathrm{Po}(I^\pi = 11^-))$=1.66(41), from which can be concluded that the presence of the two $3s_{1/2}$ holes in the magic $Z = 82$ proton core drives the nucleus towards a more deformed shape.

3.4.3 A comparison of the quadrupole moments of the ^{197}Bi($I^\pi = 9/2^-$) ground-state and the ^{195}Tl($I^\pi = 9/2^-$) isomer

In analogy with the comparison of the quadrupole moments of the ^{198}Po($I^\pi = 11^-$) and ^{196}Pb($I^\pi = 11^-$) isomers, the quadrupole moments of the ^{197}Bi($I^\pi = 9/2^-$) and the ^{195}Tl($I^\pi = 9/2^-$) isomers can be compared. The ^{197}Bi($I^\pi = 9/2^-$) ground-state has the $\pi(1h_{9/2})$ configuration, whereas the ^{195}Tl($I^\pi = 9/2^-$) isomer has the $\pi(3s_{1/2}^{-2}1h_{9/2})$ configuration. Their quadrupole moments have not been measured yet, but can be derived in a similar way as the quadrupole moment of the ^{198}Po($I^\pi = 11^-$) isomer.

The spectroscopic quadrupole moment of the $^{209}\mathrm{Bi}_{N=126}(I^\pi = 9/2^-)$ ground-state has been measured as $Q_s = -0.379(11)$ b. This value is the average of the measured quadrupole moments in Refs. [Dic67, Pow68, Eis68, Lan70, Geo70, Lee72][1]. Figure 3.7 shows that the quadrupole moments of the Bi isotopes follow

[1]The values for $Q_s(^{209}\mathrm{Bi}(I^\pi = 9/2^-))$ as mentioned in Refs. [Dic67, Pow68, Eis68, Lan70, Geo70, Lee72] are the same within the experimental uncertainty. They have been measured by applying several methods: atomic beam magnetic resonance, optical spectroscopy and the hyperfine structure of muonic X-rays. The experimental values for $Q_s(^{207}\mathrm{Bi}(I^\pi = 9/2^-))$ [BF85] and $Q_s(^{205}\mathrm{Bi}(I^\pi = 9/2^-))$ [Lin59] are determined relative to $Q_s(^{209}\mathrm{Bi}(I^\pi = 9/2^-))$. In the literature also experimental values, obtained from the hyperfine structure of pionic X-rays, are available for $Q_s(^{209}\mathrm{Bi}(I^\pi = 9/2^-))$. These are systematically larger and typically about $Q_s(^{209}\mathrm{Bi}(I^\pi = 9/2^-))$=0.5 b [Bee78, Bat81].

the same trend as a function of the neutron number as the other proton configurations in the Pb region. Therefore, we adopt also for $^{197}\mathrm{Bi}_{N=114}(I^\pi = 9/2^-)$ the effective charge $e_\pi^{emp}(N = 114) = 2.4(2)$. This results in

$$Q_s^{emp}(^{197}\mathrm{Bi}_{N=114}(I^\pi = 9/2^-)) = 2.4(2) \times -0.379(11) = -0.91(8)\ \mathrm{b}. \qquad (3.7)$$

Using the calculated value of Sagawa and Arima [Sag88], $Q_s^{sff}(1h_{9/2}) = -0.404$ b, we find

$$Q_s^{sff}(^{197}\mathrm{Bi}_{N=114}(I^\pi = 9/2^-)) = 2.4(2) \times -0.404 = -0.97\ \mathrm{b}. \qquad (3.8)$$

The spectroscopic quadrupole moment of the $^{207}\mathrm{Tl}_{N=126}(I^\pi = 9/2^-)$ isomer has not been measured yet either. However, experimental values for the quadrupole moments of the lighter $^{189,191,193}\mathrm{Tl}(I^\pi = 9/2^-)$ isomers are available [Bou85]. Figure 3.8 shows that $Q_s = -2.1(1)$ b is a reasonable extrapolated value for the $^{195}\mathrm{Tl}(I^\pi = 9/2^-)$ isomer.

The ratio $Q_s(^{195}\mathrm{Tl}(I^\pi = 9/2^-))/Q_s^{emp}(^{197}\mathrm{Bi}(I^\pi = 9/2^-))$=2.3(2) is larger than the ratio $Q_s(^{196}\mathrm{Pb}(I^\pi = 11^-))/Q_s^{emp}(^{198}\mathrm{Po}(I^\pi = 11^-))$=1.66(41), showing that the breaking of the proton core is influencing even more the quadrupole moment and, hence, the deformation of the $^{195}\mathrm{Tl}(I^\pi = 9/2^-)$ isomer than the quadrupole moment of the $^{196}\mathrm{Pb}(I^\pi = 11^-)$ isomer. This might be because the polarisation

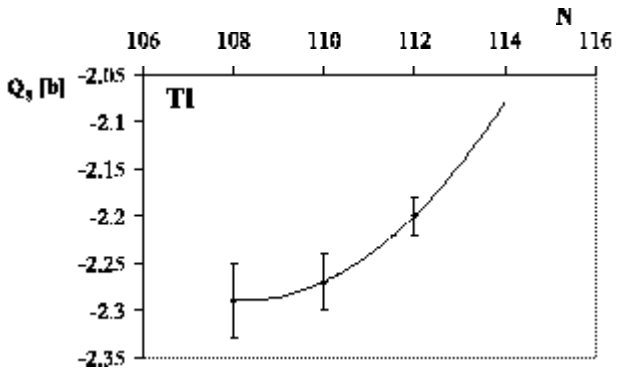

Figure 3.8: *Systematics of the spectroscopic quadrupole moment as a function of the neutron number for the ^{A}Tl$(I^\pi = 9/2^-)$ isomers. The data are taken from [Bou85].*

of the core of the corresponding normal state in ^{197}Bi ($\beta_q = 0.053(4)$) is less than the polarisation of the core of the ^{198}Po($I^\pi = 11^-$) state ($\beta_q = 0.084(12)$). Indeed, it will be shown in the next section that the presence of the valence $1i_{13/2}$ proton in addition to the valence $1h_{9/2}$ proton, induces an extra polarisation of the nuclear core.

3.4.4 The influence of the $1i_{13/2}$ proton on the quadrupole moments of the $(I^\pi = 11^-)$ isomers in ^{198}Po and ^{196}Pb

The influence of the $1i_{13/2}$ proton on the polarisation of the core can be easily verified by comparing $Q_s(^{197}\mathrm{Bi}(I^\pi = 9/2^-))+Q_s(1i_{13/2})$ and $Q_s(^{198}\mathrm{Po}(I^\pi = 11^-)$. We get

$$\begin{aligned} Q_s(^{197}\mathrm{Bi}(I^\pi = 9/2^-)) + Q_s(1i_{13/2}) &= -0.91(8) - 0.45(11)\ \mathrm{b} = -1.36(14)\ \mathrm{b} \\ &< Q_s^{emp}(^{198}\mathrm{Po}(I^\pi = 11^-)) = -2.06(31)\ \mathrm{b}, \end{aligned}$$

in which $Q_s(1i_{13/2})$ is taken from Ref. [Bec91].

The same comparison can be made for $Q_s(^{195}\mathrm{Tl}(I^\pi = 9/2^-))+Q_s(1i_{13/2})$ and $Q_s(^{196}\mathrm{Pb}(I^\pi = 11^-)$. Taking into account the polarisation of the Pb core due to the presence of the two $3s_{1/2}$ holes in the proton core, quantified by $Q_s(^{196}\mathrm{Pb}(I^\pi = 11^-))/Q_s^{emp}(^{198}\mathrm{Po}(I^\pi = 11^-))$=1.66(41), we find

$$\begin{aligned} Q_s(^{195}\mathrm{Tl}(I^\pi = 9/2^-)) + 1.66(41)\ Q_s^{eff}(1i_{13/2}) &= -2.1(1)\ \mathrm{b} - 1.66(41) \times 0.45(11)\ \mathrm{b} \\ &= -2.85(28)\ \mathrm{b} \\ &< Q_s(^{196}\mathrm{Pb}(I^\pi = 11^-)) = -3.41(66)\ \mathrm{b}. \end{aligned}$$

These results yield the ratios

$$\frac{Q_s^{emp}(^{198}\mathrm{Po}(I^\pi = 11^-))}{Q_s(^{197}\mathrm{Bi}(I^\pi = 9/2^-)) + Q_s(1i_{13/2})} = 1.5(3)$$

$$\frac{Q_s(^{196}\mathrm{Pb}(I^\pi = 11^-))}{Q_s(^{195}\mathrm{Tl}(I^\pi = 9/2^-)) + Q_s(1i_{13/2})} = 1.2(2).$$

This allows to conclude that the presence of the $1i_{13/2}$ valence proton, in addition to the $1h_{9/2}$ valence proton, induces an extra polarisation of the nuclear core.

Intuitively, it seems logical that 2 valence nucleons outside the nuclear core in nearly parallel orbitals will polarise the core more than 1 valence nucleon. Quantitatively, this means that the effective charge for a $\pi(1h_{9/2}1i_{13/2})_{11^-}$ configuration will be larger than the effective charge for a $\pi(1h_{9/2})_{9/2^-}$ configuration and, more generally, that the effective charge as a function of the number of neutron holes will increase if more valence protons in nearly parallel orbitals are present. A more detailed look to Figure 3.7 shows, indeed, that the effective charge for the Rn$[\pi(1h^4_{9/2})_{8^+}]$ configuration, with 4 valence protons, is larger than the general trend for the Po$[\pi(1h^2_{9/2})_{8^+}]$ configuration, with 2 valence protons. Similarly, the effective charge for the Bi$[\pi(1h_{9/2})]$ configuration, with 1 valence proton, seems to be smaller than the general trend for the Po$[\pi(1h^2_{9/2})_{8^+}]$ configuration. This has as a consequence that the estimation $e_\pi^{emp}(N = 114) = 2.4(2)$, based on the trend for the Po$[\pi(1h^2_{9/2})_{8^+})]$ isomers, is a good approximation for the 11^- isomers in Pb and Po, which have 2 valence protons as well. $e_\pi^{emp}(N = 114)$ for the $9/2^-$ ground-state in Bi is, however, most probably somewhat lower than the effective charge for the Po $1h^2_{9/2}$ isomers. Measured quadrupole moments for nuclear states with different numbers of valence protons and a neutron number $N < 122$ are lacking to make better estimates for e_π^{emp}. Notice also that, if the core is already deformed due to the presence of two $3s_{1/2}$ holes, the extra polarisation induced by the $1i_{13/2}$ proton is less than for a core with the magic proton number $Z = 82$.

3.4.5 Theoretical approach to the quadrupole moments of the 11^- isomers in Pb and Po, the $9/2^-$ isomers in Tl and the $9/2^-$ ground-states in Bi

According to the pure spherical shell model, the presence of two $s_{1/2}$ holes in the proton core has no influence on the spectroscopic quadrupole moment, as can be seen from expression (3.3). This is not in agreement with the experimental data, which yield a ratio $Q_s(^{196}\text{Pb}(I^\pi = 11^-))/Q_s(^{198}\text{Po}(I^\pi = 11^-))$=1.66(41), showing that the breaking of the proton core induces an extra deformation of the nucleus. This implies that a theoretical approach, where only the contributions of the

valence nucleons are considered, cannot account for the experimentally observed quadrupole moments. In [Hey92], Heyde has shown that, by taking into account the coupling of the valence protons with quadrupole vibrational excitations of the underlying core, some interesting features related to the magnetic dipole and electric quadrupole moments can be explained. This approach turned out to work well to reproduce the increasing quadrupole moments of the 8^+ isomers in the even Po-isotopes as a function of the neutron number [Ney97b]. Whereas the collective core admixture in the wave function introduces rather small, second-order modifications in the magnetic dipole moments, it induces an increase of the spectroscopic quadrupole moment ΔQ which can be as large as the single particle moment $Q_{s.p.}$ itself (Figure 3.9).

The spectroscopic quadrupole moments of the ^{196}Pb($I^\pi = 11^-$) and the ^{198}Po($I^\pi = 11^-$) isomers have been calculated by taking into account the coupling of the $1i_{13/2}1h_{9/2}$ valence protons and the 2_1^+ vibrational state of the un-

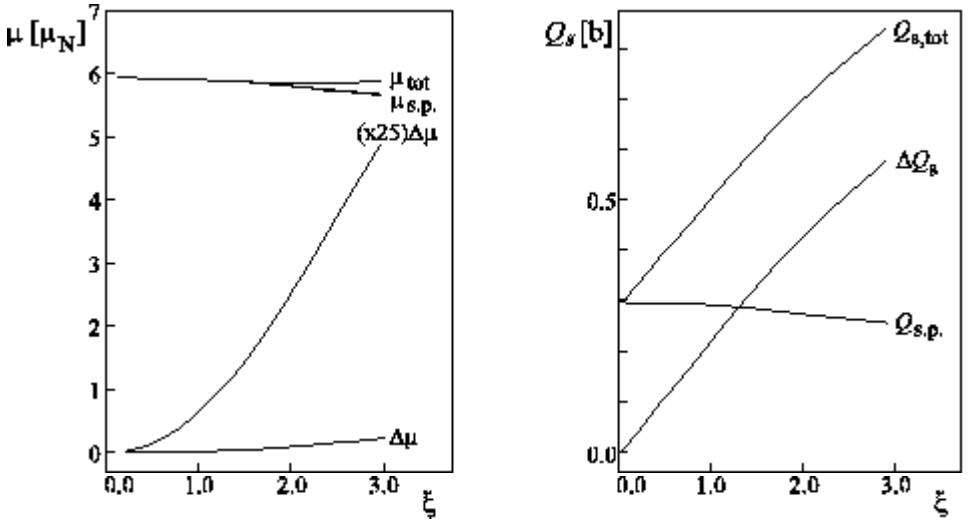

Figure 3.9: *Left: The collective, second order magnetic dipole moment correction $\Delta\mu$ as a function of the particle-core coupling strength ξ. Right: The collective, first-order quadrupole correction ΔQ, as a function of the particle-core strength ξ. The calculations of μ and Q are carried out for the $9/2^+$ $(1g_{9/2}^{-1})$ hole configuration in odd-A In nuclei [Hey92].*

derlying Hg-core and the underlying Pb-core, respectively. In a similar way the spectroscopic quadrupole moment of the ^{195}Tl($I^\pi = 9/2^-$) isomer and the ^{197}Bi($I^\pi = 9/2^-$) ground-state has been calculated by considering the coupling of the $1h_{9/2}$ valence proton with the 2_1^+ vibrational state of the underlying Hg-core and Pb-core, respectively. A comparison of the experimentally deduced quadrupole moment $Q_s(^{196}\mathrm{Pb}(I^\pi = 11^-)) = -3.41(66)$ b and the empirical quadrupole moment $Q_s^{emp}(^{198}\mathrm{Po}(I^\pi = 11^-)) = -2.06(31)$ b with the single particle quadrupole moment derived as $Q_s^{sff}(I^\pi = 11^-) = Q_s^{sff}(1i_{13/2}) + Q_s^{sff}(1h_{9/2}) = -0.568 - 0.401 = -0.969$ b, with $Q_s^{sff}(1i_{13/2})$ and $Q_s^{sff}(1h_{9/2})$ taken from the work of Sagawa and Arima [Sag88], indicates that the perturbation induced by the collective admixture in the wave function is at least of the order of the single particle quadrupole moment. Therefore, the collective admixtures to the single particle wave functions cannot be considered as a small perturbation and the first order perturbation theory, as used in Refs. [Ney97b, Ter98a], cannot be applied. The same reasoning can be made for the calculation of the quadrupole moment of the ^{195}Tl($I^\pi = 9/2^-$) isomer. There, the experimentally extrapolated value, based on the data of Ref. [Bou85], yields $Q_s = -2.1(1)$ b, while the quadrupole moment for the $1h_{9/2}$ state in Ref. [Sag88] is $Q_s = Q(1h_{9/2}) = -0.414$ b.

In this work the wave functions have been calculated by diagonalising the Hamiltonian $H = H_{s.p.} + H_{coll} + H_{int}$ in the 2-dimensional Hilbert space spanned by the wave functions $\mid 11^-_{s.p.}\rangle$ and $\mid 11^-_{s.p.} \otimes 2^+; 11^-\rangle$. Here $\mid 11^-_{s.p.}\rangle$ is a shorthand notation for $\mid 1h_{9/2}1i_{13/2}; 11^-\rangle$, which is an eigenfunction of $H_{s.p.}$, and $\mid 2^+\rangle$ is the first excited vibrational state of the underlying proton core and eigenfunction of H_{coll}. The single particle Hamiltonian $H_{s.p.}$ is the spherical shell model Hamiltonian, e.g., the Woods-Saxon or modified oscillator Hamiltonian (see expressions (1.1), (1.2) and (1.3)). H_{coll} is the collective vibrational Hamiltonian. In the second quantisation formalism, and considering quadrupole vibrations only, it yields

$$H_{coll} = \sum_{\mu=-2}^{2} \hbar\omega_2 (b^+_{2\mu} b_{2\mu} + 1/2), \tag{3.9}$$

in which $b^+_{2\mu}$ ($b_{2\mu}$) is a creation (annihilation) operator for a boson with spin 2

and $\hbar\omega_2$ the energy of the 2_1^+ vibrational state. The interaction Hamiltonian, H_{int}, accounting for the coupling of the valence nucleons with the underlying vibrational core, equals

$$H_{int} = -\xi\hbar\omega_2\sqrt{\frac{\pi}{5}}\sum_{i=1}^{N}\sum_{\mu}(b_{2\mu} + (-1)^\mu b^+_{2,-\mu})Y^\mu_2(\hat{r}_i). \tag{3.10}$$

The sum over i runs over all considered valence nucleons. ξ is the coupling strength parameter. It is related to the experimental $B(E_2; 0_1^+ \rightarrow 2_1^+)$ reduced transition probability and the excitation energy of the 2_1^+ vibrational state as [Hey94]

$$\xi = \langle r\frac{dV}{dr}\rangle\frac{\sqrt{B(E2; 0^+ \rightarrow 2_1^+)}}{\frac{3}{4\pi}ZeR_0^2\sqrt{\pi}\hbar\omega_2}. \tag{3.11}$$

The following matrix needs to be diagonalised:

$$\begin{pmatrix} \langle 11^-_{s.p.} \mid H \mid 11^-_{s.p.}\rangle & \langle 11^-_{s.p.} \mid H \mid 11^-_{s.p.} \otimes 2^+; 11^-\rangle \\ \langle 11^-_{s.p.} \otimes 2^+; 11^- \mid H \mid 11^-\rangle & \langle 11^-_{s.p.} \otimes 2^+; 11^- \mid H \mid 11^-_{s.p.} \otimes 2^+; 11^-\rangle \end{pmatrix}. \tag{3.12}$$

By solving the eigenvalue problem, the wave function $\mid \widetilde{11}\rangle = a \mid 11^-_{s.p.}\rangle + b \mid 11^-_{s.p.} \otimes 2^+; 11^-\rangle$ can be determined. The quadrupole moment is defined and calculated as

$$Q_s \equiv \sqrt{\frac{16\pi}{5}}\langle\widetilde{11}, M = 11 \mid \hat{Q}_2^0 \mid \widetilde{11}, M = 11\rangle, \tag{3.13}$$

in which

$$e\hat{Q}_2^0 \equiv \sum_i e_i r_i^2 Y_2^0(\hat{r}_i) + \frac{3}{4\pi}ZeR_0^2\sqrt{\frac{\hbar\omega_2}{2C}}(b_{20}^+ + b_{20}) \tag{3.14}$$

with

$$\frac{3}{4\pi}ZeR_0^2\sqrt{\frac{\hbar\omega_2}{2C}}\sqrt{5} = \sqrt{B(E_2; 0^+ \rightarrow 2_1^+)}. \tag{3.15}$$

As an example the full calculation is carried out for the ($I^\pi = 11^-$) isomer in ^{200}Pb in appendix E. Assuming that $\langle rdV/dr\rangle = 50$ MeV [Boh75], it results in the following expression for the 11^- isomers in Po and Pb:

$$\begin{aligned}\langle\widetilde{11} \mid \hat{e}Q_2^0 \mid \widetilde{11}\rangle &= a^2 eQ_s(11^-_{s.p.}) + b^2\ 0.932\ eQ_s(11^-_{s.p.}) \\ &- b^2\ 0.856\ eQ_s(2_1^+, core) + 2ab\sqrt{B(E2; 0^+ \rightarrow 2_1^+)}1.24,\end{aligned} \tag{3.16}$$

in which the coefficients a and b depend on the excitation energy of the 2_1^+ vibrational state. A similar expression can be obtained for the $9/2^-$ states in Bi and Tl:

$$\begin{aligned}\langle \widetilde{11} \mid e\hat{Q}_2^0 \mid \widetilde{11} \rangle &= a^2 eQ_s(9/2^-_{s.p.}) + b^2\, 0.652\, eQ_s(9/2^-_{s.p.}) \\ &- b^2\, 0.636\, eQ_s(2_1^+, core) + 2ab\sqrt{B(E2; 0^+ \rightarrow 2_1^+)}1.05.\end{aligned} \tag{3.17}$$

The results of the calculated quadrupole moments are listed in table 3.4. Unfortunately neither $B(E2; 0_1^+ \rightarrow 2_1^+)$ nor $Q_s(2_1^+)$ values are known for the lighter Pb and Hg nuclei, so that only for a few Pb, Po, Tl and Bi isotopes the quadrupole moments of the isomer of interest can be calculated. This means that only for a few cases a comparison between the calculated and experimental quadrupole moments is possible.

The calculated value for Q_s in the $N = 126$ isotones is larger than the experimental value for both the ^{209}Bi($I^\pi = 9/2^-$) ground-state and the ^{210}Po($I^\pi = 11^-$) isomer. The only other case where a comparison between the calculated and the theoretical value is possible, ^{207}Bi$_{N=124}$($I^\pi = 9/2^-$), seems to indicate that for a decreasing neutron number the calculated and the experimental values for the quadrupole moments are in agreement. The question arises whether for $N < 124$ the calculated and the experimental quadrupole moment will be in agreement as well, or whether the calculated quadrupole moment will take lower values than the experimentally determined quadrupole moment. This shows immediately the necessity of measuring more quadrupole moments in this region.

Also a comparison of the calculated ratios $Q_s(intruder)/Q_s(normal)$ with the experimental ratios is difficult due to the missing experimental data. $Q_s(^A\mathrm{Pb}(I^\pi = 11^-)/Q_s(^{A+2}\mathrm{Po}(I^\pi = 11^-)$ seems to saturate around 2 for a decreasing neutron number ($N < 124$). The calculated ratio $Q_s(^{A-1}\mathrm{Tl}(I^\pi = 9/2^-)/Q_s(^{A+1}\mathrm{Bi}(I^\pi = 9/2^-)$ seems to stabilise around 2.6 for $N < 124$. These results compare with the experimental values of 1.66(41) and 2.3(2), respectively. So, we might conclude that the calculations slightly overestimate the polarisation of the core induced by the two $3s_{1/2}$ proton holes. Notice that also the calculations show that for

Table 3.4: *Results for the calculated quadrupole moments of the $^A Pb(I^\pi = 11^-)$, $^A Po(I^\pi = 11^-)$ and $^A Tl(I^\pi = 9/2^-)$ isomers and the $^A Bi(I^\pi = 9/2^-)$ ground-states.*

iso-tope	I^π	$A_{isotope}$	proton core	A_{core}	$Q_{s.p.}$ [b][a]	$B(E2)$ [e^{2}b^2][b]	$E(2_1^+)$ [MeV][c]	$Q(2_1^+)$ [b][d]	Q_{calc} [b]	Q_{exp} [b][e]
Pb	11^-	206	Hg	204	-0.9696	0.427	0.4366	0.40	-2.09	
		204		202		0.612	0.439	1.01	-2.77	
		202		200		0.853	0.368	1.07	-3.00	
		200		198		0.990	0.412	0.82	-2.89	
Po	11^-	210	Pb	208	-0.9696	0.290	4.085	-0.7	-1.27	(-)0.86(11)
		208		206		0.100	0.803	0.05	-1.29	
		206		204		0.162	0.899	0.23	-1.39	
Tl	$9/2^-$	205	Hg	204	-0.4014	0.427	0.4366	0.40	-1.27	
		203		202		0.612	0.439	1.01	-1.79	
		201		200		0.853	0.368	1.07	-1.98	
		199		198		0.990	0.412	0.82	-1.91	
Bi	$9/2^-$	209	Pb	208	-0.9696	0.290	4.085	-0.7	-0.57	-0.379(11)
		207		206		0.100	0.803	0.05	-0.62	-0.58(11)
		205		204		0.162	0.899	0.23	-0.70	

[a] *Taken from Ref. [Sag88].*

[b] *Taken from Ref. [Ram89].*

[c] *Taken from Ref. [Ram89].*

[d] *Taken from Refs. [Esa81, Spe80, Esa77, Joy78, Rag89].*

[e] *Taken from Refs. [Bec91, Dic67, Pow68, Eis68, Lan70, Geo70, Lee72, BF85].*

Table 3.5: *Ratios of the calculated spectroscopic quadrupole moments $Q_s(^A Pb(I^\pi = 11^-))/Q_s(^{A+2} Po(I^\pi = 11^-)))$ and $Q_s(^{A-1} Tl(I^\pi = 9/2^-))/Q_s(^{A+1} Bi(I^\pi = 9/2^-)))$.*

^{A}Pb	$^{A+2}$Po	$Q_s(^A\text{Pb}(11^-))/Q_s(^{A+2}\text{Po}(11^-))$	$^{A-1}$Tl	$^{A+1}$Bi	$Q_s(^{A-1}\text{Tl}(9/2^-))/Q_s(^{A+1}\text{Bi}(9/2^-))$
206	208	1.62	205	207	2.05
204	206	1.99	203	205	2.56

the $\pi(1i_{13/2}1h_{9/2})$ configuration the extra polarisation of the core, induced by the two $3s_{1/2}$ proton-holes, is less than for the $\pi(1h_{9/2})$ configuration.

The formalism accounts hence rather well for the increase of the quadrupole moment due to the breaking of the proton core. An increase with a factor of 2 is predicted. Recent calculations, including octupole vibrations as well, result in $Q_s(^{198}\mathrm{Po}(I^\pi = 11^-)) = -1.4$ b and $Q_s(^{196}\mathrm{Pb}(I^\pi = 11^-)) = -3.54$ b [Oro01]. The theoretical value for the quadrupole moment of the 11^- isomer in ^{196}Pb is in perfect agreement with the experimental value of $Q_s = (-)3.41(66)$ b, while the theoretical value for the 11^- isomer in ^{198}Po is somewhat too small compared to the experimental value of $Q_s = (-)2.06(31)$ b. A systematic theoretical study of the quadrupole moments in this region is currently being made [Oro01].

3.5 The quadrupole moment of the ^{196}Pb($I^\pi = 16^-$) magnetic rotational bandhead

The shears band 2 in ^{196}Pb is built on the $[\pi(3s_{1/2}^{-2}1h_{9/2}1i_{13/2}) \otimes \nu(1i_{13/2}^{-2})]_{16^-}$ configuration. As we are interested in the quadrupole moment of this shears bandhead, we will express it as a linear combination of the quadrupole moments of the $\pi(3s_{1/2}^{-2}1h_{9/2}1i_{13/2})_{11^-}$ and the $\nu(1i_{13/2}^{-2})_{12^+}$ isomers by means of angular momentum algebra.

3.5.1 The coupling of $Q_s(I^\pi = 11^-)$ and $Q_s(I^\pi = 12^+)$ to $Q_s(I^\pi = 16^-)$

The wave function of the shears bandhead can be decomposed as [Hey94]

$$
\begin{aligned}
&|\,(J_\pi = 11, J_\nu = 12); 16, M\rangle = \sum_{m1,m2} \langle 11, m_1; 12, m_2 \mid 16, M\rangle \mid 11, m_1\rangle \mid 12, m_2\rangle \\
&= \sum_{m_1,m_2} \sqrt{2\times 16+1}(-1)^{11-12+M} \begin{pmatrix} 11 & 12 & 16 \\ m_1 & m_2 & -M \end{pmatrix} \mid 11, m_1\rangle \mid 12, m_2\rangle.
\end{aligned}
\tag{3.18}
$$

This decomposition is used to calculate the expectation value of the quadrupole operator $\hat{Q}_2^0$ from $Q_s(I^\pi = 11^-)$ and $Q_s(I^\pi = 12^+)$. Making use of the additivity of the quadrupole operator we get

$$\begin{aligned} Q_s(16) &= \langle 16,16 \mid \hat{Q}_2^0 \mid 16,16\rangle && (3.19)\\ &= \langle 16,16 \mid \hat{Q}_2^0(\pi) + \hat{Q}_2^0(\nu) \mid 16,16\rangle && (3.20)\\ &= \sum_{m_1,m_2} 33 \begin{pmatrix} 11 & 12 & 16 \\ m_1 & m_2 & -16 \end{pmatrix}^2 [\langle 11,m_1 \mid \hat{Q}_2^0(\pi) \mid 11,m_1\rangle \\ &\quad + \langle 12,m_2 \mid \hat{Q}_2^0(\nu) \mid 12,m_2\rangle]. && (3.21) \end{aligned}$$

The Wigner-Eckart theorem says that (see, e.g., in [Hey94])

$$\langle j,m \mid \hat{Q}_2^0 \mid j,m\rangle = (-1)^{j-m} \begin{pmatrix} j & 2 & j \\ -m & 0 & m \end{pmatrix} \langle j\|\hat{Q}_2\|j\rangle \quad (3.22)$$

$$Q_s(j) = \langle j,j \mid \hat{Q}_2^0 \mid j,j\rangle = (-1)^{j-j} \begin{pmatrix} j & 2 & j \\ -j & 0 & j \end{pmatrix} \langle j\|\hat{Q}_2\|j\rangle \quad (3.23)$$

and hence

$$\langle j,m \mid \hat{Q}_2^0 \mid j,m\rangle = (-1)^{j-m} \frac{\begin{pmatrix} j & 2 & j \\ -m & 0 & m \end{pmatrix}}{\begin{pmatrix} j & 2 & j \\ -j & 0 & j \end{pmatrix}} Q_s(j). \quad (3.24)$$

Making use of (3.24) in (3.21), the final expression of the quadrupole moment becomes (with $m_2 = 16 - m_1$):

$$\begin{aligned} Q_s(16) &= \sum_{m_1} 33 \begin{pmatrix} 11 & 12 & 16 \\ m_1 & m_2 & -16 \end{pmatrix}^2 \Bigg[(-1)^{11-m_1} \frac{\begin{pmatrix} 11 & 2 & 11 \\ -m_1 & 0 & m_1 \end{pmatrix}}{\begin{pmatrix} 11 & 2 & 11 \\ -11 & 0 & 11 \end{pmatrix}} Q_\pi(11) \\ &\quad + (-1)^{12+m_1-16} \frac{\begin{pmatrix} 12 & 2 & 12 \\ -m_2 & 0 & m_2 \end{pmatrix}}{\begin{pmatrix} 12 & 2 & 12 \\ -12 & 0 & 12 \end{pmatrix}} Q_\nu(12)\Bigg]. \quad (3.25) \end{aligned}$$

The experimental values for the spectroscopic quadrupole moments are $Q_\pi(11) = (-)3.41(66)$ b (this work) and $Q_\nu = 0.65(5)$ b [Zyw81]. The final value for $Q_s(I^\pi = 16^-)$ is

$$Q_s(I^\pi = 16^-) = -0.316(97)\,\text{b}.$$

The expression (A.5) to calculate the intrinsic quadrupole moment from the spectroscopic quadrupole moment is only valid if K is a well-defined quantum number. In the shears bands the usual assumption that $K = I$ for the bandhead is not valid, so that it is not clear what K-value should be taken. In order to derive the deformation the intrinsic quadrupole moment needs to be known. Therefore, an easy calculation of β_q is not possible and only TAC calculations allow to extract the deformation.

3.5.2 Discussion

TAC calculations have been performed to calculate the spectroscopic quadrupole moment of the $I^\pi = 16^-$ shears bandhead in ^{196}Pb [Chm, Vyv01a]. The approach has been as follows. The quadrupole moments of the neutron contribution, $\nu(1i^{-2}_{13/2})_{12^+}$, and the proton contribution, $\pi(3s_{1/2}1h_{9/2}1i_{13/2})_{11^-}$, to the magnetic rotational band have been measured separately as $Q_s(I^\pi = 12^+) = 0.65$ b and $Q_s(I^\pi = 11^-) = (-)3.41(66)$ b, respectively. In a first TAC calculation the quadrupole coupling constant, χ, has been chosen such the that quadrupole moment of the ^{196}Pb$(I^\pi = 12^+)$ isomer was reproduced (see section 1.4.6), in a second calculation χ was chosen such that $Q_s(^{196}\text{Pb}(I^\pi = 11^-))$ was reproduced. The coupling constants will be noted $\chi(12^+)$ and $\chi(11^-)$, respectively. The preliminary results of the calculations using these two coupling constants are listed in table 3.6. Taking into account a quantal correction of 1/2, the nuclear spin, I, as derived from the TAC calculations is about 1 to 2 units too high. A larger value for the nuclear spin is obtained because the angle between the proton and the neutron blade of the shears is too small in the calculation ($\theta = 68.5°$ in the calculations using $\chi(12^+)$ and $\theta = 70.7°$ in the calculations using $\chi(11^-)$, while $\theta \simeq 90°$ would give the experimental spin). Closing the shears is the way

Table 3.6: *Results of the TAC calculations for the bandhead of Band 2 in ^{196}Pb (see Figure 1.19).*

	$\chi(12^+)$	$\chi(11^-)$
ϵ_2	-0.082	-0.148
ϵ_4	0	0
γ	-127.4°	-121.1°
I	18.82	18.09
Q_s	-0.72 b	-1.5 b

to generate angular momentum in a magnetic rotational bandhead (see Figure 1.18).

The formalism to couple the quadrupole moments of the proton blade and the neutron blade, as derived above, allows to couple the quadrupole moments of the blades for different total spins I, i.e., for different angles θ. We find $Q_s(I^\pi = 17^-) = -0.61(16)$ b and $Q_s(I^\pi = 18^-) = -0.92(23)$ b. If we take the spins that correspond to the ones from the TAC calculations and compare the quadrupole moments, we see that the quadrupole moment, calculated by using $\chi(12^+)$, is lower than the value obtained from coupling the experimental $Q_s(I^\pi = 12^+)$ and $Q_s(I^\pi = 11^-)$, while the quadrupole moment, calculated by using $\chi(11^-)$, is higher. This shows that, if the coupling constant, χ, could be adjusted somewhere between $\chi(12^+)$ and $\chi(11^-)$, the calculations would result in the correct value for the quadrupole moment. This suggests that the coupling constant, χ, is different for the proton and the neutron configuration. This can also be understood from the fact that the quadrupole moment of the 11^- isomer, obtained from the TAC calculations by using $\chi(12^+)$, takes a too low value, i.e., $Q_s = -2.5$ b, compared to the experimental value of $Q_s = -3.41(66)$ b [Chm].

3.6 Experimental results on ^{194}Pb

Also in ^{194}Pb the $\pi(3s_{1/2}^{-2}1h_{9/2}1i_{13/2})_{11^-}$ isomer has been observed. An extraction of this quadrupole moment would be interesting as well. The magnetic moment of the ($I^\pi = 11^-, T_{1/2} = 122(10)$ ns) isomer has not been measured yet. Therefore, the same magnetic moment as for the ^{196}Pb($I^\pi = 11^-$) isomer has been taken, $\mu = 10.56(88)\mu_N$. This assumption is supported by the fact that the measured magnetic moments of the 11^- isomers in the Po isotopes are nearly constant as a function of the neutron number (Figure 3.10). The most intense peak depop-

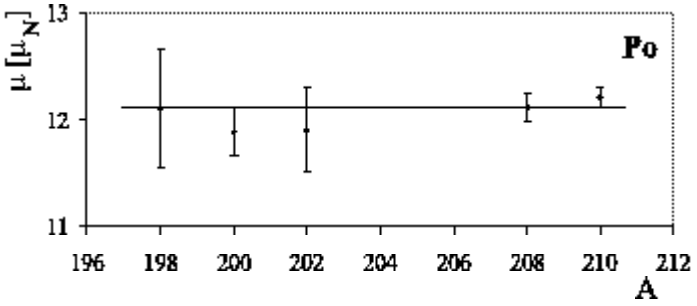

Figure 3.10: *Systematics of the magnetic moments of the* 11^- *isomers in the even Po isotopes [Rag89].*

ulating the ^{194}Pb($I^\pi = 11^-$) isomer is the 352 keV $E1$ transition (Figure 3.11 and [Fan91]). However the analysis of this peak resulted in a quadrupole interaction frequency ν_Q with a huge experimental uncertainty, $\nu_Q = 280^{+270}_{-200}$ MHz (Figure 3.12).

In a second attempt the peaks in the cascade underneath the 12^+ isomer have been analysed by a double perturbation fit. The 965 keV $E2$, 575 keV $E2$, 280 keV $E1$ and 166 keV $E2$ transitions are very intensely and purely present in the spectra (Figure 3.1), resulting in LEMS curves with good statistics (Figure 3.13). These LEMS curves are determined by the electromagnetic interactions of both the 11^- isomer and the 12^+ isomer. So, in principle the quadrupole interaction frequency of the 11^- can be derived from a double perturbation fit. Prior to our

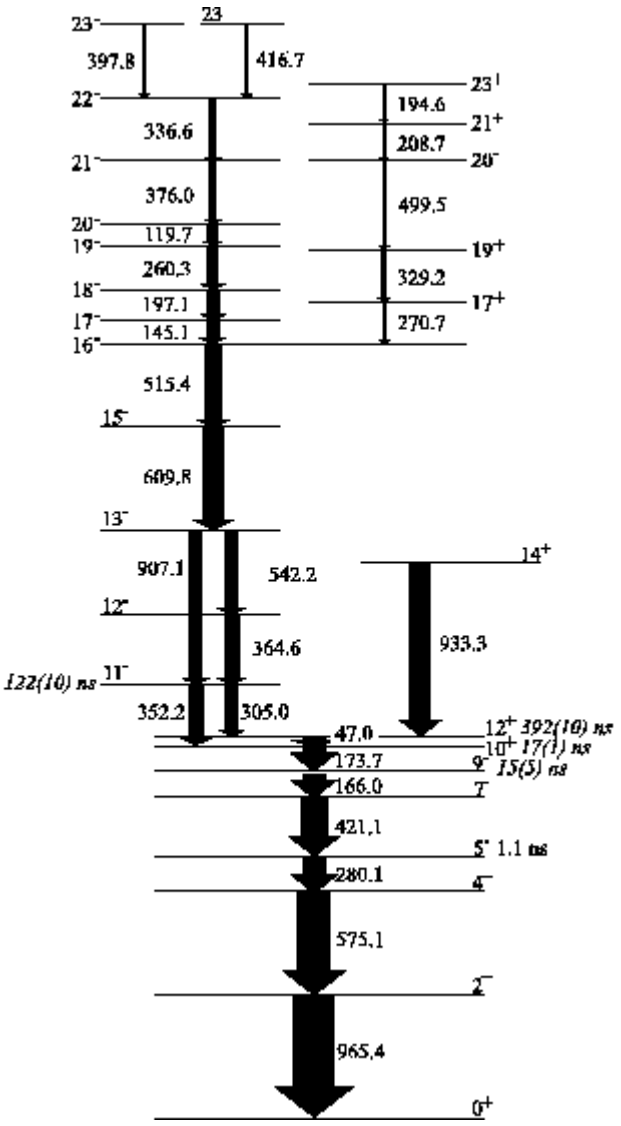

Figure 3.11: *Partial level scheme of ^{191}Pb [Fan91].*

experiments the quadrupole moment and the magnetic moment of the ^{191}Pb($I^\pi = 12^+, T_{1/2} = 392(10)$ ns) isomer have been measured as $Q_s = 0.49(3)$ b and $\mu = -2.004(24)\mu_N$ by applying the TDPAD technique [Ste85]. Hence, the EFG of Pb in Re can be deduced from the frequency $\nu_Q(^{191}\text{Pb}(I^\pi = 12^+))$. Of course this value should be in agreement with the EFG from of the LEMS curve for the ^{196}Pb($I^\pi = 12^+$) isomer. This provides a direct experimental test for the double perturbation formalism. Summarising, the double perturbation fit allows

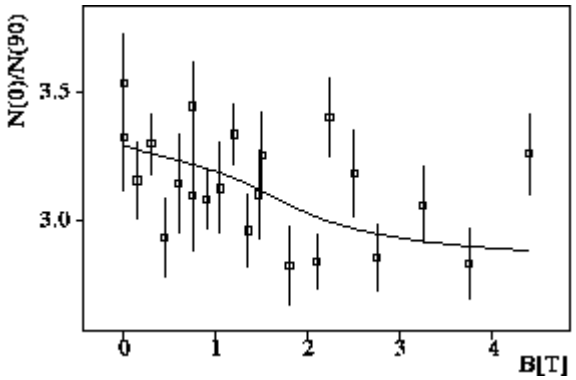

Figure 3.12: *LEMS curve for the 352 keV transition depopulating the ^{194}Pb(11^-) isomer. The fit results in $\nu_Q = 280^{+270}_{-200}$ MHz.*

to extract $Q_s(^{194}\mathrm{Pb}(I^\pi = 11^-))$ from $\nu_Q(^{194}\mathrm{Pb}(I^\pi = 11^-))$ and the EFG of Pb in Re from $\nu_Q(^{194}\mathrm{Pb}(I^\pi = 12^+))$.

In the double perturbation fit, apart from the two quadrupole interaction frequencies, also the inital orientation σ/I of the 12^+ isomer and a normalisation factor have been taken as free fit parameters. The initial orientation of the 11^- isomer has been fixed as $\sigma/I = 0.35$ to eliminate one more free parameter. The direct feedings $D1$ and $D2$ and the double perturbed fraction have been determined from the relative γ ray intensities of the 173 keV, the 352 keV, the 305 keV and the 932 keV as explained in appendix D. It is derived that 25% of the 10^+ state is fed directly from the 11^- isomer and 60% directly from the 12^+ state. The double perturbed fraction is 15%. The half-lives of the 10^+ level ($T_{1/2} = 17(1)$ ns), the 9^- level ($T_{1/2} = 15(5)$ ns) and the 5^- level ($T_{1/2} = 1.1$ ns) are too short for detectable electromagnetic interactions. Therefore, in the fit these levels are considered to be prompt.

The fit results are listed in table 3.7. The average quadrupole interaction frequency for the 12^+ isomer is $\nu_Q = 26.3^{+2.5}_{-2.1}$ MHz. By using the measured quadrupole moment $Q_s(I^+ = 12^+) = 0.49(3)$ b an EFG of Pb [Ste85] in Re of $|V_{ZZ}| = 2.21^{+0.25}_{-0.22} \cdot 10^{21}$ V/m^2 is derived. This value is in perfect agreement with the value of $|V_{ZZ}| = 2.42(27) \cdot 10^{21}$ V/m^2, which was derived from the quadrupole interaction frequency of the 12^+ isomer in ^{196}Pb. For comparison

Table 3.7: *Experimental results obtained for the transitions depopulating the* $^{191}Pb(11^- \rightarrow 12^+)$ *cascade. The double perturbed fraction is 15%, the fraction due to depopulation of the* 12^+ *isomer 60% and the fraction directly coming from the* 11^- *isomer 25%. The initial orientation of the* 11^- *isomer is fixed,* $\sigma/I(11^-) = 0.35$. *The right column contains the values for* $\nu_Q(12^+)$ *obtained from a single perturbation fit.*

E_γ [keV]	Detector ratio	$\nu_Q(12^+)$ [MHz]	$\nu_Q(11^-)$ [MHz]	$\sigma/I(12^+)$	N	$\nu_Q(12^+)$ [MHz]
166	1	$28.5^{+6.0}_{-5.5}$	270^{+150}_{-70}	0.45(5)	1.00(3)	37.5(6.0)
166	2	$33.5^{+6.5}_{-5.0}$	332^{+70}_{-50}	0.43(2)	1.31(2)	48(5)
280	1	25(10)	175(45)	0.5(2)	0.372(4)	29(3)
280	2	$19.5^{+6.0}_{-4.5}$	200^{+40}_{-30}	0.49(2)	1.07(2)	30(4)
575	1	$25^{+5.5}_{-4.5}$	320^{+450}_{-70}	0.47^{+1}_{-7}	0.276(12)	39(6)
965	1	$27^{+5}_{-4.5}$	280^{+40}_{-35}	0.47(1)	0.223(3)	41(6)

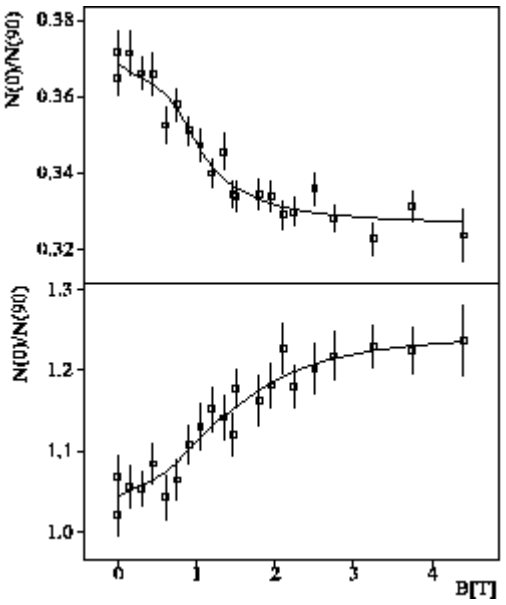

Figure 3.13: *Sample LEMS curves for the transitions depopulating the* $^{191}Pb(11^- \rightarrow 12^+)$ *cascade. The curves are normalised on the prompt 158 keV transition. Up: LEMS curve for the 280 keV E1 transition. Down: LEMS curve for the 166 keV E2 transition. The fit results are listed in table 3.7.*

also the quadrupole interaction frequencies, assuming that the depopulation of the 12^+ isomer contributes for 100% to the 166, 280, 575 and 965 keV γ ray intensities, are listed. They result in $\nu_Q = 36.0(2.5)$ MHz and $V_{ZZ} = 3.04(28)\cdot 10^{21}$ V/m^2. This value for the EFG is too high compared to the value obtained from $\nu_Q(^{196}\mathrm{Pb}(I^\pi = 12^+))$. Hence these results provide an experimental prove that the double perturbation formalism as derived in section 2.2 is correct.

3.6.1 Systematics of the measured spectroscopic quadrupole moments in the even Pb isotopes

The nice consequence of the double perturbation fit is that also the quadrupole interaction frequency of the $^{194}\mathrm{Pb}(I^\pi = 11^-)$ isomer can be extracted from the double perturbation fit as $\nu_Q = 241(38)$ MHz. The experimental uncertainty includes the uncertainty on the magnetic moment. This results in a spectroscopic quadrupole moment of $|Q_s| = 4.12(79)$ b and an intrinsic quadrupole moment $|Q_0| = 5.4(1.0)$ b by using $(K = I = 11)$ and equation (A.5). The deduced deformation is $|\beta_q| = 0.192(34)$ by using equation (A.22). The coupling of $Q_s(^{194}\mathrm{Pb}(I^\pi = 11^-))$ and $Q_s(^{194}\mathrm{Pb}(I^\pi = 12^+))$ in the same way as has been done for ^{196}Pb (equation (3.25)) results in $Q_s(^{194}\mathrm{Pb}(I^\pi = 16^-)) = -0.46(12)$ b for the $I^\pi = 16^-$ shears bandhead in ^{194}Pb.

Figure 3.14 shows the systematics of all deduced quadrupole moments of the 11^-, 12^+ and 16^- states in the Pb isotopes. Our measured values for the 11^- isomers seem to follow the trend of gradually increasing quadrupole moments with decreasing neutron number (see also Figure 3.7), although the experimental uncertainties are too big to be conclusive.

The trend of the quadrupole moments of the $\nu(1i^{-2}_{13/2})_{12^+}$ isomers is predicted by the following relationship of the reduced matrix elements within the seniority model [Tal93]:

$$\langle j^n, \nu, I_f \| \sum_{i=1}^{n} r_i^2 Y_2(\hat{r}_i) \| j^n, \nu, I_i \rangle = \frac{2j+1-2n}{2j+1-2\nu} \langle j^\nu, \nu, I_f \| \sum_{i=1}^{\nu} r_i^2 Y_2(\hat{r}_i) \| j^\nu, \nu, I_i \rangle \tag{3.26}$$

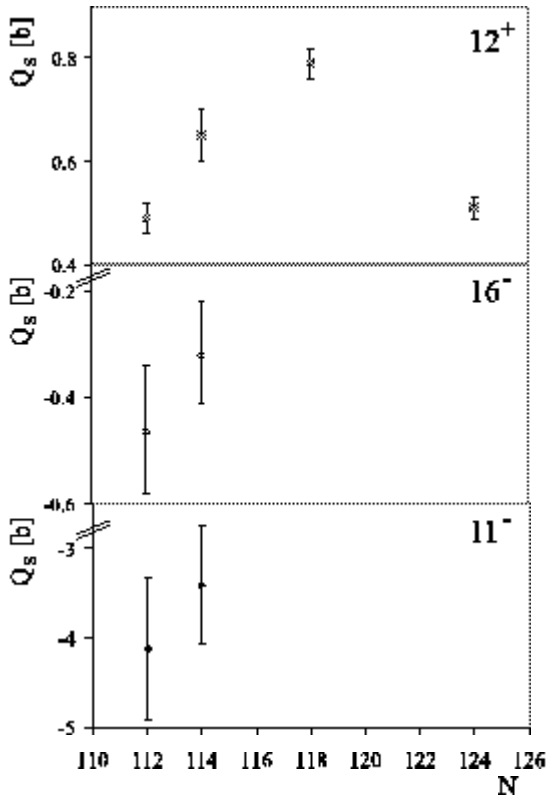

Figure 3.14: *Systematics of the experimentally deduced spectroscopic quadrupole moments of the* 11^- *(this work),* 12^+ *[Ste83, Ste85, Mah79] and* 16^- *isomers (this work).*

or

$$\langle 1i^n_{13/2}, 2, 12 \| \sum_i r_i^2 Y_2(\hat{r}_i \| j^n, 2, 12\rangle = \frac{14-2n}{10} \langle j^2, 2, 12 \| \sum_i r_i^2 Y_2(\hat{r}_i) \| j^2, 2, 12\rangle, \tag{3.27}$$

in which ν is the seniority (number of unpaired particles) and n the number of $1i_{13/2}$ particles. Taking into account that the reduced matrix element $\langle j^2, 2, 12 \| \sum_i r_i^2 Y_2(\hat{r}_i) \| j^2, 2, 12\rangle$ is negative (this can be calculated in a similar way as (E.20)) this formula predicts a quadrupole moment ranging from negative ($n < 7$) over zero (for a half-filled shell) to a positive quadrupole moment ($n > 7$). Alternatively, calculations within the Tamm-Dancoff approximation predict a change of the quadrupole moment proportional to $u^2 - v^2$, with v^2 the probability for occupation and u^2 the probability for non-occupation [Alb78]. Again the

quadrupole moment is expected to become zero for a half occupied $1i_{13/2}$ subshell. Note that the quadrupole moment of the 12^+ isomer in ^{206}Pb is deviating from the trend. The reason for this is not clear.

3.7 Conclusion

The spectroscopic quadrupole moments of the ^{196}Pb($I^\pi = 11^-$) and ^{194}Pb($I^\pi = 11^-$) isomers have been measured as $Q_s = (-)3.41(66)$ b and $Q_s = (-)4.12(79)$ b, respectively. It has been shown that both the presence of two $3s_{1/2}$ holes and the presence of the $1i_{13/2}$ particle induce an extra polarisation of the core. More generally, it can be concluded that the proton effective charge as a function of the neutron number depends on the number of valence protons. Theoretically, the polarisation of the core can be reproduced by explicitly taking into account the coupling of the valence protons to the vibrations of the underlying core.

The coupling of $Q_s(^{194,196}\text{Pb}(I^\pi = 11^-))$ and $Q_s(^{194,196}\text{Pb}(I^\pi = 12^+))$ to the quadrupole moments of the magnetic rotational bandheads ($I^\pi = 16^-$) in ^{194,196}Pb, results in $Q_s(^{196}\text{Pb}(I^\pi = 16^-)) = -0.316(97)$ b and $Q_s(^{194}\text{Pb}(I^\pi = 16^-)) = -0.46(12)$ b respectively. These small values confirm the concept of magnetic rotation. TAC calculations show that the coupling constant, χ, is different for protons and neutrons, contrary to what is often assumed.

In addition, the electric field gradient of Pb in Re has been determined as $V_{ZZ} = (-)2.42(27) \cdot 10^{21}$ V/m^2 for ^{196}Pb, and $(-)2.21^{+0.25}_{-0.22} \cdot 10^{21}$ V/m^2 for ^{194}Pb. These values are in perfect agreement with each other and fit in the systematics of the electric field gradient in Re as a function of the number of the atomic valence electrons. These results also proof experimentally the formalism for double perturbation fits as developed in section 2.2.

Chapter 4

Quadrupole moment of the 5-quasiparticle $I^\pi = K^\pi = 35/2^-$ isomer in ^{179}W

4.1 Introduction

In this chapter the experimental results derived from the measurement of the spectroscopic quadrupole moment of the 5 quasiparticle $K^\pi = 35/2^-$ isomer in ^{179}W are discussed. It addresses the question whether the deformation of the high-K multi-quasiparticle state is the same as the ground-state deformation. In order to extract the quadrupole moment of the ^{179}W($I^\pi = 35/2^-$) 5-quasiparticle state, the ^{179}W isomers were implanted in a Tl host lattice at a temperature of 473 K. The quadrupole interaction frequency, ν_Q, has been deduced by applying the LEMS technique. The electric field gradient (EFG) of W in Tl was not known before. Therefore, linear augmented plane wave (LAPW) calculations [Bla, Bla85] have been performed to calculate the EFG of W in Tl at 0 K. In order to derive the temperature dependence of the EFG a new technique, the inverted LEMS technique, has been applied.

4.2 Experimental details

4.2.1 Production and detection of the ^{179}W($K^\pi = I^\pi = 35/2^-$) isomer

The ^{179}W($K = \frac{35}{2}$) isomer was populated by the ^{170}Er(^{13}C,4n)^{179}W reaction at a beam energy of 63 MeV. A thin self-supporting, 98% enriched ^{170}Er 500μg/cm^2 target was used in the experiment. The target thickness was chosen to allow 90% of the ^{179}W nuclei to recoil out of the target. They were in-beam implanted into a thick Tl polycrystalline foil, which served as a LEMS host and as a beam stopper. The proton number Z of the host material needs to be higher than that of the target, in order to avoid background radiation originating from reactions in the host.

The ^{179}W($K^\pi = 35/2-$) isomer is a suitable case to study, because about 50% of the γ decay of the high-spin states, which are excited in heavy-ion fusion-evaporation reactions, goes through the isomer, which appears to decay predominantly to the $\nu[514]\frac{7}{2}^-$ ground-state band ([Wal94] and Figure 1.16). The prompt

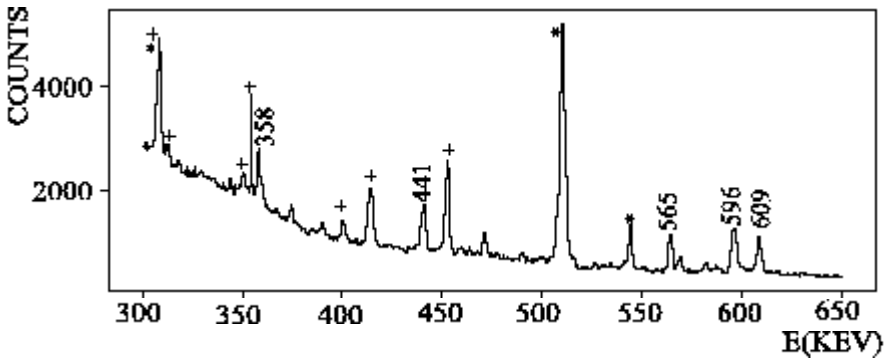

Figure 4.1: *Spectrum of delayed γ rays as obtained in the ^{170}Er(^{13}C, xn) reaction at 63 MeV. The 400 ns time gate begins 100 ns after the beam burst. The energies of the $K = \frac{35}{2}$ isomeric decay γ rays are indicated on the figure. Contaminating γ rays, originating either from β-decay or from other isomers, are indicated by asterisks or crosses respectively.*

background radiation was reduced with the help of the beam flipper (see section 2.3.3). It was tuned to provide a beam pulse every 500 ns. Several energy spectra of 1500 s were recorded for each value of the magnetic field. Dead-time corrections were made for the individual detectors. By accumulating ten spectra per magnetic field, the statistical uncertainties of the intensities of the gamma-rays of interest could be reduced below 3%. A sample spectrum which displays the delayed γ rays in ^{179}W is shown in Fig. 4.1.

4.2.2 Choice of Tl as a LEMS host

For the LEMS experiments on ^{179}W($I^\pi = K^\pi = 35/2^-$) a $_{81}$Tl host was chosen. Tl has a hexagonal structure (hcp) for temperatures below 503 K, and a cubic (bcc) lattice for temperatures above it [Wea71]. The use of Tl as a host has several advantages.

The quadrupole moment of the ^{179}W($I^\pi = 35/2^-$) isomer is expected to be large (order of 6 b [Wal94]) and, therefore, only a small EFG allows the saturation of the LEMS curve within the range of the existing magnet (4.4 Tesla). The lattice parameters ratio, c/a, of $_{81}$Tl ($c/a = 1.599$ at room temperature) is close to the value $\sqrt{8/3} = 1.633$ at which the first 12 neighbours of a lattice atom are positioned as in a fcc lattice. Therefore, a small EFG is expected. This is confirmed experimentally for several probe nuclei (see section 4.5.2). In addition, it is well known that, in the hcp phase, the EFG of Tl is strongly temperature dependent and decreases with temperature [Sch82]. By heating the host to $T = 473(1)$ K an even smaller EFG is ensured.

The heating of the host aims at two goals. Apart from reducing the EFG, it also allows to anneal the defects in the Tl host, possibly created during the in-beam implantation. The presence of defects would complicate the interpretation of the results. In this case not all the ^{179}W nuclei are interacting with the substitutional EFG, but also a fraction with a defect associated EFG [Har91c]. Each fraction corresponds with a different quadrupole interaction frequency. Tl has as an additional advantage that its melting temperature ($T_m = 576.7$ K [Wea71]) is

low. Therefore, the experiment could be performed at a temperature relatively close to the melting temperature, highly reducing the chance for defects (but increasing the chances for melting the Tl).

The phase transition from a hcp lattice structure to a bcc lattice structure at a temperature of 503 K is a useful feature of the Tl host as well. By heating up the Tl host to the cubic phase no reduction of the anisotropy of the γ radiation due to the quadrupole interaction occurs. The initial anisotropy is measured. This allows to test experimentally whether the LEMS curve is fully saturated.

4.3 Experimental results of the LEMS measurement on the $(I^\pi = 35/2^-)$ isomer in ^{179}W

In order to extract the quadrupole interaction frequency of the ^{179}W($I^\pi = 35/2^-$) isomer in Tl at a temperature of 473 K, the 358, 565 and 609 keV $E2$ transitions have been analysed (see Figure 1.16). In the previous chapter it has been illustrated how the instabilities of the beam influence the LEMS curve (Figure 3.3). There the problem could easily be solved by performing an extra normalisation by means of the prompt 158 keV γ ray transition. Due to the use of the beam flipper to clean the spectra from the prompt γ rays, the problem of an unstable beam is even a lot more pronounced in the ^{179}W experiments. This is illustrated by the middle panel in Figure 4.2. In this figure the ratio $N(0°)/N(90°)$ for the 204 keV transition, with $N(0°)$ the number of counts in the back detector and $N(90°)$ the number of counts in the side detector, is put as a function of the spectrum number (every 1500 s the spectra were saved and got a spectrum number), i.e., as a function of time. The 204 keV transition is originating from Coulomb-excitation on ^{205}Tl and hence prompt. The not gated spectra (also these spectra are taken with a pulsed beam, but no time gate was put and the data were recorded continuously in time) have been analysed. In the case of a stable beam, the ratio $N(0°)/N(90°)$ remains constant as a function of time, but, obviously, this is not the case here. Because the ^{179}W transitions have been analysed in the gated

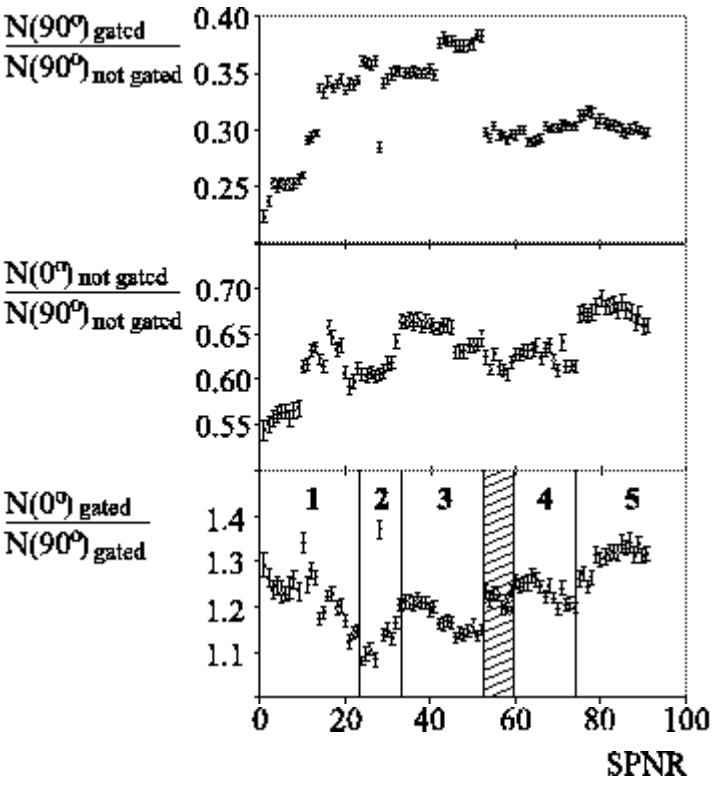

Figure 4.2: *Experimental results for the 204 keV peak, originating from Coulomb excitation in ^{205}Tl. Up: Number of counts in the spectra with a time gate divided by the number of counts in the spectra without a time gate for the side detector as a function of the spectrum number. Middle: Number of counts in the back detector divided by the number of counts in the side detector as a function of the spectrum number. The spectra without a time gate have been analysed. Down: Number of counts in the back detector divided by the number of counts in the side detector as a function of the spectrum number. The spectra with a time gate have been analysed. The five subgroups are indicated (see text). The data points in the shaded part have been disregarded.*

spectra, where the data have been recorded during the beam-off period only, an extra normalisation by means of a prompt γ ray transition is not straightforward. This is simply because the prompt γ rays are not present anymore in the spectra taken with a time gate, at the condition, of course, that the electronics providing the time gate is well tuned. Figure 3.1 illustrates this for the spectra that have

been taken in the experiments on ^{194,196}Pb in Re. However, if the beam flipper is not tuned perfectly, not only every 500 ns, but also in between, beam pulses can get partly through. As a result still some prompt γ radiation is present in the spectra. At the beginning of an experiment, typically 10 to 20% of the prompt γ ray intensity is present in the spectra. During the experiment this can further increase up to 30 to 40%, as shown in the upper panel of Figure 4.2. This has, however, the advantage that the peaks originating from Coulomb excitation in Tl (the 204 keV transition in ^{205}Tl and the 279 keV transition in ^{203}Tl) are also

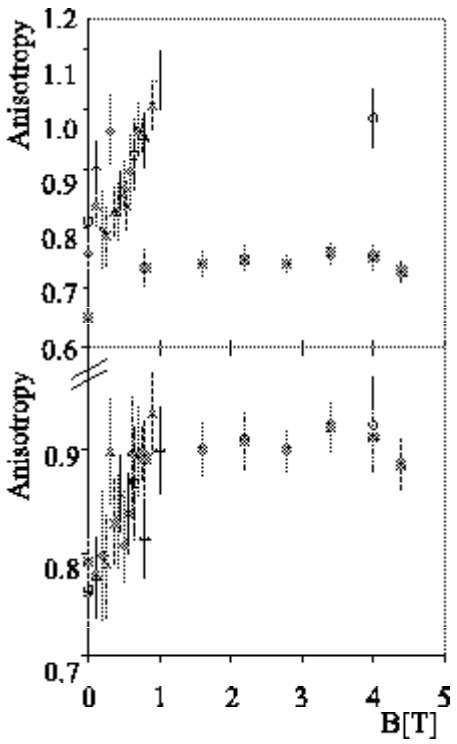

Figure 4.3: *$N(0°)/N(90°)$ for the 609 keV transition, depopulating the $^{179}W(K^\pi = 35/2^-)$ isomer, divided by $N(0°)/N(90°)$ for the 204 keV transition, originating from Coulomb excitation on ^{203}Tl. Up: The five subgroups are not renormalised with respect to each other. Down: The five subgroups are normalised with respect to each other. Data marked with the same symbol are part of the same subgroup. The data indicated by squares have been taken before a beam interruption.*

analysable in the spectra taken with a time gate. The analysis of the Coulex peaks provides a perfect means to monitor the behaviour of the beam during the experiment. The correction of the data for the beam fluctuations has been performed by the following procedure. First the ratios $N(0°)/N(90°)$ for the 358, 565 and 609 keV transitions have been divided by the ratios $N(0°)/N(90°)$ for the Coulex peaks. This eliminates the irregularities due to the movements of the beam spot, but not the irregularities due to the fact that at certain moments more prompt γ radiation comes in than at other moments. To correct for the latter unstabilities the data points have been subdivided in six groups. The subdivision is based on the down panel of Figure 4.2 and the notes in the logbook. One of the six groups has been disregarded, because it did not contain data points at both the low magnetic fields and the high magnetic fields. The five remaining groups have been renormalised with respect to each other (Figure 4.3). Six LEMS curves have been obtained this way and the results are listed in table 4.1. Sample LEMS curves are shown in Figure 4.4. By using the measured value $\mu = 8.31(8)\ \mu_N$ for the magnetic moment [Byr98, Dra00], the quadrupole interaction frequency of W in Tl has been derived as $\nu_Q = 53(8)$ MHz this way. In an earlier analysis, where no normalisation procedure was performed, the fit resulted in $\nu_Q = 66(8)$ MHz [Vyv99].

Table 4.1: *Experimental results of the LEMS measurement of the* $^{179}W(K^\pi = 35/2^-)$ *isomer in Tl. Averaging the 6 values for* ν_Q *results in* $\nu_Q = 53(8)$ *MHz.*

E_γ [keV]	normaliser [keV]	ν_Q [MHz]	σ/I	N
609	204	54(15)	0.48(2)	0.73(2)
	279	60(13)	0.52(2)	0.75(1)
565	204	48(18)	0.54(3)	0.75(3)
	279	47(14)	0.58(3)	0.76(2)
358	204	43^{+90}_{-25}	0.50(6)	0.73(4)
	279	83^{+50}_{-35}	0.54(3)	0.75(2)

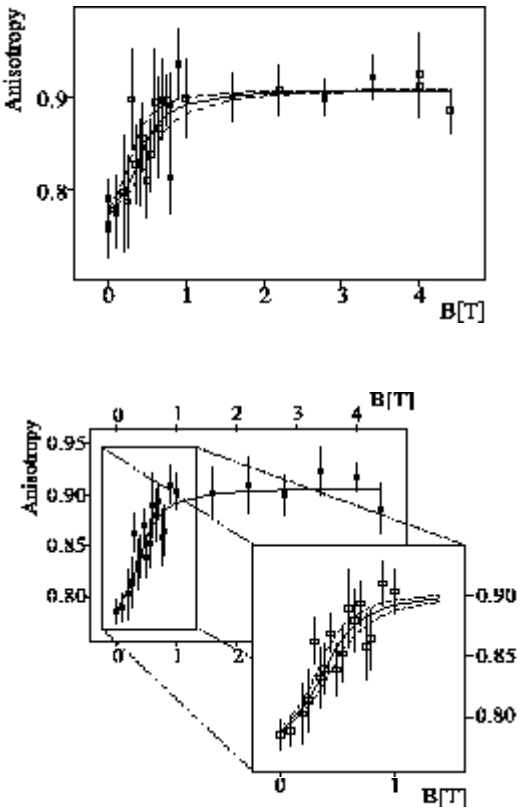

Figure 4.4: *Up: Sample LEMS curve for the 609 keV transition normalised on the 204 keV transition. The extracted frequency is* $\nu_Q = 54(15)$ *MHz. Down: LEMS curve obtained after averaging the different LEMS curves as mentioned in table 4.1. The extracted frequency is* $\nu_Q = 53(8)$ *MHz. The dashed lines correspond with the upper and lower values for the uncertainties of the quadrupole interaction frequency,* ν_Q.

4.4 The electric field gradient of W in Tl

In order to extract the quadrupole moment from the measured quadrupole interaction frequency, ν_Q, knowledge about the EFG is necessary. Also solid state physicists show particular interest in the study of the EFG, because of the sensitivity of that quantity to the exact charge state distribution in the metal [Sch82]. For a long time, electric field gradients in solids were estimated by a sum over two contributions: (i) a contribution due to the non-cubic arrangement of ions in the

lattice corrected by the Sternheimer antishielding factor for the influence of the quadrupole polarisation of the probe core electrons by charges which are further away and (ii) a contribution from the conduction electrons corrected for the interaction of the conduction electrons with the distorted ion cores [Wat65]. About 15 years ago, Blaha et al. [Bla85] developed a method to calculate EFGs in solids from first principles utilising the full-potential linearised-augmented-plane-wave LAPW bandstructure method. This method allows calculations of EFGs in simple solids without any assumptions of ionic charges or Sternheimer antishielding factors. Further development of the method and the increasing computer power nowadays allows calculated EFGs with remarkable precision [Bla]. The typical uncertainty is 10% [Duf95, Bla96, Trö93, Lan00]. However, all calculations are performed at 0 K, while the EFG is known to be temperature dependent. Therefore, experimental information at higher temperatures remains of great importance.

The EFG in a Tl lattice is of particular interest, because lattice-vibration models predict a strong temperature dependence due to the low Debye temperature (θ_D = 89 K) [Sch82]. In addition, the EFG in Tl is expected to be very sensitive to variations in the lattice constants, because of its c/a value being very close to the value $\sqrt{8/3} = 1.633$ at which the first 12 neighbours of a lattice atom are coordinated as in a fcc lattice. This results in a small EFG. Therefore, the EFG in Tl is a very good tool to test the model predictions for the EFG.

4.4.1 Ab initio calculation of the EFG of W in Tl at 0 K

In order to calculate the EFG of W in Tl at a temperature of 0 K, ab initio theoretical band-structure calculations based on density functional theory using the full-potential linearised augmented plane wave LAPW method as implemented in the WIEN97 package have been performed [Bla]. For a detailed description of these calculations the reader is referred to Refs. [Bla85, Sch92, Pet98].

In order to test the accuracy of the calculations, the EFG of Tl<u>Tl</u> was calculated first. Experimental values for the EFG of Tl in Tl are available at temper-

atures of 81 K, 200 K, 293 K and 410 K [Sch82]. Assuming that the $T^{3/2}$ law $V_{ZZ}(T) = V_{ZZ}(0\ \mathrm{K})(1 - bT^{3/2})$ [Chr76] for the temperature dependence of the EFG is valid, the factor $b = 7.0(11) \cdot 10^{-5}\ \mathrm{K}^{-3/2}$ was extracted. This yields an extrapolated value $|V_{zz}(\mathrm{Tl}\underline{Tl})| = 2.3(4) \cdot 10^{21}\ \mathrm{V/m^2}$ at 0 K. This value was nicely reproduced by the LAPW calculations, resulting in $V_{zz}(\mathrm{Tl}\underline{\mathrm{Tl}}) = -2.3 \cdot 10^{21}\ \mathrm{V/m^2}$ as well.

Next, the $_{74}$W impurity in hcp Tl was simulated by a 54 atom ($3 \times 3 \times 3$) supercell approach. This means that one supercell consists of 3 unit cells in the x-direction, 3 unit cells in the y-direction and 3 unit cells in the z-direction. In the case of a hcp lattice each unit cell contains 2 lattice atoms, so that one supercell consists of 54 lattice atoms in total. In the calculations 1 out of 54 lattice atoms is taken as a W impurity. Furthermore, full structural relaxation of three shells

Table 4.2: *Results for the LAPW calculations for W in Tl [Bla00].*

	Size supercell	Conditions	V_{ZZ} [10^{21} V/m^2]
(1)	16	not relaxed no spin-orbit	-5.8
(2)	16	relaxed no spin-orbit	-12.1
(3)	36	not fully relaxed no spin-orbit not fully converged	+2.7
(4)	36	fully relaxed no spin-orbit	+4.1
(5)	36	atoms in same lattice positions as in (4) spin-orbit	+3.16
(6)	54	fully relaxed no spin-orbit	+2.7
(7)	54	atoms in same lattice positions as in (6) spin-orbit	+2.7
(8)	54	fully relaxed spin-orbit	+2.54

of neighbouring atoms was allowed. This is necessary because of the difference in the atomic radii of W and Tl (the atomic radius is 1.41 Å for W and 1.71 Å for Tl). Due to this mismatch in atomic radii the Tl atoms in the neighbourhood of a W atom are not at exactly the same positions in the lattice as they would be without the presence of an impurity. The spin-orbit interaction was included in the calculation because of the heavy nuclei involved. The EFG was derived from the self-consistent charge density without further approximations, and a value of $V_{zz}(\underline{W}Tl) = 2.54 \cdot 10^{21}$ V/m^2 at 0 K was obtained with a typical uncertainty of 10% [Duf95, Bla96, Trö93, Lan00].

Table 4.2 shows the different results for the different steps in the calculations [Bla00]. Note that a 16-atom supercell ($2 \times 2 \times 2$) approach gives an EFG of $-5.8 \cdot 10^{21}$ V/m^2 if no relaxation is taken into account, while it results in an EFG of $-12.1 \cdot 10^{21}$ V/m^2 if relaxation is taken into account. This shows the importance of the supercell size and the resulting relaxations immediately. Obviously in smaller supercells the relaxation is more restricted [Bla00].

4.4.2 The inverted LEMS technique

Most commonly the $T^{3/2}$ law:

$$V_{ZZ} = V_{ZZ}(0\ \mathrm{K})(1 - bT^{3/2}) \tag{4.1}$$

is used to simulate the temperature dependence of the EFG in $s-p$ metals [Chr76]. Following this rule the temperature dependence of the EFG is determined by only one parameter b. b can be measured by applying the inverted LEMS technique.

The most straightforward way to measure the temperature dependence of an EFG is by measuring the quadrupole interaction frequency of the system at several temperatures. However, when the probe nucleus is a weakly produced isomeric state, the measurement of one such a quadrupole interaction frequency can take several days. The measurement of the quadrupole interaction frequency of the ^{179}W($I = K = 35/2$) isomer in Tl at 473 K, e.g., took about 10 days of beam time. Therefore, in order to save us a few months of beamtime, a new technique, the inverted level mixing spectroscopy technique, has been developed.

This technique allows the determination of the temperature dependence of the quadrupole interaction frequency in one additional experiment, in a measurement time comparable to the measurement time necessary to extract one quadrupole interaction frequency at one particular temperature.

The technique can be understood as follows. In a normal LEMS measurement the quadrupole interaction frequency is fixed because both the EFG and the quadrupole moment are fixed. The change of the anisotropy of the γ radiation as a function of an external magnetic field is measured (see section 2.1). By applying the inverted LEMS technique to measure the temperature dependence

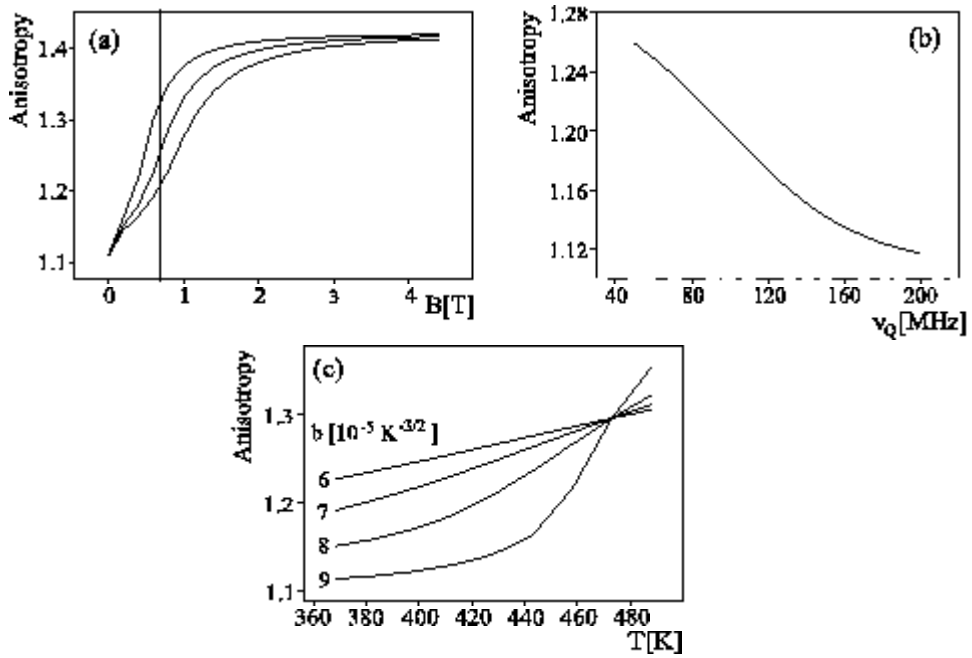

Figure 4.5: *Illustration of the inverted LEMS technique assuming a $T^{3/2}$ temperature dependence (4.1). (a) Sample LEMS curves for different quadrupole interaction frequencies ν_Q. The lowest curve corresponds with the largest frequency. (b) Sample curve for the anisotropy as a function of quadrupole interaction frequency at a fixed magnetic field. (c) Anisotropy as a function of temperature at a fixed external magnetic field. Low temperatures correspond with high quadrupole interaction frequencies ν_Q. The temperature dependence constants b are ranging from 6 to $9 \cdot 10^{-5}$ $K^{-3/2}$.*

of the EFG, the magnetic field is fixed and the quadrupole interaction frequency is varied by varying the temperature. The anisotropy of the γ radiation is measured as a function of temperature. For low temperatures the EFG and hence the quadrupole interaction frequency is high, such that it cannot be decoupled by the external magnetic field with as a consequence a lowering of the anisotropy of the γ radiation. For high temperatures the quadrupole interaction frequency is smaller and thus (more) decoupled by the external magnetic field. The anisotropy of the initial orientation is measured. In between there is a smooth transition from one regime to the other. As a result the anisotropy of the γ radiation as a function of the temperature is a raising curve as shown in Figure 4.5. Accepting the $T^{3/2}$ law, the slope depends only on the temperature dependence constant, b. The other fit parameters are the amount of initial orientation, σ/I, and a normalisation factor, N.

4.4.3 Experimental results of the inverted LEMS measurement on WTl

The experimental setup for an inverted LEMS experiment is the same as for a normal LEMS experiment (see section 4.2.1). Also the analysis is performed in a

Table 4.3: *Experimental results for the temperature dependence constant, b, of WTl.*

E_γ [keV]	normaliser [keV]	b [a] [10^5 K$^{-3/2}$]	σ/I	N	b [b] [10^5 K$^{-3/2}$]	N
609	204	$7.9^{+0.5}_{-1.5}$	0.55(8)	0.38(2)	$7.6^{+0.5}_{-1.0}$	0.374(3)
	279	$8.1^{+0.5}_{-1.0}$	0.55(8)	0.38(2)	$8.0^{+0.3}_{-0.7}$	0.376(3)
565	204	$7.3^{+1.0}_{-2.7}$	0.55(5)	0.38(1)	$7.3^{+0.3}_{-2.3}$	0.38(1)
	279	$7.7^{+0.7}_{-1.8}$	0.59(8)	0.39(2)	$7.6^{+0.6}_{-1.6}$	0.383(3)
358	204	$7.1^{+0.9}_{-1.2}$	0.48(6)	0.371(15)	$7.2^{+0.6}_{-1.1}$	0.376(3)
	279	$7.4^{+0.7}_{-1.2}$	0.50(5)	0.37(2)	$7.5^{+0.4}_{-0.7}$	0.377(3)

[a] *σ/I has been varied.*

[b] *σ/I has been kept fixed at $\sigma/I = 0.53$.*

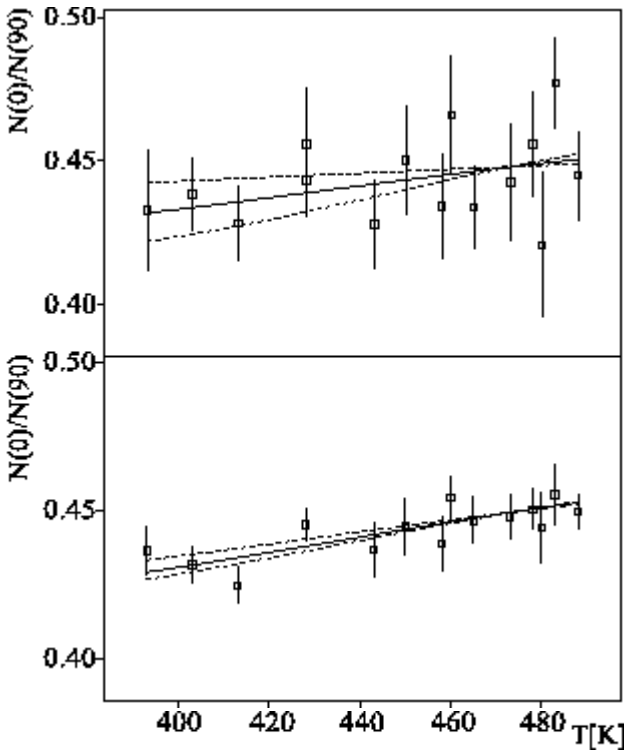

Figure 4.6: *Up: Sample inverted LEMS curve for the 565 keV transition normalised on the 204 keV transition. The extracted value is* $b = 7.3^{+0.8}_{-2.3} \cdot 10^{-5}\ K^{-3/2}$. *Down: inverted LEMS curve for the* $^{179}W(I^\pi = 35/2^-)$ *isomer implanted in a Ti polycrystal obtained after averaging the six inverted LEMS curves as mentioned in table 4.3. The solid line corresponds with* $b = 7.6^{+0.2}_{-0.1} \cdot 10^{-5}\ K^{-3/2}$. *The dashed lines correspond with the upper and lower values for the uncertainties of* b.

similar way as for the normal LEMS experiment (see section 4.3). The results are listed in table 4.3. The analysis has been performed in two different ways. Once the initial orientation, σ/I, was kept fixed at the same value as in the normal LEMS measurement. In the second analysis σ/I was a free fit parameter. In both analyses the temperature dependence constant, b, and the normalisation,

N, were taken as free fit parameters. The two ways of analysis resulted in the same value for b and a value of $b = 7.6^{+0.2}_{-0.4} \cdot 10^{-5}$ K$^{-3/2}$ has been extracted from the analysis in which σ/I has been kept fixed. This results in an EFG of $V_{ZZ}(\underline{\text{W}}\text{Tl}) = 0.55^{+0.12}_{-0.08} \cdot 10^{21}$ V/m^2 at a temperature of 473 K. The large statistical uncertainty on this value is due to the parabolic behaviour of the EFG, caused by the $T^{3/2}$ functional dependence. In addition, a theoretical uncertainty of 10% for the LAPW calculation is taken into consideration (see section 4.4.1). As a result, the spectroscopic quadrupole moment of the $K = 35/2$ isomer in ^{179}W is found to be $Q_s = 4.00^{+0.83}_{-1.06}$ b.

4.5 Discussion of the experimental results

4.5.1 The quadrupole moment of the $K^\pi = 35/2^-$ isomer in ^{179}W

Accepting that K is a good quantum number, the measured spectroscopic quadrupole moment, $Q_s = 4.00^{+0.83}_{-1.06}$ b, yields values of $Q_0 = 4.73^{+0.98}_{-1.25}$ b and $\beta = 0.185(^{+0.038}_{-0.049})$, by using the expressions (A.5) and $Q_0 = \frac{3}{\sqrt{5\pi}} ZR^2\beta$ (see (A.22)).

In the upper portion of Figure 4.7 [Bal01], the intrinsic quadrupole moment of the $K = 35/2$ isomeric state is compared to the ground-state quadrupole moments of the $_{74}$W nuclei, which have been extracted from the reduced transition probabilities $B(E2)\uparrow$, between the 0^+ ground-state and the first 2^+ state [Ram87] as described in appendix B.2. Also the Q_0 values, derived from the measured moments of the $K^\pi = 25^+$ isomer in ^{182}Os and the $K = 16$ isomer in ^{178}Hf, are added to the figure, as well as the ground-state moments for the $_{72}$Hf and $_{76}$Os nuclei. Note that the experimental data on the quadrupole moment of the $K = 25$ isomer in ^{182}Os have been reinterpreted. In Ref. [Bro91] the nuclear radius was taken equal to $r_0 = 1.1$ fm^2 in order to deduce the nuclear deformation. The authors concluded that their result for the isomeric state is in agreement with the ground-state deformation. To make a systematic comparison of the different available data possible, the nuclear radius has been taken equal to $r_0 = 1.2$ fm^2

throughout this work. The new interpretation leads to the conclusion that the measured value for the quadrupole moment of the $K = 25$ isomer in ^{182}Os, as well as the measured value for the quadrupole moment of the $K = 35/2$ isomer in ^{179}W, are significantly lower than the ground-state value. In the case of ^{178}Hf (as well as for ^{177}Lu with $Q_0 = 7.26(6)$ for the ground-state and $Q_0 = 7.33(6)$ for the isomeric state [Geo98]) the measured values for the quadrupole moments of the ground-state and the isomeric state are similar.

In addition, an independent value can be obtained for ^{179m}W by using the existing spectroscopic data for the rotational band which is built on the top of the $K = 35/2$ isomer. From the measured branching ratio of the cascade-to-crossover transitions in this band, $\lambda_b = 0.26(9)$, a value for $\mid (g_K - g_R)/Q_0 \mid = 0.045(11)$ b^{-1} was derived [Wal94] by using the relationship (B.24)

$$\left|\frac{g_K - g_R}{Q_0}\right| = 0.933 \frac{E_1}{\delta\sqrt{(I^2-1)}},$$

where the branching ratio λ_b is related to the mixing ratio δ by equation (B.22). Assuming that $g_R = 0.30(5)$, consistent with the systematics of the region [Stu95], and taking into consideration the measured magnetic moment of $\mu = 8.31(8)\mu_N$ for this state [Byr98, Dra00], a value $Q_0 = 3.9(1.5)$ b was found. These results demonstrate that the measured values for the quadrupole moments of the high-K isomers in ^{179}W and ^{182}Os, do not fit with the systematic trends, which were observed for the ground-state moments in the region [Ram87].

In the lower part of Figure 4.7 the systematic theoretical predictions for the ground-state deformations of the $_{74}$W nuclei [Ram89] are compared with the values obtained from $B(E2)\uparrow$ measurements, and with the deduced deformation of the $K = 35/2$ isomer in ^{179}W. Three approaches for the trend of the deformation as a function of the neutron number are indicated:

i. The solid line [Naz90] represents calculations where the shell correction approach as developed by Strutinsky is used ([Str67] and section 1.4.4). The average field is assumed to be of a deformed Woods-Saxon form. The monopole pairing force is taken as a short range residual interaction and the Lipkin-Nogami approach has been used to project out the correct particle number (see equation

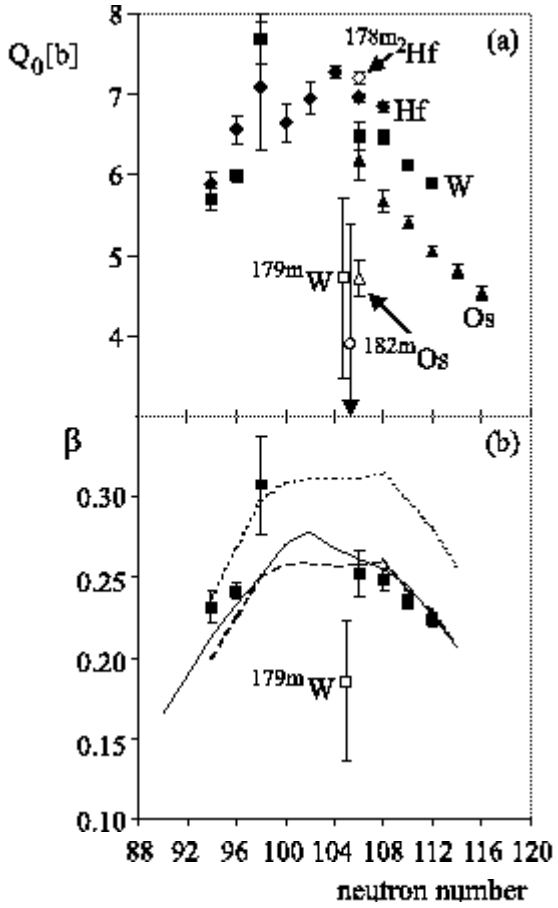

Figure 4.7: *(a) Systematics of the ground-state quadrupole moments for the $_{72}Hf$ (filled diamonds), $_{74}W$ (filled squares), and $_{76}Os$ (filled triangles) nuclei [Ram87], compared to the intrinsic quadrupole moments of the high-K isomers in ^{179}W (open square for this work and open circle for Ref. [Wal94]), ^{178}Hf (open diamond) [Boo94] and ^{182}Os (open triangle) [Bro91]. (b) The deduced quadrupole deformation of the $K = \frac{35}{2}$ isomer in ^{179}W (open square) is compared to the systematics of the ground-state deformations for the $_{74}W$ nuclei [Ram87], as well as with the hydrodynamic model of Bohr-Mottelson (dotted line) [Boh53c], the relation of Grodzins (dashed line) [Gro62], and the calculated ground-state deformations (solid line) [Naz90] (see text). The figure is taken from Ref. [Bal01].*

(1.44)). Both quadrupole and hexadecupole deformations were considered. The calculated values for the quadrupole deformation are mass deformations. The deformation, as derived from a measured quadrupole moment, is a charge deformation. It has been shown that for the Woods-Saxon potential [Dud84]

$$\beta_2^{charge} = 1.1\beta_2^{mass}. \tag{4.2}$$

Therefore, in order to compare the calculated values with the experimentally deduced charge deformations, the values as calculated by Nazarewicz et al. [Naz90] have been multiplied with 1.1 in Figure 4.7.

ii. Using the functional form derived by Bohr and Mottelson within the framework of the hydrodynamic model, all available life times τ (omitting those for closed-shell nuclei) can be fitted by [Boh53c]

$$\tau = (5.94 \pm 2.43) \cdot 10^{14} E_{2^+}^{-1} Z^{-2} A^{1/3}, \tag{4.3}$$

where E_{2^+} is the energy of the first excited 2+ state. As explained in appendix B.2, the nuclear life time is directly connected with the intrinsic quadrupole moment and, hence, with the nuclear deformation, which is represented by the dotted line in Figure 4.7.

iii. An alternative approach to reproduce the trend of the ground-state deformation as a function of the neutron number has been worked out by Grodzins [Gro62]. He found, empirically, that there is a strong correlation between the $B(E2)$ value of the first 2^+ state and its energy E_{2^+} [Gro62, Rin80]:

$$E_{2^+} B(E2, 2^+ \rightarrow 0^+) \simeq (25 \pm 8) \frac{Z^2}{A} \text{ MeV } e^2 \text{ fm}^4. \tag{4.4}$$

The relationship between the $B(E2)$ reduced transition probabilities and the intrinsic quadrupole moment can again be used to extract the nuclear deformation (see appendix B.2). These results are represented by the dashed line in Figure 4.7.

In addition, the spectroscopic quadrupole moment of the $K^\pi = 35/2^-$ isomer has been calculated by using the TAC code. It yields a value for the quadrupole moment of $Q_s = 5.73$ b if pairing is treated with the particle number projection

(PNP) technique [Alm] (which means that the wave function, as obtained from the TAC Hamiltonian, is not used as such to calculate the quadrupole moment, but only its component obtained after applying an extra projection on the correct particle number (see, e.g., in Ref. [Rin80])). The calculations without applying the PNP technique result in $Q_s = 5.84$ b (the neutron pairing is zero in this case). These values of the quadrupole moment correspond to an axially symmetric nucleus with deformations $\epsilon_2 = 0.228$ and $\epsilon_4 = 0.038$, which coincide with the calculated ground-state deformations for ^{179}W: $\epsilon_2 = 0.226$ and $\epsilon_4 = 0.039$ and contradict the measured quadrupole moment for the isomer. The calculations show that Coriolis-mixing (see section 1.2.1) is not responsible for the low value of the quadrupole moment.

Independent Total Routhian Surface calculations [Xu98] give also very similar deformations for the ground state and high-K bands in ^{178}W.

Summarising, the experimental values for the $K^\pi = 35/2^-$ isomer in ^{179}W are about 2σ off all theoretical estimates. This is also the case for the six quasiparticle isomer in ^{182}Os. However, the low value of the spectroscopic quadrupole moment of the ^{182}Os($K^\pi = 25^+$) isomer could be understood as due to triaxiality of the nuclear mean field [Xu98], while in the case of the 35/2 five quasiparticle isomer in ^{179}W a consistent explanation is still missing. A possible explanation might be related to the fact that in order to create a multi-quasiparticle high-K state a few particles need to be excited to high-Ω orbits, which are localised close to the equatorial plane of the nucleus. This changes the nuclear mass distribution and influences the symmetries of the mean-field. A configuration dependence in this case cannot be excluded. Similar effects have been discussed for the nuclei in the Mg-region [Röp00]. In any case, we can conclude that the deformation of a high-K isomeric state can deviate substantially from the ground-state deformation, contrary to what is usually assumed.

4.5.2 The electric field gradient of W in Tl

Table 4.4 shows the EFG at 0 K and the temperature dependence constant, b, for several probes in Tl. For all impurities, except from W, the values V_{ZZ}(0 K) and b have been derived by measuring the quadrupole interaction frequencies at different temperatures and fitting the experimental data by means of the

Table 4.4: *V_{ZZ}(0 K) and the temperature dependence constant, b, for several probes in Tl assuming the $T^{3/2}$ temperature dependence for the EFG.*

probe	Z	I^π(isomer)	Q_s [b]	ν_Q(0 K) [MHz]	V_{ZZ}(0 K) [10^{21} V/m^2]	b [10^{-5} K$^{-3/2}$]	Reference
^{69}Ge	32	$9/2^+$	1.0(2)	8.61(3)	0.35(7)	4.85(5)	[Sem81], [Sch88]
^{111}Cd	48	$5/2^+$	0.77(12)	10.9(1)	0.58(9)	5.9(2)	[Hen79]
^{179}W	74	$35/2^-$	$4.00^{+0.83}_{-1.06}$		2.54[a]	$7.6^{+0.2}_{-0.4}$	this work
^{192}Tl	81	8^-	0.44(7)	24.0(15)	2.3(4)	7.0(11)	[Sch82]
^{204}Pb	82	4^+	0.45(3)	16.6(1)	1.5(1)	4.74(4)	[Iva92]
^{202}Bi	83	10^-	0.12(2)	3.2(8)	1.1(2)	6.2(8)	[Sch91]

[a] *Calculated value*

Table 4.5: *V_{ZZ}(0 K) and the temperature dependence constant, c, for several probes in Tl assuming a linear temperature dependence for the EFG. The values for ν_Q(0 K) and c are determined from a fit through the data taken from the cited reference.*

probe	Z	I^π(isomer)	Q_s [b]	ν_Q(0 K) [MHz]	V_{ZZ}(0 K) [10^{21} V/m^2]	c [10^{-3} K^{-1}]	Reference
^{69}Ge	32	$9/2^+$	1.0(2)	10.12(5)	0.42(8)	1.21(1)	[Sem81], [Sch88]
^{111}Cd	48	$5/2^+$	0.77(12)	11.65(15)	0.63(10)	1.16(6)	[Hen79]
^{179}W	74	$35/2^-$	$5.4^{+1.3}_{-1.5}$		2.54[a]	$1.778^{+0.053}_{-0.081}$	this work
^{192}Tl	81	8^-	0.44(7)	27.4(19)	2.6(4)	1.51(23)	[Sch82]
^{204}Pb	82	4^+	0.45(3)	18.5(1)	1.7(1)	1.13(1)	[Iva92]
^{202}Bi	83	10^-	0.12(2)	3.2(8)	1.1(2)	1.4(2)	[Sch91]

[a] *Calculated value*

expression

$$\nu_Q(T) = \nu_Q(0\ \mathrm{K})(1 - bT^{3/2}), \tag{4.5}$$

in which $\nu_Q(0\ \mathrm{K})$ and b were taken as free fit parameters. In order to extract the EFG from the quadrupole interaction frequencies, ν_Q, measured quadrupole moments were used. As expected from the c/a ratio, being close to the value $\sqrt{8/3}$=1.633, at which the EFG is close to zero, the EFG is small for all probes in Tl. Furthermore, the temperature dependence of the EFG in Tl is strong for all probe nuclei, as predicted by the low Debye temperature ($\theta_D = 89$ K). The b value for W is somewhat large compared to the other b values. Note, however, that because of possible systematic errors due to beam fluctuations, the value $b = 7.6^{+0.2}_{-0.4} \cdot 10^{-5}\ \mathrm{K}^{-3/2}$ should rather be considered as an upper limit for b (see section 4.4.3). Lower values for b correspond with larger values for V_{ZZ} and, hence, lower values for the spectroscopic quadrupole moment Q_s.

It is worthwhile to mention that in Ref. [Iva92] a linear temperature dependence

$$V_{ZZ}(T) = V_{ZZ}(0\ \mathrm{K})(1 - cT) \tag{4.6}$$

for the EFG of ^{204}Pb in Tl is claimed. Figure 4.8 shows a systematic study of the existing data for the EFG as a function of temperature for several probe nuclei in Tl. The data are fitted twice, once assuming a linear temperature dependence and once assuming a $T^{3/2}$ temperature dependence. It shows that a linear temperature dependence cannot be excluded. Table 4.5 lists the values for c and $V_{ZZ}(0\ \mathrm{K})$ if a linear temperature dependence for the EFG is assumed. The difference in χ^2 between a $T^{3/2}$ fit and a linear temperature dependence fit of the data, obtained from the inverted LEMS experiment, is typically about 0.5% for the different transitions, indicating that our data do not allow to distinguish between the exponents 3/2 and 1. In the case a linear fit of the data, we get the values $c = 1.778^{+0.053}_{-0.081} \cdot 10^{-3}\ \mathrm{K}^{-1}$, $V_{ZZ}(473\ \mathrm{K}) = 0.404^{+0.097}_{-0.075} \cdot 10^{21}\ \mathrm{V/m}^2$, $Q_s(^{179}\mathrm{W}(K^\pi = 35/2^-)) = 5.4^{+1.3}_{-1.5}$ b, $Q_0(^{179}\mathrm{W}(K^\pi = 35/2^-)) = 6.4^{+1.5}_{-1.8}$ b and $\beta = 0.250^{+0.059}_{-0.070}$. In other words, the values for the quadrupole moment and the deformation derived

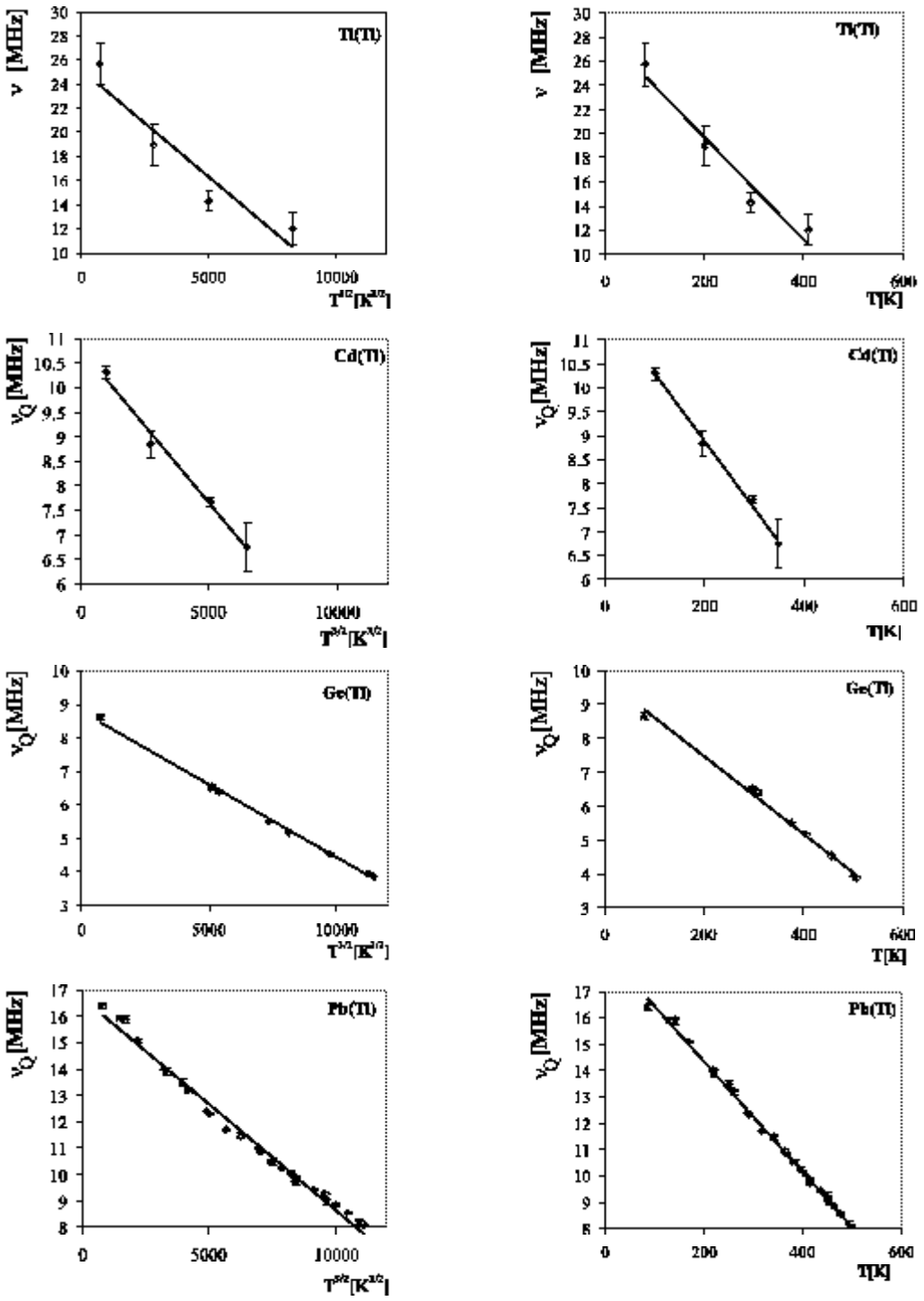

Figure 4.8: *Quadrupole interaction frequency ν_Q as a function of $T^{3/2}$ (left) and T (right) for Tl in Tl, Cd in Tl, Ge in Tl and Pb in Tl. The data are taken from Refs. [Sch82, Heu79, Sem81, Iva92].*

this way are in agreement with the theoretical predictions (Figure 4.7). This, however, would mean that Tl is the first $s-p$ metal where the commonly accepted $T^{3/2}$ law is not followed. Furthermore, the value for Q_0 as deduced from the existing spectroscopic data for the $K^\pi = 35/2^-$ rotational band yields $Q_0 = 3.9(1.5)$ b (see section 4.5.1). The latter value is in better agreement with the value for the quadrupole moment, $Q_0 = 4.73^{+0.98}_{-1.25}$ b, as found by assuming the $T^{3/2}$ law for the temperature dependence of W in Tl.

4.6 Conclusions and outlook

In this chapter we have derived the spectroscopic quadrupole moment of the high-K 5-quasiparticle isomer ($K^\pi = 35/2^-, T_{1/2} = 750(80)$ ns) in ^{179}W. A value $Q_s = 4.00^{+0.83}_{-1.06}$ b is found, which corresponds to an intrinsic quadrupole moment $Q_0 = 4.73^{+0.98}_{-1.25}$ b and to a quadrupole deformation $\beta = 0.185^{+0.038}_{-0.049}$. These values differ significantly from the deduced ground-state quadrupole moments and are in disagreement with the current theoretical predictions in this mass region.

Note that in practice not the spectroscopic quadrupole moment itself, but the quadrupole interaction frequency of the ^{179}W($K^\pi = 35/2^-$) isomer in Tl at $T = 473$ K has been measured as $\nu_Q = 53(8)$ MHz. The EFG has been calculated at 0 K as $2.54 \cdot 10^{21}$ V/m^2 [Bla00]. Accepting the $T^{3/2}$ law, the temperature dependence constant, b, has been determined as $b = 7.6^{+0.2}_{-0.1} \cdot 10^{-5}$ K$^{-3/2}$ by applying the inverted LEMS technique for the first time.

The conclusion for the quadrupole moment is based on the assumption that the $T^{3/2}$ law for the temperature dependence of the EFG is valid. However, experimental data on the EFG of ^{204}Pb in Tl indicate that a linear temperature dependence for the EFG in Tl might be possible [Iva92]. If, unexpectedly, the temperature dependence of the EFG of W in Tl shows a linear behaviour the extracted value for the spectroscopic quadrupole moment is $Q_s(^{179}\mathrm{W}(K^\pi = 35/2^-)) = 5.4^{+1.3}_{-1.5}$ b. This results in an intrinsic quadrupole moment $Q_0(^{179}\mathrm{W}(K^\pi = 35/2^-)) = 6.4^{+1.5}_{-1.8}$ b and a deformation $\beta = 0.250^{+0.059}_{-0.070}$. These values are in agreement with the theoretical predictions, but somewhat high compared to an independent ex-

perimental value, $Q_0 = 3.9(1.5)$ b, derived from the spectroscopic data for the $K^\pi = 35/2^-$ rotational band [Wal94] in combination with the measured g factor [Byr98, Dra00].

The obtained results show that a direct measurement of the EFG of W in Tl and its temperature dependence is of uttermost importance from both nuclear physics and solid state physics point of view. Therefore, we hope to perform such an experiment in the near future.

Chapter 5

Conclusions and outlook

In this work, the experimental results of the quadrupole moment measurements performed on the $(I^\pi = 11^-)$ isomers in ^{194,196}Pb and the $(I^\pi = 35/2^-)$ isomer in ^{179}W have been extensively discussed. Whereas the $_{82}$Pb nuclei have a magic proton number, the $^{179}_{74}$W nucleus has a proton and neutron number that are far away from the closed shells. Throughout the nuclear map the deformation plays a crucial role for the understanding of the nuclear properties. Therefore, measured quadrupole moments, which are related to the deformation of the nucleus, provide a stringent test for the nuclear models, as has been shown in this thesis.

The ^{196}Pb$(I^\pi = 11^-)$ isomer has the $(\pi 3s_{1/2}^{-2} 1h_{9/2} 1i_{13/2})$ intruder configuration. Its quadrupole moment has been measured as $Q_s = (-)3.41(66)$ b. A comparison with the quadrupole moment of the corresponding normal $(\pi 1h_{9/2} 1i_{13/2})$ state in ^{198}Po, $Q_s^{emp} = (-)2.06(31)$ b, shows that the presence of the two $3s_{1/2}$ holes drives the isomeric states towards larger deformations. Furthermore, a comparison with the quadrupole moments of the $(\pi 1h_{9/2})$ ground-state in ^{197}Bi and the $(\pi 3s_{1/2}^{-2} 1h_{9/2})$ isomeric state in ^{195}Tl reveals that the presence of the $i_{13/2}$ valence particle, in addition to the $1h_{9/2}$ valence particle, induces an extra polarisation of the underlying nuclear core. Intuitively, this can be understood from the fact that 11^- isomers in Pb and Po contain 2 valence nucleons in nearly parallel orbitals, compared to 1 valence nucleon for the $9/2^-$ states in ^{197}Bi and ^{195}Tl. This conclusion can be extended towards more valence nucleons: if more

valence nucleons are present in more or less parallel orbitals the nuclear core is more polarised, resulting in larger proton effective charges.

Note that the quadrupole moments of the ^{198}Po($I^\pi = 11^-$) isomer, the ^{195}Tl($I^\pi = 9/2^-$) isomer and the ^{197}Bi($I^\pi = 9/2^-$) ground-state have not been measured yet. The value for the quadrupole moment of the ^{195}Tl($I^\pi = 9/2^-$) isomer has been extrapolated from the trend of the quadrupole moments of the $^{189-193}$Tl($I^\pi = 9/2^-$) chain. The values for the quadrupole moments of the ^{198}Po($I^\pi = 11^-$) and the ^{197}Bi($I^\pi = 9/2^-$) states have been extracted from the measured quadrupole moments of the corresponding $N = 126$ isotopes, taking into account a proton effective charge. The latter has been taken equal to the proton effective charge of the 8^+ isomers in the ^{A}Po chain. To check the validity of this assumption measured quadrupole moments are necessary. Recently, a project has been started to extract the quadrupole moment of the 11^- isomers in ^{A}Po chain. Also the $9/2^-$ isomer in ^{195}Tl seems to be a good candidate for a future experiment. Unfortunately, the $9/2^-$ state in Bi is the ground-state and LEMS is not suitable to measure quadrupole moments of ground-states.

The ratios of the quadrupole moments of the 11^- and the $9/2^-$ states can be reproduced by shell model calculations, taking into account the coupling of the valence protons to the vibrations of the underlying core (a Hg-core for the ^{195}Tl($I^\pi = 9/2^-$) and the ^{196}Pb($I^\pi = 11^-$) isomers and a Pb-core for the ^{197}Bi($I^\pi = 9/2^-$) ground-state and the ^{198}Po($I^\pi = 11^-$) isomeric state). Only quadrupole vibrations were considered. This means that, despite the fact that the calculations do not reproduce the absolute values of the quadrupole moments, they do predict the correct trend and, hence, take into account correctly the polarisation of the core. Unfortunately, experimentally deduced quadrupole moments are lacking for a systematic comparison between the theoretically and experimentally deduced values. Only for a few ^{A}Hg and ^{A}Pb isotopes the quadrupole moments of the first excited 2^+ states have been extracted, restricting the range of the calculated quadrupole moments to $^{200-206}$Pb($I^\pi = 11^-$), $^{199-205}$Tl($I^\pi = 9/2^-$), $^{206-210}$Po($I^\pi = 11^-$) and $^{205-209}$Bi($I^\pi = 9/2^-$). Only for ^{210}Po($I^\pi = 11^-$) and ^{207,209}Bi($I^\pi = 9/2^-$) the quadrupole moments have been measured. A comparison shows that for both the

^{210}Po($I^\pi = 11^-$) isomer and ^{209}Bi($I^\pi = 9/2^-$) ground-state ($N = 126$) the calculated value for the quadrupole moment is too high, while for the ^{207}Bi($I^\pi = 9/2^-$) ground-state ($N = 124$) the calculated and the experimental value agree. The question arises whether for lower neutron numbers $N < 124$ the measured and the calculated quadrupole moments will continue to agree, or whether the calculated moments will be lower than the experimental values. Therefore, more quadrupole moment measurements are necessary. Also a systematic theoretical study of the region, taking into account octupole vibrations as well is currently being made. The first results with $Q_s(^{196}\text{Pb}(I^\pi = 11^-)) = -3.54$ b and $Q_s(^{198}\text{Po}(I^\pi = 11^-)) = -1.4$ b are promising [Oro01].

The measurement of the quadrupole moments of the 11^- isomer in ^{196}Pb is also particularly interesting, because it has the same $(\pi s_{1/2}^{-2} h_{9/2} i_{13/2})$ configuration as a shears bandhead. Coupling the quadrupole moment of the 11^- isomer with the measured quadrupole moment of the 12^+ isomer in ^{196}Pb, which has the same proton configuration as the shears bandhead, the quadrupole moment of the shears bandhead could be extracted as $Q_s(^{196}\text{Pb}(I^\pi = 16^-)) = -0.316(97)$ b. This small value shows that magnetic rotation is the only way to explain the rotational band built on the 16^- state. TAC calculations for the shears bandhead reveal that the quadrupole coupling constant, χ, is not the same for protons and neutrons, contrary to what is usually assumed [Chm].

In the experiments on the 11^- isomer in ^{196}Pb also the ^{194}Pb($I^\pi = 11^-$) isomer has been produced. Besides the ($I^\pi = 11^-$) shape isomer, the ^{194,196}Pb isomers contain the ($I^\pi = 12^+$) spin trap as well. By analysing the transitions below the $11^- \rightarrow 12^+$ cascade the quadrupole moment of the 11^- isomer in ^{194}Pb could be extracted as $Q_s = (-)4.12(79)$ b. This was the first experimental application of the LEMS technique, including perturbations of a sequence of 2 isomers. It is experimentally proven that this is a valuable extension of the LEMS technique. This has been done by comparing the EFG of Pb in Re, as extracted from the double perturbation fit of the $11^- \rightarrow 12^+$ cascade in ^{194}Pb by the EFG of Pb in Re, as extracted from the LEMS analysis of the 12^+ isomer in ^{196}Pb. Values of $V_{ZZ} = (-)2.21^{+0.25}_{-0.22} \cdot 10^{21}$ V/m^2 and $V_{ZZ} = (-)2.42(27) \cdot 10^{21}$ V/m^2 have been

derived for ^{194}Pb and ^{196}Pb, respectively, being in perfect agreement with each other and fitting well in the systematics of the EFGs in Re.

In another series of experiments the quadrupole moment of the high-K 5-quasiparticle isomer ($K^\pi = 35/2^-$) isomer in ^{179}W has been measured as $Q_s = 4.00^{+0.83}_{-1.06}$ b. This corresponds to an intrinsic quadrupole moment $Q_0 = 4.73^{+0.98}_{-1.25}$ b and to a quadrupole deformation $\beta = 0.185^{+0.038}_{-0.049}$. These values differ considerably from the deduced ground-state quadrupole moments and are in disagreement with the current theoretical predictions in this mass-region. TAC calculations yield a value of $Q_s = 5.73$ b, if pairing is treated with particle number projection and $Q_s = 5.84$ b if pairing is treated without it. Only one other case is known where the quadrupole moment of the high-K isomeric state is deviating from the quadrupole moment of the ground-state, namely, the quadrupole moment of the $K^\pi = 25^+$ isomer in ^{182}Os [Bro91]. There, the discrepancy has been explained as due to γ deformation of the nucleus [Xu98] whereas for the $K^\pi = 35/2^-$ isomer in ^{179}W a consistent explanation is still missing.

It is important to note, however, that not the spectroscopic quadrupole moment itself, but the quadrupole interaction frequency, ν_Q, is measured. In order to extract the spectroscopic quadrupole moment, the EFG needs to be known. The ^{179}W nuclei were implanted in a Tl host lattice at temperature of 473 K. In order to extract the EFG of W in Tl linear augmented plane wave calculations have been performed. They resulted in $V_{ZZ}(0\text{ K}) = 2.54 \cdot 10^{21}$ V/m^2 [Bla00]. In order to extract the EFG at 473 K an inverted LEMS experiment has been performed. It was the first time that the technique has been applied. Assuming that the $T^{3/2}$ law for the temperature dependence of the EFG is valid a temperature dependence constant $b = 7.6^{+0.2}_{-0.4} \cdot 10^{-5}$ K$^{-3/2}$ has been extracted. However, experimental data on the EFG of ^{204}Pb in Tl reveal that a linear temperature dependence for the EFG in Tl cannot be excluded [Iva92]. This would mean that Tl is the first $s-p$ metal where the $T^{3/2}$ law is not valid. Assuming a linear temperature dependence of the EFG, the fits result in a temperature dependence constant $c = 1.778^{+0.053}_{-0.081} \cdot 10^{-3}$ K^{-1} and $V_{ZZ}(473\text{ K}) = 0.404^{+0.097}_{-0.075} \cdot 10^{21}$ V/m^2. The extracted value for the spectroscopic quadrupole moment is then,

$Q_s(^{179}\mathrm{W}(I^\pi = 35/2^-)) = 5.4^{+1.3}_{-1.5}$ b, corresponding with an intrinsic quadrupole moment of $Q_0 = 6.4^{+1.5}_{-1.8}$ b and a quadrupole deformation of $\beta = 0.250^{+0.059}_{-0.070}$. These values are in agreement with the theoretical predictions. They are, however, somewhat higher than an independent experimental value for the intrinsic quadrupole moment, derived from the spectroscopic data for the rotational band which is built on the $K^\pi = 35/2^-$ isomer [Wal94]. This data in combination with the measured g factor [Byr98, Dra00] result in $Q_0 = 3.9(1.5)$ b. The obtained results show that a direct measurement of the EFG of W in Tl and its temperature dependence is extremely important from both nuclear physics and solid state physics points of view. Therefore, such an experiment is planned in the near future.

The general conclusion of this thesis might be that the nuclear models which have been highlighted, i.e., the shell model and the TAC model, account well for the nuclear features from the qualitative point of view. Shell model calculations, taking into account the particle-core coupling with the underlying core, are able to reproduce the ratios of the quadrupole moments of interest. The quadrupole moment of the 16^- state in ^{196}Pb is indeed small, proving the concept of magnetic rotation, which is one of the major achievements of the TAC model. From the quantitative point of view some improvements are still possible. As mentioned before, the influence of octupole vibrations on the quadrupole moments of the states of interest in the Pb region is currently being investigated. The coupling constant, χ, is not always the same for protons and neutrons in the TAC model. None of the currently available models seems to be able to explain the low value for the quadrupole moment of the $35/2^-$ isomer in ^{179}W at this point.

Appendix A

Deformation parameters and quadrupole moments - definitions

The nuclear deformation plays a crucial role throughout this whole thesis. However, in the literature different deformation parameters are used and sometimes different quantities are represented by the same symbol. Therefore, it seems to be necessary to summarise the relations and definitions of the most frequently used deformation parameters. Also the definitions of the electric quadrupole moment are reviewed. The formulae are taken from [Löb70],[deS74] and [Nil55], although sometimes notations are changed to be consistent with the notations of the rest of this text.

A.1 Intrinsic versus spectroscopic quadrupole moment

Classically the electric quadrupole moment is defined as

$$eQ_{el} = \sqrt{\frac{16\pi}{5}} \int r^2 Y_2^0(\theta) \rho(\vec{r}) dV. \tag{A.1}$$

Quantum mechanically a distinction between the intrinsic and the spectroscopic quadrupole moment needs to be made. The intrinsic quadrupole moment, Q_0, of a nuclear state is given by the expectation value of the electric quadrupole moment

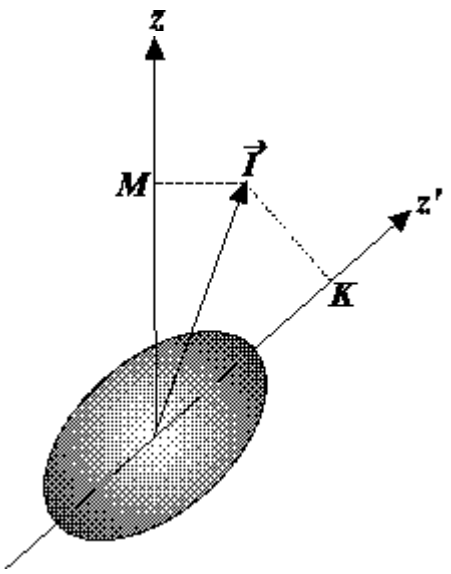

Figure A.1: *Definition of the intrinsic and the laboratory axis system. The z'-axis of the intrinsic axis system is oriented parallel to the symmetry axis of the nucleus, the z-axis of the laboratory system has an arbitrary orientation.*

tensor component $\hat{Q}_2^0$ defined relative to the intrinsic coordinate system. For an axially symmetric nucleus, the intrinsic coordinate system is the axis system with the z'-axis parallel to the symmetry axis of the nucleus (Figure A.1). We get:

$$eQ_0 = e\langle IK \mid \hat{Q}_2^0 \mid IK \rangle \tag{A.2}$$

in which

$$\hat{Q}_2^0 = \sqrt{\frac{16\pi}{5}} \sum_i r_i'^2 Y_2^0(\theta_i', \phi_i'). \tag{A.3}$$

K denotes the z'-component of the angular momentum in the intrinsic system. Q_0 is the quadrupole moment that would be measured in the intrinsic coordinate system if such a measurement were possible. The spectroscopic quadrupole moment, Q_s, is given by the expectation value of the quadrupole moment operator $\hat{Q}_2^0$ in the laboratory system (see Figure A.1). For a nuclear state with spin I and M as the z-component of the spin in the laboratory system, it is defined as

$$eQ_s = e\langle IM \mid \hat{Q}_2^0 \mid IM \rangle_{M=I}. \tag{A.4}$$

$M = I$ indicates that the expectation value is calculated for the nuclear states whose magnetic quantum number $M = I$. This corresponds to the maximum observable spectroscopic quadrupole moment.

The relation between the intrinsic and the spectroscopic quadrupole moment is obtained by transforming the quadrupole moment operator $\hat{Q}_2^0$ relative to the laboratory system into the quadrupole moment operator relative to the intrinsic coordinate system of the nucleus. For K being a good quantum number and $K > 1$ this results in

$$Q_s = Q_0 \frac{3K^2 - I(I+1)}{(I+1)(2I+3)}. \tag{A.5}$$

If a constant charge distribution within the nucleus is assumed then the intrinsic quadrupole moment determines the basic features of the nuclear shape:

$Q_0 = 0$ spherical nuclei;

$Q_0 > 0$ prolate nuclei (shaped like a cigar);

$Q_0 < 0$ oblate nuclei (shaped like a disk).

A.2 The deformation of atomic nuclei

In general the nuclear radius of a deformed nucleus is described by [Rin80]

$$R(\theta, \phi) = R_{av}[1 + \sum_{\lambda=0}^{\infty} \sum_{\mu=-\lambda}^{\lambda} \alpha_\lambda^\mu Y_\lambda^\mu(\theta, \phi)] \tag{A.6}$$

where R_{av} is the radius of a sphere with the same volume, usually taken equal to $r_0 A^{1/3}$ with $r_0 = 1.2$ fm and A the mass number of the nucleus. The constant α_0^0 describes changes of the nuclear volume. Since it is known that in a first approximation the nuclear matter is incompressible, it is required that the volume is kept fixed for all deformations as

$$V = \frac{4}{3}\pi R_{av}^3. \tag{A.7}$$

The term $\lambda = 1$ is normally excluded as it describes only a translation of the nucleus as a whole.

Axially symmetric nuclei are ϕ independent if the z'-axis is chosen parallel to the symmetry axis of the nucleus. Therefore, only the $\alpha_\lambda^{\mu=0}$ are different from 0 for axial symmetry. Usually the deformation parameters α_λ^0 are called β_λ. The quadrupole deformation β_2 is the most important one, although also higher order axially symmetric effects have been observed in nuclei, such as hexadecupole deformations quantified by β_4.

In the case of quadrupole deformations five parameters α_λ^μ need to be considered. Two of them describe the shape of the nucleus and three of them correspond to the three Euler angles and determine only the orientation of the nucleus in space. By a suitable rotation to the body-fixed system the five coefficients α_λ^μ reduce to two real independent variables a_2^0 and $a_2^2 = a_2^{-2}$ ($a_2^1 = a_2^{-1} = 0$). Together with the three Euler angles, this gives a complete description of the system. Instead of a_2^0 and a_2^2 it is more convenient to use the coordinates β_2 and γ defined by

$$a_2^0 = \beta_2 \cos\gamma \qquad \text{and} \qquad a_2^2 = a_2^{-2} = \frac{1}{\sqrt{2}}\beta_2 \sin\gamma. \tag{A.8}$$

γ is measured in degrees where $\gamma = 0°$ and $\gamma = 60°$ correspond to prolate and oblate shapes, respectively. Completely triaxial shapes have $\gamma = +/-30°$.

In the following paragraphs only axial quadrupole deformations are considered. Higher multipoles are neglected. Two different shapes of prolate deformed nuclei with constant charge distributions are treated in the literature: the 'rotational ellipsoid' and the 'quadrupoloid'. A rotational ellipsoid is specified by the length of the semiaxis c parallel to the z'-axis (intrinsic coordinate system) and the semiaxis a perpendicular to the z'-direction. The intrinsic quadrupole moment Q_0 of a rotational ellipsoid is given by:

$$Q_0 = \frac{2}{5}Z(c^2 - a^2). \tag{A.9}$$

A quadrupoloid is defined by

$$R = R_0(1 + \alpha_0^0 Y_0^0 + \alpha_2^0 Y_2^0) \tag{A.10}$$

$$= R_0(1 + \alpha_0^0 Y_0^0 + \beta Y_2^0). \tag{A.11}$$

If the $\alpha_0^0 Y_0^0$ term is omitted the deformation parameter β' is obtained:

$$R = R_0'(1 + \beta' Y_2^0). \tag{A.12}$$

The difference between the rotational ellipsoid and the quadrupoloid (A.10) is seen by expanding the shape of a prolate rotational ellipsoid in spherical harmonics:

$$\begin{aligned} R(\theta) &= a(1 - \mathcal{E}^2 cos^2\theta)^{-1/2} \\ &= a(\alpha_0^0 Y_0^0 + \alpha_2^0 Y_2^0 + \alpha_4^0 Y_4^0 + ...) \end{aligned} \tag{A.13}$$

where $\mathcal{E}$ is the excentricity of the rotational ellipsoid. The coefficients α_0^0, α_2^0, α_4^0 and α_6^0 are all different from 0. For a realistic prolate deformation $\mathcal{E} = 2/3$, which corresponds with $\beta \approx 0.3$, the coefficients have the following values [Löb70]:

$$R(\theta) = a(3.88021 Y_0^0 + 0.33323\ Y_2^0 + 0.03701\ Y_4^0 + 0.0046\ Y_6^0). \tag{A.14}$$

The relationship between β' and the semiaxes c and a can be derived from equation (A.12) assuming that, in spite of the inequality of a rotational ellipsoid and a quadrupoloid, equation (A.12) describes the surface of a rotational ellipsoid.

$$\begin{aligned} c &= R_0'(1 + \frac{1}{2}\sqrt{\frac{5}{\pi}}\beta') \\ a &= R_0'(1 - \frac{1}{4}\sqrt{\frac{5}{\pi}}\beta'). \end{aligned} \tag{A.15}$$

From equations (A.15) follows:

$$\beta' = \frac{4}{3}\sqrt{\frac{\pi}{5}}\frac{\Delta R'}{R_0'} = 1.06\frac{\Delta R'}{R_0'} \tag{A.16}$$

where $\Delta R' = c - a$. It must be emphasized that R_0' does not correspond to the radius of a sphere with the same volume as that of the deformed nucleus.

Equation (A.12) corresponds with a rotational ellipsoid fulfilling the constant-volume condition, if R_0' is replaced by

$$R_0(1 - \frac{15}{16\pi}\beta^2 + \frac{5}{32\pi}\sqrt{\frac{5}{\pi}}\beta^3)^{-1/3} \tag{A.17}$$

with β the deformation parameter as defined by (A.11). Then

$$\begin{aligned} Q_0 &= \frac{3}{\sqrt{5\pi}} Z R_0^2 \beta (1 + \frac{1}{8}\sqrt{\frac{5}{\pi}}\beta + \frac{5}{8\pi}\beta^2 + ...) \\ &= \frac{3}{\sqrt{5\pi}} Z R_0^2 \beta (1 + 0.158\beta + 0.199\beta^2 + ...). \end{aligned} \tag{A.18}$$

R_0 denotes the radius of a sphere with the same volume as the rotational ellipsoid. The terms of order 4 and higher in the deformation parameter β contribute less than 0.1 % to the intrinsic quadrupole moment Q_0.

The deformation parameter β_q is defined by

$$R = R_{0q}(1 + \alpha_0^0 Y_0^0 + \beta_q Y_2^0) \tag{A.19}$$

where the constant-volume condition is required for the quadrupoloid. This results in

$$\alpha_0^0 Y_0^0 = -\frac{\beta_q^2}{4\pi} - \frac{2\sqrt{5}}{21}\frac{\beta_q^3}{4\pi\sqrt{4\pi}} - ... \tag{A.20}$$

and

$$R = R_{0q}(1 + \beta_q Y_2^0 - \frac{\beta_q^2}{4\pi} - \frac{2\sqrt{5}}{21}\frac{\beta_q^3}{4\pi\sqrt{4\pi}} - ...) \tag{A.21}$$

where R_{0q} denotes the radius of a sphere with the same volume of a quadrupoloid. The relationship between Q_0 and β_q is:

$$\begin{aligned} Q_0 &= \frac{3}{\sqrt{5\pi}} Z R_{0q}^2 \beta_q (1 + \frac{2}{7}\sqrt{\frac{5}{\pi}}\beta_q + \frac{1}{14\pi}\beta_q^2 - ...) \\ &= \frac{3}{\sqrt{5\pi}} Z R_{0q}^2 \beta_q (1 + 0.360\beta_q + 0.0227\beta_q^2 - ...) \end{aligned} \tag{A.22}$$

Neglecting the terms of order 3 and higher in β_q makes a difference of less than 0.5 % for Q_0.

For the same intrinsic quadrupole moment one can calculate the deformation parameters β and β_q with the constant-volume condition for the rotational ellipsoid and quadrupoloid, respectively. These two values will differ by up to 4%. The experimental uncertainty on Q_s and hence Q_0 is typically of the order of 15 % in our experiments. Therefore, often only the first order term in β (or β_q) is

taken into account for extracting β (or β_q) from the intrinsic quadrupole moment. In the first order $\beta^{(1)} = \beta_q^{(1)}$. If higher order terms in the deformation are considered in this work, the β_q values are taken. This approach for the deformation is often used in the literature, e.g., in Refs. [Bou85] and [Bro91] and others.

Usually the radii R_{av},R_0, R_0' and R_{0q} are all set equal to $r_0 A^{1/3}$ with $r_0 = 1.2$ fm and A the mass number of the nucleus.

Besides the deformation parameters β_2, β and β_q also the Nilsson deformation parameters δ and ϵ are often used in the literature. The Nilsson Hamiltonian is defined as [Nil55]

$$h = h_0 + C\vec{l}.\vec{s} + D\vec{l}^2, \tag{A.23}$$

where

$$h_0 = -\frac{\hbar^2}{2m}\Delta' + \frac{m}{2}(\omega_{x'}^2 x'^2 + \omega_{y'}^2 y'^2 + \omega_{z'}^2 z'^2). \tag{A.24}$$

$\omega_{x'}$, $\omega_{y'}$ and $\omega_{z'}$ denote the anisotropic oscillator frequencies in the body-fixed system. In the case of axial symmetry they can be written as a function of one single parameter of deformation δ.

$$\omega_{x'}^2 = \omega_{y'}^2 = \omega_0(\delta)^2(1 + \frac{2}{3}\delta) \tag{A.25}$$

$$\omega_{z'}^2 = \omega_0(\delta)^2(1 - \frac{4}{3}\delta). \tag{A.26}$$

Neglecting the $\vec{l}.\vec{s}$ and $\vec{l}^2$ terms the condition of constant volume of the nucleus leads to

$$R_0^3 = a^2 c \propto \frac{1}{\omega_{x'}\omega_{y'}\omega_{z'}} = constant. \tag{A.27}$$

Keeping this condition in combination with (A.25) and (A.26), ω_0 has to depend on δ in the following way:

$$\omega_0(\delta) = \mathring{\omega}_0\ (1 - \frac{4}{3}\delta^2 - \frac{16}{27}\delta^3)^{-\frac{1}{6}}. \tag{A.28}$$

$\mathring{\omega}_0$ is the value of $\omega_0(\delta)$ for δ=0. The relation between δ and the intrinsic quadrupole moment is obtained through the quadrupole moment of a rotational ellipsoid (A.9) and tabulated in table A.1.

Alternatively, the anisotropic oscillator frequencies can be defined by introducing the deformation parameter ϵ.

$$\omega_{x'} = \omega_{y'} = \omega_0(\epsilon)(1 + \frac{1}{3}\epsilon) \tag{A.29}$$

$$\omega_{z'} = \omega_0(\epsilon)(1 - \frac{2}{3}\epsilon). \tag{A.30}$$

From the constant-volume condition follows:

$$\omega_0(\epsilon) = \mathring{\omega}_0 \, (1 - \frac{1}{3}\epsilon^2 - \frac{2}{27}\epsilon^3)^{-1/3}. \tag{A.31}$$

The relationship between the different deformation parameters is tabulated in table A.2. For all relationships in tables A.1 and A.2 only quadrupole deformations are taken into account. Although this approximation is somewhat crude, it provides a good idea of the general scaling between the different deformations.

In principle the Nilsson potential can be expanded to higher multipole deformations and triaxial shapes as well [Naz96]. There is no unique way to relate the

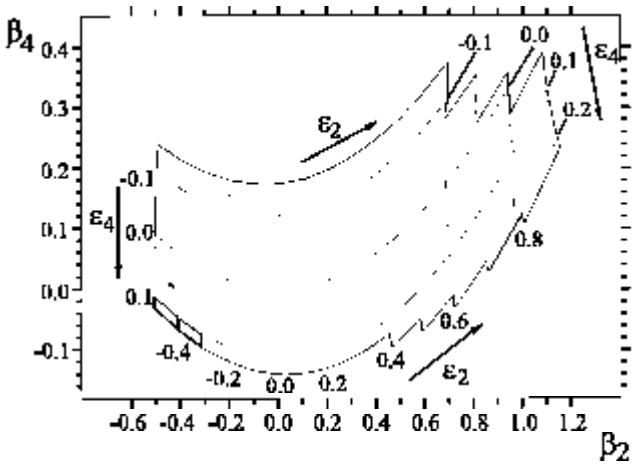

Figure A.2: *The transformation diagram between* $(\epsilon \equiv \epsilon_2, \epsilon_4)$ *and* (β_2, β_4). *Deformation parameters* β_λ *with* $\lambda \leq 12$ *were considered in the fit, where the* Q_λ *moments with* $\lambda = 2, 4, 6, 8, 10$ *and 12 were required to be the same. Note that (i) the transformation between* ϵ *and* β_2 *is rather insensitive to hexadecupole deformations, (ii) the shapes along the* $\epsilon_4 = 0$ *and* $\beta_4 = 0$ *lines are very different, and (iii)* ϵ_4 *and* β_4 *have opposite signs. The figure is taken from [Naz96].*

set of deformation parameters β_λ to the set ϵ_λ. A standard method of comparing shapes is to require equality between multipole moments as is done in Figure A.2 [Ben89a].

Table A.1: *Relation of the different deformation parameters to Q_0 [Löb70].*

Deformation parameter	Definition (constant volume condition)	Relation to Q_0
β_q	$R = R_{0q}(1 + \alpha_0^0 Y_0^0 + \beta_q Y_2^0)$ (for quadrupoloid)	$Q_0 = \frac{3}{\sqrt{5\pi}} Z R_{0q}^2 \beta_q (1 + \frac{1}{14\pi}\beta_q^2 - ...)$ $= 0.757 Z R_{0q}^2 \beta_q (1 + 0.360\beta_q + 0.0227\beta_q^2 - ...)$
β	$R = R_0(1 + \alpha_0^0 Y_0^0 + \beta Y_2^0)$ (for rotational ellipsoid)	$Q_0 = \frac{3}{\sqrt{5\pi}} Z R_0^2 \beta (1 + \frac{1}{8}\sqrt{\frac{5}{\pi}}\beta + \frac{1}{8}\frac{5}{\pi}\beta^2 - ...)$ $= 0.757 Z R_0^2 \beta (1 + 0.158\beta + 0.199\beta^2 - ...)$
β'	$R = R_0'(1 + \beta' Y_2^0)$ (no)	$Q_0 = \frac{3}{\sqrt{5\pi}} Z R_0'^2 \beta' (1 + \frac{1}{8}\sqrt{\frac{5}{\pi}}\beta')$ $= 0.757 Z R_0'^2 \beta' (1 + 0.158\beta')$
δ	$\omega_{x'}^2 = \omega_{y'}^2 = \omega_0(\delta)^2(1 + \frac{2\delta}{3})$ $\omega_z^2 = \omega_0(\delta)^2(1 - \frac{4\delta}{3})$ (for rotational ellipsoid)	$Q_0 = \frac{4}{5} Z R_0^2 \delta (1 + \frac{2}{3}\delta + \frac{8}{9}\delta^2 + \frac{80}{81}\delta^3 + ...)$ $= 0.8 Z R_0^2 \delta (1 + 0.667\delta + 0.889\delta^2 + 0.988\delta^3 + ...)$
ϵ	$\omega_{x'} = \omega_{y'} = \omega_0(\epsilon)(1 + \frac{\epsilon}{3})$ $\omega_{z'} = \omega_0(\epsilon)(1 - \frac{2\epsilon}{3})$ (for rotational ellipsoid)	$Q_0 = \frac{4}{5} Z R_0^2 \epsilon (1 + \frac{1}{2}\epsilon + \frac{4}{9}\epsilon^2 - \frac{49}{162}\epsilon^3 + ...)$ $= 0.8 Z R_0^2 \epsilon (1 + 0.5\epsilon + 0.667\epsilon^2 - 0.302\epsilon^3 + ...)$

Table A.2: *Relations between the different deformation parameters [Löb70].*

$$
\begin{aligned}
\beta_q &= \beta - \tfrac{9}{56}\sqrt{\tfrac{5}{\pi}}\beta^2 + \tfrac{397}{392\pi}\beta^3 - \tfrac{367751}{724416\pi}\sqrt{\tfrac{5}{\pi}}\beta^4 + ... \\
&= \sqrt{\tfrac{\pi}{5}}(\tfrac{1}{3}\epsilon + \tfrac{10}{63}\epsilon^2 + \tfrac{2896}{6615}\epsilon^3 + \tfrac{519751}{1584195}\epsilon^4 + ...) \\
&= \sqrt{\tfrac{\pi}{5}}(\tfrac{1}{3}\delta + \tfrac{2}{21}\delta^2 + \tfrac{5696}{6615}\delta^3 + \tfrac{2991688}{1584195}\delta^4 + ...) \\
\hline
\beta &= \beta_q + \tfrac{9}{56}\sqrt{\tfrac{5}{\pi}}\beta_q^2 - \tfrac{169}{224\pi}\beta_q^3 - \tfrac{167561}{827904\pi}\sqrt{\tfrac{5}{\pi}}\beta_q^4 + ... \\
&= \sqrt{\tfrac{\pi}{5}}(\tfrac{1}{3}\epsilon + \tfrac{1}{9}\epsilon^2 + \tfrac{1}{27}\epsilon^3 + \tfrac{1}{81}\epsilon^4 + ...) \\
&= \sqrt{\tfrac{\pi}{5}}(\tfrac{1}{3}\delta + \tfrac{2}{3}\delta^2 + \tfrac{2}{3}\delta^3 + \tfrac{11}{18}\delta^4 + ...) \\
\hline
\epsilon &= \tfrac{3}{4}\sqrt{\tfrac{5}{\pi}}\beta_q - \tfrac{75}{224\pi}\beta_q^2 - \tfrac{81}{128\pi}\sqrt{\tfrac{5}{\pi}}\beta_q^3 + \tfrac{890105}{1103872\pi^2}\beta_q^4 + ... \\
&= \tfrac{3}{4}\sqrt{\tfrac{5}{\pi}}\beta - \tfrac{15}{16\pi}\beta^2 + \tfrac{15}{64\pi}\sqrt{\tfrac{5}{\pi}}\beta^3 - \tfrac{75}{256\pi^2}\beta^4 + ... \\
&= \delta + \tfrac{1}{6}\delta^2 + \tfrac{5}{18}\delta^3 + \tfrac{37}{216}\delta^4 + ... \\
\hline
\delta &= \tfrac{3}{4}\sqrt{\tfrac{5}{\pi}}\beta_q - \tfrac{15}{56\pi}\beta_q^2 - \tfrac{57}{56\pi}\sqrt{\tfrac{5}{\pi}}\beta_q^3 + \tfrac{43115}{17248\pi^2}\beta_q^4 + ... \\
&= \tfrac{3}{4}\sqrt{\tfrac{5}{\pi}}\beta - \tfrac{15}{32\pi}\beta^2 + \tfrac{675}{512\pi^2}\beta^4 + ... \\
&= \epsilon - \tfrac{1}{6}\epsilon^2 - \tfrac{2}{9}\epsilon^3 + \tfrac{1}{27}\epsilon^4 + ...
\end{aligned}
$$

Appendix B

Measurable quantities allowing to extract the intrinsic quadrupole moment and the deformation of atomic nuclei

The intrinsic quadrupole moment and the nuclear deformation cannot be measured directly. This appendix shows some directly measurable quantities from which the intrinsic quadrupole moment and deformation can be extracted and their relationship to the intrinsic quadrupole moment or deformation. For a complete overview the reader is referred to [Naz96] and the references therein.

B.1 The spectroscopic quadrupole moment

The hyperfine interaction techniques allow a direct measurement of the quadrupole interaction frequency ν_Q (or ω_Q) from which the spectroscopic quadrupole moment can be extracted if the electric field gradient (EFG) is known. All these techniques measure in a direct or indirect way the hyperfine splitting of the nuclear levels due to the interaction of the spectroscopic quadrupole moment and the EFG at the nuclear site $V_{ZZ} = \partial^2 V/\partial Z^2$. The intrinsic quadrupole moment

can be extracted from the spectroscopic quadrupole moment as explained in appendix A. In the principal axis system of the EFG the energies of the quadrupole splitting can be written as

$$E_m = \hbar\omega_Q[3m^2 - I(I+1)], \tag{B.1}$$

where

$$\hbar\omega_Q = \frac{eQ_s V_{ZZ}}{4I(2I-1)} = \frac{h\nu_Q}{4I(2I-1)} \tag{B.2}$$

The level mixing spectroscopy and level mixing resonance techniques belong to this group of techniques, as well as the Mössbauer spectroscopy [Mös59, Wer64], the nuclear quadrupole resonance method (NQR)[Has75], the collinear laser spectroscopy [Neu88] and the time differential perturbed angular distribution technique (TDPAD) [Ste75].

B.2 The $B(E2)$ reduced transition probabilities

The transition probability per unit time for the emission of a photon of energy E_γ and of multipolarity λ, if the nucleus undergoes a transition from the initial state i to the final state f, is given by [deS74, Ald75]

$$T(\lambda) = \frac{8\pi(\lambda+1)}{\hbar\lambda[(2\lambda+1)!!]^2}\left(\frac{E_\gamma}{\hbar c}\right)^{2\lambda+1} B(\lambda, I_i \to I_f) \tag{B.3}$$

where

$$B(\lambda, I_i \to I_f) = \frac{1}{I_i+1}|\langle I_f \| T_\lambda \| I_i\rangle|^2 \tag{B.4}$$

is the reduced transition probability. For electric quadrupole radiations the transition tensor $\hat{T}^\mu_2$ is related to the electric quadrupole operator by

$$\hat{T}^\mu_2 = e\sqrt{\frac{5}{16\pi}}\hat{Q}^\mu_2. \tag{B.5}$$

From (B.4) and (B.5) can be calculated that for electric quadrupole transitions ($\lambda = 2$) within a rotational band

$$B(E2, KI_i \to KI_f) = \frac{5}{16\pi}e^2(Q_0)^2(2I_f+1)\begin{pmatrix} I_f & 2 & I_i \\ -K & 0 & K \end{pmatrix}^2 \tag{B.6}$$

for $K \neq 1/2, 1$. An experimental determination of the reduced transition probability, therefore, allows to deduce the intrinsic quadrupole moment Q_0.

This can be done by measuring the nuclear life time τ as the transition probability $T(\lambda)$ in equation (B.3) is nothing else than the reversed life time. A nice overview of all possible techniques to measure life times is given in Ref. [Nol79].

Also the cross-section for Coulomb excitation is directly proportional to the upward reduced transition probability $B(E2)\uparrow$ (see [Ald56] for the formulae). Note that equation (B.6) is valid for both the upward reduced transition probability $B(E2)\uparrow$ and the downward reduced transition probability $B(E2)\downarrow$, provided that I_i and I_f are correctly assigned. For $B(E2)\uparrow$, I_f is the total angular momentum of the excited state, while for $B(E2)\downarrow$, I_f corresponds to the angular momentum of the ground-state. For Coulomb excitation from a 0^+ ground-state to a 2^+ excited state K equals 0 and (B.6) reduces to

$$B(E2)\uparrow = \frac{5}{16\pi} e^2 (Q_0)^2. \tag{B.7}$$

The Weisskopf single-particle estimate

Weisskopf calculated the reduced matrix elements $|\langle I_f \| T_\lambda \| I_i \rangle|$ in a spherical basis with quantum numbers $|Nsljm\rangle$. For the electrical multipolarity he found [Rin80, Wei51]

$$B(E\lambda) \approx \frac{e^2}{4\pi} \left(\frac{3}{\lambda + 3} \right)^2 R_0^{2\lambda} \tag{B.8}$$

with $R_0 = r_0 A^{1/3}$ and $r_0 = 1.2$ fm. The value for $T(\lambda)$ (B.3), obtained by putting the Weisskopf $B(E\lambda; I_i \rightarrow I_f)$ reduced transition probability, is called the Weisskopf single-particle estimate and gives a rough estimate for the life times of the state I_i. It is proportional to $E_\gamma^{2\lambda+1}$ (thus higher transition rates and shorter life times for increasing E_γ). Furthermore, it predicts that higher transition multipolarities λ have lower transition rates. An analog expression can be calculated for magnetic transitions as well [Rin80].

B.3 Nuclear radii - $E0$ moments

The charge density of an axially deformed nucleus can be written as [Boh75]

$$\rho(\vec{r'}) = \rho(r'[1 - \frac{\beta_q^2}{4\pi} + \beta_q Y_2^0]^{-1}) \tag{B.9}$$

in the intrinsic coordinate system and restricting to quadrupole deformations only. The mean square radius of the charge distribution is

$$\int \rho(\vec{r'}) r'^2 dV' = (1 + \frac{5}{4\pi}\langle\beta_q^2\rangle)\langle r'^2\rangle_0 \tag{B.10}$$

where $\langle r'^2\rangle_0$ represents the mean square radius of the charge distribution for a spherical nucleus (β_q=0). Since the change in $\langle r'^2\rangle$ is proportional to β_q^2, not only the static deformation (as revealed in the quadrupole moments or the $E2$ transition probabilities between rotational states), but also the fluctuations in the nuclear shape (as revealed in $E2$ transition rates to vibrational states) contribute to the effective charge radius. To indicate that the shape fluctuations are taken into account the notation $\langle\beta_q^2\rangle$ is used.

Collinear laser spectroscopy is one of the techniques which allows to extract the charge radius $\langle r'^2\rangle$ provided that the atomic electron density $|\psi(0)|^2$ at the nuclear site is known [Neu88].

B.4 The mixing ratio

The mixing ratio δ of the γ rays in an electric rotational band is directly related to the ratio of the moments $|\frac{g_K - g_R}{Q_0}|$ with g_R and g_K the rotational and the intrinsic gyromagnetic ratio, respectively [Ale64]. This relationship can be derived from the branching ratio λ_b of the intra-band transitions [Ale64, Whe99]. The branching ratio is defined as the ratio of the γ ray transition rate with $\Delta I = 2$, T_2, to the γ' ray transition rate with $\Delta I = 1$, T_1. The $\Delta I = 2$ transitions are assumed to have a pure $E2$ character as any admixture of $M3$ (or higher multipoles) will be very small. For the $\Delta I = 1$ transition a mixed $M1/E2$ transition should be considered. Hence λ_b is

$$\lambda_b = \frac{T_2(E2)}{T_1(E2) + T_1(M1)}. \tag{B.11}$$

The mixing ratio δ is defined by

$$\frac{T_1(M1)}{T_1(E2)} = \frac{1}{\delta^2}. \tag{B.12}$$

The transition rates are related to the reduced transition probabilities by [Löb75]

$$B(E2; KI_i \rightarrow KI_f) = \frac{1}{1.225 \cdot 10^9 E_\gamma^5} T(E2; KI_i \rightarrow KI_f) \tag{B.13}$$

$$B(M1; KI_i \rightarrow KI_f) = \frac{1}{1.758 \cdot 10^{13} E_\gamma^3} T(M1; KI_i \rightarrow KI_f). \tag{B.14}$$

E_γ is the γ-ray transition energy in MeV. The $B(E2)$ and $B(M1)$ reduced transition probabilities have units of $e^2\text{fm}^2$ adn μ_N^2, respectively. Hence

$$\lambda_\delta = (\frac{E_2}{E_1})^5 \frac{B_2(E_2) \cdot 1.225 \cdot 10^9}{B_1(E2) \cdot 1.225 \cdot 10^9 + B_1(M1) E_1^{-2} \cdot 1.758 \cdot 10^{13}}. \tag{B.15}$$

The reduced in-band transition probabilities are given by [deS74]

$$B(E2; KI_i \rightarrow K(I_f = I_i - 2)) = \frac{5}{16\pi} e^2 (Q_0)^2 (2I_f + 1) \begin{pmatrix} I_f & 2 & I_i \\ -K & 0 & K \end{pmatrix}^2 \quad K \neq 1/2, 1 \tag{B.16}$$

$$B(E2; KI_i \rightarrow K(I_f = I_i - 1)) = \frac{5}{16\pi} e^2 (Q_0)^2 (2I_f + 1) \begin{pmatrix} I_f & 2 & I_i \\ -K & 0 & K \end{pmatrix}^2 \quad K \neq 1/2, 1 \tag{B.17}$$

$$B(M1; KI_i \rightarrow K(I_f = I_i - 1)) = \frac{3}{4\pi} (g_K - g_R)^2 K^2 (2I_f + 1) \begin{pmatrix} I_f & 1 & I_i \\ -K & 0 & K \end{pmatrix}^2 \quad K \neq 1/2 \tag{B.18}$$

The relevant $3j$ symbols are [Con63]

i. for an $E2$ transition with $I_i = I$ and $I_f = I - 2$:

$$(2I_f + 1) \begin{pmatrix} I_f & 2 & I_i \\ -K & 0 & K \end{pmatrix}^2 = \frac{3(I-K)(I-K-1)(I+K)(I+K-1)}{(2I-2)(2I-1)I(2I+1)} \tag{B.19}$$

ii. for an $E2$ transition with $I_i = I$ and $I_f = I - 1$:

$$(2I_f + 1) \begin{pmatrix} I_f & 2 & I_i \\ -K & 0 & K \end{pmatrix}^2 = K^2 \frac{3(I-K)(I+K)}{(I-1)I(2I+1)(I+1)} \tag{B.20}$$

iii. for an $M1$ transition with $I_i = I$ and $I_f = I - 1$:

$$(2I_f + 1)\begin{pmatrix} I_f & 1 & I_i \\ -K & 0 & K \end{pmatrix}^2 = \frac{(I-K)(I+K)}{I(2I+1)} \tag{B.21}$$

By combining all expressions above one can calculate that

$$\lambda_b = (\frac{E_2}{E_1})^5 \frac{[\frac{(I-K-1)(I+K-1)(I+1)}{(2I-1)2K^2}]}{1+\frac{1}{\delta^2}} \tag{B.22}$$

and

$$\lambda_b = (\frac{E_2}{E_1})^5 \frac{[\frac{(I-K-1)(I+K-1)(I+1)}{(2I-1)2K^2}]}{1+\frac{1}{5}[\frac{(g_K-g_R)}{(Q_0)^2 E_1^2}(I^2-1)(1.435\cdot 10^4)]} \tag{B.23}$$

where the factor 10^4 in the denominator drops if Q_0 is expressed in units of barn instead of fm^2. By combining (B.22) and (B.23), the following relationship can be extracted:

$$|\frac{g_K - g_R}{Q_0}| = 0.933 \frac{E_1}{\delta\sqrt{(I^2-1)}}. \tag{B.24}$$

Note that experimentally only δ^2 is deduced via (B.12). So only the absolute value $|\frac{(g_K-g_R)}{Q_0}|$ can be extracted experimentally.

The experimental g-factor is related to the rotational g-factor, g_R, and the intrinsic g-factor, g_K, by [deS74]

$$g = g_R + (g_K - g_R)\frac{K^2}{I(I+1)} \qquad K \neq 1/2. \tag{B.25}$$

Hence measuring the g-factor and fixing either g_R or g_K allows to deduce $(g_R - g_K)$ and thus Q_0. Note that for a $K = 1/2$ rotational band, also the decoupling constant b_0 should be taken into account [deS74].

Appendix C

The influence of the $\vec{I} \cdot \vec{J}$ interaction on the LEMS technique

This appendix shows how the influence of the combined magnetic dipole + $\vec{I} \cdot \vec{J}$ interaction on the anisotropy of the γ radiation can be calculated. The first section discusses the combined magnetic + $\vec{I} \cdot \vec{J}$ interaction. The second section explains how the $\vec{I} \cdot \vec{J}$ interaction is included in the LEMS formalism. This theoretical study + the experimental results (see section 2.4) are published in [Vyv00].

C.1 The combined magnetic + $\vec{I} \cdot \vec{J}$ interaction

The Hamiltonian of the combined magnetic + $\vec{I} \cdot \vec{J}$ interaction, which takes place during the flight of the recoiling ions during their flight through the vacuum, is given by [Ste75]:

$$\mathcal{H}_{IJ} = a\vec{I} \cdot \vec{J} + \vec{\mu}_J \cdot \vec{B} - \vec{\mu}_I \cdot \vec{B}. \tag{C.1}$$

with $a = \frac{\mu_I (B_{hf}(0))}{IJ\hbar^2}$ being the coupling constant, $\vec{\mu}_I$ the nuclear magnetic moment, $\vec{\mu}_J$ the electronic magnetic moment and B_{hf} the hyperfine field induced by the atomic electrons.

It can be shown that the nuclear density matrix elements of the 2-spin system can be written as [CT88]:

$$\langle m_I \mid \rho_I(t) \mid m'_I \rangle = \sum_{m_J} \langle m_I m_J \mid \rho_{IJ}(t) \mid m'_I m_J \rangle. \tag{C.2}$$

with ρ_I the density matrix describing the nuclear spin system and ρ_{IJ} the density matrix describing the total ensemble of nuclear and atomic spins. Further note, since the nuclear spin system and the atomic spin system are not coupled at $t = 0$ (the moment of the recoil out of the target), the following relationship holds:

$$\langle m_I m_J \mid \rho_{IJ}(t=0) \mid m'_I m'_J \rangle = \langle m_I \mid \rho_I(t=0) \mid m'_I \rangle \langle m_J \mid \rho_J(t=0) \mid m'_J \rangle. \tag{C.3}$$

with ρ_J the density matrix describing the atomic spin system. Using the relationships (C.2) and (C.3), the $\vec{I} \cdot \vec{J}$ perturbation factor can be calculated in a similar way as the LEMS perturbation factor:

$$\begin{aligned} &G^{00}_{kk'}(I, J, \mathcal{H}_{IJ}, t) = \\ &\frac{\sqrt{2k+1}\sqrt{2k'+1}}{2J+1} \sum_{m_I, m_J, \mu_I, \mu_J, N, N'} (-1)^{m_J - \mu_J} \begin{pmatrix} I & I & k \\ -m_I & m_I & 0 \end{pmatrix} \begin{pmatrix} I & I & k' \\ -\mu_I & \mu_I & 0 \end{pmatrix} \\ &\times \exp(-i\omega_{NN'}t) \langle m_I m_J \mid N \rangle \langle N \mid \mu_I \mu_J \rangle \langle \mu_I \mu_J \mid N' \rangle^* \langle N' \mid m_I m_J \rangle^*. \end{aligned} \tag{C.4}$$

with $\omega_{NN'} = \frac{E_N - E_{N'}}{\hbar}$ and E_N and $\mid N \rangle$ the eigenvalues and eigenvectors of $\mathcal{H}_{IJ}$. Further the $\vec{I} \cdot \vec{J}$ perturbation factor will be noted as:

$$G^{00}_{kk'}(I, J, \mathcal{H}_{IJ}, t) = \sum_{NN'} (f^{IJ}_{NN'})^{00}_{kk'} \exp(-i\omega^{IJ}_{NN'}t). \tag{C.5}$$

Only the $G^{00}_{kk'}$ terms need to be taken into account, because of the axial symmetry with respect to the axis of the initial orientation.

The main difference with Refs. [Bro73, Lit80] is the way in which the time integration of the perturbation factor is performed. In Refs. [Bro73, Lit80] it is assumed that all nuclei decay in flight. In our formalism we also consider the case when the nuclei survive the flight and decay in a cubic host (cubic to exclude the quadrupole interaction, which, if present, also influences the anisotropy of the

radiation). During the time interval $[0,T]$, with T the flight time (of order 10 ns for a recoil-distance of 6 cm), the $\vec{I}\cdot\vec{J}$ interaction will perturb the orientation. Once the nuclei reach the host the orientation is kept, since the $\vec{I}\cdot\vec{J}$ is only active when the atom is free (apart from some exceptional cases where the $\vec{I}\cdot\vec{J}$ interaction is also active in insulators [Ste75, Ell53]). In the time integration of the $\vec{I}\cdot\vec{J}$ perturbation factor, not only a weight $\exp(-t/\tau)$ to incorporate the lifetime is taken into account, but also a Gaussian weight over the flight time T: $\exp(-\frac{(T-T_0)^2}{\sigma_T^2})$, with $T_0 = \sqrt{\frac{m}{2}}\frac{1}{\sqrt{E_0}}d$ the average flight time and $\sigma_T = |\sqrt{\frac{m}{2}}\frac{1}{\sqrt{E_0-\sigma_E}}d - T_0|$ the standard deviation. Here d is the recoil distance on which the flight time T_0 and the standard deviation σ_T depend linearly. E_0 is the average energy with which the nuclei leave the target, i.e., the recoil energy minus the loss of energy due to the travel of the nucleus through the target. σ_E is the spread in energy with which the atoms leave the target. This spread in energy, and as a consequence the spread in flight time, is mainly caused due to the fact that the nuclei are produced throughout the whole target thickness and follow different trajectories before leaving the target, resulting in different energy losses, which can e.g. be demonstrated by TRIM [Zie85] calculations.

The following expression for the time integrated $\vec{I}\cdot\vec{J}$ perturbation factor is obtained:

$$G^{00}_{kk'}(I,J,\mathcal{H}_{IJ},\tau,T_0) = \frac{\int_0^\infty \exp(-\frac{(T-T_0)^2}{\sigma_T^2})(\int_0^T \exp(-t/\tau)G^{00}_{kk'}(I,J,\mathcal{H}_{IJ},t) + G^{00}_{kk'}(I,J,\mathcal{H}_{IJ},T)\int_T^\infty \exp(-t/\tau))dtdT}{\int_0^\infty \exp\left(-\frac{(T-T_0)^2}{\sigma_T^2}\right)\int_0^\infty \exp(-t/\tau)dtdT}. \tag{C.6}$$

The integrals can be calculated in an analytical way, resulting in:

$$\begin{aligned} G^{00}_{kk'}(I,J,\mathcal{H}_{IJ},\tau,T_0) &= \sum_{NN'}(f^{IJ}_{NN'})^{00}_{kk'} \\ &\times\{\frac{1}{1+(\omega^{IJ}_{NN'}\tau)^2} + \frac{\exp\{-T_0/\tau - \frac{\sigma_T^2}{4\tau^2}[(\omega^{IJ}_{NN'}\tau)^2-1]\}}{1+(\omega^{IJ}_{NN'}\tau)^2} \\ &\times[-cos(-\omega^{IJ}_{NN'}T_0 + \frac{\sigma_T^2\omega^{IJ}_{NN'}}{2\tau}) - \omega^{IJ}_{NN'}\tau sin(-\omega^{IJ}_{NN'}T_0 + \frac{\sigma_T^2\omega^{IJ}_{NN'}}{2\tau})] \\ &+ \exp(-T_0/\tau - \frac{\sigma_T^2}{4\tau^2}[(\omega^{IJ}_{NN'}\tau)^2-1])[cos(-\omega^{IJ}_{NN'}T_0 + \frac{\sigma_T^2\omega^{IJ}_{NN'}}{2\tau})]\}. \end{aligned} \tag{C.7}$$

Usually the last 2 terms are negligible: for small $\omega^{IJ}_{NN'}\tau$ they cancel each other, for large $\omega^{IJ}_{NN'}\tau$ the exponentials go to 0. This means that in most of the cases the expression reduces to the $\frac{1}{1+(\omega^{IJ}_{NN'}\tau)^2}$ term, i.e. the term which is obtained by assuming all nuclei decay in flight, which is the result considered in Refs. [Gol82, Bro73, Lit80]. However, the $G^{00}_{kk}(I,J,\mathcal{H}_{IJ},\tau,T_0)$ perturbation factors should go to 1 and the $G^{00}_{kk'}(I,J,\mathcal{H}_{IJ},\tau,T_0), k\neq k'$ perturbation factors to 0 when the interaction time approaches 0. The interaction time is equal to the lifetime of the nucleus or the flight time, depending on which of them is the shortest. It is clear from expression (C.7) that for a zero flight time (both T_0 and σ_T going to 0) this condition is only fulfilled when the last two terms are present. So they are necessary in the case when a short flight time reduces the interaction time too much to reach the hard core value for the anisotropy.

Note that in reality not the flight time distribution, but the energy distribution is a Gaussian, resulting in a $\frac{md^2}{T^3}\exp(-\sigma'^4_T(\frac{1}{T^2}-\frac{1}{T_0^2})^2)dT$ distribution function for the flight time T. Here σ'_T is defined as $\sqrt{\frac{m}{2}}\frac{1}{\sqrt{\sigma_E}}d$. The latter distribution function results in a summation of integrals which have to be calculated in a numerical way. We prefer to mention the Gaussian approach, because its analytical solution has a direct physical interpretation. Only when the flight time is too short to reach the hard-core value for the anisotropy, the results obtained by using the Gaussian approximation for T differ up to 15% from the correct ones. In all other cases the difference is negligible. In addition it is straightforward that the calculation time will be a lot longer when numerical calculations for the integrals are needed.

Simulations of the anisotropy as a function of the magnetic field for the combined $\vec{I}\cdot\vec{J}$ interaction show that the $\vec{I}\cdot\vec{J}$ interaction frequency $\nu_{IJ}=\frac{\hbar}{2\pi}a$ influences the decoupling value of the curve. The larger ν_{IJ}, and thus the interaction between the atomic electrons and the nucleus, the larger the decoupling field. This can also be understood from the condition $\langle\vec{\mu}_j\cdot\vec{B}\rangle > \langle a\vec{I}\cdot\vec{J}\rangle$. The amplitude of the curve depends on the atomic spin J, more precisely on the ratio of the atomic spin J to the nuclear spin I. Intuitively it is clear that a large atomic spin J compared to the nuclear spin I will disturb the nuclear orientation a lot

more, than a smaller one [Gol82].

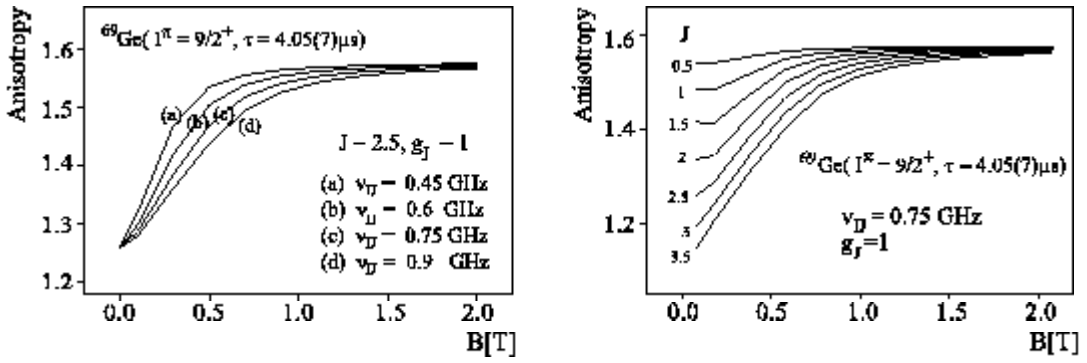

Figure C.1: *Simulations of the change of the anisotropy as a function of the magnetic field due to the combined $\vec{I} \cdot \vec{J}$ + magnetic dipole interaction for the $^{69}Ge(I^{\pi} = 9/2^{+}, \tau = 4\ \mu s,\ \mu_I = -1.0011(32)\ \mu_N)$ isomer. In the left panel the $\vec{I} \cdot \vec{J}$ interaction frequency $\nu_{IJ} = (\hbar/2\pi)a$ has been varied, in the right panel the atomic spin J has been varied.*

C.2 The LEMS formalism including the $\vec{I} \cdot \vec{J}$ interaction

If there is a recoil-distance between target and host and an EFG is present in the host, consecutively the combined $\vec{I} \cdot \vec{J}$ + magnetic dipole interaction (during recoil) and the combined electric quadrupole + magnetic dipole interaction (after implantation) take place. The change of the orientation during the time interval $[0, T]$ is taken into account by the $\vec{I} \cdot \vec{J}$ perturbation factor $G^{00}_{kk'}(I, J, \mathcal{H}_{IJ}, t)$ and the change in the time interval $[T, \infty]$ by the LEMS perturbation factor $G^{nn'}_{kk'}(I, \mathcal{H}_{LEMS}, t)$. The time integration, again including a weight $e^{-t/\tau}$ to incorporate the nuclear lifetime and a Gaussian weight for the flight time, yields

$$G^{00}_{kk'}(I, \quad J \quad, \mathcal{H}_{IJ} + \mathcal{H}_{LEMS}, \tau, T_0) = \frac{\int_0^\infty e^{-\frac{(T-T_0)^2}{\sigma_T^2}} \int_0^T e^{-t/\tau} G^{00}_{kk'}(I, J, \mathcal{H}_{IJ}, t) dt dT}{\int_0^\infty e^{-\frac{(T-T_0)^2}{\sigma_T^2}} dT \int_0^\infty e^{-t/\tau} dt}$$

$$+\frac{\sum_l \int_0^\infty e^{-\frac{(T-T_0)^2}{\sigma_T^2}} G_{kl}^{00}(I,J,\mathcal{H}_{IJ},T)\int_T^\infty e^{-t/\tau} G_{lk'}^{00}(I,\mathcal{H}_{LEMS},t)dtdT}{\int_0^\infty e^{-\frac{(T-T_0)^2}{\sigma_T^2}} dT \int_0^\infty e^{-t/\tau}dt}. \tag{C.8}$$

Again an analytical solution is obtained:

$$\begin{aligned}
&G_{kk'}^{00}(I,J,\mathcal{H}_{IJ}+\mathcal{H}_{LEMS},\tau,T_0) = \\
&\sum_{NN'}(f_{NN'}^{IJ})_{kk'}^{00}\frac{1}{1+(\omega_{NN'}^{IJ}\tau)^2}\{1+\exp[-T_0/\tau-\frac{\sigma_T^2}{4\tau^2}((\omega_{NN'}^{IJ}\tau)^2-1)\} \\
&[-\cos(-\omega_{NN'}^{IJ}T_0+\frac{\sigma^2\omega_{NN'}^{IJ}}{2\tau})-\omega_{NN'}^{IJ}\tau sin(-\omega_{NN'}^{IJ}T_0+\frac{\sigma^2\omega_{NN'}^{IJ}}{2\tau})]\} \\
&+\sum_l\sum_{NN'}\sum_{MM'}(f_{NN'}^{IJ})_{kl}^{00}(f_{MM'}^{LEMS})_{lk'}^{00}\frac{1}{1+(\omega_{MM'}^{LEMS}\tau)^2}\exp[-T_0/\tau-\frac{\sigma_T^2}{4\tau^2}(((\omega_{NN'}^{IJ}+\omega_{MM'}^{LEMS})\tau)^2-1)] \\
&[\cos(-(\omega_{NN'}^{IJ}+\omega_{MM'}^{LEMS})T_0+\frac{\sigma^2(\omega_{NN'}^{IJ}+\omega_{MM'}^{LEMS})}{2\tau}) \\
&+\omega_{MM'}^{LEMS}\tau\sin(-(\omega_{NN'}^{IJ}+\omega_{MM'}^{LEMS})T_0+\frac{\sigma^2(\omega_{NN'}^{IJ}+\omega_{MM'}^{LEMS}}{2\tau})].
\end{aligned} \tag{C.9}$$

We restrict ourselves to the $G_{kk'}^{00}$ terms, because in a LEMS experiment usually a polycrystal is providing the EFG [Har91b], resulting in an axial symmetry with respect to the initial orientation axis. If a single crystal is used, the $G_{kk'}^{n0}(n\neq 0)$ terms need to be considered [Har91b].

If no quadrupole interaction takes place, the expression for $G_{kk'}^{00}(I,J,\mathcal{H}_{IJ}+\mathcal{H}_{LEMS},\tau,T_0)$ reduces to the $G_{kk'}^{00}(I,J,\mathcal{H}_{IJ},\tau,T_0)$ perturbation factor, because of the properties of the $(f_{MM'}^{LEMS})_{lk'}^{00}$ factors. In this case the eigenstates of the LEMS Hamiltonian $\mid M\rangle$ are equal to the $\mid m_I\rangle$ states. It can be seen from expression (2.10) that the corresponding $(f_{MM'}^{LEMS})_{lk'}^{00}$ factors are 0 for $(M\neq M', l\neq k')$ and 1 for $(M=M', l=k')$. As a consequence, only the terms with $\omega_{M=M'}^{LEMS}=0$ need to be considered.

Also if all nuclei decay in flight $(T_0>\tau)$, the $G_{kk'}^{00}(I,J,\mathcal{H}_{IJ}+\mathcal{H}_{LEMS},\tau,T_0)$ perturbation factor reduces to the $G_{kk'}^{00}(I,J,\mathcal{H}_{IJ},\tau,T_0)$ perturbation factor. When no recoil distance is present $(T_0=\sigma_T=0)$ the expression reduces to the $G_{kk'}^{00}(I,\mathcal{H}_{LEMS},\tau)$ perturbation factor. If no $\vec{I}\cdot\vec{J}$ interaction takes place during the flight through the vacuum, e.g., because the recoiling ions are fully stripped or are in an atomic noble-gas-like configuration [Jän88, Daf85, And78], the pure LEMS perturbation factor is not immediatly obtained. If part of the nuclei do

not reach the host (T_0 comparable to or smaller than the nuclear lifetime τ), the LEMS amplitude will be reduced. Only when all nuclei reach the host ($\tau >> T_0$), the hard-core value of the anisotropy due to the combined electric quadrupole + magnetic dipole interaction will be reached.

Appendix D

Calculating the double perturbed fraction and the direct feedings

As explained in section 2.2.3 a transition underneath a cascade of two isomers contains four different contributions (Figure D.1): the direct fractions $D1$ and $D2$, the double perturbed fraction $2P$ and a prompt component due to side feeding. The different fractions are calculated by determining the relative intensities of the involved γ ray transitions. Here the example of the 337 keV transition in ^{196}Pb will be worked out.

The total intensity I_{337} equals

$$I_{337} = I_{498} + I_{548} + I_{959} + x + y. \tag{D.1}$$

The contribution $D1$, directly originating from the 11^- isomer and bypassing the 12^+ isomer, is $D1 = I_{548}/I_{337}$. The double perturbed fraction yields $2P = I_{498}/I_{337}$. The fraction $D2$, not bypassing the 11^- isomer, equals $(I_{\Delta E} - I_{498})/I_{337}$. However, the $12^+ \rightarrow 10^+$ $E2$ transition is very low in energy and, therefore, highly converted (see below). As a consequence the γ ray intensity of the ΔE transition is very low and not detectable. Alternatively, $D2$ can be deduced as $D2 = (I_{959} + x)/I_{337}$ in which the side feeding x is not known. It can be approached by taking the average value of I_{959}/I_{337} and $(I_{337} - I_{498} - I_{548})/I_{337} = (I_{959} + x + y)/I_{337}$. The γ ray intensities are not just the measured intensities.

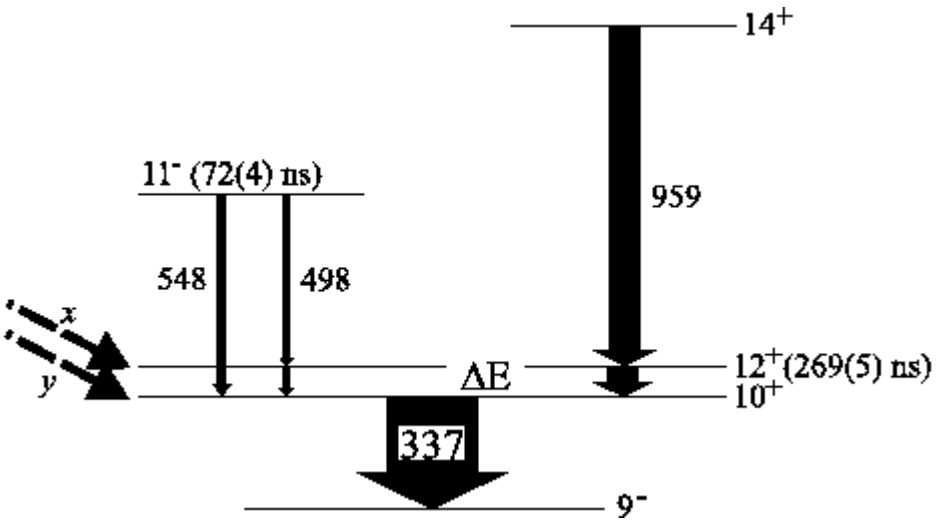

Figure D.1: *Partial level scheme of ^{196}Pb, showing the different contributions to the 337 keV transition. The letters x and y denote the side feedings towards the 12^+ and 10^+ level respectively [Ruy86].*

They need to be corrected for the relative detector efficiency and the conversion electrons.

Not every γ ray which is emitted is also detected. The ratio of the detected γ rays and the emitted γ rays is the absolute efficiency, ϵ, of a detector.

$$\frac{I_{detected}}{I_{emitted}} = \epsilon \text{ or } I_{emitted} = \frac{I_{detected}}{\epsilon}. \tag{D.2}$$

The efficiency is energy dependent. Therefore, if ratios of intensities of γ transitions with different energies are taken, a correction for the energy dependent efficiency of the detector needs to be made. The standard procedure is to put at the target position a γ source, of which the relative intensities of the emitted γ rays for the different energies are known. By comparing the ratio of the measured γ ray intensities with the ratio of the emitted γ ray intensities, the correction factor can be extracted. We have performed the efficiency calibration with a ^{133}Ba source, which has intense 276.3, 302.9, 356.0 and 383.8 keV transitions. Figure D.2 shows the efficiency of the detector as a function of the energy, where the efficiency has been scaled such that it corresponds with 1 for the 276.3 keV transition.

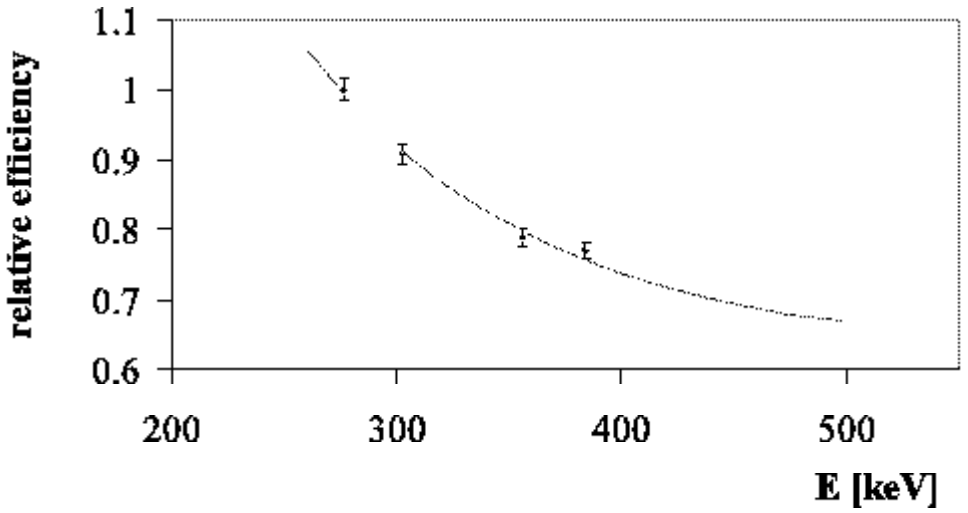

Figure D.2: *Relative detector efficiency as a function of energy for the detector positioned at 0° degrees with respect to the magnetic field. The data are taken with a ^{133}Ba source. The efficiencies are scaled such that the efficiency of the 276.3 keV transition equals 1.*

The interpolated relative efficiency for the 337 keV transition yields 0.85(2). The extrapolated relative efficiency for the 498 keV transition yields 0.65(6). In one hour of measurement time $1.64(1)\cdot 10^5$ γ rays with an energy of 337 keV were recorded, compared to $1.08(3)\cdot 10^4$ events for the 498 keV transition. The ratio, corrected for the relative detector efficiencies, is hence:

$$\frac{I_{498}}{I_{337}} = \frac{1.08(3)\cdot 10^4 \times 0.85(2)}{1.64(1)\cdot 10^5 \times 0.65(6)} = 9(1)\%. \qquad \text{(D.3)}$$

This value is in excellent agreement with the ratio $I_{498}/I_{337} = 10(1)\%$ as derived in Ref. [Ruy86]. Therefore, all relative intensities of Ref. [Ruy86] have been adopted. In the experiments of Van Ruyven et al. the ^{196}Pb nucleus has been produced by two different nuclear reactions, the ^{188}Os(^{12}C,xn) reaction at a beam energy of 75 MeV and the ^{198}Hg$(\alpha, 6n)$ reaction at a beam energy of 75 MeV, respectively. In a similar way the relative intensities of the γ rays in ^{194}Pb have been adopted from [Ruy86] as well, where the ^{194}Pb has been produced in the

^{188}Os(^{12}C,6n) reaction at a beam energy of 100 MeV. The only exception is the $I_\gamma(352)/I_\gamma(305)$ ratio (the 352 keV transition is the $11^- \rightarrow 10^+$ transition and the 305 keV transition is the $11^- \rightarrow 12^+$ transition in ^{194}Pb (see Figure 3.11)), which was taken from [Fan91]. The relative intensities for the γ transitions in ^{194}Pb and ^{196}Pb are tabulated in table D.1.

The relative γ ray intensities need not only to be corrected for the relative detector efficiencies, but also for the decay via conversion electrons. The emission of γ radiation can be strongly influenced by the presence of electrons near the nucleus. The vicinity of electrons opens other channels of deexcitation for a nucleus in an excited state, i.e., the direct transfer of the excitation energy to the electrons in the various atomic shells and subshells and the ejection of these electrons into an unbound state [Ald75]. The total intensity of emitted radiation of a nuclear state is, therefore, the sum of the intensity of the emitted γ radiation and the intensity of the emitted conversion electrons:

$$I_{total} = I_\gamma + I_e \tag{D.4}$$

$$= I_\gamma + \alpha I_\gamma \tag{D.5}$$

$$= I_\gamma(1+\alpha) \tag{D.6}$$

in which the conversion coefficient α is defined as I_e/I_γ. The values for α are tabulated for the different atomic shells and subshells K, L_I, L_{II}, L_{III}, M_I,... in Ref. [Hag68].

The final results, obtained for the fractions $D1$, $D2$ and $2P$ by taking the ratios of the corrected γ ray intensities, are listed in table D.2. Note that the side feeding towards the 10^+ state, denoted by y in Figure D.1, is neglected and that $D1$, $D2$ and $2P$ are rescaled such that their sum $D1 + D2 + 2P$ equals 100%. The side feeding can be neglected because it is a prompt component in the total γ ray intensity, which does not influence the extracted frequency ν_Q.

Table D.1: *The relative intensities of the relevant transitions in ^{196}Pb and ^{194}Pb.*

[a] *Relative intensities adopted from [Ruy86].*

[b] *Relative intensities adopted from [Fan91].*

[c] *Conversion coefficient determined as $\alpha = \alpha_K + \alpha_L + \alpha_M$, with α_K, α_L and α_M taken from [Hag68]. If the energy of the γ transition is not present in the tables of Ref. [Hag68], a linear interpolated value has been taken.*

^{196}Pb	E[keV]	I^{a}	$(1+\alpha)I^{c}$	^{194}Pb	E[keV]	$I^{a,b}$	$(1+\alpha)I^{c}$
	337	56(2)	57.3		173	75(5)	83.7
	498	5.7(7)	5.76		305	12(2)	11.9
	548	2.7(6)	2.72		352	19(3)	19.4
	959	33(2)	3.32		933	34(3)	34.3

Table D.2: *The obtained values for the fractions $D1$, $D2$ and $2P$. They are rescaled such that their sum $D1 + D2 + 2P$ equals 100%.*

^{196}Pb			^{194}Pb		
$D1$	I_{548}/I_{337}	5.5 %	$D1$	I_{352}/I_{173}	24.9%
$D2$	average of I_{959}/I_{337} and	82.9%	$D2$	average of I_{933}/I_{173} and	59.7%
	$(I_{337} - I_{498} - I_{548})/I_{337}$			$(I_{173} - I_{305} - I_{352})/I_{173}$	
$2P$	I_{498}/I_{337}	11.6%	$2P$	I_{305}/I_{173}	15.3%

Appendix E

Calculation of the quadrupole moment of the $\pi(3s_{1/2}^{-2}1h_{9/2}1i_{13/2})_{11^-}$ isomer in ^{200}Pb by taking into account particle-core coupling

In this appendix the spectroscopic quadrupole moment of the $(\pi 3s_{1/2}^{-2}1h_{9/2}1i_{13/2})_{11^-}$ state in ^{200}Pb will be calculated by considering the coupling of the proton 2-particle configuration $|1h_{9/2}1i_{13/2};11^-\rangle$ to the vibrations of the underlying Hg-core[1]. This then approximates the $2p-2h$ configuration in a rather realistic way. First the wave functions need to be determined, after which the expectation value of the quadrupole operator can be calculated. Only quadrupole vibrations are considered.

The wave functions are deduced by the diagonalisation of the Hamiltonian $H = H_{s.p.} + H_{coll} + H_{int}$ in the 2-dimensional Hilbert space spanned by the wave

[1]In this appendix the quadrupole moment of the $(\pi 3s_{1/2}^{-2}1h_{9/2}1i_{13/2})_{11^-}$ state is calculated for the ^{200}Pb nucleus instead of for the ^{196}Pb nucleus, because for a calculation of $Q_s(^{196}\mathrm{Pb}(I^\pi = 11^-))$ not all necessary experimental data are available.

functions $|\,11^-_{s.p.}\rangle$ and $|\,11^-_{s.p.}\otimes 2^+;11^-\rangle$. Here $|\,11^-_{s.p.}\rangle$ is a shorthand notation for $|\,1h_{9/2}1i_{13/2};11^-\rangle$, which is an eigenfunction of $H_{s.p.}$, and $|\,2^+\rangle$ is the first excited vibrational state of the underlying proton core and eigenfunction of H_{coll}. The three contributions to the Hamiltonian are:

i. $H_{s.p.}$: the spherical shell model Hamiltonian.

ii. H_{coll}: the collective vibrational Hamiltonian. In the second quantization formalism, it yields

$$H_{coll} = \sum_{\mu=-2}^{2} \hbar\omega_2 (b^+_{2\mu} b_{2\mu} + 1/2), \tag{E.1}$$

in which $b^+_{2\mu}$ ($b_{2\mu}$) is a creation (annihilation) operator for a boson with spin 2 and $\hbar\omega_2$ the energy of the 2^+_1 vibrational state.

iii. H_{int}, accounting for the coupling of the valence nucleons with the underlying vibrational core. It equals

$$H_{int} = -\xi\hbar\omega_2\sqrt{\frac{\pi}{5}}\sum_{i=1}^{N}\sum_{\mu}(b_{2\mu} + (-1)^{\mu} b^+_{2,-\mu}) Y^{\mu}_2(\hat{r}_i). \tag{E.2}$$

The sum over i runs over all considered valence nucleons. ξ is the coupling strength parameter. It is related to the experimental $B(E_2; 0^+_1 \rightarrow 2^+_1)$ reduced transition probability and the excitation energy of the 2^+_1 vibrational state as [Hey94]

$$\xi = \langle r\frac{dV}{dr}\rangle \frac{\sqrt{B(E2; 0^+ \rightarrow 2^+_1)}}{\frac{3}{4\pi}ZeR_0^2\sqrt{\pi}\hbar\omega_2}. \tag{E.3}$$

Therefore, the following matrix needs to be diagonalised:

$$\begin{pmatrix} \langle 11^-_{s.p.} \mid H \mid 11^-_{s.p.}\rangle & \langle 11^-_{s.p.} \mid H \mid 11^-_{s.p.}\otimes 2^+;11^-\rangle \\ \langle 11^-_{s.p.}\otimes 2^+;11^- \mid H \mid 11^-\rangle & \langle 11^-_{s.p.}\otimes 2^+;11^- \mid H \mid 11^-_{s.p.}\otimes 2^+;11^-\rangle \end{pmatrix}, \tag{E.4}$$

in which

$$\begin{aligned} \langle 11^-_{s.p.} \mid H \mid 11^-_{s.p.}\rangle = E_1 &= E(11^-_{s.p.}) + E_{coll}(0^+) \\ &= E(11^-_{s.p.}) + \hbar\omega_2 5/2 \\ \langle 11^-_{s.p.}\otimes 2^+;11^- \mid H \mid 11^-_{s.p.}\otimes 2^+;11^-\rangle = E_2 &= E(11^-_{s.p.}) + E_{coll}(2^+) \\ &= E(11^-_{s.p.}) + \hbar\omega_2(1+5/2). \end{aligned}$$

It is sufficient to consider the relative energy $E_1 - E_2$ for the diagonal elements. For the off-diagonal elements, the shorthand notation $\langle V \rangle$ will be used.

$$\begin{aligned} \langle V \rangle &= \langle 11^-_{s.p.} \otimes 2^+; 11^- \mid H \mid 11^-_{s.p.} \rangle \\ &= \langle 11^-_{s.p.} \otimes 2^+; 11^- \mid H_{int} \mid 11^-_{s.p.} \rangle. \end{aligned} \tag{E.5}$$

The eigenvalues λ_- and λ_+ can be deduced by solving

$$\begin{vmatrix} 0-\lambda & \langle V \rangle \\ \langle V \rangle & \hbar\omega_2 - \lambda \end{vmatrix} = 0. \tag{E.6}$$

We get

$$\lambda_\pm = \frac{1}{2}\left[\hbar\omega_2 \pm \sqrt{(\hbar\omega_2)^2 + 4\langle V \rangle^2}\right]. \tag{E.7}$$

The values for $\hbar\omega_2$ are listed in the table of Raman et al. [Ram89]. For ^{198}Hg it yields 0.412 MeV. The interaction matrix element $\langle V \rangle$ can be calculated as

$$\langle V \rangle = \langle 11^-_{s.p.} \otimes 2^+; 11^- \mid H_{int} \mid 11^-_{s.p.} \rangle \tag{E.8}$$

$$= \langle 11^-_{s.p.} \otimes 2^+; 11^- \mid -\sqrt{\frac{\pi}{5}}\xi\hbar\omega_2 \sum_i b_2^+ . Y_2(\hat{r}_i) \mid 11^-_{s.p.} \rangle. \tag{E.9}$$

By applying the Wigner-Eckart theorem we get

$$\begin{aligned} \langle V \rangle &= -\sqrt{\frac{\pi}{5}}\xi\hbar\omega_2 \begin{pmatrix} 11 & 0 & 11 \\ -11 & 0 & 11 \end{pmatrix} \langle 11^-_{s.p.} \otimes 2^+; 11^- \| \sum_i b_2^+ . Y_2(\hat{r}_i) \| 11^-_{s.p.} \rangle \\ &= -\sqrt{\frac{\pi}{5}}\xi\hbar\omega_2 \frac{1}{\sqrt{23}} \langle 11^-_{s.p.} \otimes 2^+; 11^- \| \sum_i b_2^+ . Y_2(\hat{r}_i) \| 11^-_{s.p.} \rangle. \end{aligned} \tag{E.10}$$

Using the reduction rules for tensor products (see, e.g., in Ref. [Hey94]) this gives:

$$\begin{aligned} \langle V \rangle &= -\sqrt{\frac{\pi}{5}}\xi\hbar\omega_2 \frac{1}{\sqrt{23}} \sqrt{23}(-1)^{2+11+11} \begin{Bmatrix} 2 & 11 & 11 \\ 11 & 0 & 2 \end{Bmatrix} \\ &\quad \langle 11^-_{s.p.} \| \sum_i Y_2(\hat{r}_i) \| 11^-_{s.p.} \rangle \langle 2^+ \| b_2^+ \| 0^+ \rangle \end{aligned} \tag{E.11}$$

$$= -\sqrt{\frac{\pi}{5}}\xi\hbar\omega_2 \frac{1}{\sqrt{23}} \langle 11^-_{s.p.} \| \sum_i Y_2(\hat{r}_i) \| 11^-_{s.p.} \rangle. \tag{E.12}$$

By using expression (E.3) to write the interaction coupling strength, ξ, explicitly, this results in

$$\langle V\rangle = -\sqrt{\frac{\pi}{5}}\hbar\omega_2\frac{1}{\sqrt{23}}\langle r\frac{dV}{dr}\rangle\frac{\sqrt{B(E2;0^+\rightarrow 2_1^+)}}{\frac{3}{4\pi}ZeR_0^2\sqrt{\pi}\hbar\omega_2}\langle 11^-_{s.p.}\|Y_2(\hat{r}_i)\|11^-_{s.p.}\rangle. \tag{E.13}$$

The reduced matrix element $\langle 11^-_{s.p.}\|Y_2(\hat{r}_i)\|11^-_{s.p.}\rangle$ can be calculated via its relationship with the quadrupole moment $Q_s(11^-_{s.p.}) = Q_s(1h_{9/2}) + Q_s(1i_{13/2}) = -0.9696$ b [Sag88].

$$Q_s(11^-_{s.p.}) \equiv \sqrt{\frac{16\pi}{5}}\langle 11,11\mid\sum_i r_i^2Y_2^0(\hat{r}_i)\mid 11,11\rangle \tag{E.14}$$

$$\simeq \sqrt{\frac{16\pi}{5}}\langle r_{av}^2\rangle\langle 11,11\mid\sum_i Y_2^0(\hat{r}_i)\mid 11,11\rangle \tag{E.15}$$

$$= \sqrt{\frac{16\pi}{5}}\langle r_{av}^2\rangle\begin{pmatrix}11 & 2 & 11\\ -11 & 0 & 11\end{pmatrix}\langle 11^-_{s.p.}\|\sum_i Y_2(\hat{r}_i)\|11^-_{s.p.}\rangle \tag{E.16}$$

$$= \sqrt{\frac{16\pi}{5}}\langle r_{av}^2\rangle\sqrt{\frac{11\cdot 21}{23\cdot 25\cdot 12}}\langle 11^-_{s.p.}\|\sum_i Y_2(\hat{r}_i)\|11^-_{s.p.}\rangle. \tag{E.17}$$

The mean square radius $\langle r_{av}^2\rangle$ is taken as:

$$\langle r_{av}^2\rangle = \frac{1}{2}(\langle r^2_{1i_{13/2}}\rangle + \langle r^2_{1h_{9/2}}\rangle) \tag{E.18}$$

$$= \frac{1}{2}(42.20 + 36.36) = 39.28\ \text{fm}^2, \tag{E.19}$$

in which $\langle r^2_{1i_{13/2}}\rangle$ and $\langle r^2_{1h_{9/2}}\rangle$ are adopted from Ref. [Sag88]. By combining equations (E.17) and (E.19) we get

$$\langle 11^-_{s.p.}\|\sum_i Y_2(\hat{r}_i)\|11^-_{s.p.}\rangle = -4.258. \tag{E.20}$$

Using the result (E.20) in (E.13) and taking $\langle rdV/dr\rangle = 50$ MeV [Boh75] and $\sqrt{B(E2;0^+\rightarrow 2_1^+)} = 9900\ e^2\text{fm}^2$, we find for $\langle V\rangle$:

$$\langle V\rangle = -\sqrt{\frac{\pi}{5}}\frac{1}{\sqrt{23}}\frac{-4.258\times 50\times\sqrt{9900}\times 4\pi}{3\times(1.2)^2\times 194^{2/3}80\sqrt{\pi}} \tag{E.21}$$

$$= 2.11\ \text{MeV}. \tag{E.22}$$

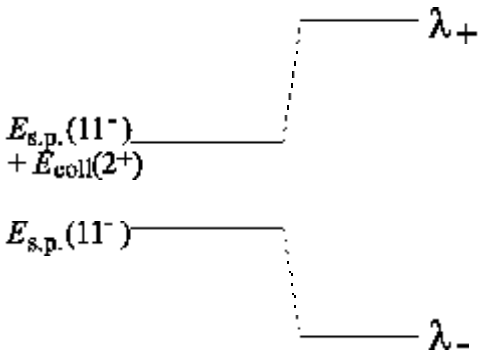

Figure E.1: *Schematic representation of the eigenvalues λ_- and λ_+ with respect to the single particle energy $E_{s.p.}(I^\pi = 11^-)$.*

By using $\hbar\omega_2 = 0.412$ MeV and $\langle V \rangle = 2.11$ MeV, we find for the eigenvalues $\lambda_\pm$ (E.7):

$$\lambda_+ = 2.330 \text{ MeV} \tag{E.23}$$

$$\lambda_- = -1.918 \text{ MeV}, \tag{E.24}$$

of which λ_- is the eigenvalue which is needed here (Figure E.1). The wave functions are determined from the equation:

$$\begin{pmatrix} 0 & \langle V \rangle \\ \langle V \rangle & \hbar\omega_2 \end{pmatrix} \begin{pmatrix} a \\ b \end{pmatrix} = \begin{pmatrix} \lambda_- & 0 \\ 0 & \lambda_+ \end{pmatrix} \begin{pmatrix} a \\ b \end{pmatrix} \tag{E.25}$$

or

$$0 \cdot a + \langle V \rangle b = \lambda_- a \tag{E.26}$$

$$b = \frac{\lambda_- a}{\langle V \rangle}. \tag{E.27}$$

The wave function becomes:

$$|\widetilde{11^-}\rangle = a\left[|\, 11^-_{s.p.}\rangle + \frac{\lambda_-}{\langle V \rangle} |\, 11^-_{s.p.} \otimes 2; 11^-\rangle\right], \tag{E.28}$$

in which a is scaled such that the norm of the wave function equals 1.

$$|\widetilde{11^-}\rangle = a\,|\, 11^-_{s.p.}\rangle + b\,|\, 11^-_{s.p.} \otimes 2^+; 11^-\rangle \tag{E.29}$$

$$= 0.741\,|\, 11^-_{s.p.}\rangle - 0.672\,|\, 11^-_{s.p.} \otimes 2^+; 11^-\rangle. \tag{E.30}$$

This wave function allows us to calculate the expectation value of the quadrupole operator $\hat{Q}_2^0$.

$$eQ_2^0 \equiv e\hat{Q}_{2,s.p.}^0 + e\hat{Q}_{2,coll}^0 \tag{E.31}$$

$$\equiv \sum_i e r_i^2 Y_2^0(\hat{r}_i) + \frac{3}{4\pi} ZeR_0^2 \sqrt{\frac{\hbar\omega_2}{2C}}(b_{20}^+ + b_{20}). \tag{E.32}$$

The spectroscopic quadrupole moment of the 11^- isomer becomes

$$eQ_s(\widetilde{11^-}) \equiv \langle 11, M=11 \mid e\hat{Q}_2^0 \mid 11, M=11\rangle \tag{E.33}$$

$$\equiv \sqrt{\frac{16\pi}{5}} \begin{pmatrix} 11 & 2 & 11 \\ -11 & 0 & 11 \end{pmatrix} \langle 11 \| e\hat{Q}_2 \| 11\rangle \tag{E.34}$$

$$= \sqrt{\frac{16\pi}{5}} \sqrt{\frac{11\cdot 21}{23\cdot 25\cdot 12}} \langle 11 \| e\hat{Q}_2 \| 11\rangle \tag{E.35}$$

$$= \sqrt{\frac{16\pi}{5}} \sqrt{\frac{11\cdot 21}{23\cdot 25\cdot 12}} \langle 11 \| \sum_i e r_i^2 Y_2(\hat{r}_i) + \frac{3}{4\pi} ZeR_0^2 \sqrt{\frac{\hbar\omega_2}{2C}}(b_2^+ + b_2) \| 11\rangle \tag{E.36}$$

$$= 0.580\, \langle 11 \| \sum_i e r_i^2 Y_2(\hat{r}_i) + \frac{3}{4\pi} ZeR_0^2 \sqrt{\frac{\hbar\omega_2}{2C}}(b_2^+ + b_2) \| 11\rangle. \tag{E.37}$$

The quadrupole moment contains the following three contributions:

$$A: \quad 0.580\, a^2 \langle 11^-_{s.p.} \| \sum_i e r_i^2 Y_2(\hat{r}_i) \| 11^-_{s.p.}\rangle = a^2 eQ_s(11^-_{s.p.}) \tag{E.38}$$

$$B: \quad 0.580\, b^2 \langle 11^-_{s.p.} \otimes 2^+; 11^- \| \sum_i e r_i^2 Y_2(\hat{r}_i) + \frac{3}{4\pi} ZeR_0^2 \sqrt{\frac{\hbar\omega_2}{2C}}(b_2^+ + b_2) \| 11^-_{s.p.} \otimes 2^+; 11^-\rangle \tag{E.39}$$

$$C: \quad 0.580\, 2ab \langle 11^-_{s.p.} \| \frac{3}{4\pi} ZeR_0^2 \sqrt{\frac{\hbar\omega_2}{2C}}(b_2^+ + b_2) \| 11^-_{s.p.} \otimes 2^+\rangle, \tag{E.40}$$

in which

$$\frac{3}{4\pi} ZeR_0^2 \sqrt{\frac{\hbar\omega_2}{2C}} \sqrt{5} = \sqrt{B(E2; 0^+ \to 2_1^+)}. \tag{E.41}$$

Contribution B splits up in two parts. The first part equals:

$$B1: \quad 0.580\, b^2 \langle 11^-_{s.p.} \otimes 2^+; 11^- \| \sum_i e r_i^2 Y_2(\hat{r}_i) \| 11^-_{s.p.} \otimes 2^+; 11^-\rangle$$

$$= \sqrt{23}\sqrt{23}\, b^2 \begin{Bmatrix} 11 & 11 & 2 \\ 11 & 11 & 2 \end{Bmatrix} \langle 11^-_{s.p.} \| \sum_i e r_i^2 Y_2(\hat{r}_i) \| 11^-_{s.p.} \rangle \quad \text{(E.42)}$$

$$= 0.580\, b^2\, 0.932\, \langle 11^-_{s.p.} \| \sum_i e r_i^2 Y_2(\hat{r}_i) \| 11^-_{s.p.} \rangle \quad \text{(E.43)}$$

$$= b^2\, 0.932\, eQ_s(11^-_{s.p.}). \quad \text{(E.44)}$$

The second part becomes:

$$B2: \quad 0.580\, b^2 \langle 11^-_{s.p.} \otimes 2^+; 11^- \| e\hat{Q}_2 \| 11^-_{s.p.} \otimes 2^+; 11^- \rangle \quad \text{(E.45)}$$

$$= 0.580\, b^2\, 23\, \langle 2^+ \| e\hat{Q}_2 \| 2^+ \rangle \begin{Bmatrix} 2 & 11 & 11 \\ 11 & 2 & 2 \end{Bmatrix}. \quad \text{(E.46)}$$

By applying the Wigner-Eckart theorem, the quadrupole moment of the 2^+ state in the underlying Hg-core yields:

$$eQ_s(Hg(2^+)) \equiv \sqrt{\frac{16\pi}{5}} \begin{pmatrix} 2 & 2 & 2 \\ 2 & 0 & 2 \end{pmatrix} \langle 2^+ \| e\hat{Q}_{2,coll} \| 2^+ \rangle \quad \text{(E.47)}$$

$$= \sqrt{\frac{2 \cdot 3}{5 \cdot 7 \cdot 3}} \sqrt{\frac{16\pi}{5}} \langle 2^+ \| e\hat{Q}_{2,coll} \| 2^+ \rangle. \quad \text{(E.48)}$$

It follows that

$$\langle 2^+ \| e\hat{Q}_{2,coll} \| 2^+ \rangle = 1.32\, eQ_s(Hg(2^+)). \quad \text{(E.49)}$$

The contribution $B2$ becomes:

$$B2: \quad 0.580\, b^2\, 23\, (-0.0485)\, 1.32\, eQ_s(Hg(2^+)) = -b^2\, 0.856\, eQ_s(Hg(2^+)). \quad \text{(E.50)}$$

Contribution C equals:

$$C: \quad 0.580\, 2ab \langle 11^-_{s.p.} \| \frac{3}{4\pi} Ze R_0^2 \sqrt{\frac{\hbar\omega_2}{2C}} (b_2^+ + b_2) \| 11^-_{s.p.} \otimes 2^+ \rangle \quad \text{(E.51)}$$

$$= 0.580\, 2ab \frac{3}{4\pi} Ze R_0^2 \sqrt{\frac{\hbar\omega_2}{2C}}\, 23 \langle 0 \| b_2 \| 2^+ \rangle \begin{Bmatrix} 0 & 11 & 11 \\ 11 & 2 & 2 \end{Bmatrix} \quad \text{(E.52)}$$

$$= 0.580\, 2ab \frac{3}{4\pi} Ze R_0^2 \sqrt{\frac{\hbar\omega_2}{2C}} \sqrt{5} \sqrt{\frac{23}{5}} \quad \text{(E.53)}$$

$$= 0.580\, 2ab \sqrt{B(E2; 0^+ \to 2_1^+)} \sqrt{\frac{23}{5}} \quad \text{(E.54)}$$

$$= 2ab\, 1.24\, \sqrt{B(E2; 0^+ \to 2_1^+)}. \quad \text{(E.55)}$$

The quadrupole moment for the 11^- state becomes

$$Q_s(\widetilde{11^-}) = a^2 Q_s(11^-_{s.p.}) + b^2 0.932\, Q_s(11^-_{s.p.}) \quad \text{(E.56)}$$

$$- \; b^2\, 0.856\, Q_s(Hg(2^+)) + 2ab\, 1.24 \sqrt{B(E2;0^+ \to 2_1^+)}. \quad \text{(E.57)}$$

By using

$$a = 0.741 \quad \text{(E.58)}$$

$$b = -0.672 \quad \text{(E.59)}$$

$$Q_s(11^-_{s.p.}) = -0.9696 \text{ b} \quad \text{[Sag88]} \quad \text{(E.60)}$$

$$B(E2;0^+ \to 2_1^+) = 0.990\ e^2\text{b}^2 \quad \text{[Ram89]} \quad \text{(E.61)}$$

$$Q_s(\text{Hg}(2_1^+)) = 0.82 \text{ b} \quad \text{[Esa77]}, \quad \text{(E.62)}$$

we find

$$Q_s(^{200}\text{Pb}(I^\pi = 11^-)) = -2.89 \text{ b}. \quad \text{(E.63)}$$

Samenvatting

Fysische achtergrond

Een kern bevat 1 tot 300 deeltjes die bijeen gehouden worden door de sterke interactie. De vele deeltjes maken een microscopische beschrijving, waarbij elk deeltje in rekening gebracht wordt, onmogelijk. Toch zijn er te weinig deeltjes om een statistische beschrijving toe te laten. Kernfysici behelpen zich daarom met kernmodellen. Die modellen worden getest door bepaalde fysische grootheden, zoals de vervorming, het magnetische moment of de excitatieënergieën van de aangeslagen toestanden van een kern te meten en de experimentele resultaten te vergelijken met de waarden die het model voorspelt. De experimentele informatie is vooral belangrijk voor kerntoestanden onder extreme omstandigheden, meer bepaald voor kerntoestanden met een hoge excitatieënergie E, een hoge spin I, een hoog neutrongetal N, of een hoog protongetal Z. Juist daar is de kans groot dat eventuele tekortkomingen van de modellen aan het licht komen.

Deze thesis spitst zich toe op een studie van metastabiele kerntoestanden, ook 'isomere toestanden' genoemd, bij hoge excitatieënergie en hoge spin. Door hun lange levensduur zijn isomeren interessante studieobjecten. We kunnen ons al onmiddellijk afvragen waarom hun verval vertraagd verloopt. De oorzaak is altijd dat een eigenschap van de isomere toestand teveel verschilt van de toestand waarnaar hij vervalt, hetzij de vorm ('vormisomeren'), hetzij de spin ('spinisomeren'), hetzij de orientatie van zijn spin t.o.v. de symmetrie-as van de kern ('K-isomeren', waarbij K gedefinieerd is als de projectie van spin op de symmetrie-as van de kern). Bovendien geeft de lange levensduur ons experimentele toegang tot eigenschappen die anders niet meetbaar zijn. Door hun levensduur kunnen

isomeren immers interageren met magnetische en/of elektrische velden, wat ons toelaat om het magnetische moment $\vec{\mu}$ en het spektroscopische quadrupoolmoment Q_s te meten. Het spektroscopische quadrupoolmoment geeft ons informatie over de vervorming van de kern. Voor vervormde kernen kan de vervorming β uit Q_s berekend worden als

$$Q_s = Q_0 \frac{3K^2 - I(I+1)}{(I+1)(2I+3)}$$
$$Q_0 = \frac{3}{\sqrt{5\pi}} Z R_0^2 \beta$$

met β de quadrupooldeformatie, Q_0 het intrinsiek quadrupoolmoment en R_0 de straal van een bolvormige kern met hetzelfde volume.

Eén van de belangrijkste kernmodellen is het schillenmodel [May49]. Dit model steunt op het feit dat bepaalde proton- en/of neutronaantallen (ook de magische getallen genoemd) resulteren in een extra stabiele kern, naar analogie met de edelgassen in de atomaire fysica. Daarom wordt in het schillenmodel verondersteld dat de nucleonen onafhankelijk van elkaar bewegen in een gemiddelde potentiaal, die de nucleonen zelf creëren. Die veronderstelling maakt het mogelijk om de kern te beschrijven als een bolvormige romp met enkele valentienucleonen (deeltjes of gaten) daar rond. Als er verschillende valentienucleonen buiten de bolvormige romp aanwezig zijn, moet ook hun onderlinge interactie (de residuele interactie) en, in een volgende stap, het polariserend effect van de nucleonen op de romp in rekening gebracht worden. Dit heeft als gevolg dat kernen met een proton- en een neutrongetal tussen de magische getallen in vervormd zijn. Merk op dat soms ook voor kernen met een magisch proton- en/of neutrongetal vervormde kerntoestanden bij lage excitatieënergieën voorkomen.

De excitatie van een kern in de buurt van een gesloten schil gebeurt in de eerste plaats door individuele nucleonen te exciteren. Vervormde axiaal-symmetrische kernen daarentegen kunnen daarnaast ook als een geheel roteren rond een as die loodrecht op hun symmetrie-as staat. Kwantummechanisch is er geen rotatie rond een symmetrie-as mogelijk, omdat dit resulteert in een kerntoestand die niet te onderscheiden is van de oorspronkelijke toestand. Dat is de reden waarom bolvormige kernen niet kunnen roteren.

Experimentele resultaten tonen aan dat het beeld, zoals hierboven geschetst, te eenvoudig is. De $_{82}$Pb kernen b.v. hebben een gesloten $Z = 82$ protonschil. Daarom neemt men aan dat deze kernen bolvormig zijn. Nochtans zijn er in deze kernen rotatiebanden waargenomen [Bal91, Ami00]. Deze rotatiebanden kunnen nu verklaard worden binnen het kader van de 'theorie met schuine rotatieas' (Engels : 'tilted axis cranking (TAC) theory'). De theorie toont aan dat deze kerntoestanden kunnen roteren omwille van een asymmetrische stroomverdeling [Fra00a], daar waar vervormde kernen kunnen roteren omwille van hun asymmetrische ladingsverdeling. Deze nieuwe vorm van rotatie heeft daarom de naam 'magnetische rotatie' gekregen, als tegenhanger van de 'elektrische rotatie' van vervormde kernen. Experimenteel kan men magnetische van elektrische rotors onderscheiden door o.a. de vervorming van deze kerntoestanden te meten.

Nog andere interessante fenomenen doen zich voor in de buurt van de gesloten schillen. Experimenteel heeft men deeltje-gatexcitaties doorheen de magische schil waargenomen met excitatieënergieën die lager liggen dan wat het schillenmodel voorspelt [VD84, Hey83, Woo92]. Nu begrijpt men dat dit zo is omdat de valentiedeeltjes zich in de zogenaamde 'indringorbitalen' bevinden. Deze orbitalen verminderen hun energie t.o.v. de schillenmodelenergie als de kern zich gaat vervormen. In het loodgebied gaat het om de orbitalen van de $\pi 1h_{9/2}$ en de $\pi 1i_{13/2}$ protonen. Bovendien is het zo dat even-deeltjes-even-gatexcitaties energetisch voordeliger zijn dan oneven-deeltjes-oneven-gatexcitaties. Zo heeft men onlangs ontdekt dat de 2-deeltjes-2-gat- en de 4-deeltjes-4-gatexcitaties de laagste aangeslagen toestanden doorheen de $Z = 82$-schil in de ^{186}Pb-kern zijn [And00]. Dit toont aan dat, naast de vervorming van de kern, ook de paring een belangrijke rol speelt in de verklaring van deze kerntoestanden.

De combinatie van vervorming (het deel van de nucleon-nucleoninteractie met een ver bereik) en paring (het deel van de nucleon-nucleoninteractie met een kort bereik) is eveneens belangrijk voor het verklaren van de kernstructuur ver van de gesloten schillen. Zo is het traagheidsmoment van een elektrische rotor een factor 3 kleiner dan het traagheidsmoment van een star lichaam. Dat is een gevolg van de paringcorrelaties tussen de nucleonen. De grondtoestand van een kern bestaat

uit een superpositie van $I^\pi = 0^+$ gepaarde configuraties. Deze paring van twee fermionen is vergelijkbaar met de elektron-elektronparing in supergeleidende materialen. Supergeleiders verliezen hun eigenschappen door warmte en/of de aanwezigheid van magnetische velden. In kernen breken de interne excitatieënergie en de collectieve rotatie de paringcorrelaties. Het belangrijkste verschil tussen kernen en supergeleiders is het aantal deeltjes. Het beperkt aantal deeltjes in een kern heeft als gevolg dat er geen scherpe faseovergang plaats vindt, maar dat de paring stap voor stap verbroken wordt. Hierbij kan men zich de vraag stellen hoeveel paren er moeten gebroken worden vooraleer alle paringcorrelaties geblokkeerd zijn [Wal99]. Experimenteel kan men dit doen door het meten van het traagheidsmoment van een rotatieband gebouwd op een toestand met veel ongepaarde deeltjes (een 'multi-quasideeltjestoestand') en dat te vergelijken met het traagheidsmoment van een star lichaam. Als alle paringcorrelaties geblokkeerd zijn, verwacht men dat die twee traagheidsmomenten gelijk zijn aan elkaar. Het is evenwel belangrijk op te merken dat het traagheidsmoment niet alleen van de paring, maar ook van de vervorming van de kern afhangt. Tot nu toe veronderstelt men dat de vervorming van de grondtoestand en de vervorming van een multi-quasideeltjestoestand gelijk zijn aan elkaar. Er zijn echter maar weinig vervormingen van multi-quasideeltjestoestanden experimenteel bepaald en de vraag stelt zich dan ook of we die veronderstelling mogen maken. Merk ten slotte nog op dat de individuele spins van de quasideeltjes dikwijls koppelen tot een totale spin met een hoge K-waarde, zodat er relatief veel isomere multi-quasideeltjestoestanden in de natuur voorkomen.

Een eerder nieuwe benadering die toelaat de K-isomeren en de magnetische rotors theoretisch te beschrijven, is de TAC-theorie [Fra00a]. Dit model berekent de golffuncties van de kern in een roterend assensysteem. De rotatieas is niet evenwijdig met één van de hoofdassen van de kern. De gebruikte residuele interacties (de residuele interactie V_{res} is het verschil tussen de Hamiltoniaan H en de schillenmodelhamiltoniaan H_{sh}) zijn de paringsinteractie en de quadrupool-quadrupoolinteractie. Deze laatste is evenredig met $\hat{Q} \cdot \hat{Q}$, waarbij $\hat{Q}$ de quadrupooloperator is. De evenredigheidsconstante zal verder als χ geno-

teerd worden. Zowel de magnetische rotors als de K-isomeren hebben een spin die niet evenwijdig is met een hoofdas. In het geval van de magnetische rotors is dat omdat de proton- en de neutronspin in goede benadering loodrecht op elkaar staan en de protonspin ongeveer evenwijdig is met de symmetrie-as van de kern. In de rotatiebanden met een hoog K-kwantumgetal heeft de spin uiteraard een grote component evenwijdig met de symmetrie-as, namelijk K, en een component loodrecht op de symmetrie-as, namelijk de bijdrage tot de spin ten gevolge van collectieve rotatie. Ook in deze banden valt de richting van de totale spin dus niet samen met één van de hoofdassen.

Het woord 'vervorming' loopt als een rode draad doorheen deze inleiding. Het experimenteel bepalen van de vervorming van kerntoestanden vormt dan ook een cruciale test voor de kernmodellen. Ondanks het belang van deze parameter, blijkt uit literatuurstudies dat voor opvallend weinig kerntoestanden de vervorming experimenteel bepaald is. De enige indringtoestanden in het loodgebied waarvan de deformatie gemeten is, zijn de grondtoestanden in de ^{185,186}Au-kernen [Wal87] en de oneven $^{181-185}$Hg-kernen [Bon72, Ulm86] en de $(I^\pi = 9/2^-)$- en $(I^\pi = 13/2^+)$-isomeren in de respectievelijke oneven $^{189-193}$Tl- [Bou85] en $^{185-199}$Hg-kernen [Ulm86]. Ook in de kernen met massagetal $A \approx 180$ zijn enkel de deformaties van de ^{182}Os$(I^\pi = K^\pi = 25^+)$- [Bro91], de ^{178}Hf$(I^\pi = K^\pi = 16^+)$- [Boo94, Lub96] en de ^{177}Lu$(I^\pi = K^\pi = 23/2^-)$- [Geo98] isomeren gemeten. Verder was voor de aanvang van dit werk was nog geen enkele meting van de vervorming van een magnetische rotor gebeurd. Deze thesis heeft zich dan ook als doel gesteld om de spektroscopische quadrupoolmomenten van de ^{196}Pb$(I^\pi = 11^-)$-indringisomeer en de 5-quasideeltjes-^{179}W$(I^\pi = K^\pi = 35/2^-)$-K-isomeer experimenteel te bepalen. Kennis van het quadrupoolmoment van de ^{196}Pb$(I^\pi = 11^-)$-isomeer zal ook toelaten om het quadrupoolmoment van de ^{196}Pb$(I^\pi = 16^-)$-toestand af te leiden. Dit is de eerste, zij het onrechtstreekse, experimentele bepaling van het quadrupoolmoment van een magnetische rotor. De techniek die voor de quadrupoolmomentmetingen gebruikt is, is toestandsmengingsspektroscopie (Engels : 'level mixing spectroscopy (LEMS)'). Die techniek is tijdens de jaren '80 in Leuven door de groep o.l.v.

Prof. Coussement ontwikkeld en is zeer geschikt voor het meten van spektroscopische quadrupoolmomenten van isomeren met hoge spin [Har91b]. Ook andere informatie, zoals elektrische veldgradiënten (EVG), kan men uit zo'n meting afgeleiden.

Het quadrupoolmoment van de ^{194,196}Pb($I^\pi = 11^-$)-isomeren

De ^{196}Pb isomeer heeft de $(\pi 3s_{1/2}^{-2} 1h_{9/2} 1i_{13/2})_{11^-}$ intruderconfiguratie. Deze isomeer vermindert zijn energie t.o.v. de overeenkomstige schillenmodelenergie door een oblate vervorming aan te nemen en het $1i_{13/2}$-proton, het $1h_{9/2}$-proton en de $3s_{1/2}$-gaten in het respectievelijke $13/2^+[606]$-, het $9/2^+[505]$- en het $1/2^+[400]$-orbitaal te plaatsen. De experimentele waarde voor het quadrupoolmoment is $Q_s = (-)3.41(66)$ b.

Een vergelijking met het geschatte quadrupoolmoment $Q_s = (-)2.06(31)$ b van de corresponderende normale toestand, de $(\pi 1h_{9/2} 1i_{13/2})_{11^-}$-toestand in ^{198}Po, leert ons dat de aanwezigheid van de $3s_{1/2}$ gaten in de $(Z = 82)$-protonromp een sterkere vervorming van de isomere toestand in Pb tot gevolg heeft. Bovendien toont een vergelijking met de quadrupoolmomenten van de $(\pi 3s_{1/2}^{-2} 1h_{9/2})$-isomeer in ^{185}Tl en de $(\pi 1h_{9/2})$-grondtoestand in ^{197}Bi aan dat ook de aanwezigheid van het $1i_{13/2}$-valentieproton naast het $1h_{9/2}$-valentieproton voor een sterkere polarisatie van de kernromp zorgt. Intuitief is het gemakkelijk te vatten dat 2 valentienucleonen in nagenoeg parallelle orbitalen (dit is het geval voor de 11^--isomeren in Pb en Po) de kernromp sterker zullen polariseren dan 1 valentienucleon (dit is het geval voor de $9/2^-$- toestanden in Bi en Tl). Meer algemeen toont een systematische studie aan dat, als meerdere valentienucleonen in min of meer parallelle orbitalelen aanwezig zijn, de kernromp meer gepolariseerd wordt. Dit resulteert in grotere effectieve ladingen (de effectieve lading is gedefineerd als $e^{eff} = Q_s/Q_{s.p.}$, waarbij $Q_{s.p.}$ het quadrupoolmoment is dat men bekomt door de quadrupoolmomenten van de individuele protonen op te tellen in het speciale geval van gestrekte koppeling).

Merk op dat zowel van de ^{198}Po($I^\pi = 11^-$)-, als van de ^{195}Tl($I^\pi = 9/2^-$)-isomeer en de ^{197}Bi($I^\pi = 9/2^-$)-grondtoestand het quadrupoolmoment nog niet

gemeten is. Het quadrupoolmoment voor de ^{195}Tl($I^\pi = 9/2^-$)-isomeer is geëxtrapoleerd uit de systematiek van de quadrupoolmomenten van de $^{189-193}$Tl($I^\pi = 9/2^-$)-ketting. De waarden voor de quadrupoolmomenten van de ^{198}Po($I^\pi = 11^-$)- en de ^{197}Bi($I^\pi = 9/2^-$)-toestanden zijn geëxtraheerd uit de gemeten quadrupoolmomenten van de corresponderende ($N = 126$)-toestanden. Hierbij is verondersteld dat voor alle protonconfiguraties de verhouding $Q_s(N < 126)/Q_s(N = 126)$ dezelfde is als die voor de $(\pi h^2_{9/2})_{8^+}$-isomeren in de ^{A}Po-ketting. Het zou goed zijn om de geldigheid van deze veronderstellingen experimenteel na te gaan. Daarom is onlangs een project gestart om de quadrupoolmomenten van de 11^--isomeren in de ^{A}Po-ketting te meten. Ook de $9/2^-$-isomeer in ^{195}Tl lijkt een goede kandidaat voor een toekomstig experiment.

De verhoudingen van de quadrupoolmomenten van de 11^-- en de $9/2^-$-toestanden kunnen gereproduceerd worden door schillenmodellenberekeningen die de koppeling van de valentieprotonen met de quadrupoolvibraties van de onderliggende romp in rekening brengen (een Hg-romp voor de ^{195}Tl($I^\pi = 9/2^-$)- en de ^{196}Pb($I^\pi = 11^-$)-isomeren en een Pb-romp voor de ^{197}Bi($I^\pi = 9/2^-$)-grondtoestand en de ^{198}Po($I^\pi = 11^-$)-isomeer). Dit betekent dat, ondanks het feit dat de absolute waarden niet gereproduceerd worden, de berekeningen de correcte trend voor de quadrupoolmomenten voorspellen. Ze brengen m.a.w. de romppolarisatie op een correcte manier in rekening. Voor een systematische vergelijking van de theoretische en experimentele waarden ontbreken evenwel experimenteel bepaalde quadrupoolmomenten. Slechts voor een beperkt aantal ^{A}Hg en ^{A}Pb-isotopen zijn de quadrupoolmomenten van de eerste geëxciteerde toestanden bekend. Dit beperkt de berekende quadrupoolmomenten tot $^{200-206}$Pb($I^\pi = 11^-$), $^{199-205}$Tl($I^\pi = 9/2^-$), $^{206-210}$Po($I^\pi = 11^-$) en $^{205-209}$Bi($I^\pi = 9/2^-$). Enkel voor de ^{210}Po($I^\pi = 11^-$) en de ^{207,209}Bi($I^\pi = 9/2^-$)-toestanden zijn de quadrupoolmomenten gemeten. Een vergelijking toont aan dat zowel voor de ^{210}Po($I^\pi = 11^-$)-isomeer als voor de ^{209}Bi($I^\pi = 9/2^-$)-grondtoestand (beiden hebben als neutrongetal $N = 126$) de berekende waarde voor het quadrupoolmoment groter is dan de experimentele waarden. Voor de ^{207}Bi($I^\pi = 9/2^-$)-grondtoestand ($N = 124$) daarentegen is er goede overeenkomst tussen de berekende en de

experimentele waarde. Deze vaststelling leidt tot de vraag of er voor neutrongetallen kleiner dan 124 nog altijd een goede overeenkomst tussen de berekende en de gemeten waarden is, dan wel of de berekende waarden kleiner zullen zijn dan de experimentele. Ook om deze vraag te kunnen beantwoorden, zijn meer gemeten quadrupoolmomenten noodzakelijk. Ondertussen is er ook een systematische theoretische studie van de regio, waarbij ook octupoolvibraties in rekening gebracht worden, bezig. De eerste resultaten, $Q_s(^{196}\mathrm{Pb}(I^\pi = 11^-)) = -3.54$ b en $Q_s(^{198}\mathrm{Po}(I^\pi = 11^-)) = -1.4$ b, zijn veelbelovend [Oro01].

De meting van het quadrupoolmoment van de 11^--isomeer in ^{196}Pb is ook bijzonder interessant, omdat het dezelfde $(\pi s_{1/2}^{-2} 1h_{9/2} 1i_{13/2})$-protonconfiguratie als een magnetisch bandhoofd heeft. De koppeling van het quadrupoolmoment van de 11^--isomeer met het quadrupoolmoment van de 12^+-isomeer in ^{196}Pb laat toe het quadrupoolmoment van het $(I^\pi = 16^-)$-bandhoofd in ^{196}Pb af te leiden. De 12^+-isomeer heeft dezelfde $(\nu i_{13/2}^{-2})$-neutronconfiguratie als het magnetisch bandhoofd en zijn quadrupoolmoment werd reeds voor de aanvang van dit werk gemeten [Zyw81]. De koppeling resulteert in $Q_s(^{196}\mathrm{Pb}(I^\pi = 16^-)) = -0.316(97)$ b voor het magnetische bandhoofd. Deze kleine waarde toont aan dat magnetische rotatie de enige verklaring is voor de waarneming van de rotatieband gebouwd op de 16^--toestand. TAC-berekeningen tonen aan dat de quadrupoolkoppelingconstante χ verschillend is voor protonen en neutronen, in tegenstelling tot wat meestal aangenomen wordt [Chm].

Het quadrupoolmoment van de $^{196}\mathrm{Pb}(I^\pi = 11^-)$-isomeer is in werkelijkheid bepaald door de quadrupoolinteractiefrequentie, $\nu_Q = eQ_sV_{ZZ}/h$, van deze isomeer in Re te meten. Om het quadrupoolmoment te bepalen, is het dus nodig dat we de EVG (V_{ZZ}) kennen. De experimentele waarde voor de frequentie ν_Q van de 12^+-isomeer in ^{196}Pb heeft toegelaten om de veldgradiënt af te leiden: $V_{ZZ} = (-)2.42(27) \cdot 10^{21}$ V/m^2. Ook de $^{196}\mathrm{Pb}(12^+)$-isomeer is immers bevolkt tijdens het experiment en, zoals hoger vermeld, is het quadrupoolmoment van deze isomeer reeds voor de aanvang van dit werk gemeten [Zyw81]. De bekomen waarde voor de elektrische veldgradiënt past perfect in de systematiek van de gemeten veldgradiënten voor verschillende onzuiverheden in Re als functie van

het aantal valentieëlektronen.

Tijdens de experimenten op het 11^--isomeer in ^{196}Pb zijn ook de 11^-- en de 12^+-isomeren in ^{194}Pb geproduceerd. Uit de analyse van de γ-overgangen onder de $(11^- \rightarrow 12^+)$-cascade kan het quadrupoolmoment van de ^{194}Pb$(I^\pi = 11^-)$-isomeer bepaald worden als $Q_s = (-)4.12(79)$ b. Dit is de eerste experimentele toepassing van de LEMS-techniek waarbij de storing van twee opeenvolgende isomeren in rekening gebracht is. Een vergelijking van de waarde voor de EVG van Pb in Re die uit de analyse van de $(11^- \rightarrow 12^+)$-cascade bekomen is, $V_{ZZ} = (-)2.21^{+0.25}_{-0.22} \cdot 10^{21}$ V/m^2, met de waarde van de EVG voor ^{196}Pb in Re levert het experimentele bewijs voor de geldigheid van het formalisme. Beide waarden zijn immers in goede overeenstemming.

Het quadrupoolmoment van de $I^\pi = K^\pi = 35/2^-$-isomeer in ^{179}W

In een andere reeks experimenten is het quadrupoolmoment van de $(K^\pi = 35/2^-)$-5-quasideeltjesisomeer in ^{179}W gemeten als $Q_s = 4.00^{+0.83}_{-1.06}$ b. Deze waarde komt overeen met een intrinsiek quadrupoolmoment $Q_0 = 4.73^{+0.98}_{-1.25}$ b en een quadrupooldeformatie $\beta = 0.185^{+0.038}_{-0.049}$. Deze waarden verschillen aanzienlijk van de quadrupoolmomenten van de grondtoestand en zijn niet in overeenstemming met de huidige theoretische voorspellingen in deze regio. Zo resulteren de TAC-berekeningen in een waarde $Q_s = 5.73$ b of een waarde $Q_s = 5.84$ b, naargelang de manier waarop de paring en het probleem van het behoud van het correcte aantal deeltjes in de kern dat hiermee gepaard gaat, in rekening gebracht is. Er is slechts één ander isomeer met hoge K-waarde gekend waarvan het quadrupoolmoment afwijkt van het quadrupoolmoment van de grondtoestand, namelijk de $(K^\pi = 25^+)$-isomeer in ^{182}Os [Bro91]. Hier neemt men aan dat een triaxiale kernvorm de oorzaak is van de afwijking [Xu98], terwijl voor de $(K^\pi = 35/2^-)$-isomeer nog een consistente verklaring ontbreekt.

Merk echter op dat niet het spektroscopische quadrupoolmoment zelf, maar de quadrupoolinteractiefrequentie ν_Q gemeten wordt. De ^{179}W-kernen zijn in een Tl-gastrooster dat opgewarmd is tot een temperatuur van 473 K, ingeplant. We moeten dus de EVG van W in Tl kennen om het quadrupoolmoment te

kunnen afleiden. Gelineariseerde veredelde vlakke-golfberekeningen (Engels : 'linearised augmented plane wave (LAPW) calculations') resulteren in $V_{ZZ}(0$ K$) = 2.54 \cdot 10^{21}$V/m^2. Om de temperatuursafhankelijkheid van de veldgradiënt te bepalen werd de omgekeerde LEMS-methode (Engels : 'inverted LEMS technique') voor het eerst toegepast. Net zoals bij een normale LEMS-meting zijn de kernen onderhevig aan een gecombineerde magnetische dipool- en elektrische quadrupoolinteractie. Bij een normale LEMS-meting wordt de anisotropie van de straling gemeten als functie van het uitwendig aangelegd magneetveld, waarbij de quadrupoolinteractiefrequentie constant gehouden wordt. Bij de omgekeerde LEMS-methode wordt het magneetveld constant gehouden. De meting gebeurt als functie van de quadrupoolinteractiefrequentie, die gevarieerd wordt door de temperatuur van het gastrooster te veranderen. De helling van de aldus bekomen curve hangt af van de sterkte van de temperatuursafhankelijkheid. Als we aannemen dat de $T^{3/2}$-wet, $V_{ZZ}(T) = V_{ZZ}(0$ K$)(1 - bT^{3/2})$, voor de temperatuursafhankelijkheid van de EVG geldig is, vinden we de experimentele waarde $b = 7.6^{+0.2}_{-0.4} \cdot 10^{-5}$ K$^{-3/2}$ en $V_{ZZ}(473$ K$)= 0.55^{+0.12}_{-0.08}$. Er bestaan echter experimentele data voor ^{201}Pb in Tl die aantonen dat een lineaire temperatuursafhankelijkheid voor de EVG niet uitgesloten is [Iva92]. Dit zou betekenen dat Tl het eerste $(s-p)$-materiaal is, waarvoor de $T^{3/2}$-wet niet opgaat. Als we een lineaire temperatuursafhankelijkheid, $V_{ZZ}(T) = V_{ZZ}(0$ K$)(1 - cT)$ voor de EVG veronderstellen, vinden we als resultaten: $c = 1.778^{+0.053}_{-0.081} \cdot 10^{-3}$ K^{-1} en $V_{ZZ}(473$ K$)= 0.404^{+0.097}_{-0.075} \cdot 10^{21}$ V/m^2. Dit resulteert in een spectroscopisch quadrupoolmoment $Q_s(^{179}\mathrm{W}(I^\pi = 35/2^-) = 5.4^{+1.3}_{-1.5}$ b, een intrinsiek quadrupoolmoment $Q_0 = 6.4^{+1.5}_{-1.8}$ b en een quadrupooldeformatie $\beta = 0.250^{+0.059}_{-0.070}$. Deze waarden zijn in overeenstemming met de theoretische voorspellingen. De waarde voor het intrinsieke quadrupoolmoment is dan echter hoger dan een andere, onafhankelijke experimentele waarde. Het is namelijk mogelijk om het intrinsieke quadrupoolmoment te bepalen uit de verhouding van de intensiteiten van de γ-overgangen in de $(K^\pi = 35/2^-)$-rotatieband in combinatie met de gemeten g-factor [Byr98, Dra00]. Deze data resulteren in $Q_0 = 3.9(1.5)$ b.

Deze resultaten tonen aan dat een directe meting van de EVG van W in Tl

en zijn temperatuursafhankelijkheid meer dan wenselijk is. We hopen dan ook om zo'n meting te kunnen uitvoeren in de nabije toekomst.

Besluit

De metingen hebben aangetoond dat zowel het schillenmodel, als het TAC-model, de kerneigenschappen kwalitatief goed beschrijven. Schillenmodelberekeningen die de koppeling van de valentieprotonen met de quadrupoolvibraties van de onderliggende romp in rekening brengen, reproduceren de verhoudingen van de beschouwde quadrupoolmomenten. Het quadrupoolmoment van het $(I^\pi = 16^-)$ magnetische bandhoofd is inderdaad klein. Dit bevestigt het principe van de magnetische rotatie, wat één van de belangrijkste verwezenlijkingen van het TAC-model is. Kwantitief gezien zijn er nog verbeteringen mogelijk. Zoals hoger vermeld, onderzoekt men momenteel de invloed van de octupoolvibraties op de quadrupoolmomenten in het loodgebied. De koppelingsconstante χ is niet altijd dezelfde voor protonen en neutronen in het TAC-model. Geen van de huidige theorieën lijkt in staat om de lage waarde voor het quadrupoolmoment van de $(I^\pi = 35/2^-)$-isomeer in ^{179}W te reproduceren.

Bibliography

[Alb78] G. Albouy, G. Auger, J. M. Lagrange, M. Pautrat, H. Richel, C. Roulet, H. Sergolle, and J. Vanhorenbeeck, Nucl. Phys. **A303** (1978) 521.

[Ald56] K. Alder, A. Bohr, T. Huus, B. Mottelson, and A. Winther, Rev. Mod. Phys. **28** (1956) 432.

[Ald75] K. Alder and R. M. Steffen, in *The Electromagnetic Interaction in Nuclear Spectroscopy*, p. 1, (North-Holland, Amsterdam, 1975), edited by W. D. Hamilton.

[Ale64] P. Alexander, F. Boehm, and E. Kankeleit, Phys. Rev. **133** (1964) B284.

[Alm] D. Almehed and *et al.*, to be published.

[Ami00] Amita, A. K. Jain, and B. Singh, Atomic Data Nucl. Data Tables **74** (2000) 283.

[And78] H. R. Andrews, R. L. Graham, J. S. Geiger, J. R. Beene, O. Häusser, D. Ward, and D. Horn, Hyperfine Interact. **4** (1978) 110.

[And00] A. N. Andreyev, M. Huyse, P. Van Duppen, L. Weissman, D. Ackermann, J. Gerl, F. P. Heßberger, S. Hofmann, A. Kleinböhl, G. Münzenberg, S. Reshitko, C. Schlegel, H. Schaffner, P. Cagarda, M. Matos, S. Saro, A. Keenan, C. Moore, C. D. O'Leary, R. D. Page, M. Taylor, H. Kettunen, M. Leino, A. Lavrentiev, R. Wyss, and K. Heyde, Nature **405** (2000) 430.

[Bal91] G. Baldsiefen, H. Hübel, D. Mehta, B. V. T. Rao, U. Birkental, G. Frölingsdorf, M. Neffgen, N. Nenoff, S. C. Pancholi, N. Singh, W. Schmitz, K. Theine, P. Willsau, H. Grawe, J. Heese, H. Kluge, K. H. Maier, M. Schramm, R. Schubart, and H. J. Maier, In *Proceedings of the Xth International School on Nuclear Physics and Nuclear Energy (Varna)*, (ed. W. Andreitscheff and D. Elenkov, University of Sofia, 1991), and Phys. Lett. **B275** (1992) 252.

[Bal94] G. Baldsiefen, H. Hübel, W. Korten, D. Mehta, N. Nenoff, B. V. Thirumala Rao, and P. Willsau, Nucl. Phys. **A574** (1994) 521.

[Bal96] G. Baldsiefen, H. Hübel, W. Korten, U. J. van Severen, J. A. Cizewski, J. H. Medina, D. R. Napoli, C. R. Alvarez, G. Lo Bianco, and S. Signorelli, Z. Phys. A **355** (1996) 337.

[Bal00] G. Baldsiefen, (2000), *et al., Updated level scheme of [Bal96], private communication with S. Chmel.*

[Bal01] D. L. Balabanski, K. Vyvey, G. Neyens, N. Coulier, R. Coussement, G. Georgiev, A. Lépine-Szily, S. Ternier, S. Teughels, M. Mineva, P. M. Walker, P. Blaha, D. Almehed, and S. Frauendorf, Phys. Rev. Lett. **86** (2001) 604.

[Bar57] J. Bardeen, L. N. Cooper, and J. R. Schrieffer, Phys. Rev. **108** (1957) 1175.

[Bat81] C. J. Batty, S. F. Biagi, R. A. J. Riddle, B. L. Roberts, G. J. Pyle, G. T. A. Squier, D. M. Asbury, and A. S. Clough, Nucl. Phys. **A355** (1981) 383.

[Bec91] J. A. Becker, A. Berger, J. Blomqvist, D. J. Decman, R. Estep, E. Henry, K. H. Maier, L. G. Mann, R. A. Meyer, N. A. F. M. Poppelier, N. Roy, W. Stoff, G. L. Strubble, and L. D. Wood, Nucl. Phys. **A522** (1991) 483.

[Bee78] R. Beetz, F. W. N. de Boer, J. K. Panman, J. Konijn, P. Pavlopoulos, G. Tibell, K. Zioutas, I. Bergström, K. Fransson, L. Tauscher, P. Blüm, R. Guigas, H. Koch, H. Poth, and L. M. Simons, Z. Phys. A **286** (1978) 215, and references therein.

[Ben79] R. Bengtsson and S. Frauendorf, Nucl. Phys. **A327** (1979) 139.

[Ben86] R. Bengtsson, S. Frauendorf, and F. R. May, At. Data Nucl. Data Tables **35** (1986) 49.

[Ben89a] R. Bengtsson, J. Dudek, W. Nazarewicz, and P. Oleanders, Phys. Scr. **39** (1989) 196.

[Ben89b] R. Bengtsson and W. Nazarewicz, Z. Phys. A **334** (1989) 269.

[Ben89c] T. Bengtsson, R. A. Broglia, E. Vigezzi, F. Barranco, F. Dönau, and J. Y. Zhang, Phys. Rev. Lett. **62** (1989) 2448.

[Ber78a] F. Bernthal, B. B. Back, O. Bakander, J. Borggreen, J. Pedersen, G. Sletten, H. Beuscher, D. Haenni, and R. Lieder, Phys. Lett. **B74** (1978) 211.

[Ber78b] F. Bernthal, B. B. Back, O. Bakander, J. Borggreen, J. Pedersen, G. Sletten, H. Beuscher, D. Haenni, and R. Lieder, Phys. Lett. **B74** (1978) 211.

[Bet36] H. A. Bethe and R. F. Bacher, Rev. Mod. Phys. **8** (1936) 1982.

[BF85] M. Barboza-Flores, O. Redi, and H. H. Stroke, Z. Phys. A **321** (1985) 85.

[Bij98] N. Bijnens, *Intruder States in Neutron-Deficient Even Po Nuclei and the Stability of the Z=82 Shell Closure*, (PhD thesis, K. U. Leuven, 1998, unpublished).

[Bil95] J. Billowes and P. Campbell, J. Phys. G **21** (1995) 707.

[Bla] P. Blaha, K. Schwarz, and J. Luitz, WIEN97 (Technological University Vienna, 1997, ISBN 3-9501031-0-4).

[Bla85] P. Blaha, K. Schwarz, and P. Herzig, Phys. Rev. Lett. **54** (1985) 1192.

[Bla96] P. Blaha, P. Dufek, K. Schwarz, and H. Haas, Hyperfine Interact. **96/97** (1996) 3.

[Bla00] P. Blaha, (2000), private communication.

[Boh53a] A. Bohr and B. R. Mottelson, Phys. Rev. **90** (1953) 717.

[Boh53b] A. Bohr and B. R. Mottelson, Phys. Rev. **89** (1953) 316.

[Boh53c] A. Bohr and B. R. Mottelson, Mat. Fys. Medd. Dan. Vidensk. Selsk. **27** (1953) No 16.

[Boh75] A. Bohr and B. R. Mottelson, *Nuclear Structure*, (Benjamin, London, 1975).

[Bon72] J. Bonn, G. Huber, H.-J. Kluge, L. Kugler, and E.-W. Otten, Phys. Lett. **B38** (1972) 308.

[Boo94] N. Boos, F. Le Blanc, M. Krieg, J. Pinard, G. Huber, M. D. Lunney, D. Le Du, R. Meunier, M. Hussonnious, O. Constantinescu, J. B. Kim, C. Briançon, J. E. Crawford, H. T. Duong, Y. P. Gangrski, T. Kühl, B. N. Markov, Y. T. Oganessian, P. Q. amd B. Roussière, and J. Sauvage, Phys. Rev. Lett. **72** (1994) 2689.

[Bou85] J. A. Bounds, C. R. Bingham, B. Juncar, H. K. Carter, G. A. Leander, R. L. Mlekodaj, E. H. Spejewski, and W. M. Fairbank, Jr., Phys. Rev. Lett. **55** (1985) 2269.

[Bra96] F. Brandolini, M. Ionescu-Bujor, N. H. Medina, R. V. Ribas, D. Bazzacco, M. De Poli, P. Pavan, C. R. Alvarez, G. de Angelis, S. Lunardi, D. De Acuna, D. R. Napoli, and S. Frauendorf, Phys. Lett. **B388** (1996) 468.

[Bri68] D. M. Brink and G. R. Satchler, *Angular momentum*, (Clarendon Press, Oxford, 1968).

[Bro73] C. Broude, M. B. Goldberg, G. Goldring, M. Hass, M. J. Renan, B. Sharon, Z. Shkedi, and D. F. H. Start, Nucl. Phys. **A215** (1973) 617.

[Bro89] M. Broidioi, *Pulsatie van de cyclotronbundel in het 10 to 1000 nanoseconden gebied*, (Diploma thesis, K. U. Leuven, 1989, unpublished).

[Bro91] C. Broude, M. Hass, G. Goldring, A. Alderson, I. Ali, D. M. Cullen, P. Fallon, F. Hanna, J. W. Roberts, and J. F. Sharpey-Shafer, Phys. Lett. **B264** (1991) 17.

[Bur80] B. Burghardt, R. Harzer, H. J. Hoeffgen, and G. Meisel, Phys. Lett. **B92** (1980) 64.

[Byr98] A. P. Byrne and *et al.*, ANU, Department of Nuclear Physics Annual Report **ANU-P/1381** (1998) 30, unpublished.

[Chm] S. Chmel and *et al.*, private communication.

[Chm97] S. Chmel, F. Brandolini, R. V. Ribas, G. Baldsiefen, A. Görgen, , M. De Poli, P. Pavan, and H. Hübel, Phys. Rev. Lett. **79** (1997) 2002.

[Chm01] S. Chmel, S. Frauendorf, and H. Hübel, (2001), to be published.

[Cho88] P. Chowdury, B. Fabricius, C. Christensen, F. Azgui, S. Bjørnholm, J. Borggreen, A. Holm, J. Pedersen, G. Sletten, M. A. Bentley, D. Howe, A. R. Mokhtar, J. D. Morrisson, J. F. Sharpey-Shafer, P. M. Walker, and R. M. Lieder, Nucl. Phys. **A485** (1988) 136.

[Chr76] J. Christiansen, P. Heubes, R. Keitel, W. Klinger, W. Loeffler, W. Sandner, and W. Witthuhn, Z. Phys. B **24** (1976) 177.

[Cla] R. M. Clark and A. O. Macchiavelli, An. Rev. Nucl. Part. Sci., to be published.

[Cla93] R. M. Clark, R. Wadsworth, E. S. Paul, C. W. Beausang, I. Ali, A. Astier, D. M. Cullen, P. J. Dagnall, P. Fallon, M. J. Joyce, M. Meyer, N. Redon, P. H. Regan, J. F. Sharpey-Shafer, W. Nazarewicz, and R. Wyss, Nucl. Phys. **A562** (1993) 121.

[Cla97] R. M. Clark, S. J. Asztalos, G. Baldsiefen, J. A. Becker, L. Bernstein, M. A. Deleplanque, , R. M. Diamond, P. Fallon, I. M. Hibbert, H. Hübel, R. Krücken, I. Y. Lee, A. O. Macchiavelli, R. W. MacLeod, G. Schmid, F. S. Stephens, K. Vetter, R. Wadsworth, and S. Frauendorf, Phys. Rev. Lett. **78** (1997) 1868.

[Cla98] R. M. Clark, R. Kruchen, S. J. Asztalos, J. A. B. B. Busse, S. Chmel, M. A. Deleplanque, R. M. Diamond, P. Fallon, D. Jenkins, K. Hauschild, I. M. Hibbert, H. Hübel, I. Y. Lee, A. O. Macchiavelli, R. W. MacLeod, G. Schmid, F. S. Stephens, U. J. van Severen, K. Vetter, R. Wadsworth, and S. Wan, Phys. Lett. **B440** (1998) 251.

[Con63] E. U. Condon and G. H. Shortley, *The Theory of Atomic Spectra*, (Cambridge University Press, Cambridge, 1963), p. 76-77.

[Cou85] R. Coussement, P. Put, G. Scheveneels, and F. Hardeman, Hyperfine Interact. **26** (1985) 1021.

[Cou99] N. Coulier, G. Neyens, S. Teughels, D. L. Balabanski, R. Coussement, G. Georgiev, S. Ternier, and K. Vyvey, Phys. Rev. C **59** (1999) 1935.

[CT88] C. Cohen-Tannoudji, J. Dupont-Roc, and G. Grynberg, *Processus d'Interaction Entre Photons et Atoms*, (Inter Editions, Paris, 1988).

[Cul00] D. M. Cullen, S. L. king, A. T. Reed, J. A. Simpson, P. M. Walker, C. Wheldon, F. Xu, G. D. Dracoulis, I.-Y. Lee, A. O. Machiavelli, R. W. MacLeod, A. N. Wilson, and C. Barton, Phys. Rev. C **60** (2000) 064301.

[Cum85] J. B. Cumming and D. E. Alburger, Phys. Rev. C **31** (1985) 1494.

[Daf85] E. Dafni, J. Bendahan, C. Broude, G. Goldring, M. Hass, E. Naim, M. H. Rafailovich, C. Chasman, O. C. Kistner, and S. Vajda, Nucl. Phys. **A443** (1985) 135.

[deS74] A. deShalit and H. Feshbach, *Theoretical Nuclear Physics, Volume I: Nuclear Structure*, (John Wiley and Sons, New York, 1974).

[Dic67] L. O. Dickie and F. M. Kelly, Can. Journ. Phys. **45** (1967) 2249.

[Dim00] V. I. Dimitrov, S. Frauendorf, and F. Dönau, Phys. Rev. Lett. **84** (2000) 5732.

[Dra98] G. D. Dracoulis, F. G. Kondev, and P. M. Walker, Phys. Lett. **B419** (1998) 7, and references therein.

[Dra00] G. D. Dracoulis, Phys. Scripta **T88** (2000) 54.

[Dud84] J. Dudek, W. Nazarewicz, and P. Olanders, Nucl. Phys. **A420** (1984) 285.

[Duf95] P. Dufek, P. Blaha, and K. Schwarz, Phys. Rev. Lett. **75** (1995) 3445.

[Edm57] A. R. Edmonds, *Angular Momentum in Quantum Mechanics*, (Princeton University Press, Princeton, 1957).

[Eis68] G. Eisele, I. Koniordos, G. Müller, and R. Winkler, Phys. Lett. **B28** (1968) 256.

[Ell53] R. J. Elliot and K. W. H. Stevens, Proc. R. Soc. London **218** (1953) 553.

[Esa77] M. T. Esat, D. C. Kean, R. H. Spear, M. P. Fewell, and A. M. Baxter, Phys. Lett. **B72** (1977) 49.

[Esa81] M. T. Esat, M. P. Fewell, R. H. Spear, and T. H. Zabel, Nucl. Phys. **A362** (1981) 227.

[Fan59] U. Fano and G. Racah, *Irreducible Tensorial Sets*, (Academic Press Inc., New York, 1959).

[Fan87] B. Fant, T. Weckström, H. C. Jain, L. O. Norlin, K. G. Rensfelt, P. Carlé, and U. Rosengård, Nucl. Phys. **A475** (1987) 338.

[Fan91] B. Fant, R. J. Tanner, P. A. Butler, A. N. James, G. D. Jones, R. J. Poynter, C. A. White, K. L. Ying, D. J. G. Love, J. Simpson, and K. A. Connell, J. Phys. G **17** (1991) 319.

[Fir96] R. B. Firestone, *Table of Isotopes, eight edition*, (John Wiley and Sons, New York, 1996), edited by V. S. Shirley.

[Fra74] S. Frauendorf and V. V. Pashkevich, Phys. Lett. **B55** (1974) 365.

[Fra93] S. Frauendorf, Nucl. Phys. **A557** (1993) 259c.

[Fra97] S. Frauendorf, Z. Phys. A **358** (1997) 163.

[Fra00a] S. Frauendorf, Rev. Mod. Phys. (2000), in print.

[Fra00b] S. Frauendorf, Nucl. Phys. **A677** (2000) 115.

[Fra00c] S. Frauendorf, (2000), private communication.

[Fra00d] S. Frauendorf, K. Neergård, J. A. Sheikh, and P. M. Walker, Phys. Rev. C **61** (2000) 064324.

[Gad97] A. Gadea, G. de Angelis, C. Fahlander, M. De Poli, E. Farnea, Y. Li, D. R. Napoli, Q. Pan, P. Spoalore, D. Bazzacco, S. M. Lenzi, S. Lunardi, C. M. Petrache, F. Brandolini, P. Pavan, C. R. Alvarez, M. Sferrazza, P. G. Bizzeti, A. M. B. Sona, J. Nyberg, M. Lipoglavsek, J. Persson, J. Cederkall, D. Seweryniak, A. Johnson, H. Grawe, F. Soramel, M. Ogawa, A. Makishima, R. Schubart, and S. Frauendorf, Phys. Rev. C **55** (1997) 1, and references therein.

[Geo70] S. George and R. A. Klingberg, Journ. Opt. Soc. Am. **60** (1970) 869.

[Geo98] U. Georg, W. Borchers, M. Klein, P. Lievens, R. Neugart, M. Neuroth, P. M. Rao, C. Schulz, and the ISOLDE Collaboration, Eur. Phys. J. A **3** (1998) 225.

[Gol82] G. Goldring, in *Heavy Ion Collisions*, p. 483, (North-Holland, Amsterdam, 1982), edited by R. Bock.

[Gör] A. Görgen, N. Nenoff, H. Hübel, G. Baldsiefen, J. A. Becker, A. P. Byrne, S. Chmel, R. M. Clark, M. A. Deleplanque, R. M. Diamond, P. F. adn K. Hauschild, I. M. Hibbert, W. Korten, R. Krücken, I. Y. Lee, A. O. Macchiavelli, E. S. Paul, U. J. Van Severen, F. S. Stephens, K. Vetter, R. Wadsworth, A. N. Wilson, and J. N. Wilson, Nucl. Phys. **A** , in print.

[Gro62] L. Grodzins, Phys. Lett. **2** (1962) 88.

[Gus67] C. Gustafson, I. L. Lamm, B. Nilsson, and S. G. Nilsson, Arkiv Fysik **36** (1967) 613.

[Haa73] H. Haas and D. A. Shirley, J. Chem. Phys. **58** (1973) 3339.

[Hag68] R. S. Hager and E. C. Seltzer, Nucl. Data Tables **A4** (1968) 1.

[Har91a] F. Hardeman, *Nucleaire quadrupoolmomenten van hoge spin toestanden in de Franciumisotopen*, (PhD thesis, K. U. Leuven, 1991, unpublished).

[Har91b] F. Hardeman, G. Scheveneels, G. Neyens, R. Nouwen, G. S'heeren, M. V. den Bergh, and R. Coussement, Phys. Rev. C **43** (1991) 130.

[Har91c] F. Hardeman, G. Scheveneels, G. Neyens, R. Nouwen, G. S'heeren, M. V. den Bergh, and R. Coussement, Phys. Rev. C **43** (1991) 514.

[Has75] R. C. Haskell, F. D. Correll, and L. Madansky, Phys. Rev. B **11** (1975) 3268.

[Hel68] R. G. Helmer and C. W. Reich, Nucl. Phys. **A114** (1968) 649.

[Hel73] R. G. Helmer and C. W. Reich, Nucl. Phys. **A211** (1973) 1.

[Heu79] F. Heubes, W. Keppner, and G. Schatz, Hyperfine Interact. **7** (1979) 93.

[Hey83] K. Heyde, P. V. Isacker, J. L. Wood, and R. A. Meyer, Phys. Rep. **102** (1983) 291.

[Hey87] K. Heyde, J. Jolie, J. Moreau, J. Ryckebusch, M. Waroquier, P. Van Duppen, M. Huyse, and J. L. Wood, Nucl. Phys. **A466** (1987) 189.

[Hey92] K. Heyde, Hyperfine Interact. **75** (1992) 69.

[Hey94] K. L. G. Heyde, *The Nuclear Shell Model, 2nd edition*, (Springer-Verlag, New York, Berlin and Heidelberg, 1994), and references therein.

[Hüb97] H. Hübel, Prog. Part. Nucl. Phys. **38** (1997) 89.

[Hug93] J. R. Hughes, Y. Liang, R. V. F. Janssens, A. Kuhnert, J. A. Becker, I. Ahmad, I. G. Bearden, M. J. Brinkman, J. Burde, M. P. Carpenter, J. A. Cizewski, P. J. Daly, M. A. Deleplanque, R. M. Diamond, J. E. Draper, C. Duyar, B. Fornal, U. Garg, Z. W. Grabowski, E. A. Henry, R. G. Henry, W. Hesselink, N. K. Nayestanaki, W. H. Kelly, T. L. Khoo, T. L. adn R. H. Mayer, D. Nissius, J. R. B. Oliveira, A. J. M. Plompen, W. Reviol, E. Rubel, F. Soramel, F. S. Stephens, M. A. Stoyer, D. Vo, and T. F. Wang, Phys. Rev. C **47** (1993) R1337, and references therein.

[Huy91] M. Huyse, *Indringtoestanden in het Loodgebied*, (Habilitation thesis, K. U. Leuven, 1991, unpublished).

[Iva92] E. A. Ivanov, G. Nicolescu, and D. Plostinaru, Z. Phys. B **89** (1992) 57.

[Jän88] H. J. Jänsch and D. Fick, Z. Phys. D **9** (1988) 117.

[Joh71] A. Johnson, H. Ryde, and J. Sztarkier, Phys. Lett. **B34** (1971) 605.

[Joy78] A. M. R. Joye, A. M. Baxter, S. Hinds, D. C. Kean, and R. H. Spear, Phys. Lett. **B72** (1978) 307.

[Juu94] S. Juutinen, R. Julin, M. Piiparen, P. Ahonen, B. Cederwall, C. Fahlander, A. Lampinen, T. Lönnroth, A. Maj, S. Mitarai, D. Müller, J. Nyberg, P. Simeck, M. Sugawara, I. Thorslund, S. Törmänen, A. Virtanen, and R. Wyss, Nucl. Phys. **A573** (1994) 306.

[Ker81] A. K. Kerman and N. Onishi, Nucl. Phys. **A361** (1981) 179.

[Kon00] P. Kondev and *et al.*, In *NS2000, Book of Abstracts (East Lansing conference)*, (2000), and to be published.

[Kut95] T. Kutsavora, R. M. Lieder, H. Schnare, G. Hebbinghaus, D. L. Balabanski, W. Gast, A. Krämer-Flecken, M. A. Bentley, P. Fallon, D. Howe, A. R. Mokhtar, J. F. Sharpey-Schafer, P. M. Walker, P. Chowdury, B. Fabricius, G. Sletten, and S. Frauendorf, Nucl. Phys. **A587** (1995) 111.

[Lag91] J. M. Lagrange, M. Pautrat, J. S. Dionisio, C. Vieu, and J. Vanhorenbeeck, Nucl. Phys. **A530** (1991) 437.

[Lan70] D. A. Landman and A. Lurio, Phys. Rev. A **1** (1970) 1330.

[Lan00] S. Lany, P. Blaha, J. Hamann, V. Ostheimer, H. Wolf, and T. Wichert, Phys. Rev. B **62** (2000) R2259.

[Lee72] W. Y. Lee, M. Y. Chen, S. C. Chen, E. R. Macaguo, A. M. Rushton, and C. S. Wu, Nucl. Phys. **A181** (1972) 14.

[Lie78] R. M. Lieder and H. Ryde, in *Advances in Nuclear Physics*, volume 10, p. 1, (Plenum Press, New York-London, 1978).

[Lin59] I. Lindgren and C. M. Johansson, Arkivför Fysik **15** (1959) 445.

[Lin78] C. G. Linden, I. Bergström, J. Blomqvist, and C. Roulet, Z. Phys. A **284** (1978) 217.

[Lit80] A. Little, H. C. Jain, S. M. Lazarus, T. K. Saylor, B. B. Triplett, and S. S. Hanna, Hyperfine Interact. **8** (1980) 3.

[Löb68] K. E. G. Löbner, Phys. Lett. **B26** (1968) 369.

[Löb70] K. E. G. Löbner, M. Vetter, and V. Honig, Nucl. Data Tables A **7** (1970) 495, and references therein.

[Löb75] K. E. G. Löbner, in *The Electromagnetic Interaction in Nuclear Spectroscopy*, p. 141, (North-Holland, Amsterdam, 1975), edited by W. D. Hamilton.

[Lub96] E. Lubkiewicz, H. J. Wollersheim, R. Kulessa, C. Briançon, W. Brüchle, O. Constantinescu, M. Dębovski, E. Ditzel, H. Folger, J. Gerl, F. Hannachi, T. Happ, M. Hussonios, E. Jäger, S. Karamian, M. Kaspar, T. Kröll, Y. T. Oganessian, I. Peter, H. Schaffner, S. Schremmer, R. Schubert, N. Traumann, K. Vetter, and G. Zauner, Z. Phys. A **355** (1996) 377.

[Lup83] C. H. P. Lupis, *Chemical Thermodynamics of Materials*, (North-Holland, 1983).

[Mah79] H.-E. Mahnke, T. K. Alexander, H. R. Andrews, O. Häusser, P. Taras, D. Ward, E. Dafni, and G. D. Sprouse, Phys. Lett. **B88** (1979) 48.

[Mah87] H.-E. Mahnke, Hyperfine Interact. **34** (1987) 47.

[Mat62] E. Matthias, W. Schneider, and R. M. Steffen, Phys. Rev. **125** (1962) 261.

[May49] M. G. Mayer, Phys. Rev. **75** (1949) 1969.

[MM84] M. I. Macias-Marques, C. Bourgeois, P. Kilcher, B. Roussire, J. Sauvage, M. C. Abreu, and M. G. Porquet, Nucl. Phys. **A427** (1984) 205.

[Mor76] H. Morinaga and T. Yamazaki, *In-beam Gamma-ray Spectroscopy*, (North-Holland, Amsterdam, 1976).

[Mös59] R. Mössbauer, Z. Naturforsch. A **14** (1959) 211.

[Mot60] B. R. Mottelson and J. G. Valatin, Phys. Rev. Lett. **5** (1960) 511.

[Mue99] W. F. Mueller, H. Q. Jin, J. M. Lewis, W. Reviol, L. L. Riedinger, M. P. Carpenter, C. Baktash, J. D. Garrett, N. R. Johnson, I. Y. Lee, F. K. McGowan, and C.-H. Yu, Phys. Rev. C **59** (1999) 2009.

[Naz90] W. Nazarewicz, M. A. Riley, and J. D. Garrett, Nucl. Phys. **A512** (1990) 61.

[Naz96] W. Nazarewicz and I. Ragnarsson, in *Handbook of Nuclear Properties*, edited by D. N. Poenaru and W. Greiner, p. 80, (Clarendon Press, Oxford, 1996), and references therein.

[Nef95] M. Neffgen, G. Baldsiefen, S. Frauendorf, H. Grawe, J. Heese, H. Hübel, H. Kluge, A. Korichi, W. Korten, K. H. Maier, D. Mehta, J. Meng, N. Nenoff, M. Piiparen, M. S. andR. Schubart, U. J. van Severen, N. Singh, G. Sletten, B. V. Rao Thirumala, and P. Willsau, Nucl. Phys. **A595** (1995) 499.

[Neu88] R. Neugart, Hyperfine Interact. **43** (1988) 441.

[New67] J. O. Newton, F. S. Stephens, R. M. Diamond, K. Kotajima, and E. Matthias, Nucl. Phys. **A95** (1967) 357.

[Ney93a] G. Neyens, *Ontwikkeling van een Doelgerichte LEMS-opstelling en Bepalen van het Quadrupoolmoment van Isomere Toestanden in Radiumisotopen*, (PhD thesis, K. U. Leuven, 1993, unpublished).

[Ney93b] G. Neyens, R. Nouwen, G. S'heeren, M. V. D. Bergh, and R. Coussement, Nucl. Phys. **A555** (1993) 629.

[Ney94] G. Neyens, R. Nouwen, and R. Coussement, Nucl. Instr. and Meth. A **340** (1994) 555.

[Ney97a] G. Neyens, N. Coulier, S. Ternier, K. Vyvey, S. Michiels, R. Coussement, D. L. Balabanski, J. M. Casandijan, M. Chartier, D. Cortina-Gil, M. Lewitowicz, W. Mittig, A. N. Ostrowski, P. Roussel-Chomaz, N. Alamanos, and A. Lépine-Szily, Phys. Lett. **B393** (1997) 36.

[Ney97b] G. Neyens, S. Ternier, N. Coulier, K. Vyvey, R. Coussement, and D. L. Balabanski, Nucl. Phys. **A625** (1997) 668.

[Ney99] G. Neyens, N. Coulier, S. Teughels, G. Georgiev, B. A. Brown, W. F. Rogers, D. L. Balabanski, R. Coussement, A. Lépine-Szily, M. Lewitowicz, W. Mittig, F. de Oliveira Santos, P. Roussel-Chomaz, S. Ternier, K. Vyvey, and D. Cortina-Gil, Phys. Rev. Lett. **82** (1999) 497.

[Nil55] S. G. Nilsson, Mat. Fys. Dan. Vid. Selsk. **29** (1955) No. 16.

[Nil95] S. G. Nilsson and I. Ragnarsson, *Shapes and Shells in Nuclear Structure*, (Cambridge University Press, Cambridge, 1995).

[Nol79] P. J. Nolan and J. F. Sharpey-Schafer, Rep. Prog. Phys. **42** (1979) 1.

[Ori73] H. Orihara, Y. Ishizaki, G. F. Trentelman, M. Kanazawa, K. Abe, and H. Yamaguchi, Phys. Rev. C **9** (1973) 266.

[Oro01] A. M. Oros and K. Heyde, (2001), private communication.

[Pas75] V. V. Pashkevich and S. Frauendorf, Sov. J. Nucl. Phys. **20** (1975) 588.

[Pea97] C. J. Pearson, P. M. Walker, C. S. Purry, G. D. Dracoulis, S. Bayer, A. P. Byrne, T. Kibedi, F. G. Kondev, T. Shimuza, R. A. Bark, G. Sletten, and S. Frauendorf, Phys. Rev. Lett. **79** (1997) 605.

[Pen87] J. Penninga, W. H. A. Hesselink, A. Balanda, A. Stolk, H. Verheul, J. van Klinken, H. J. Riezebos, and M. J. A. de Voigt, Nucl. Phys. **A471** (1987) 535.

[Pet98] H. M. Petrilli, P. E. Blöchl, P. Blaha, and K. Schwarz, Phys. Rev. B **57** (1998) 14690.

[Pow68] J. P. Powers, Phys. Rev. **169** (1968) 1.

[Pra73] H. C. Pradhan and Y. Nogami, Nucl. Phys. **A201** (1973) 357.

[Pur95] C. S. Purry, P. M. Walker, G. D. Dracoulis, T. Kibédi, S. Bayer, A. M. Bruce, A. P. Byrne, M. Dasgupta, W. Gelletly, F. Kondev, P. H. Regan, and C. Thwaites, Phys. Rev. C **75** (1995) 406.

[Rac42] G. Racah, Phys. Rev. **62** (1942) 438.

[Rag89] P. Raghavan, At. Data Nucl. Data Tables **60** (1989) 287, and references therein.

[Ram87] S. Raman, C. H. Malarkey, W. T. Milner, C. W. Nestor, Jr., and P. H. Stelson, At. Data Nucl. Data Tables **36** (1987) 1.

[Ram89] S. Raman, C. W. Nestor, S. Kahane, and K. H. Bhatt, At. Data Nucl. Data Tables **42** (1989) 1.

[Rin80] P. Ring and P. Schuck, *The Nuclear Many Body Problem*, (Springer-Verlag, New York, 1980).

[Röp00] H. Röpke, Nucl. Phys. **A674** (2000) 95.

[Ros57] M. E. Rose, *Elementary Theory of Angular Momentum*, (John Wiley and Sons, New York, 1957).

[Rut11] E. Rutherford, Philosophical Magazine **1911** (1911) 669.

[Ruy86] J. J. V. Ruyven, J. Penninga, W. H. A. Hesselinck, P. V. Nes, K. Allaart, E. J. Hengeveld, and H. Verheul, Nucl. Phys. **A449** (1986) 579.

[Sag88] H. Sagawa and A. Arima, Phys. Lett. **B202** (1988) 15.

[Sat94] W. Satula, R. Wyss, and P. Magierski, Nulc. Phys. **A578** (1994) 45.

[Sch82] G. Schatz, E. Dafni, H. H. Bertschat, C. Broude, F. D. Davidosky, and M. Hass, Z. Phys. B **49** (1982) 23, and references therein.

[Sch88] G. Scheveneels, *Toestandsmengingsspectroscopie voor in-bundel quadrupoolinteractiemetingen*, (PhD thesis, K. U. Leuven, 1988, unpublished).

[Sch89] G. Scheveneels, F. Hardeman, G. Neyens, and R. Coussement, Hyperfine Interact. **52** (1989) 257.

[Sch91] G. Scheveneels, F. Hardeman, G. Neyens, and R. Coussement, Phys. Rev. C **43** (1991) 2560.

[Sch92] K. Schwarz and P. Blaha, Z. Naturforsch. A **47** (1992) 197.

[Sch96] H. Schumacher, H. J. Brede, V. Dangendorf, W. D. Newhauser, R. Nolte, U. J. Schrewe, and J. P. Muelders, CYCLONE annual report (1996) 101.

[Sch99] H. Schnare, R. Schwengner, S. Frauendorf, F. Dönau, L. Käubler, H. Prade, A. Jungclaus, K. P. Lieb, C. Lingk, S. Skoda, J. Eberth, G. de Angelis, A. Gadea, E. Farnea, D. R. Napoli, C. A. Ur, and G. Lo Bianco, Phys. Rev. Lett. **82** (1999) 4408.

[Sem81] W. Semmler, P. Raghavan, and M. Senba, Z. Phys.B **45** (1981) 29.

[She66] E. Sheldon and D. M. Patter, Rev. Mod. Phys. **38** (1966) 143.

[Sob79] I. I. Sobleman, *Atomic Spectra and Radiative Transitions*, (Springer-Verlag, Berlin, 1979).

[Spe80] R. H. Spear, M. T. Esat, M. P. Fewell, D. C. Kean, and T. H. Zabel, Nucl. Phys. **A345** (1980) 252.

[Ste72] F. S. Stephens and R. S. Simon, Nucl. Phys. **A286** (1972) 257.

[Ste75] R. M. Steffen and K. Alder, in *The Electromagnetic Interaction in Nuclear Spectroscopy*, p. 505, (North-Holland, Amsterdam, 1975), edited by W. D. Hamilton.

[Ste83] C. Stenzel, H. Grawe, H. Haas, H. E. Mahnke, and K. H. Maier, Nucl. Phys. **A411** (1983) 248.

[Ste85] C. Stenzel, H. Grawe, H. Haas, H.-E. Mahnke, and K. H. Maier, Z. Phys. A **322** (1985) 83.

[Sto] W. Stoeffl, FITEK program (Lawrence Levermore National Laboratory, 1984).

[Str67] V. M. Strutinsky, Nucl. Phys. **A95** (1967) 420.

[Stu95] A. E. Stuchbery, Nucl. Phys. **A589** (1995) 222.

[Tal93] I. Talmi, *Simple Models of Complex Nuclei: The Shell Model and Interacting Boson Model*, (Harwood Academic Publishers, Chur, 1993).

[Ter98a] S. Ternier, *Extending the applicability of the Level Mixing Spectroscopy method*, (PhD thesis, K. U. Leuven, 1998, unpublished).

[Ter98b] S. Ternier, G. Neyens, K. Vyvey, J. Odeurs, N. Coulier, S. Michiels, R. Coussement, D. L. Balabanski, and R. Kulkarni, Nucl. Instrum. Methods Phys. Res. B **140** (1998) 235.

[Trö93] W. Tröger, T. Butz, P. Blaha, and K. Schwarz, Hyperfine Interact. **80** (1993) 1109.

[Ulm86] G. Ulm, S. K. Bhattacherjee, P. D. adn G. Huber, H.-J. Kluge, T. Kül, H. Lochmann, E.-W. Otten, and K. Wendt, Z. Phys. A **325** (1986) 247.

[VD84] P. Van Duppen, E. Coenen, K. Deneffe, M. Huyse, K. Heyde, and P. V. Isacker, Phys. Rev. Lett. **52** (1984) 1974.

[Via87] R. Vianden, Hyperfine Interact. **35** (1987) 1079, and references therein.

[vW35] C. F. von Weiszäcker, Z. Phys. **96** (1935) 431.

[Vyv97] K. Vyvey, G. Neyens, S. Ternier, N. Coulier, S. Michiels, R. Coussement, D. L. Balabanski, and A. Lépine-Szily, Acta Phys. Pol. B **28** (1997) 329.

[Vyv99] K. Vyvey, G. Neyens, D. L. Balabanski, S. Ternier, N. Coulier, S. Teughels, G. Georgiev, R. Wyckmans, R. Coussement, M. Mineva, P. M. Walker, A. P. Byrne, G. D. Dracoulis, and P. Blaha, J. Phys. G **25** (1999) 767.

[Vyv00] K. Vyvey, G. Neyens, N. Coulier, R. Coussement, G. Georgiev, S. Ternier, and S. Teughels, Phys. Rev. C **62** (2000) 034317.

[Vyv01a] K. Vyvey, S. Chmel, G. Neyens, H. Hübel, D. L. Balabanski, D. Borremans, N. Coulier, R. Coussement, W. De Clercq, G. Georgiev, N. Nenoff, S. Pancholi, D. Rossbach, R. Schwengner, and S. Teughels, (2001), to be published.

[Vyv01b] K. Vyvey, G. Neyens, S. Cottenier, N. Coulier, R. Coussement, G. Georgiev, S. Ternier, and S. Teughels, Nucl. Instr. Methods Phys. Res. A (2001), accepted for publication.

[Wal87] K. Wallmeroth, G. Bollen, A. Dohn, P. Egelhof, J. Grüner, F. Lindenlauf, U. Krönert, J. Campos, A. Rodriguez Yunta, M. J. G. Borge, A. Venugopalan, J. L. Wood, R. B. Moore, and H.-J. Kluge, Phys. Rev. Lett. **58** (1987) 1516.

[Wal91] P. M. Walker, G. D. Dracoulis, A. P. Byrne, B. Fabricius, T. Kibedi, and A. E. Stuchbery, Phys. Rev. Lett. **67** (1991) 433.

[Wal93] P. M. Walker, K. C. Yeung, G. D. Dracoulis, P. H. Regan, G. J. Lane, P. M. Davidson, and A. E. Stuchbery, Phys. Lett. **B309** (1993) 17.

[Wal94] P. M. Walker, G. D. Dracoulis, A. P. Byrne, B. Fabricius, T. Kibedi, A. E. Stuchbery, and N. Rowley, Nucl. Phys. **A568** (1994) 397.

[Wal97] P. M. Walker, D. M. Cullen, C. S. Purry, D. E. Appelbe, A. P. Byrne, G. D. Dracoulis, T. Kibédi, F. G. Kondev, L. Y. Lee, A. O. Macchiavelli, A. T. Reed, P. H. Regan, and F. Xu, Phys. Lett. **B408** (1997) 42.

[Wal99] P. M. Walker and G. D. Dracoulis, Nature **399** (1999) 35.

[Wat65] R. E. Watson, A. G. Gessard, and Y. Yafet, Phys. Rev. A **375** (1965) 140.

[Wea71] R. C. Weast, *Handbook of Chemistry and Physics*, (The Chemical Rubber Company, Cleveland, Ohio, 1971).

[Wei51] V. F. Weisskopf, Phys. Rev. C **83** (1951) 1073.

[Wer64] G. K. Wertheim, *Mösshauer Effect: Principles and Applications*, (Academic Press, New York, 1964).

[Whe99] C. Wheldon, *K-Isomerism at High-Spin Beyond the Fusion Limit*, (PhD thesis, University of Surrey, 1999, unpublished).

[Wig59] E. P. Wigner, *Group Theory and its Application to the Quantum Mechanics of Atomic Spectra*, (Academic Press, New York, 1959).

[Woo54] R. D. Woods and D. S. Saxon, Phys. Rev. **95** (1954) 577.

[Woo92] J. L. Wood, K. Heyde, W. Nazarewicz, M. Huyse, and P. Van Duppen, Phys. Rep. **215** (1992) 101.

[Wyc98] R. Wyckmans, *Bepalen van de quadrupoolfrequentie van de 35/2⁻ K-isomeer van* ^{179}*WTI*, (Diploma thesis, K. U. Leuven, 1998, unpublished).

[Xu98] F. R. Xu, P. M. Walker, J. A. Sheikh, and R. Wyss, Phys. Lett. **B435** (1998) 257, and private communication.

[Zen83] J. Y. Zeng and T. S. Cheng, Nucl. Phys. **A405** (1983) 1.

[Zie85] J. F. Ziegler and J. P. Biersack, *TRIM, TRansport of Ions in Matter*, (Pergamon, New York, 1985).

[Zyw81] S. Zywietz, H. Grawe, H. Haas, and M. Menningen, Hyperfine Interact. **9** (1981) 109.